Osaka University Knowledge Archive

Title	Reactive Synthetic Processing and Mechanical Characterization of Aluminide Intermetallics and Their Composites
Author(s)	井上, 雅博
Citation	大阪大学, 2001, 博士論文
Version Type	VoR
URL	https://hdl.handle.net/11094/2413
rights	
Note	

Osaka University Knowledge Archive : OUKA

https://ir.library.osaka-u.ac.jp/

Osaka University

工乙 8348

Reactive Synthetic Processing and Mechanical Characterization of Aluminide Intermetallics and Their Composites

（アルミナイド系金属間化合物およびその複合材料の
反応合成プロセッシングと機械的特性評価）

2001

Masahiro Inoue

Osaka University

Reactive Synthetic Processing and Mechanical Characterization of Aluminide Intermetallics and Their Composites

（アルミナイド系金属間化合物およびその複合材料の
反応合成プロセッシングと機械的特性評価）

2001

Masahiro Inoue

Osaka University

Synopsis

This thesis discusses fabrication processes and material design concept for Ni, Fe and Ti aluminides and their matrix composites which are promising as novel high temperature structural materials.

Ni_3Al, NiAl and FeAl alloys are successfully fabricated by reactive synthesis processes such as reactive hot-pressing and reactive infiltration－post annealing. Because these processes strongly depend on the formation of transient liquid phase by self-propagating reaction, control of the exothermic reaction between the transient metals and Al is the most important factor for fabricating these alloys with good quality. The alloying designs (micro- and macro-alloying with third elements) and composite material designs for these alloys are achieved by the reactive synthetic processes. In the present work, a reactive surface treatment process for intermetallics has been also developed as well as these processes. The nitrided layers with a graded composition are formed on TiAl alloys with reactive plasma generated at low gas pressure. These reactive synthetic processes are expected to generate new material designs for structural intermetallics.

The influential factors in determining the mechanical behavior of these alloys and composites and the strategies of material design are clarified through the mechanical characterization. Their mechanical properties are determined by intrinsic and extrinsic (environmental) factors. Their brittleness is basically determined by the intrinsic factors such as chemical bonding nature, grain boundary cohesion and defect structure. However, the fracture toughness of the alloys with relatively high ductility is always affected by the environmental effect. The present work proposes the alloying approach to suppress the environmental embrittlement. Furthermore, guidelines for the composite material designs with ceramic fine particles and fibers are proposed to improve their strength and reliability. The material design concept described in this thesis is believed to contribute to progress in structural intermetallics.

Contents

Synopsis i

Chapter 1 Introduction

1-1 General Introduction 1
1-2 Background to Ni, Fe and Ti Aluminides 2
1-2-1 Ni aluminides 2
1-2-2 Fe aluminides 4
1-2-3 Ti aluminides 6
1-3 Development of Novel Processing for Intermetallics 7
1-4 Objectives of Present work 8

References 9

Chapter 2 Reactive Synthetic Processes of Ni and Fe Aluminides

2-1 Introduction 11
2-2 Processing 11
2-2-1 Reactive hot-pressing 11
2-2-2 Reactive infiltration and post hot-pressing of infiltrated precursors 12
2-3 Results and Discussion 12
2-3-1 Reactive hot-pressing of Ni and Fe aluminides 12
(1) NiAl alloys 12
(2) FeAl alloys 20
2-3-2 Reactive infiltration and post hot-pressing of infiltrated precursors 24
(1) Ni aluminides 24
(2) Fe aluminides 29
2-4 Conclusion 33

References 34

Chapter 3 Mechanical Behaviors of Ni and Fe Aluminides Fabricated by Reactive Hot-pressing

3-1 Introduction 36

3-2 Experimental Procedure 36

3-2-1 Processing 36

3-2-2 Evaluation 36

3-3 Results and Discussion 38

3-3-1 Mechanical properties at ambient temperatures 38

(1) Compositional dependency 38

(2) Environmental effect 43

(3) Effect of alloying elements 47

3-3-2 Mechanical Properties at Elevated Temperatures 56

(1) Ni_3Al alloys 56

(2) NiAl and related alloys 64

(3) FeAl alloys 68

3-4 Conclusion 68

Appendix ch.3 : Metallic character (metallic bond) of substances 69

References 71

Chapter 4 Thermodynamic Properties and Interfacial Reactivity of Ni and Fe Aluminides

4-1 Introduction 73

4-2 Background of Thermodynamic investigation 73

4-2-1 Activity of constitutional elements in Ni and Fe aluminides 73

4-2-2 Thermodynamic calculation 74

4-3 Background to Molecular Orbital Simulation of Condensed Matters with Cluster Models 77

4-4 Experimental Procedure 79

4-5 Results and Discussion 79

4-5-1 Activity of constitutional elements in Ni and Fe aluminides 79

4-5-2 General description for interfacial reaction mechanism 82
4-5-3 Interfacial reactivity of Ni aluminides 83
4-5-4 Interfacial reactivity of FeAl alloys 90
4-6 Conclusion 97

Appendix ch.4 : Relationship between thermodynamic parameters estimated by inter-atomic potential and by molecular orbital 97

References 98

Chapter 5 Composite Material Designs for FeAl alloys

5-1 Introduction 99
5-2 Experimental Procedure 99
5-2-1 Processing 99
5-2-2 Characterization and evaluation 100
5-3 Results and Discussion 101
5-3-1 FeAl matrix composites with particles, whiskers and short fibers 101
(1) Fabrication 101
(2) Screening test of mechanical properties 104
(3) Fracture mechanism of particle reinforced composites at ambient temperatures 109
(4) Fracture mechanism of whisker and short fiber reinforced composites at ambient temperatures 113
(5) Tensile properties at ambient and elevated temperatures 116
5-3-2 Continuous fiber reinforced composites 120
5-4 Conclusion 127

References 128

Chapter 6 Composite Material Design for Ni Aluminides

6-1 Introduction 129

6-2 Experimental Procedure 129

6-3 Results and Discussion 130

6-3-1 Composites with ceramic fine particles 130

(1) Ni_3Al matrix composites 130

(2) NiAl matrix composites 141

(3) Theoretical consideration of optimum dispersoid radius for dispersion strengthening of NiAl at elevated temperatures 143

6-3-2 Fiber reinforced composites 146

6-4 Conclusion 152

References 153

Chapter 7 Direct Surface Modification of TiAl Alloys by Reactive Plasma Processing

7-1 Introduction 155

7-2 Reactive Plasma Processing 155

7-3 Experimental Procedure 157

7-4 Results and Discussion 160

7-4-1 Structure and mechanical properties of nitrided layers 160

7-4-2 Formation mechanism of Ti_2AlN layer 162

7-4-3 Oxidation resistance at elevated temperatures 170

7-5 Conclusion 171

References 171

Chapter 8 Remarks and Conclusion 173

List of Publications 176

Acknowledgement 180

Chapter 1

Introduction

1-1 General Introduction

In the 1950's, intermetallics had been recognized as one of novel structural materials for next generation [1]. In the early stage of the studies for structural intermetallics, Ni_3Al alloys attracted great interests because they had been already utilized as reinforcement phase in Ni based superalloys. As the results of these studies, interesting phenomena, such as yield stress anomaly in Ni_3Al, and defect hardening in NiAl [2], were discovered. Although the discovery of these phenomena stimulated many researchers in academic field, their practical applications had never established due to their brittleness. At the end of 1970's, a historic paper of Aoki and Izumi, concerning with ductilization of Ni_3Al alloys at ambient temperatures, was published in a Japanese journal [3]. They made a great success in ductilizing polycrystalline Ni_3Al alloys by B doping. Furthermore, another Japanese research group found large plastic deformability of TiAl alloys with Ti rich composition at the early years of 1980's [4]. These reports gave an impetus to material scientists and engineers who study structural intermetallics in the world. The challenges for developing high performance intermetallic base materials have been continuing for the last 20 years.

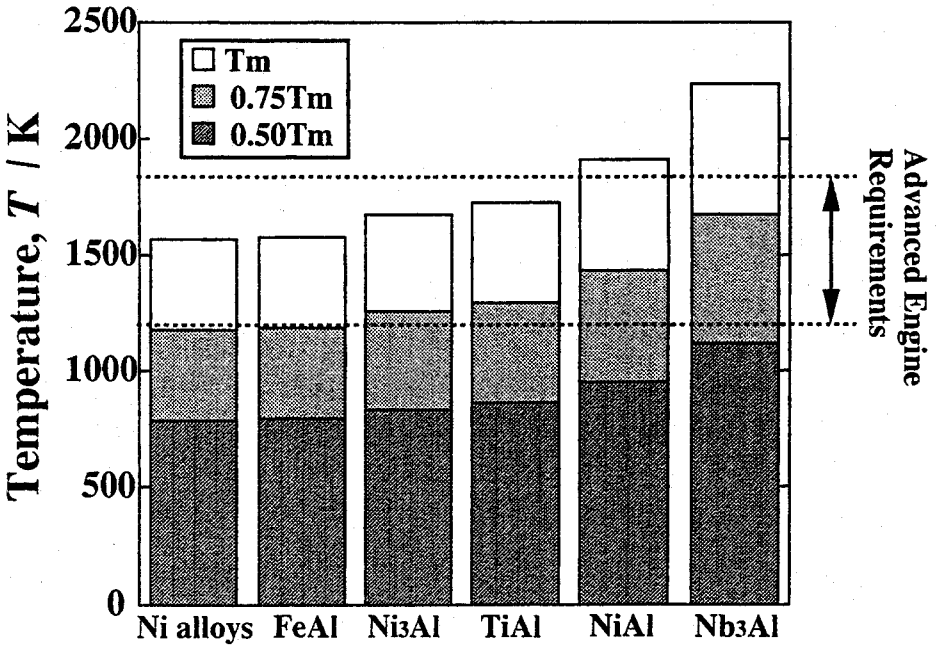

Fig. 1.1 Applicable temperatures of advanced intermetallics [5].

Figure 1.1 briefly shows applicable temperatures of advanced intermetallics that are promising as the candidates of novel structural materials in aerospace industry [5]. Because most materials retain significant strength up to approximately 0.5 to 0.6 of their melting point (T_m), $0.7T_m$ is a convenient criterion for selection of structural materials [5]. This thesis will discuss material designs of Ni_3Al, NiAl, FeAl and TiAl alloys for high temperature structural applications.

1-2 Background to Ni, Fe and Ti Aluminides

1-2-1 Ni aluminides

Figure 1.2 shows the equilibrium phase diagram of Ni-Al binary system [6]. In this system, Ni_3Al ($L1_2$ type structure) and NiAl (B2 type structure) alloys are expected as high temperature structural materials. Because Ni_3Al alloys have sufficient number of slip systems for extensive plastic deformation due to their crystal structure based on face-centered cubic (fcc) and metallic bonding character, they potentially have high ductility and fracture toughness. However, the ductility of polycrystalline Ni_3Al alloys is limited by weak grain boundary cohesion [7]. The dislocation motion in a grain must propagate to adjacent grains to appear large plastic deformability in polycrystalline alloys. The weak grain boundaries interrupt the propagation of dislocation motion among the grains. The weak grain boundaries of the alloys are related with their grain boundary structure and atomic

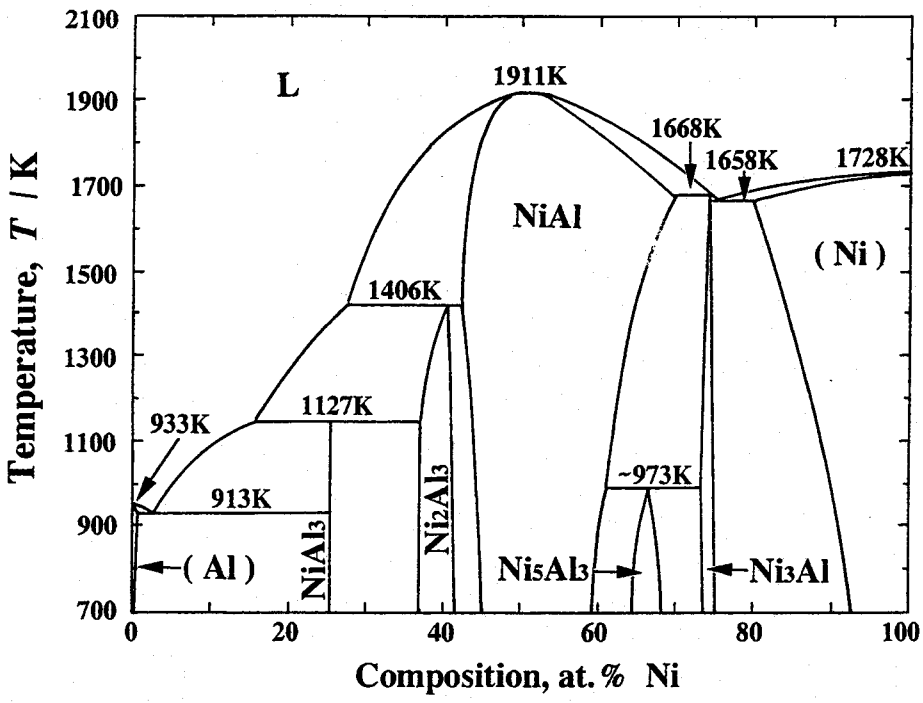

Fig. 1.2 Equilibrium phase diagrams of Ni-Al binary systems [6].

nature of the constitutional elements, such as electronegativity, valency and atomic size [7]. Moreover, the environmental factor also affects deterioration of grain boundary cohesion at ambient temperatures [8], as described in detail in Chapter 3.

Ni_3Al alloys are well-known to exhibit yield stress anomaly up to 900-1000 K [9], which provide them an advantage for structural applications at elevated temperatures. This anomalous behavior is explained by Kear-Wilsdorf mechanism [9] based on a particular behavior of super-lattice dislocation pairs. The dislocations in the alloys can slip along (111) at these temperatures, however, APB (anti-phase boundary) energy of these super-lattice dislocation pairs on (111) is much higher than that on (100). Hence, these dislocations tend to cross-slip from (111) to (100). Yield strength and hardness of the alloys increase with increasing temperature due to locking of the cross-slipped dislocations because (100) is not an active slip plane in this temperature range. Nevertheless, their strength drastically decreases above 1000 K because the dislocations can slip along (100). The strength and creep resistance above 1000 K is one of the most important problems in establishing their practical applications.

In contrast, NiAl alloys are inherently brittle because they have B2 type structure based on body-centered cubic (bcc) and the chemical bonding with large ionic character [10]. They have high anti-phase boundary (APB) energy due to their high ionicity. Consequently, they do not satisfy von Mises's criterion for extensive plastic deformability. In addition to their inherent brittleness, the mechanical properties of NiAl alloys is strongly governed by the defect structure [2]. The alloys with nonstoichiometric composition have higher yield strength and hardness rather than the stoichiometric alloy at ambient temperatures. The formation of point defects, such as substitutional Ni atoms on Al sites in the alloys with Ni-rich composition and Ni vacancies in ones with Al-rich composition, enhance the resistance for dislocation motion. The APB energy of the alloys should decrease to improve their ductility. Unfortunately, nobody has succeeded in decreasing their APB energy by the alloying with the third elements [11]. Their ductility is improved by refinement of their microstructure at 673 K as reported by Schulson and Barker [12]. However, the creep resistance of the alloys with such a fine grain size is drastically deteriorated by the grain boundary sliding at elevated temperatures. Therefore, the composite material designs with metallic and ceramic reinforcements are expected to improve their mechanical properties. The composites with ductile metals, including NiAl/Mo and NiAl/Cr(Mo) eutectic composites, are effective to improve their fracture toughness. In these eutectic composites, fibers and layered structure of ductile phase provide significant crack bridging [13]. On the other hand, the composite design with ceramic particles such as Y_2O_3 and AlN is useful approach to improve their creep resistance at elevated temperatures [14].

1-2-2 Fe aluminides

Figure 1.3 shows the equilibrium phase diagram of Fe-Al binary system [6]. In Fe-Al binary system, Fe_3Al ($D0_3$ type structure) and FeAl alloys (B2 type structure) attract great interests as the candidates for structural applications. Because the FeAl alloys have relatively low melting point, their application temperature is restricted up to intermediate temperatures (~1000 K). However, the alloys potentially offer many advantages such as high specific strength, superior oxidation and sulfidation resistance, and low material cost.

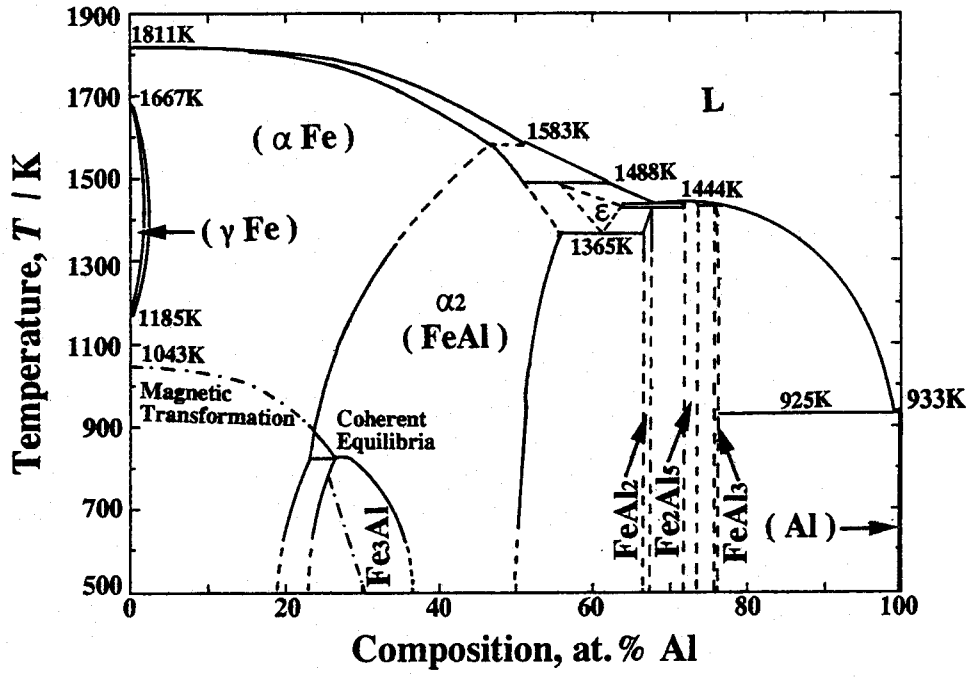

Fig. 1.3 Equilibrium phase diagrams of Fe-Al binary systems [6].

Although the FeAl alloys have B2 type structure, their mechanical properties are quite different from those of NiAl alloys. The difference in their mechanical properties is originated from the difference in chemical bonding nature between these alloys [10]. Figures 1.4 (a) and (b) show the density of state (DOS) and partial density of state (PDOS) of stoichiometric NiAl and FeAl alloys calculated by Eibler and Neckel [15], and Fu et al [16]. The calculation results approximately agrees with the experimental results of X-ray photoelectron spectroscopy (XPS) and ultraviolet photoelectron spectroscopy (UPS). The DOS of B2 aluminides is distinguished by a pseudo gap separating the bonding and anti-bonding states. The FeAl alloys have an electronic state with unfilled d-shell and the Fermi level within the bonding state region below the pseudo gap. The NiAl alloys have a more closed d-shell. In B2 aluminides, the chemical bonding is formed by hybridization of d-orbital of transient metal atoms with valence p-orbital of Al atoms, and

subsequent charge transfer from Al atoms to transient metal atoms. In FeAl, the cohesive directional d-bonding is formed resulting form the p-d hybridization and the charge transfer, in contrast to NiAl that have high ionicity. The bonding nature of FeAl leads to their high cleavage strength and ductility. The bonding nature of B2 aluminides can be divided into two categories [17]; FeAl type and NiAl type. RuAl and OsAl belong to the FeAl type category. On the other hand, CoAl, RhAl, IrAl, PdAl and PtAl have high inoicity in a similar manner to NiAl.

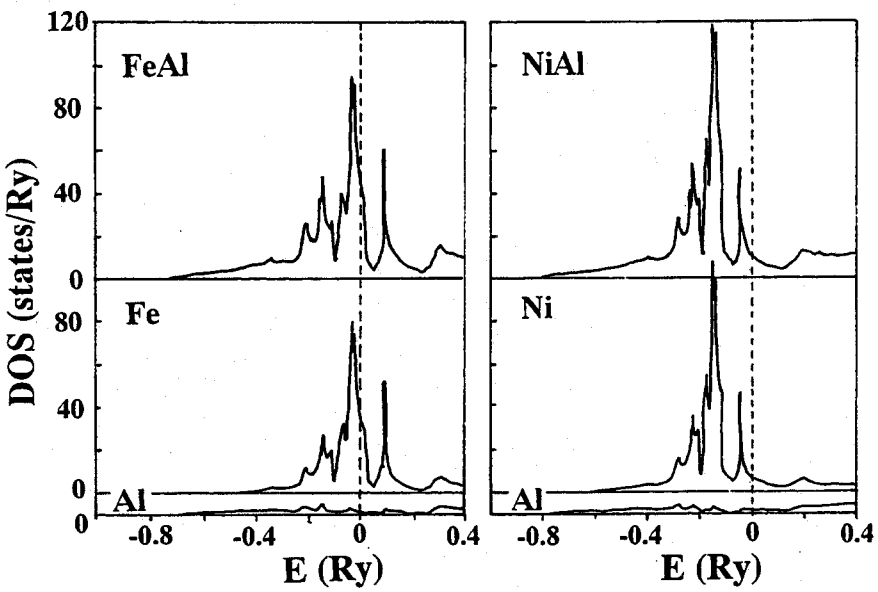

Fig. 1.4 DOS of stoichiometric (a) NiAl and (b) FeAl (B2) alloys [15-16].

FeAl alloys potentially have high plastic deformability resulting from <111> slip of dislocations. However, they often exhibit complex mechanical behavior at ambient and elevated temperatures. The complexity in their mechanical behavior is caused by the effect of point defects [18]. The thermal vacancies, that generate as di-vacancies at ~700 K, are permitted to retain even after cooling in the alloys. The retained vacancies strongly influence their mechanical properties by significant dislocation pinning effect [19]. The retained vacancies can be removed by annealing at 673 K for 100 h. FeAl alloys without retained vacancies reveal a yield stress anomaly originating from the thermal vacancy formation up to 700 K [18]. Therefore, the effect of vacancies is not ignorable in characterizing their mechanical properties.

Their mechanical properties are also governed by the environmental factor. Their ductility is suppressed by the moisture induced hydrogen embrittlement at ambient temperatures [20], although they have potentially significant plastic deformability. The mechanism of the environmental embrittlement will be discussed in detail in chapter 3. The environmental effect is also important for establishing the composite material design concept, because the mechanical properties of their composites with low volume fraction of reinforcements are governed by the effect.

1-2-3 Ti aluminides

Figure 1.5 shows the equilibrium phase diagram of Ti-Al binary system [6]. TiAl ($L1_0$ type structure) based alloys are desired to utilize as high temperature structural materials in aerospace and automobile industries because they have marked low density (3.76 x 10^3 kg m^{-3}) and high specific strength [21]. Their ductility exhibits a maximum value in the composition range of 47-48 at%Al. Furthermore, their ductility and fracture toughness are directly connected with their microstructural feature. In the 45-49 at%Al alloys, their microstructure is successfully controlled depending on conditions of processing and subsequent heat treatment. They can form several microstructures consisting TiAl and Ti_3Al ($D0_{19}$ type structure) such as duplex and fully lamella structures. The alloys with duplex structure show higher strength rather than the lamella ones below 1000 K. However, the alloys with lamella structure have higher strength above 1000 K than the duplex alloys. Moreover, the lamella alloys reveal a characteristic fracture behavior to improve their fracture toughness (20-35 MPa $m^{1/2}$) [22]. The large stress shielding is accomplished in the lamella alloys due to significant crack deflection resulting from lamella boundary splitting. The ductility of Ti_3Al phase is affected by the environmental factor, but not TiAl phase. The fracture toughness of the duplex alloys is suppressed by the moisture induced hydrogen embrittlement at ambient temperatures. However, the fracture toughness of the lamella alloys is unrelated with the environmental effect because the predominant factor in determining their toughness is their characteristic fracture

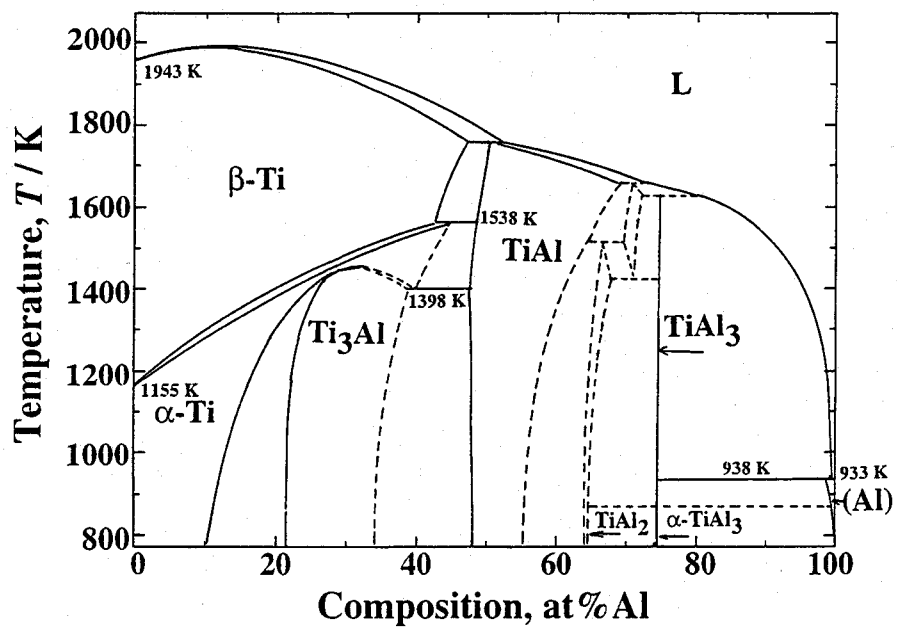

Fig. 1.5 Equilibrium phase diagrams of Ti-Al binary systems [6].

behavior. In addition, the composite material design with ceramic particles (TiB_2, etc.) [23] and fibers (SiC, etc.) [21] are examined as well as the microstructural control to improve strength and creep resistance at elevated temperatures.

1-3 Development of Novel Processing for Intermetallics

How are these intermetallics and related materials fabricated ? Conventional casting and powder metallurgy (PM) processes are applicable for fabricating intermetallics. However, intermetallics are unavoidable to spend high cost even by conventional casting because they require a vacuum condition at high temperatures. In PM processes, the starting powders of the alloys are necessary to be prepared before the sintering process. Recently, mechanical alloying (MA) of elementary powders attracts great interests as the preparation process of the starting powders [24]. The fully densified sintered bodies of intermetallics, that have characteristic microstructure such as "nano-scale structure", can be obtained by hot-pressing, hot isostatic pressing (HIP) and pulse electric current sintering (PECS) of the MA powders [24]. Unfortunately, the PM processes using MA powders have the disadvantage in mass production of large components.

To pursue economical benefit as well as improvement of their mechanical properties, novel processes using reactive synthesis of intermetallics, including reactive sintering [25], self-propagating high-temperature synthesis (SHS) [26], reactive infiltration [27-28] and exo-melt [29], have been studyed for the last 15 years. Furthermore, intermetallic matrix composites with ceramic powders and whiskers can be also fabricated by a reactive synthetic process (XD process) [23].

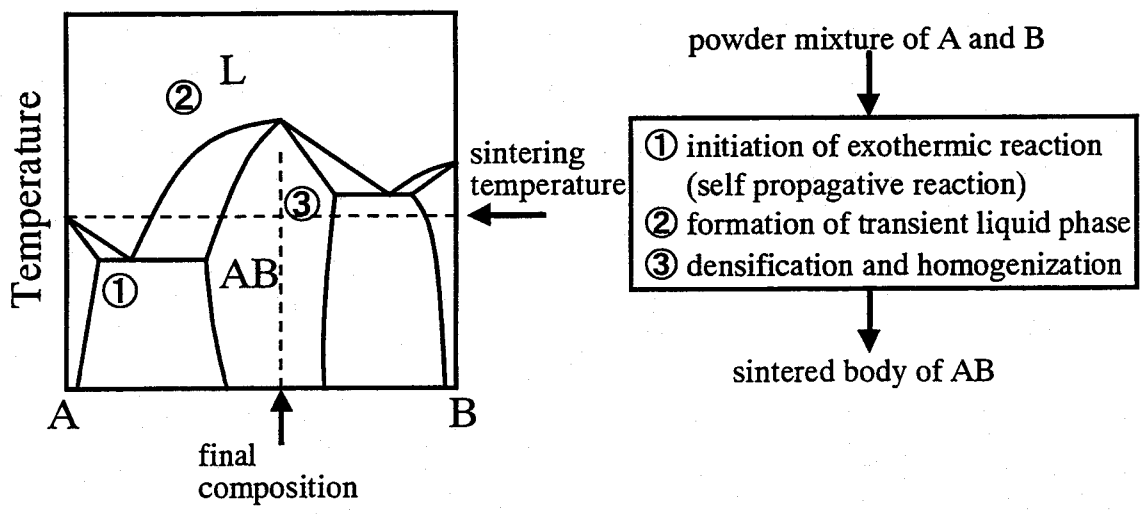

Fig. 1.6 Schematic illustration of a binary phase diagram for reactive sintering system [23].

German et al. [25] have clearly explained the principle of reactive synthetic processes. Figure 1.6 schematically shows a binary phase diagram for reactive sintering system. When a stoichiometric mixture of A and B powders is used, the reaction occurs above the lowest eutectic temperature in the system. Heat is liberated due to the thermodynamic stability of high melting temperature compounds. If heat is sufficiently generated, a transient liquid phase is spontaneously formed by the exothermic reaction. The reactive synthesis and densification of intermetallics can be accomplished by the effect of the liquid phase. In the case of the synthetic process of intermetallic matrix composites (XD process), the reinforcement materials are simultaneously formed with the matrix alloy. Therefore, the reactively synthesized composites are generally called "in-situ composites".

1-4 Objectives of Present Work

In spite of great activities in this field, only few practical applications of intermetallics have been established. The present work aims to obtain fundamental information for establishing high performance aluminides based materials. The problems in processing and material design of Ni, Fe and Ti aluminides will be discussed in the following chapters:

Chapter 2 : Reactive Synthetic Processes of Ni and Fe Aluminides

In the fabrication processes of intermetallics based on reactive synthesis, the exothermic reaction, subsequent homogenization and densification processes should be carefully controlled to obtain the alloys with high performance. The sintering mechanism in reactive hot-pressing is investigated to optimize the process condition. Furthermore, reactive infiltration process, that potentially have economical benefits rather than reactive hot-pressing, is applied to fabricate these aluminides. The suitable condition for fabricating these alloys is discussed in this chapter.

Chapter 3 : Mechanical Behaviors of Ni and Fe Aluminides Fabricated by Reactive Hot-Pressing

The complexity in mechanical behaviors of aluminides is caused by both of intrinsic and extrinsic factors. Their mechanical properties are determined by the combination of several phenomena originating from these factors. In Chapter 3, the author proposes a fracture mechanical test with variation of loading rate in several environments to examine kinetics of the environmental embrittlement. The mechanical behaviors resulting from the intrinsic factor are clearly discriminated with the environmental effect. Furthermore, the effect of several alloying elements is investigated to improve their mechanical properties.

Chapter 4 : Thermodynamic properties and interfacial reactivity of Ni and Fe aluminides

The thermodynamic properties of these alloys, which are measured by electromotive force (emf) technique [30], are discussed from the view point of quantum chemistry. The investigation method of interfacial reactivity of these alloys at bi-material interfaces is established using these thermodynamic parameters. The chemical compatibility of several ceramics with these alloys are theoretically and experimentally investigated to chose suitable reinforcements for these aluminides.

Chapters 5 & 6 : Composite Material Designs for Fe and Ni aluminides

These chapters investigate the mechanical behaviors of FeAl, Ni_3Al and NiAl matrix composites with ceramic fine particles, whiskers and continuous fibers fabricated by reactive hot-pressing. The objectives in these chapter are to be clarified reinforcing mechanism with these reinforcements and synergic effect of the matrix alloys. The guideline for developing high performance composites will be proposed for these alloys.

Chapter 7 : Direct Surface Modification of TiAl Alloys by Reactive Plasma Processing

Surface treatment for intermetallics is expected to be one of the important techniques to expand their applications as well as the composite designs. The present work investigates nitridation process of TiAl surface using reactive plasma generated under a low gas pressure [31]. The microstructure and mechanical properties of the modified layers will be discussed in Chapter 7.

References

[1] J. H. Westbrook, Intermetallic Compounds, vol.1, John Wiliey & Sons Ltd., (1994) 1

[2] J. H. Westbrook, J. Electrochem. Soc., 103 (1956) 54

[3] K. Aoki and O. Izumi, J. Jpn. Inst. Metals, 43 (1979) 1190

[4] T. Tsujimoto, K. Hashimoto and M. Nobuki, Mater. Trans. JIM, 33 (1992) 989

[5] D. L. Anton, D. M. Shah, D. N. Duhl and A. F. Giamei, JOM, 41 (9) (1989) 12

[6] T. B. Massalski (ed.), Binary Alloy Phase Diagrams, 2nd ed., vol.1, TMS, (1990)

[7] O. Izumi and T. Takasugi, J. Mater. Res., 3 (1988) 426

[8] E. P. George, C. T. Liu and D. P. Pope, Acta Mater., 44 (1996) 1757

[9] C. T. Liu and D. P. Pope, Intermetallic Compounds, vol.2, John Wiliey & Sons Ltd., (1995) 17

[10] C. L. Fu and M. H. Yoo, Acta Metall. Mater., 40 (1992) 703

[11] K. Ishida, R. Kainuma, N. Ueno and T. Nishizawa, Metall. Trans., 22A (1991) 441

[12] E. M. Shulson and D. R. Barker, Scripta Metall., 17 (1983) 519

[13] F. E. Heredia, M. Y. He, G. E. Lucas, A. G. Evans, H. E. Deve and D. Konitzer, Acta Metall. Mater., 41 (1993) 505.

[14] J. D. Whittenberger, E. Arzt and M. J. Luton, J. Mater. Res., 5 (1990) 271

[15] R. Eibler and A. Neckel, J. Phys. F: Metal Phys., 10 (1980) 2179

[16] C. L. Fu and M. H. Yoo, Acta Metall. Mater., 40 (1992) 703

[17] A. F. Voter, in ref.1, 77

[18] K. Yoshimi, S. Hanada and M. H. Yoo, Mat. Res. Soc. Symp. Proc., vol.460 (1997) 313

[19] M. Kogachi and T. Haraguchi, Mater. Sci., Eng., A230 (1997) 124

[20] C. T. Liu, E. H. Lee and C. G. Mckamey, Scripta Metall., 23 (1989) 875

[21] F. H. Froes, C. Suryanarayana and D. Eliezer, J. Mater. Sci., 27 (1992) 5113

[22] K. S. Chan and Y.-W. Kim, Metall. Trans., 23A (1992) 1663

[23] K. S. Kumar, J. A. S. Green, D. E. Larsen Jr. and L. D. Kramer, Advanced Mater. Process., 148 (4) (1995) 35

[24] H. Kimura, Rapid Solidification Technology, Technomic, (1993) 71

[25] A. Bose, B. H. Rabin and R. M. German, Powder Metallurgy Inter., 20 (1988) 25

[26] A. Makino and C. K. Law, J. Am. Ceram. Soc., 77 (1994) 778.

[27] D. C. Dunand, J. L. Sommer and A. Mortensen, Metall. Trans. 24A (1993) 2161

[28] K. Suganuma, Mater. Letters, 16 (1993) 22

[29] V. K. Sikka, S. C. Deevi and J. D. Vought, Advanced Mater. Process., 148 (5) (1995) 29

[30] A. Mikula, Thermodynamics of alloy formation, ed. by Y. A. Chang and F. Sommer, TMS (1997) 77

[31] M. Nunogaki, Y. Susuki, K. Kitahama, Y. Nakata, F. Hori, R. Oshima and S. Emura, Proc. Mat. Res. Soc. Symp., vol. 551 (1999) 303

Chapter 2

Reactive Synthetic Processes of Ni and Fe Aluminides

2-1 Introduction

Intermetallics and their related materials cost us considerable economical responsibility in their fabrication process due to their high melting point and poor machinability. It is one of the serious problems to establish their practical applications. Therefore, novel fabrication processes are necessary to be establish to pursue economical benefit as well as the improvement of their mechanical properties for utilizing these materials. The reactive synthetic processes with simultaneous consolidation such as reactive sintering [1-10], SHS [11-16], exo-melt [17] and reactive infiltration [18-20] are proposed to overcome the economical disadvantage. These processes basically depend on the formation of transient liquid phase by exothermic reaction. However, the process conditions are difficult to be optimized without exact understanding of the synthetic and consolidation mechanisms. In this chapter, the synthetic and consolidation mechanisms of Ni and Fe aluminides by reactive hot-pressing and reactive infiltration are investigated to optimize the process condition of these alloys.

2-2 Processing

2-2-1 Reactive hot-pressing

Raw powders of Ni (Fukuda Metals & Foils Co., Ltd. : apparent particle size 7μm, purity 99.7%), Fe (Mitsuwa Chem. Co., Ltd. : 5μm, 99.5%) and Al (Toyo Aluminum Co., Ltd. : ≦63 μm, 99.3%) were used as the starting materials for Ni and Fe Aluminides. These powders were mixed by ball milling in ethanol for 24 h. After drying the mixtures, they were hot-pressed at 1573-1773 K for NiAl and at 1273-1473 K for FeAl, with an applied pressure of 20-30 MPa in vacuum (~10^{-4} Torr) to obtain their sintered bodies of 50 mm ϕ x 5 mm h in dimension. The heating rate was 0.833 K/sec. To investigate the microstructural evolution in these samples, the hot-pressing was stopped on the way to the isothermal holding step. The density of these alloys was measured by the Archimedes method with toluene. Their microstructure was observed by optical microscopy (OM), scanning electron microscopy–energy dispersive X-ray analysis (SEM-EDX) and transmission electron

microscopy (TEM) after furnace-cooling. The constitutional phases were identified by X-ray diffraction (XRD) with Cu Kα radiation.

The reaction mechanism of the powder mixtures were also examined by differential thermal analysis (DTA). The DTA analysis was conducted in the temperature range of 300 – 1100 K with a heating rate of 0.167 K sec^{-1} under Ar gas flow (3.33×10^{-7} m^3 sec^{-1}).

2-2-2 Reactive infiltration and post hot-pressing of infiltrated precursors

Two kinds of raw powders of Ni with particle sizes of ≦44 μm and ≦100 μm (Fukuda Metals & Foils Co., Ltd. : 99.5 %) and a raw powder of Fe (Soekawa Chem. Co., Ltd. : 74 μm, 99.5 %) were sintered in vacuum to prepare preformes with a designed porosity. The preforms were preheated at 723-1123 K (preform temperature ; T_P) in air or in a reducing atmosphere. Aluminum melt (JIS 1070, 99.7 %) at a temperature of 1013-1123 K (melt temperature ; T_M) was infiltrated into the preheated preforms with an applied pressure of 50 MPa at a ram speed of 15 mm sec^{-1} in air (Fig. 2.1).

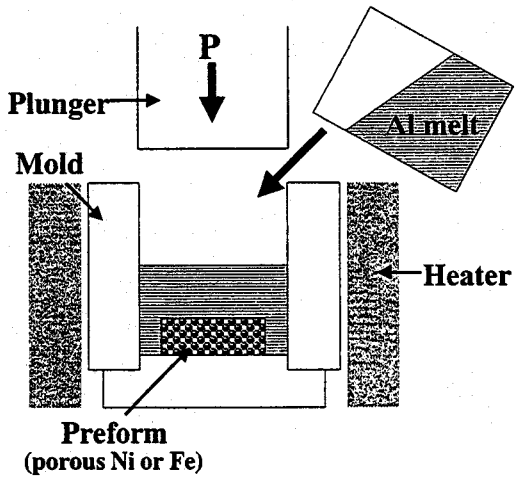

Fig. 2.1 Schematic illustration of apparatus for reactive infiltration.

For the inhomogeneous aluminides formed by the infiltration, post hot-pressing was carried out at 1273-1473 K with isothermal holding of 1 h in vacuum. The uniaxial pressure of 30 MPa was applied to the specimens through γ-Al_2O_3 powder beds during the post hot-pressing. The microstructure of the synthesized aluminides was characterized by OM, SEM-EDX, TEM and XRD.

2-3 Results and Discussion

2-3-1 Reactive hot-pressing of Ni and Fe aluminides

(1) NiAl alloys

Typical DTA curve of Ni-Al powder mixture is shown in Fig. 2.2. The initial reaction (exothermic reaction) among Ni and Al particles starts at ~850 K as indicated by the arrow in Fig. 2.2. German

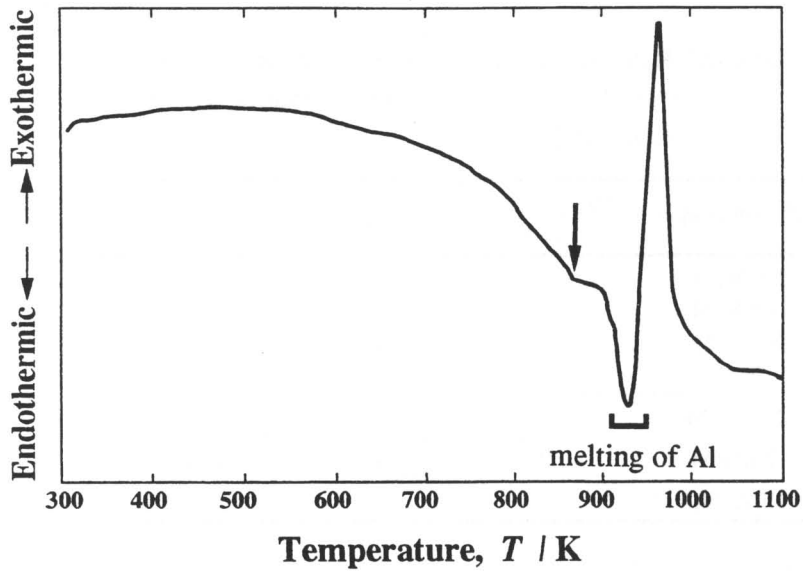

Fig. 2.2 DTA curve of Ni-Al powder mixture for stoichiometric NiAl. The arrow indicates the initiation of reaction between Ni and Al powders.

and his colleagues [1] reported that the initial reaction always occurs at the lowest eutectic temperature in reactive sintering process of metallic powder mixtures. However, the initial reaction for the Ni-Al powder mixtures is found to occur below the lowest eutectic temperature of Ni-Al binary system (913 K). The solid-state reaction among these particles, resulting in swelling [21] seems to occur prier to the liquid phase formation. Then, the remarkable exothermic reaction occurs concurrently with the melting of Al particles.

Figure 2.3 shows the OM micrograph of Ni-47at%Al alloys which was immediately cooled at 873 K during reactive hot-pressing. Two types of reaction products can be observed around the Ni particles. These products were identified to be $NiAl_3$ and Ni_2Al_3 by XRD and EDX. Janssen and Rieck [22-23], and Hibino [14] have found an anisotropic diffusion behavior at the interfaces between Ni or Al and intermetallic compounds in Ni-Al binary system as shown in Table 2.1. The ratio of the intrinsic diffusion coefficients D_{Al}/D_{Ni}

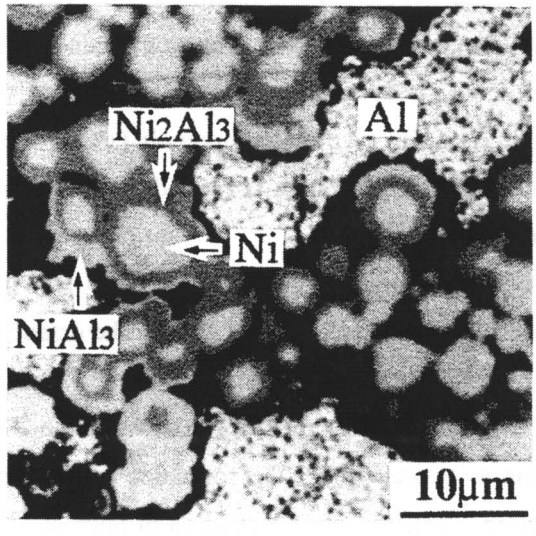

Fig. 2.3 Intermediate products in the initial reaction of Ni-47at%Al powder mixture.

Table 2.1 Ratio of intrinsic diffusion coefficients, D_{Al}/D_{Ni} or D_{Ni}/D_{Al}, in several diffusion couples reported by Janssen [21-22]

Diffusion couple	Temperature, T / K	D_{Ni}/D_{Al} or D_{Al}/D_{Ni}	
Ni_2Al_3/Al NiAl/Al Ni_3Al/Al Ni/Al	883	D_{Al}/D_{ni} : infinite	D_{Al}(in Ni_2Al_3) : 1.8×10^{-8} cm^2 sec^{-1}
Ni_2Al_3/Ni NiAl/Ni Ni_3Al/Ni	1273	D_{Ni}/D_{Al} : infinite	D_{Ni}(in NiAl) : 1.6×10^{-9} cm^2 sec^{-1}

was estimated to be infinite for Al-$NiAl_3$ and Al-Ni_2Al_3 at 883 K [21]. Hence, the predominant diffusion of Al occurs through the reaction layer. According to Hibino [14], the diffusion coefficient of Al (D_{Al}) at 973-1373 K has experimentally determined to be

$$D_{Al} / \text{mol m}^{-1} \text{sec}^{-1} = 1.20 \times 10^{-3} \exp(-89000/RT) \qquad (2\text{-}1)$$

When the specific volumes of Al(liquid), Ni(solid) and the Ni aluminides (solid) were assumed to be 11.3, 6.6 and 25.4 m^3/mol, the formation of reaction layer results in decreasing total volume. The decrease of volume is compensated if the particle rearrangement could induced by the liquid phase. Unfortunately, the particle rearrangement is hardly expected due to the predominant diffusion of Al and subsequent formation of reaction products. Therefore, many voids are generated with the initial reaction. Moreover, the specimen temperature significantly increases with the heat (enthalpy) of formation (ΔH_f) of these compounds [17, 24]. Nishimura and Liu [2-3] experimentally confirmed that transient liquid phase is formed by heat-releasing during the initial reaction in a Ni-Al powder compact.

Figures 2.4 and 2.5 (a)-(d) show XRD patterns and microstructural feature of the Ni-47at%Al compacts hot-pressed at 873-1273 K. The drastic change of microstructure is observed between 873 and 973 K. The compact processed at 973 K consists only with Ni_3Al and NiAl phases, while that at 873 K exhibits many phases as shown in the XRD pattern. This drastic microstructural evolution seems to be caused by the formation of transient liquid phase and the subsequent liquid phase reaction. Then, the homogenization of microstructure occurs above 1273 K. The fully homogeneous sintered bodies are obtained at 1473 K.

On the other hand, the different type of microstructural evolution was observed in the compacts

with the stoichiometric (50 at%Al) and Al-rich compositions as shown in Figs. 2.6 and 2.7 (a)-(f). The initial reaction occurs at 873 K in a similar manner of the compacts with Ni-rich composition. However, the drastic microstructural change by the liquid phase formation was not observed at 873-973 K. The penetration of Al into Ni particles resulting in the formation of many voids occurs between 973 and 1073 K. The disappearance of $NiAl_3$ and the formation of Ni_3Al were confirmed by SEM-EDX and XRD at 1073 K. Subsequently, fine NiAl particles with 3-5 μm in size are formed at 1173 K. The homogenization and densification occur above 1273 K. In the case of the compacts with high Al content, the self-heating induced by the initial exothermic reaction is considered to be suppressed by the endothermic melting reaction of Al. Hence, drastic microstructural change with the transient liquid phase formation cannot occur at 973-1073 K.

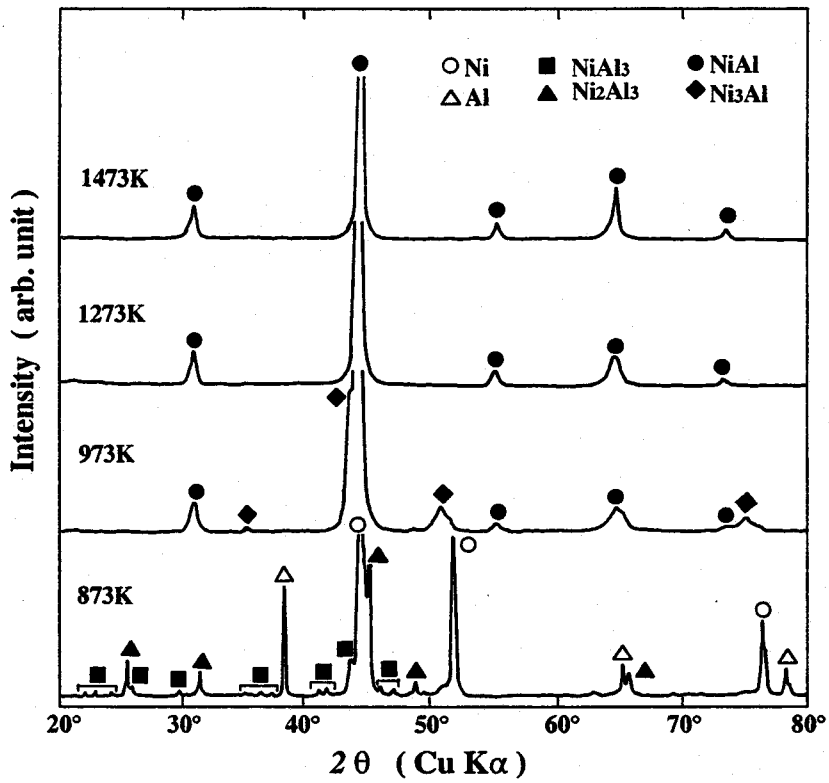

Fig. 2.4 XRD patterns of Ni-47at%Al specimens hot-pressed at 873-1473 K.

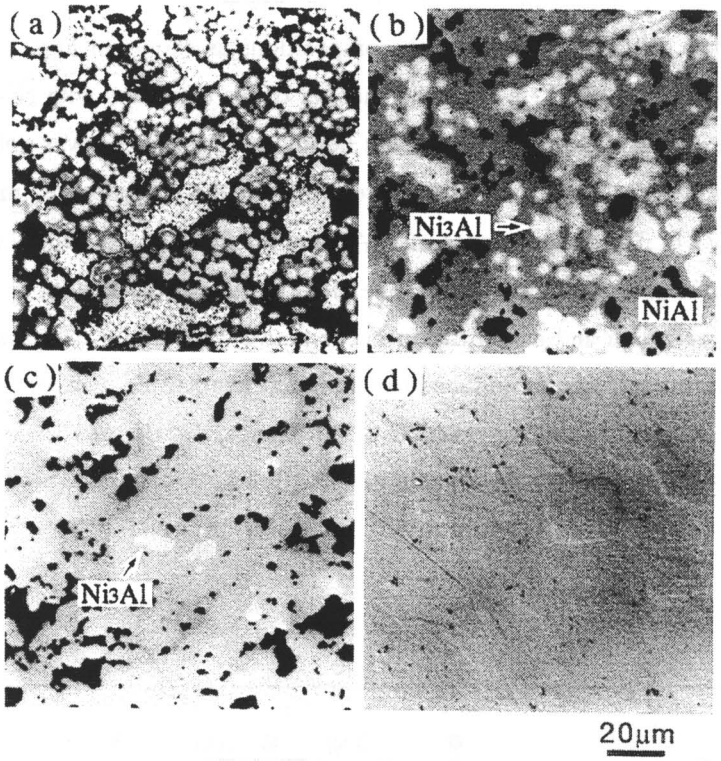

Fig. 2.5 OM photographs of Ni-47at%Al specimens hot-pressed at (a) 873, (b) 973, (c) 1273 and (d) 1473 K.

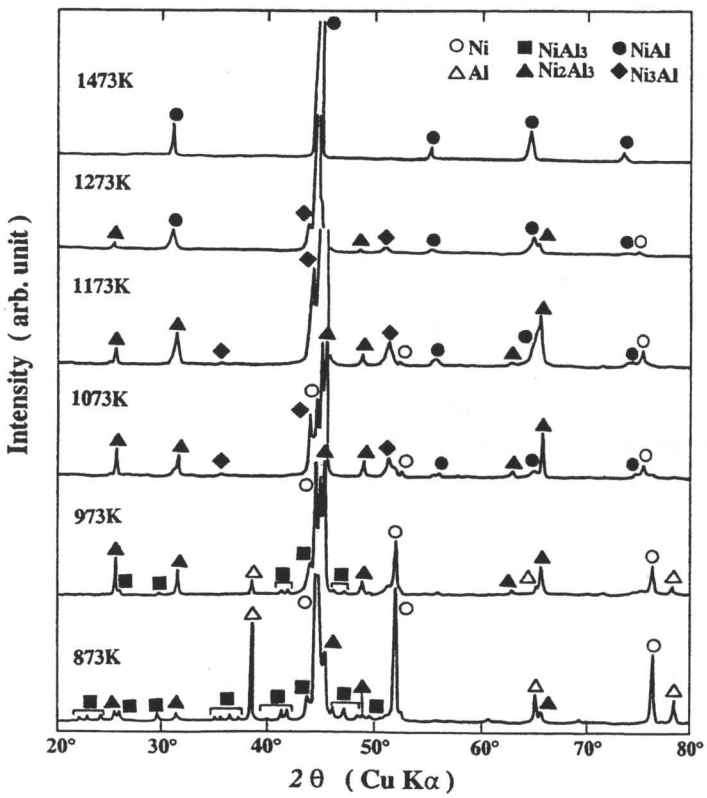

Fig. 2.6 XRD patterns of Ni-50at%Al specimens hot-pressed at 873-1473 K.

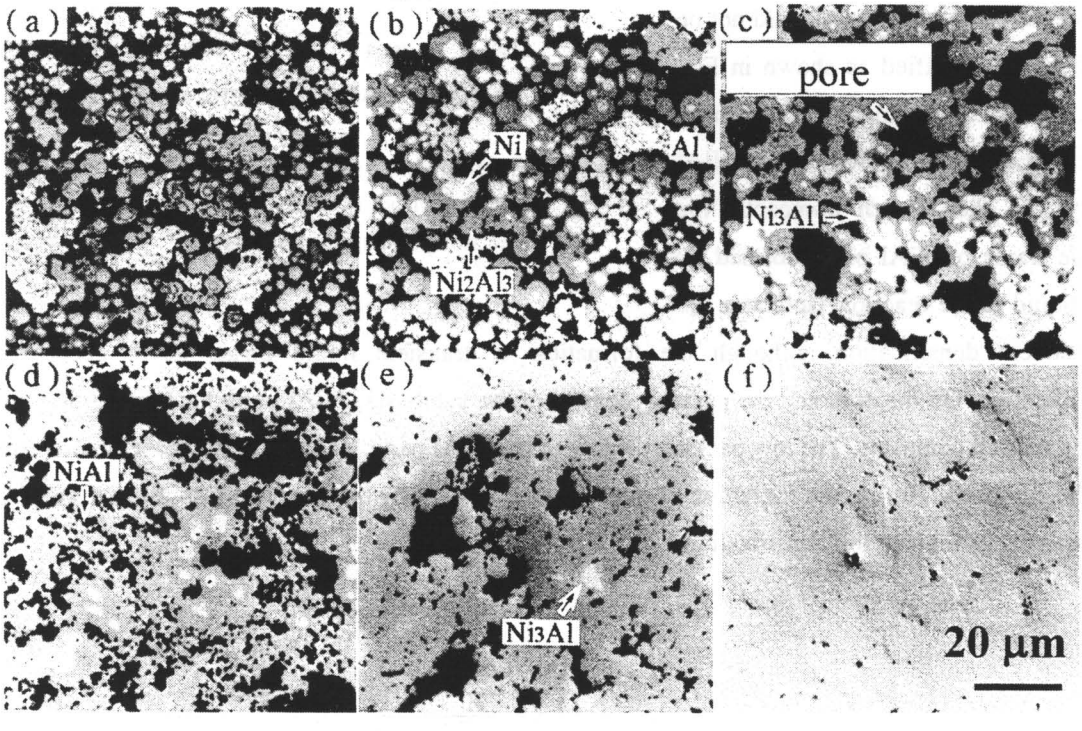

Fig. 2.7 OM photographs of Ni-47at%Al specimens hot-pressed at (a) 873, (b) 973, (c) 1073, (d) 1173, (e) 1273 and (f) 1473 K.

Figure 2.8 shows the relationship between relative density and hot-pressing temperature of NiAl sintered bodies. The full densification (above 99 % of relative density) is achieved by hot-pressing above 1573 K in the case of Ni-rich composition. The compact of the stoichiometric composition are densified up to 98 % of relative density. However, the Al-rich ones could not be sufficiently densified as shown in Fig. 2.8. Figure 2.9 schematically illustrates the reactive sintering behavior of NiAl alloys. In the Ni-rich compacts, the dense frame of NiAl phase formed by the liquid phase reaction facilitates the subsequent densification, although the formation of transient liquid phase never accelerates densification. On the contrary, the packing density of the synthesize NiAl particles is extremely low in the Al-rich compacts. The low packing density of the NiAl particles leads to decrease final density of the compacts. Hence, the formation of dense frame of NiAl by the transient liquid phase reaction is essential to achieve full densification.

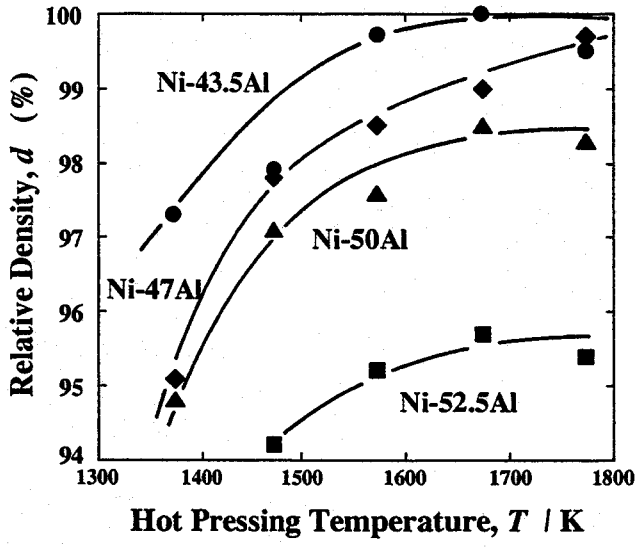

Fig. 2.8 Relationship between relative density of NiAl sintered bodies with various compositions and hot-pressing temperature.

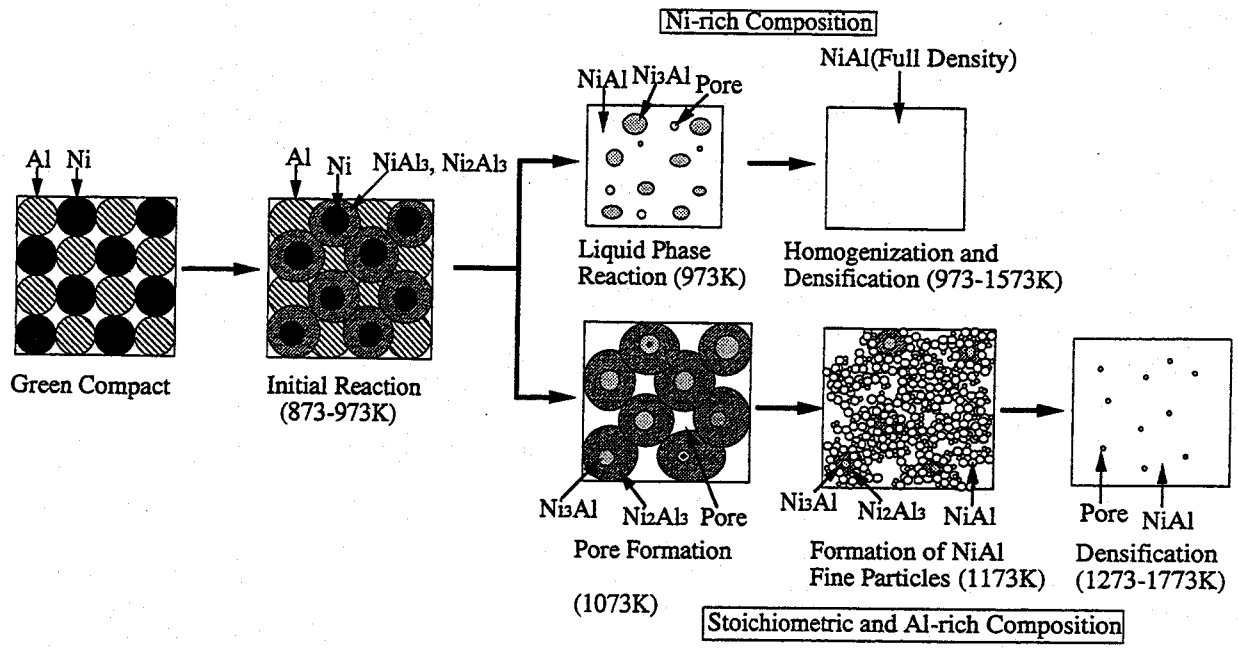

Fig. 2.9 Schematic diagram for the reactive sintering processes of NiAl alloys.

In aluminide sintered bodies fabricated by the reactive sintering process, fine Al_2O_3 particles, originating from impurity oxygen in raw powders, are always synthesized concurrently with the formation of aluminides, without disturbing nucleation. Figure 2.10 indicates high resolution TEM micrograph of an interface between Al_2O_3 particles and Ni_3Al matrix hot-pressed at 1573 K. The particle is identified as α-Al_2O_3. The grain growth of aluminide matrix is suppressed by the pinning effect of the particles dispersed along grain boundaries [8]. Therefore, the apparent grain size of the alloys is much smaller than that fabricated by the other processes (a few hundreds mm by cast processes) as shown in Fig. 2.11.

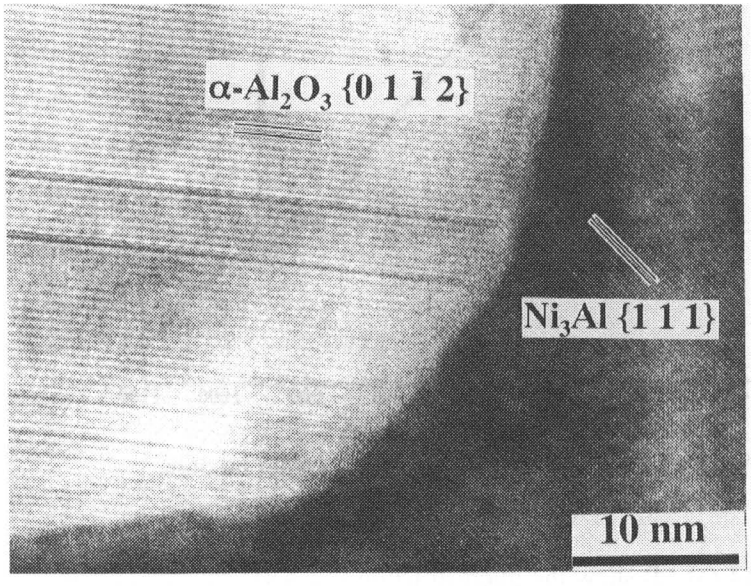

Fig. 2.10 TEM micrograph of interface between α-Al_2O_3 fine particles and Ni_3Al matrix.

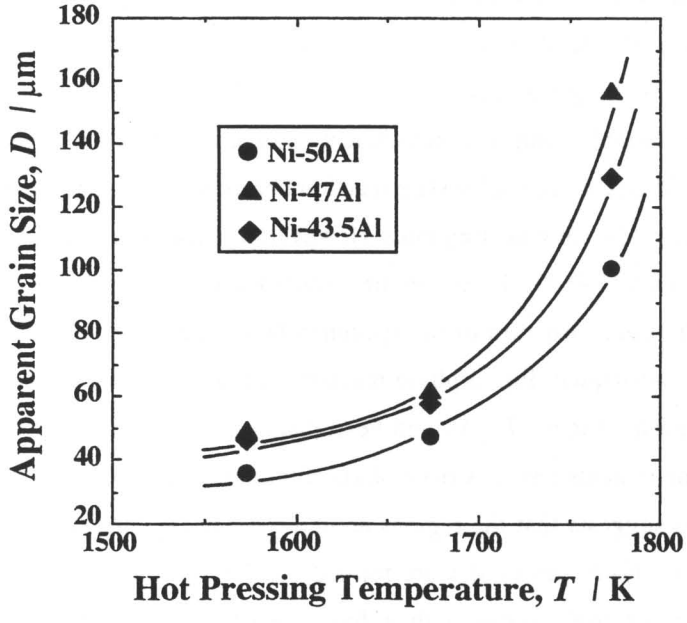

Fig. 2.11 Relationship between apparent grain size of NiAl alloys and hot-pressing temperature.

(2) FeAl alloys

Figure 2.12 illustrates the DTA curve of Fe-40at%Al powder mixture measured in Ar. This curve indicates that the exothermic reaction is initiated at 500-600 K. The reaction behavior at 900-1000 K is similar to that of Ni-Al powder mixtures. Rabin and Wright [7] have been also confirmed the exothermic reaction at about 550 K by DTA analysis though they did not directly observe the reaction products.

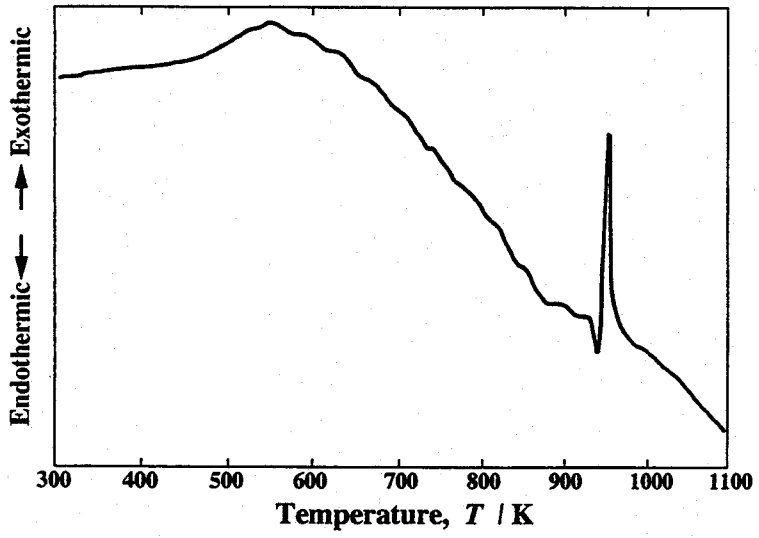

Fig. 2.12 DTA curve of Fe-40at%Al powder mixture.

Figures 2.13 and 2.14 (a)-(d) show the microstructure and XRD patterns of Fe-40at%Al compacts hot-pressed at 573-1273 K. The reaction layer, which indicates as R in Fig. 2.14 (a), is observed in the specimen hot-pressed at 573 K. Although the reaction product was difficult to be identified by XRD, it seems to be $FeAl_3$ by the quantitative analysis with EDX. Rabin and Wright [7] inferred that the reaction products reasonably suppress subsequent exothermic reaction which induces the formation of transient liquid phase. The solid-state reaction before the exothermic reaction at ~950 K can be a serious problem at the slow heating rates. However, it is confirmed that the reaction is not affected at a heating rate of 0.417–0.833 K sec^{-1} in the present work.

Figure 2.14 (b) show the microstructure of the specimen hot-pressed at 975 K. The formation of transient liquid phase and subsequent liquid phase reaction sufficiently occur in this specimen. The microstructure, which consists of α-Fe, Fe_2Al_5 and FeAl phases, is considered to form by the liquid phase reaction. The regions indicated as α is α-Fe phase containing 10 at% of Al according to EDX analysis. The analysis also suggests that the regions around α-Fe phase consist of Fe_2Al_5 and FeAl. Furthermore, many voids of 10-20 μm in size are formed. Lee and German [6], who examined the reactive sintering behavior of α-Fe alloys with a few at% of Al, have found the predominate diffusion of Al atoms into Fe [25] in the initial reaction between Fe and Al particles.

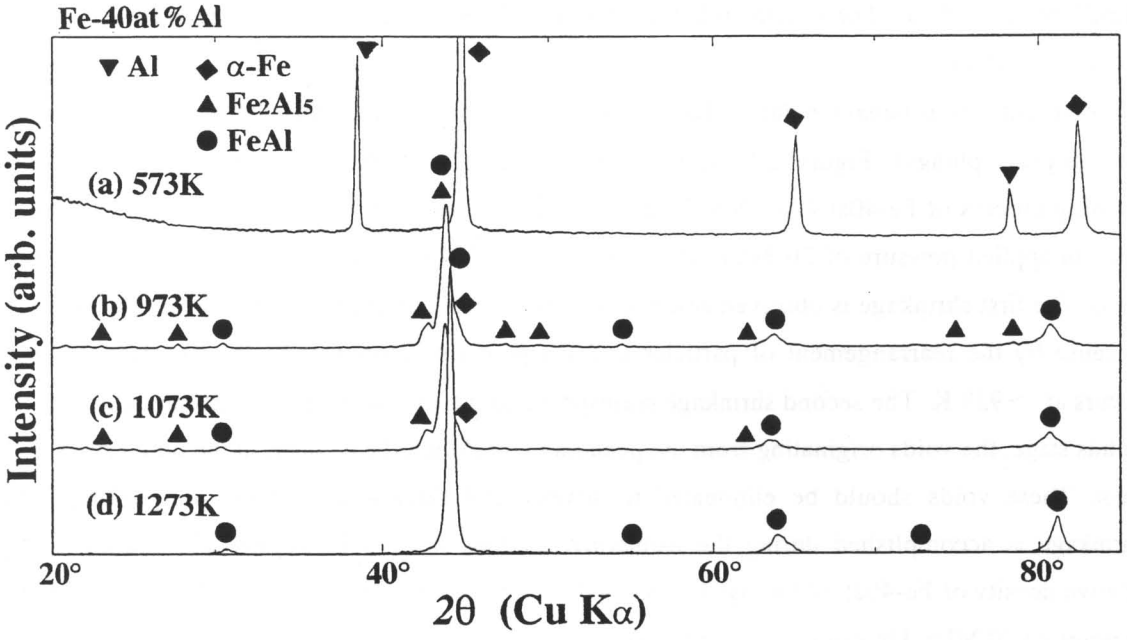

Fig. 2.13 XRD patterns of hot-pressed specimens at (a) 573, (b) 973, (c) 1073 and (d) 1273 K.

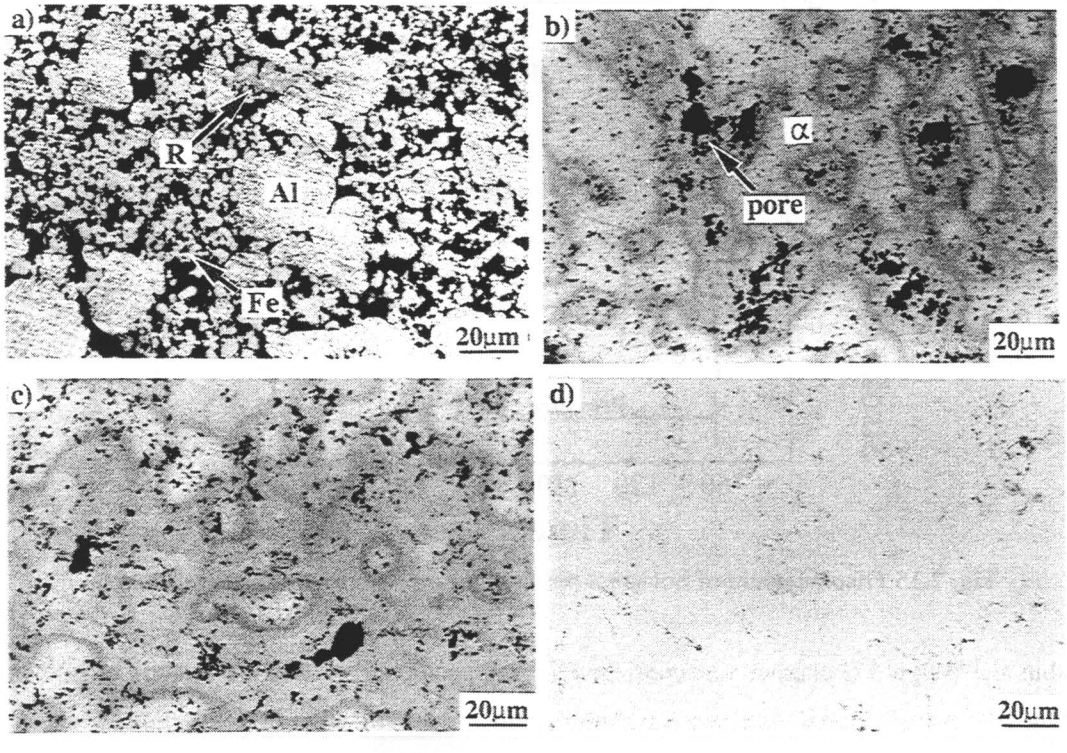

Fig. 2.14 OM photographs of hot-pressed specimens at (a) 573, (b) 973, (c) 1073 and (d) 1273 K.

The homogenization and densification occurs in the temperature range of 1073-1273 K as shown in Figs. 2.14 (c) and (d). The specimen hot-pressed at 1273 K is completely homogenized although a few pores still remain.

The densification behavior during hot-pressing can be qualitatively detected by displacement of the hot-press plunger. Figure 2.15 shows the displacement of plunger during the reactive hot-pressing process of Fe-40at%Al alloy. In this case, hot-pressing was conducted at 1273 K for 0.5 h with an applied pressure of 20 MPa. The densification of this specimen is achieved through three steps. The first shrinkage is observed at the same time of applying pressure. This shrinkage behavior is cause by the rearrangement of particles under a pressure. Subsequently, the second shrinkage occurs at ~923 K. The second shrinkage corresponds to the formation of the transient liquid phase. In this stage, the voids originating from the penetration of Al into Fe particles in the initial stage still exist. These voids should be eliminated to achieve full densification of the alloys. The final shrinkage is accomplished during the isothermal holding at 1273 K. Figure 2.16 illustrates the relative density of Fe-40at%Al alloys hot-pressed at different temperatures for 0.5 h with an applied pressure of 20 MPa. Unfortunately, the full densification of the alloys is hardly achieved below 1273 K even with the isothermal holding. The fully densified alloys (above 99 % of relative density) is successfully obtained above 1273 K.

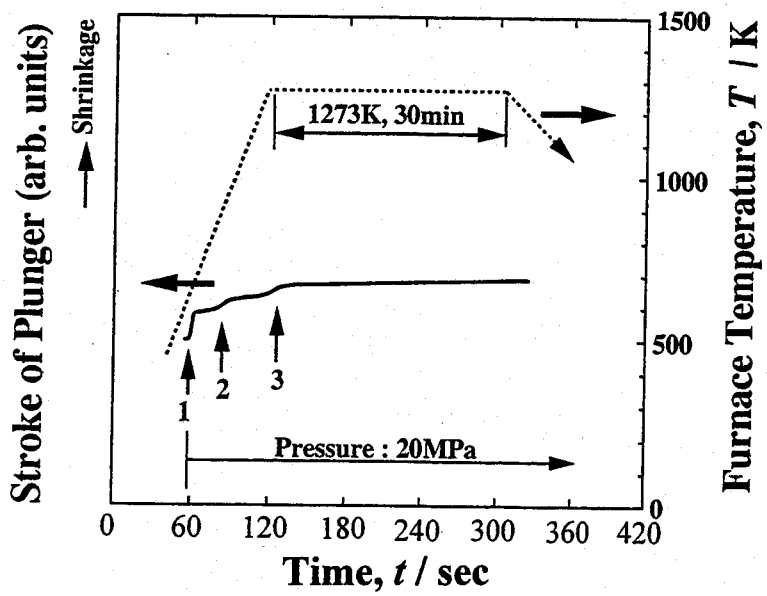

Fig. 2.15 Displacement of hot-press plunger during a reactive sintering process.

Rabin and Wright [7] claimed that continued heating above the reaction temperature or isothermal holding at elevated temperature provide little benefit for densification of FeAl alloys because the main mechanism is capillary-induced rearrangement by the formation of transient liquid phase. In the case of reactive hot-pressing process without the isothermal holding, the alloys are fully densified with an applied pressure above 70 MPa. However, the present results indicate that the

pores can be completely eliminated by diffusion above 1273 K. The alloys can be fully densified without such a high pressure.

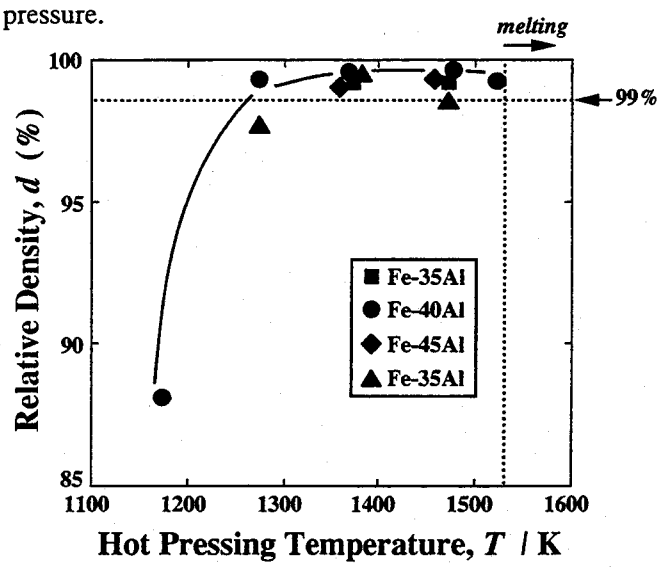

Fig. 2.16 Hot-pressing temperature dependence of relative density for Fe-40at%Al sintered bodies.

Fine Al_2O_3 particles, which come from impurity oxygen, are formed through the reactive hot-pressing process. The Al_2O_3 particles are dispersed along the grain boundaries and also within the grains. The grain size of the reactively hot-pressed alloys (Fig. 2.17) is much smaller than that of alloys fabricated by another process, such as conventional casting process (a few hundreds μm), because the particles dispersed along grain boundaries prevent anomalous grain growth as shown in Fig. 2.18. The volume fraction of the synthesized Al_2O_3 particles is estimated to be 1-2 vol% based on the content of impurity oxygen in the starting powders in the present work.

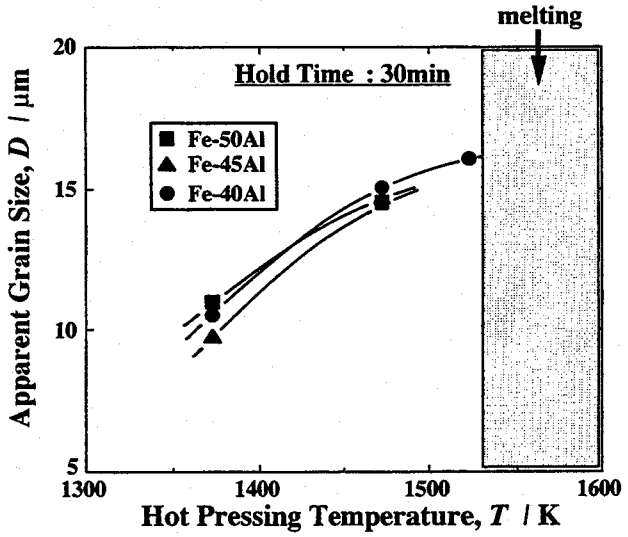

Fig. 2.17 Relationship between apparent grain size of FeAl alloys and hot-pressing temperature.

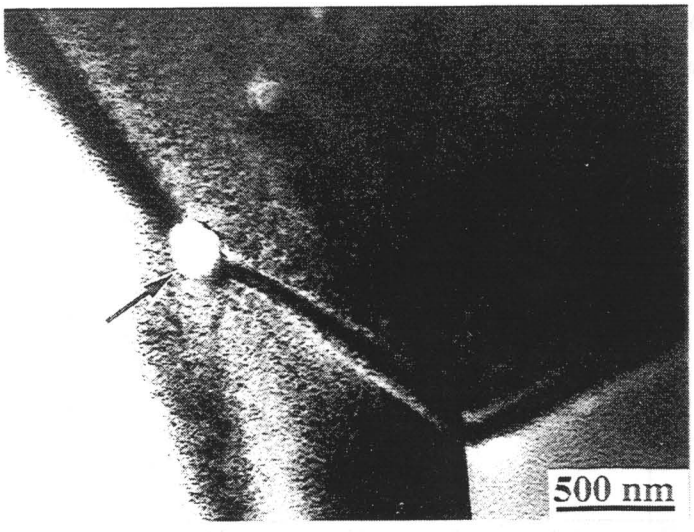

Fig. 2.18 Grain boundary pinning by an Al_2O_3 particle synthesized from impurity oxygen.

2-3-2 Reactive infiltration and post hot-pressing of infiltrated precursors

(1) Ni aluminides

In the reactive infiltration process, aluminides are synthesized by reaction between transition metal particles and Al melt. When the reaction condition is insufficient, i.e., temperature is low, homogeneous aluminides are hardly obtained. Figure 2.19 shows such a typical microstructure of inhomogeneous specimens fabricated by the reactive infiltration. The reaction products were identified as $NiAl_3$ and Ni_2Al_3 by EDX and XRD. The ring-like patterns indicated as A consists of α-Al_2O_3 formed by the reduction reaction between NiO on the surface of Ni particles, which is formed during the preheating process in air, and the infiltrated Al melt [20]. Hence, these patterns indicate the exact positions of Ni particles before the infiltration. Figure 2.19 indicates that Ni dissolved into the melt, precipitates in the form of $NiAl_3$ by the local liquid phase reaction. The layers of Ni_2Al_5 were also formed between $NiAl_3$ and remaining Ni particles. For the in-situ formation of uniform aluminides, the whole Ni particles are necessary to disappear by the liquid phase reaction.

The condition needed to obtain uniform aluminides by the in-situ reaction was examined as the function of T_M and T_P. Figures 2.20 (a) and (b) show the results of reactive infiltration under various conditions for Ni powder size $\leqq$44 μm and $\leqq$100 μm, respectively. The porosity of the preforms was controlled to give the stoichiometric Ni_3Al. The uniform Ni_3Al (Fig. 2.21) was successfully fabricated by the in-situ reaction under the conditions in the shaded areas in Figs. 2.20 (a) and (b). The precipitation of α-Al_2O_3 can hardly observed in Fig. 2.21 because the preform was preheated in a reducing atmosphere. The total reaction mass per unit time between the Ni preforms and Al melt

largely depends on the particle size (total surface area) of Ni raw powders. Uniform aluminide can be fabricated at relatively low preform and melt temperatures when finer nickel particles are used.

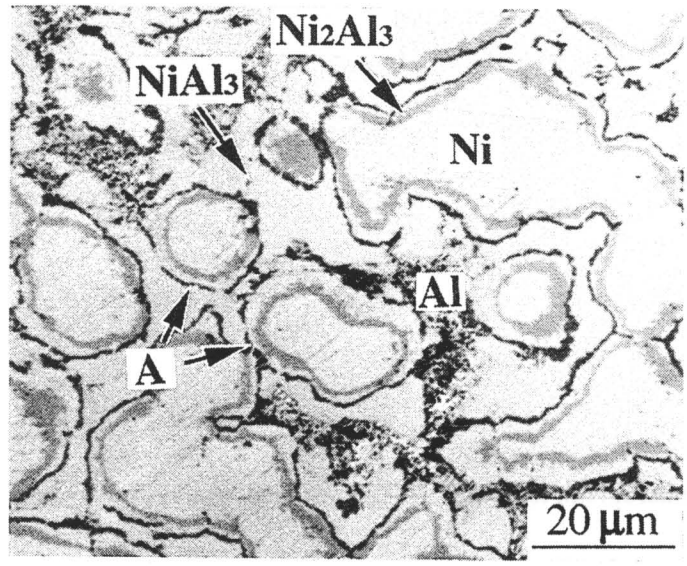

Fig. 2.19 OM micrograph of a specimen (nickel particle size : ≦44 μm, expected composition : Ni-25at%Al) prepared by reactive infiltration under the condition of T_P = 723 K and T_M = 1013 K. A indicates ring-like distribution of α-Al_2O_3 [20].

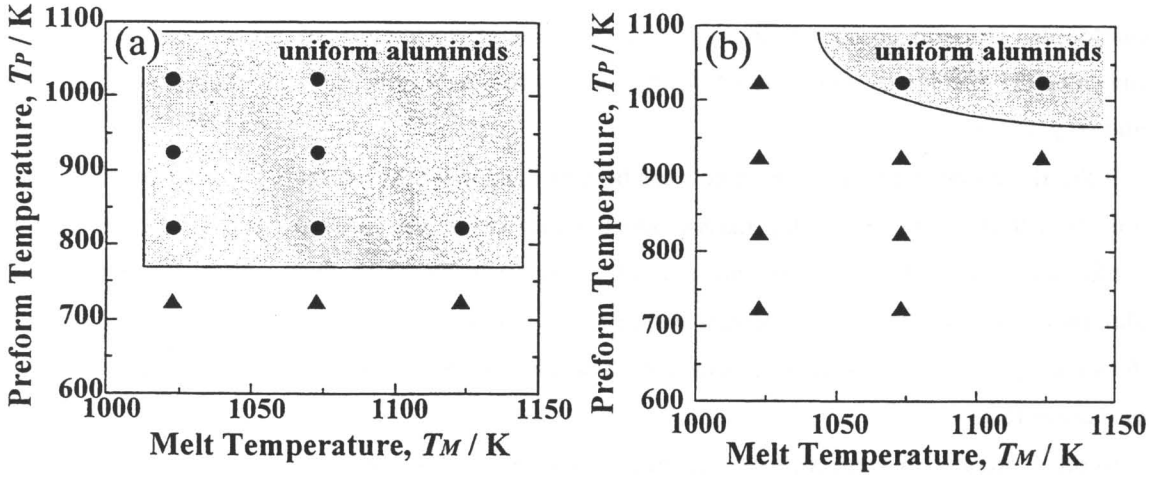

Fig. 2.20 Results of reactive infiltration for the preforms prepared from nickel particles with size of (a)≦44 μm and (b) ≦100 μm. The shaded area indicates the conditions for the formation of uniform aluminides.

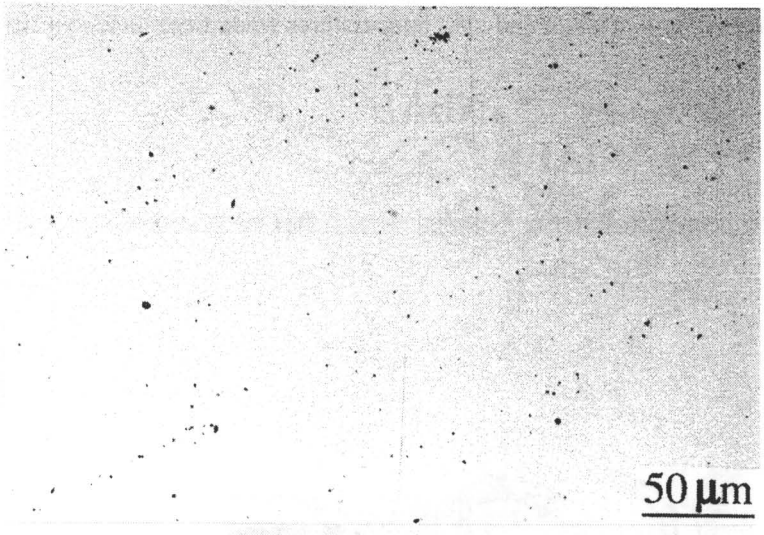

Fig. 2.21 OM micrograph for uniform aluminide ingot synthesized by in-situ reaction.

As Suganuma [20] have clarified, the composition and constitutional phases of the synthesized aluminide ingots can be controlled by porosity of the preforms. Figure 2.22 (a) indicates a typical microstructure of the synthesized Ni_3Al alloy. The alloy consists of fine grains below 1 μm in size. The grain size of the alloy is extremely smaller than that of the alloys fabricated by the other methods such as melting and powder metallurgical processes. Figure 2.22 (b) shows a microstructure of the synthesized Ni-40at%Al alloys. In Ni-Al system, the martensitic phase transformation, which causes the shape memory effect [26], is induced by quenching NiAl compounds with the composition of ~40at%Al. The NiAl alloys synthesized by the reactive infiltration have a martensite structure as shown in Fig. 2.22 (b). The microstructure of these alumindes clearly indicates the specimens were cooled down quickly after the exothermic reaction between Al melt and Ni particles.

If the aluminides without large defects can be fabricated in a near-net shap, the reactive infiltration will be a useful process for the mass-production. However, the eutectic regions surrounding the synthesized aluminide were frequently formed as shown in Fig. 2.23. Furthermore, the synthesized aluminides without such large defects exhibited inferior strength due to the micro-cracks formed during the process. Therefore, it is necessary to develop the techniques for preventing the formation of these defects.

Another process to form uniform aluminides is post annealing of reactive-infiltrated precursors [19]. Dunand has claimed that numerous pores are formed during the annealing process due to the predominate diffusion of Ni atoms into Ni_2Al_5 phase [19,22]. Hence, the annealing should be performed under pressure to avoid the pore formation. In the present work, the post hot-pressing of the infiltrated precursors was performed at 1273-1473 K for 1 h with 30 MPa. Figure 2.24 (a) shows

the microstructure of Ni precursors using particles $\leqq 44$ μm with the expected composition of Ni-25at%Al. In the specimen post-hot-pressed at 1273 K, Ni_3Al and NiAl had been already formed as shown in Fig. 2.24 (b). However, network pattern of α-Al_2O_3 indicated by A in Fig. 2.24 (c) was concurrently formed during the synthetic reaction of Ni_3Al and NiAl, because the preform was preheated in air before the infiltration of Al melt. Figure 2.25 is a SEM micrograph of the network pattern. The pattern consists of many fine particles smaller than one micrometer in size. Dense and uniform nickel aluminides with precipitates of α-Al_2O_3 particles are confirmed to be fabricated successfully up to the composition of 45 at% Al by the reactive infiltration and post-hot-pressing process. Dunand [19] reported that the Ni particles still remained after the vacuum annealing and the post HIPing of the reactive-infiltrated precursors at 1473K when the Ni particles with the size of 150-220 μm were used as the starting material. The imperfect homogenization in these specimens might be caused by the low reaction mass per unit time of such large particles.

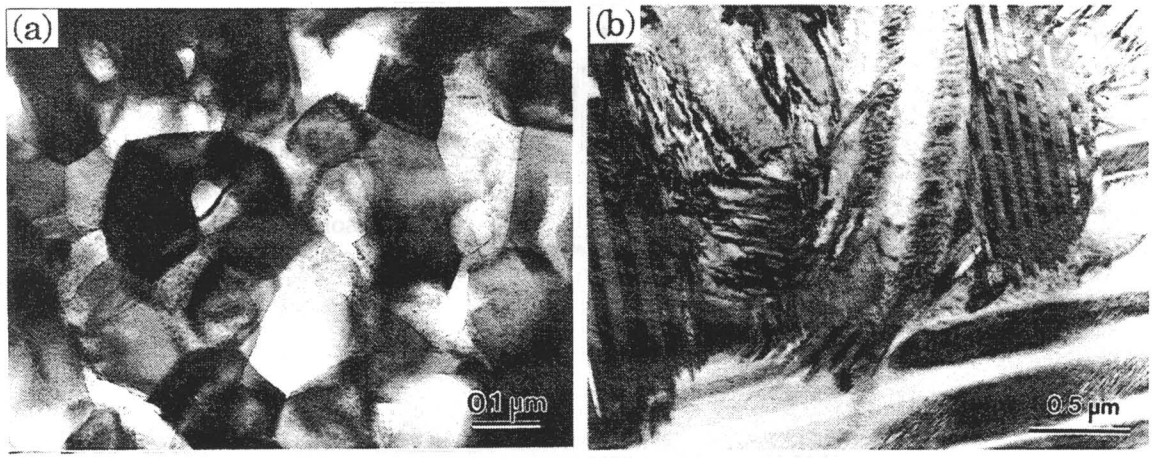

Fig. 2.22 TEM micrographs of (a) Ni_3Al and (b) NiAl alloys fabricated by in-situ reaction.

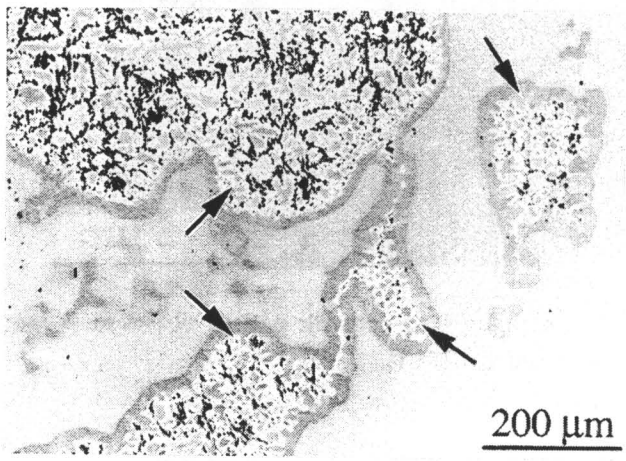

Fig. 2.23 Surrounding eutectic regions formed by in-situ reaction.

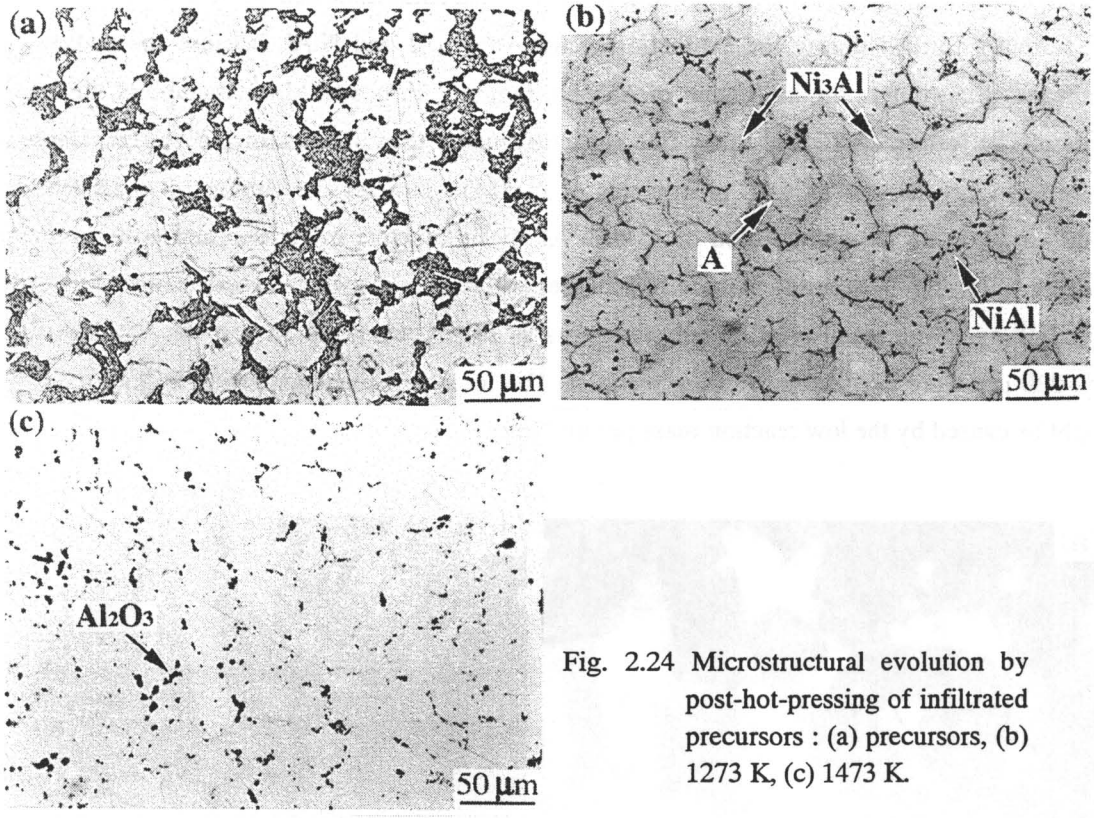

Fig. 2.24 Microstructural evolution by post-hot-pressing of infiltrated precursors : (a) precursors, (b) 1273 K, (c) 1473 K.

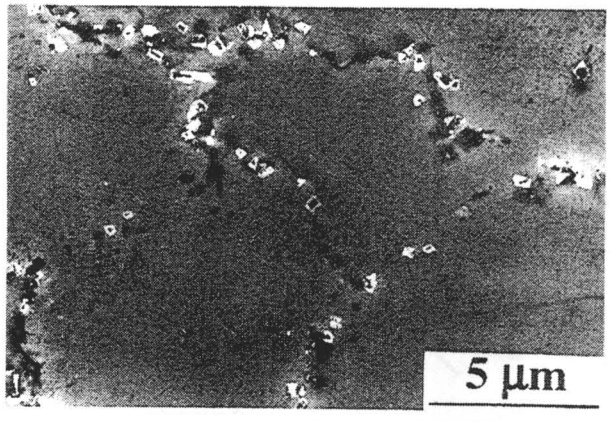

Fig. 2.25 SEM micrograph of network pattern observed in the specimen hot-pressed at 1273 K.

(2) Fe aluminides

The present work also examines the synthesis of Fe aluminides by the reactive infiltration. The relative density and expected composition after infiltration of Fe preforms are listed in Table 2.2. As a typical example, the experimental results for the preform No.2 in Table 2.2 will be described in detail. Fe-42.1at%Al alloy is expected to be synthesized from this preform. Figure 2.26 (a) shows the XRD pattern of the specimen after the infiltration of Al melt. The as-infiltrated specimen consists of α-Fe, Fe_2Al_5 and FeAl phases. Figures 2.27 and 2.28 (a)-(b) show the cross-sectional views and microstructure of the specimen, respectively. The uniform aluminide is formed in the center of the specimen (region (a)). The Fe content in this region is estimated to be about 5 at% higher than the expected value by a quantitative analysis with EDX. Unfortunately, the microstructure of the region (b) is not uniform as shown in Fig. 2.28 (b). The elements included in the region F is found to be Fe with little quantity of Al by EDX. Hence, it corresponds to α-Fe phase detected by XRD. On the other hand, the region A have an Al-rich composition. It seems to correspond to Fe_2Al_5. The microstructure shown in Fig. 2.28 (b), which is formed by the imperfect reaction between Al melt and Fe particles, gives us information about the synthetic reaction mechanism of FeAl alloys , i.e., 1) Fe_2Al_5 is formed as the product in the initial reaction, 2) FeAl can be synthesized if the specimen temperature sufficiently increases to form transient liquid phase by the initial exothermic reaction. As indicated in Table 2.3, heat released by the formation of Fe_2Al_5 is relatively smaller than that in the other systems [17]. Therefore, additional heating process is necessary to synthesize uniform FeAl alloys by the in-situ reaction.

Table 2.2 List of preform density and expected composition after reactive infiltration process.

Preform No.	Relative density (%)	Composition (expected) (at%Al)
1	45.6	46.0
2	49.3	42.1
3	57.7	34.2
4	70.6	28.5

To homogenize the infiltrated precursors, post annealing was carried out. The precursor can be completely homogenized by the annealing at 1273 K for 1 h as shown in Fig. 2.26 (b). Figure 2.29 (a) shows OM micrograph of the specimen annealed at 1273 K without any applied pressure. Although the homogenization of microstructure occurs, many voids of 5-10 μm in size are formed by the annealing. The heating was stopped at 1073 K to clarify the formation mechanism of these voids during the annealing process. The voids are already formed in the α-Fe regions at 1073 K as shown in Fig. 2.30. The void formation is considered to be originated by the decrease of volume accompanied with the reaction between α-Fe and Fe_2Al_5. The post hot-pressing of the infiltrated

precursors was conducted to eliminate the voids concurrently with homogenization. Figure 2.29 (b) shows the microstructure of the hot-pressed specimen. The dense and homogeneous aluminide are obtained by the post-hot-pressing.

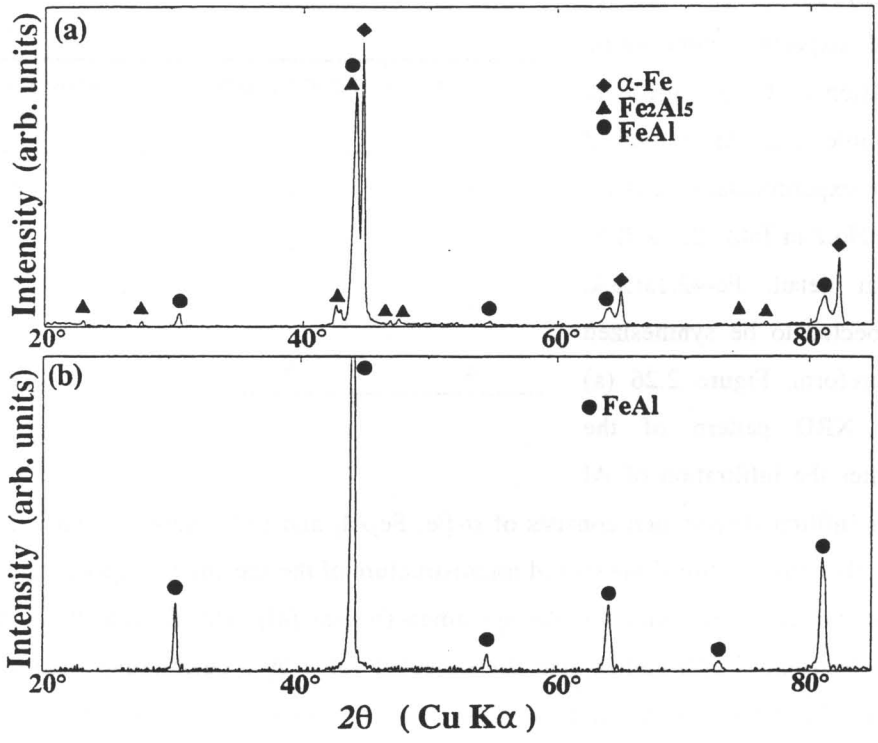

Fig. 2.26 XRD patterns of Fe aluminide ingot fabricated by SQ method (preform density : 49.3%). (a) as-cast, (b) after annealing at 1273 K.

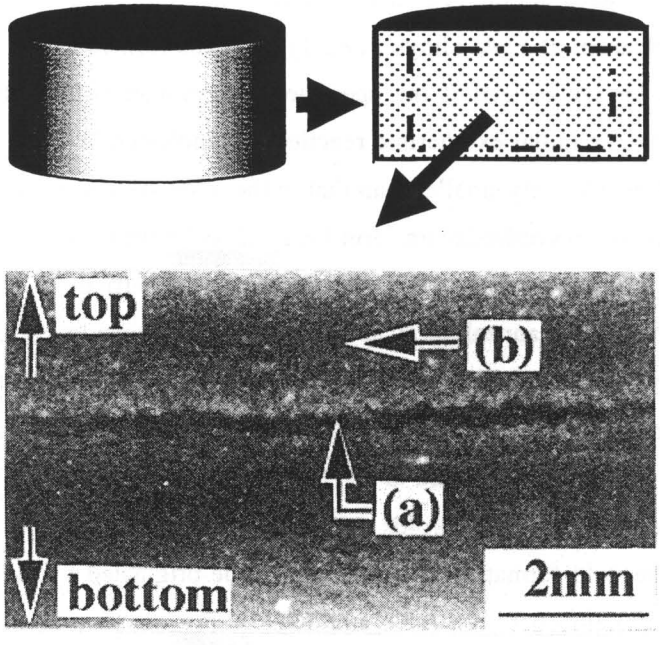

Fig. 2.27 Cross-sectional view of as-cast Fe aluminide ingot.

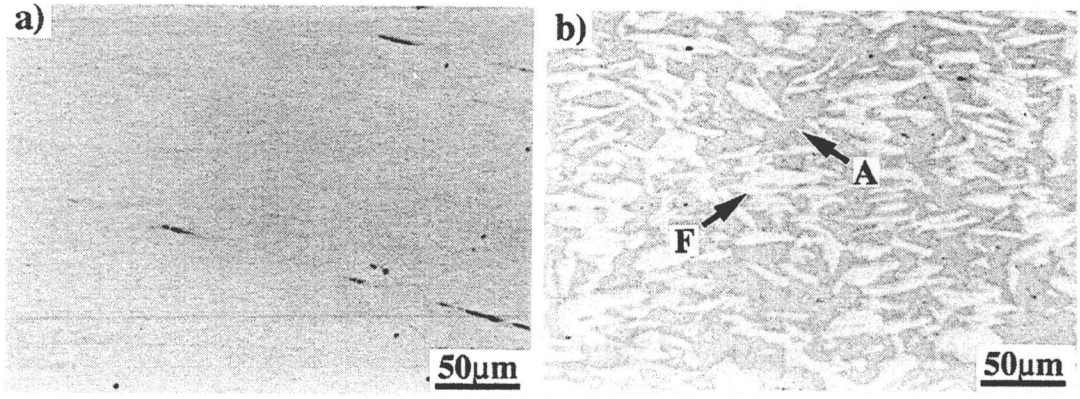

Fig. 2.28 OM photographs of microstructure in the area of (a) and (b) in Fig. 2.27.

Table 2.3 Standard formation enthalpy of various binary aluminides

Intermetallics	ΔH°_{f298} / kJ mol^{-1}
Ni aluminides	
Ni_3Al	-253.7
NiAl	-118.9
Ni_2Al_3	-283.5
$NiAl_3$	-151.2
Fe aluminides	
Fe_3Al	-67.2
FeAl	-50.4
Fe_2Al_5	-144.1
Ti aluminides	
Ti_3Al	-98.7
TiAl	-73.1
$TiAl_3$	-142.8

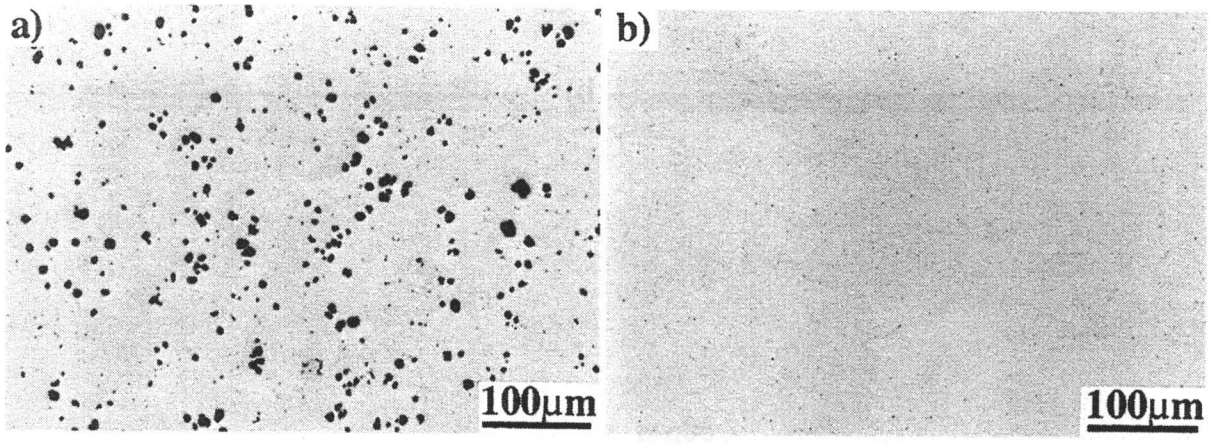

Fig. 2.29 Microstructures of Fe aluminide ingot after heat treatment at 1273 K, (a) without pressure and (b) post-hot-pressing with an applied pressure of 30 MPa.

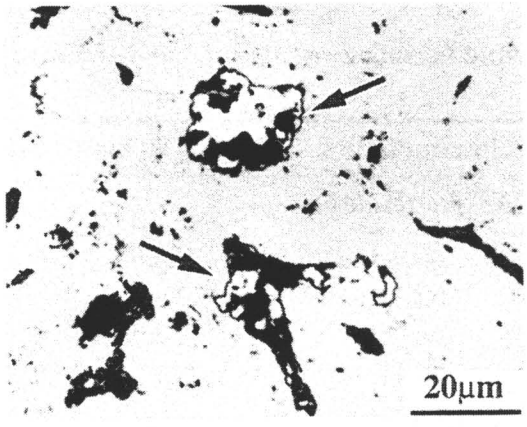

Fig. 2.30 Microstructure of a specimen heat treated at 1073 K. Arrows indicate α-Fe phase.

The experimental results are summarized in Table 2.4. The compositions of aluminides fabricated from the preforms No. 3 and 4 are almost the same as the expected values. The composition and constitutional phase of the synthesized aluminides can be controlled by the porosity of preforms in this composition range. However, the composition of aluminide synthesized from the preform No.2 shifts to the Fe-rich side by ~6 at%. This preform seems to compressed during the pressure infiltration. The mechanical properties of the specimens after the post hot-pressing are equal to those of the alloys fabricated by the other processes (Fig. 2.31).

Table 2.4 Experimental results of reactive infiltration and post hot-pressing treatment with various Fe preforms.

Preform No.	as-cast	after post HP treatment		
	Phase	Phase	Composition (at%Al)	Apparent grain size (D/μm)
1	α-Fe, Fe_2Al_5, FeAl	—	—	—
2	α-Fe, Fe_2Al_5, FeAl	FeAl	36.0	11.5
3	α-Fe, Fe_2Al_5, FeAl	FeAl	34.5	14.8
4	α-Fe, Fe_2Al_5	α-Fe	26.0	13.8

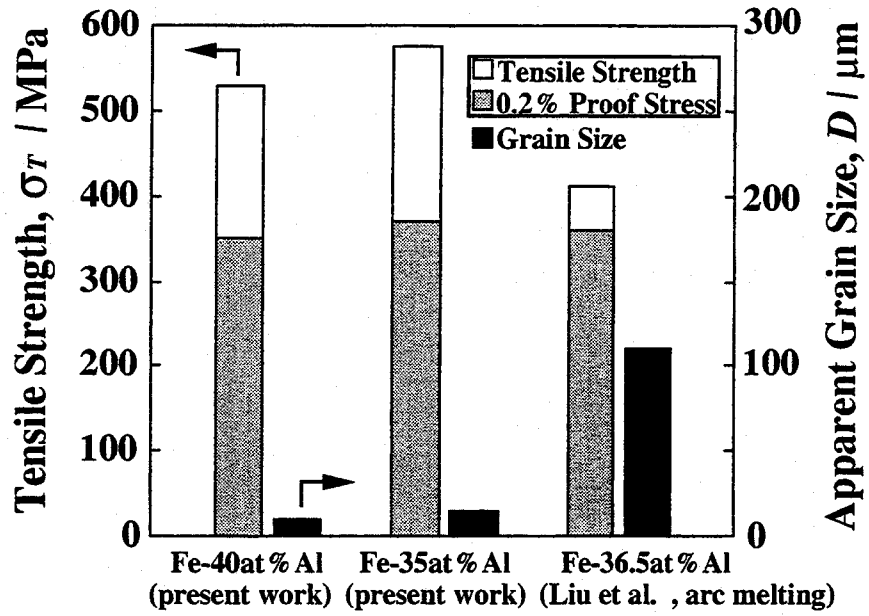

Fig. 2.31 Tensile strength and apparent grain size of FeAl alloys fabricated by reactive infiltration-post hot-pressing.

2-4 Conclusions

In this chapter, the reactive hot-pressing and the infiltration processes of Ni and Fe aluminides were examined. The results of this chapter are summarized as below:

Reactive hot-pressing

(1) The reactive sintering of powder mixtures of transition metals and Al proceeds through the following four steps; 1) initial reaction below the lowest eutectic temperature, 2) exothermic reaction with transient liquid phase formation at ~900 K, 3) homogenization of microstructure at 1000-1273 K and 4) final densification above 1273 K.

(2) The applied pressure is needed for full densification of these alloys because it is difficult to remove pores formed by the initial and subsequent exothermic reactions with pressureless sintering.

(3) Fine Al_2O_3 particles originated from impurity oxygen in starting powders are formed concurrently with the aluminide formation.

Reactive infiltration

(1) The temperatures of Al melt and preform are two of the important parameters to obtain uniform aluminides. However, the eutectic regions surrounding the synthesized aluminide are frequently formed when the exothermic reaction sufficiently occurs.

(2) The uniform aluminides without large defects can be obtained by post-annealing with an applied pressure above 1273 K.

References

[1] A. Bose, R. H. Rabin and R. M. German, Powder Metall. Inter., 20 (1988) 25

[2] C. Nishimura and C. T. Liu, Scripta Metall., 26 (1992) 381

[3] C. Nishimura and C. T. Liu, Acta Metall. Mater., 41 (1993) 113

[4] D. E. Alman, J. Mater. Sci. Lett., 13 (1994) 483

[5] S. D. Dunmead, Z. A. Munir, J. B. Holt and D. D. Kingman, J. Mater. Sci., 26 (1991) 2410

[6] D. J. Lee and R. M. German, Inter. J. Powder. Metall. & Powder Technol., 21 (1985) 9

[7] B. H. Rabin and R. N. Wright, Metall. Trans., 22A (1991) 277

[8] B. H. Rabin, J. K. Wright, R. N. Wright and C. H. Sellers, J. Mater. Res., 9 (1994) 1384

[9] J. C. Murray and R. M. German, Metall. Trans., 23A (1992) 2357

[10] I. M. Wolff, Metall. Trans., 27A (1996) 3688

[11] A. Makino and C. K. Law, J. Am. Ceram. Soc., 77 (1994) 778

[12] O. Yamada and Y. Miyamoto, J. Jpn. Inst. Metals, 56 (1992) 938

[13] A. Hibino, J. Jpn. Inst. Metals, 56 (1992) 1435

[14] A. Hibino, J. Jpn. Inst. Metals, 57 (1993) 767

[15] A. Hibino, J. Jpn. Inst. Metals, 59 (1995) 717

[16] W. C. Williams and G. C Stangle, J. Mater. Res., 10 (1995) 1736
[17] V. K. Sikka, S. C. Deevi and J. D. Vought, Advanced Mater. Process, 148 (6) (1995) 29
[18] D. C. Dunand , J. L. Sommer and A Mortensen, Metall. Trans., 24A (1993) 2161
[19] D. C. Dunand, J. Mater. Sci., 29 (1994) 4056
[20] K. Suganuma, Mater. Letters, 16 (1993) 22
[21] R. M. German, "Liquid phase sintering", Plenum publishing Co., New York (1985)
[22] M. M. P. Janssen and G. D. Rieck, Trans. Metall. Soc. AIME, 239 (1967) 1372
[23] M. M. P. Janssen, Metall Trans., 4 (1972) 1623
[24] Thermodynamic database MALT2, Science and Technology Co., Ltd., Tokyo (1992)
[25] J. S. Sheasby, Inter. J. Powder. Metall. & Powder Technol., 15 (1979) 301
[26] S. Ochiai, O. Noguchi and M. Ueno, J. Jpn. Inst. Metals, 51 (1987) 686

Chapter 3

Mechanical Behaviors of Ni and Fe Aluminides Fabricated by Reactive Hot-Pressing

3-1 Introduction

This chapter presents alloying designs for Ni and Fe aluminides to improve their mechanical properties by the reactive hot-pressing. The primary factors in determining the mechanical properties of intermetallics are briefly divided into two categories. One category is inherent factors such as their crystal structures, chemical bond characteristics and unique behaviors of defects. In particular, the behavior of defects in intermetallics are currently being studied by many researchers because this field is recognized as one of the unsolved problems in metallurgy [1-3]. The other category is the environmental effects originating from chemical reactions with the constituents of air, such as H_2O and O_2, on their surfaces. Alloys that are sensitive to environmental effect exhibit time-dependent fracture behavior. In this chapter, the mechanical properties of Ni and Fe aluminides fabricated by reactive hot-pressing are investigated in order to clarify the essence of their mechanical behavior and to achieve a suitable alloy design for these aluminides.

3-2 Experimental Procedure

3-2-1 Processing

Ni aluminides (24-52.5 at%Al) and Fe aluminides (35-50 at%Al) were fabricated by reactive hot-pressing. Raw powders of B (≦45 μm, 99 % ; Rare Metallic Co., Ltd.) and Si (≦10 μm, 99.9 % ; Kojundo Chem. Co., Ltd.) were used as the additional alloying elements. The processing details were described in Chapter 2 (p.11).

3-2-2 Evaluation

(1) Flexural strength

The hot-pressed specimens were cut into rectangular bars of 3 mm x 4 mm x 40 mm in dimension. A four point bending test, with an upper span of 10 mm and a lower span of 30 mm, was performed using the bars at a cross-head speed of 8.3×10^{-3} mm sec^{-1}. The tensile surface of the specimens,

which was polished to be a mirror surface with a polishing cloth and an Al_2O_3 slurry (0.3 μm), was placed perpendicular to the hot-pressing axis. The proportional limit and flexural strength of the alloys were evaluated from load-displacement curves.

(2) Tensile strength

The specimens for the tensile test had a gauge section of 0.5 mm x 1 mm x 8 mm, and were tested at a strain rate of 1.04×10^{-3} sec^{-1} at 300-1273 K in air. The specimens were heated to testing temperatures at 1.67×10^{-1} K sec^{-1}, and then held for 600 sec at testing temperatures before the tensile tests were carried out.

(3) Fracture toughness

Chevron-notched testing bars of 8 mm x 4 mm x 35 mm in dimension and a notch length (a_0) of 4 mm were prepared for toughness testing. The fracture toughness of the alloys was estimated by a three point bending test with a span length of 30 mm in several environments such as in air, Ar, silicone oil (SRX310 : Toray Dow Corning Silicon Co., Ltd.) and water at 300 K. The loading rate for toughness measurement was varied in the range of 10^{-2} – 10 MPa $m^{1/2}$ sec^{-1}. The fracture surface of the specimens was observed by SEM.

(4) Hardness

The surfaces of rectangular specimens was polished to be a mirror surface. The Vickers hardness of the alloys was measured by the indentation on the polished surface under a load of 9.8 N for 10 sec at temperatures between 300 to 1073 K.

(5) First principle simulation of electronic structure

A first principle simulation by the discrete variational (DV)-Xα method was conducted by a program, code SCAT, with the cluster models illustrated in Fig. 3.1 in order to clarify the bond behavior of Ni and Fe aluminides. Details of the calculations in the DV-Xα method will be described in Chapter 4. The total energy calculation was conducted by a commercial program, $Dmol^3$ code packaged in Cerius2, with a non-local density function of the generalized gradient approximation.

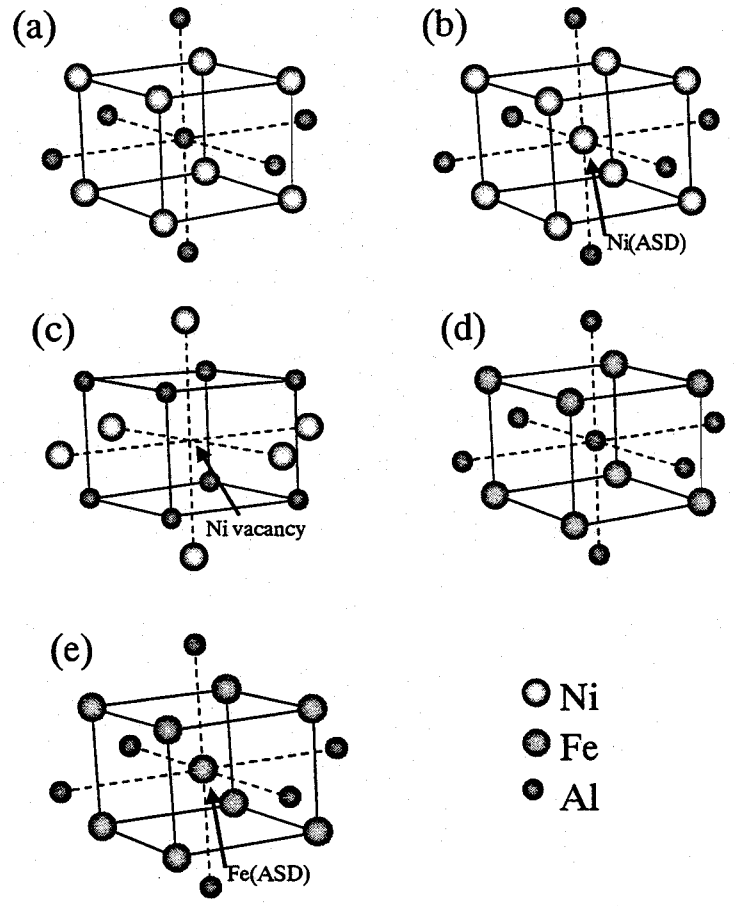

Fig. 3.1 Cluster models of Ni and Fe aluminides for molecular orbital simulation by DV-Xα method. (a) NiAl, (b)ASD Ni in NiAl, (c) Ni vacancy in NiAl, (d) FeAl, (e) ASD Fe in FeAl

3-3 Results and discussion

3-3-1 Mechanical Properties at Ambient Temperatures

(1) Compositional dependency

Ni aluminides

Figures 3.2 (a) and (b) show the compositional dependence of the flexural strength, Vickers hardness and fracture toughness (10^{-2} MPa $m^{1/2}$ sec^{-1}) of Ni aluminides in the composition range of 24-50.5 at%Al fabricated by reactive hot-pressing. The mechanical properties of Ni_3Al and NiAl are quite different due to the difference in their crystal structures and bond characteristics (cf. Appendix ch.3; fundamental concept of metallic bonding is discussed). Because Ni_3Al alloys, which have the $L1_2$ type structure based on fcc, have a sufficient number of slip systems for extensive plastic deformation, they have inherently high ductility and fracture toughness.

By contrast, NiAl alloys are intrinsically brittle because they have the B2 type structure based on bcc and chemical bonds with large ionic character. The fracture toughness of NiAl alloys is 5-6 MPa $m^{1/2}$ over the composition range of 40-50 at%Al. However, these alloys exhibit a characteristic compositional dependence of strength and hardness, which is called defect strengthening [4-5]. The stoichiometric NiAl alloy exhibits an elastic-plastic deformation behavior with the lowest proportional limit (about 180 MPa). In the case of Ni rich NiAl alloys, which have the substitutional Ni atoms in the Al sites [6], the flexural strength increases to 500-700 MPa, although these alloys fracture in a brittle manner. The defect strengthening seems to be also achieved in Al-rich compositions (by Ni vacancies [6]) because their proportional limit increases with increasing Al content within the composition range.

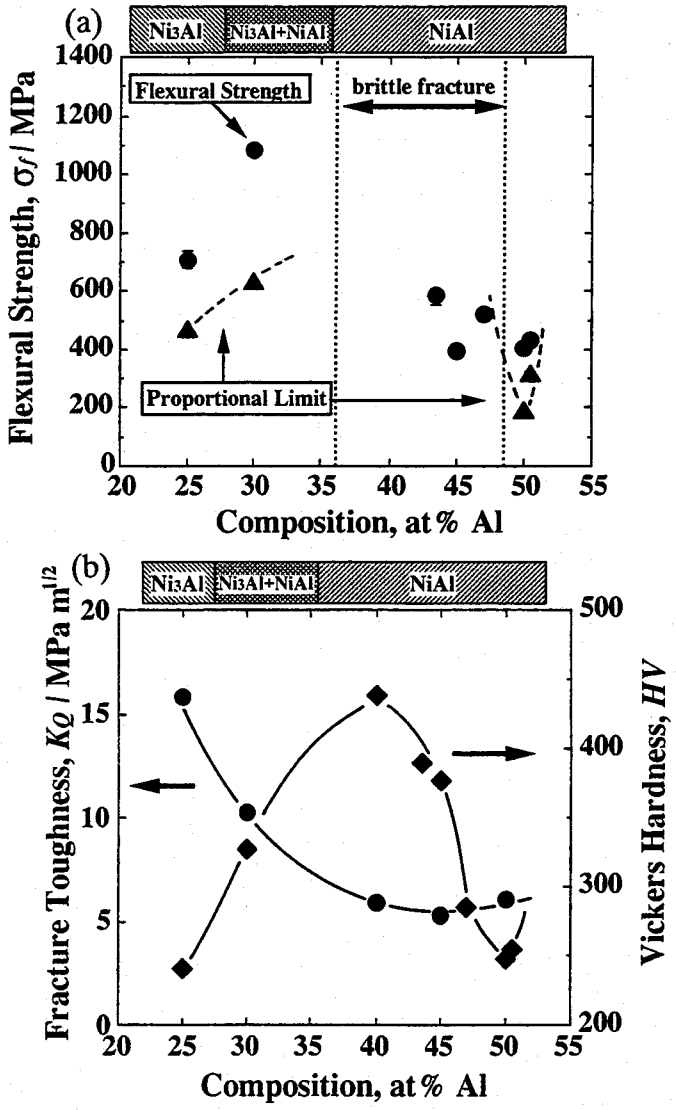

Fig. 3.2 Compositional dependence of (a) flexural strength and (b) Vickers hardness and fracture toughness (10^{-1} MPa $m^{1/2}$ sec^{-1}) of Ni aluminides in the composition range of 24-50.5 at%Al fabricated by reactive hot-pressing.

Tan et. al [5] claimed that the defect strengthening of NiAl alloys cannot be interpreted by conventional theory for the strengthening mechanism of diluted solid solutions. In order to examine the origin of the defect strengthening in NiAl alloys, the electronic structure proximal to point defects was simulated by DV-Xα method as indicated in Figs. 3.3 (a)-(c). Anti-site Ni atoms have negative charge as a results of charge transfer from nearest-neighbor Al atoms. Hence, an atmosphere of negatively-charged Ni atoms is formed as shown in Fig. 3.3 (b). The modulation of the Coulomb potential filed is expected to be one of the important factors for achieving anomalous strengthening behavior. On the other hand, Ni vacancies can also significant strengthen Al-rich alloys. The Al atoms in the vicinity of the Ni vacancy are positively charged due to charge transfer to nearest-neighbor Ni atoms (Fig. 3.3 (c)). Furthermore, the contribution of σ component consisting of the Al 2p orbital is increased by the chemical bonds between Al atoms around the vacancy. The modulation of bond characteristics and the Coulomb potential filed can provide the defect strengthening.

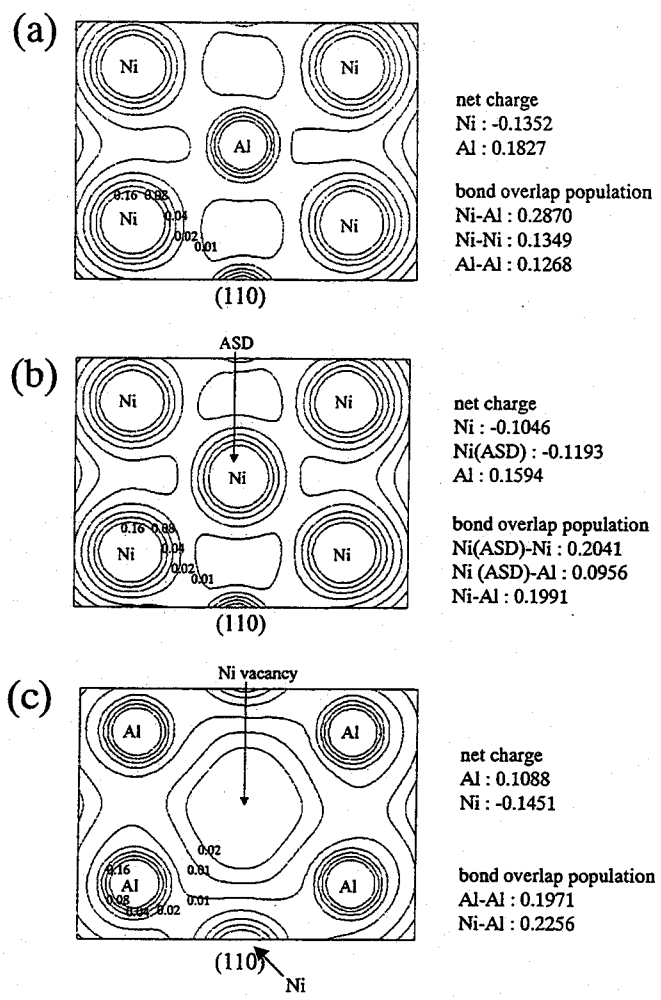

Fig. 3.3 Results of molecular orbital simulation. (a) NiAl without point defects, (b) NiAl with Ni(ASD), (c) NiAl with Ni vacancy, (d) FeAl without point defect and (e) FeAl with Fe(ASD).

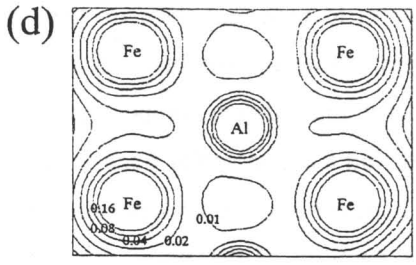

Fig. 3.3 *Continued*

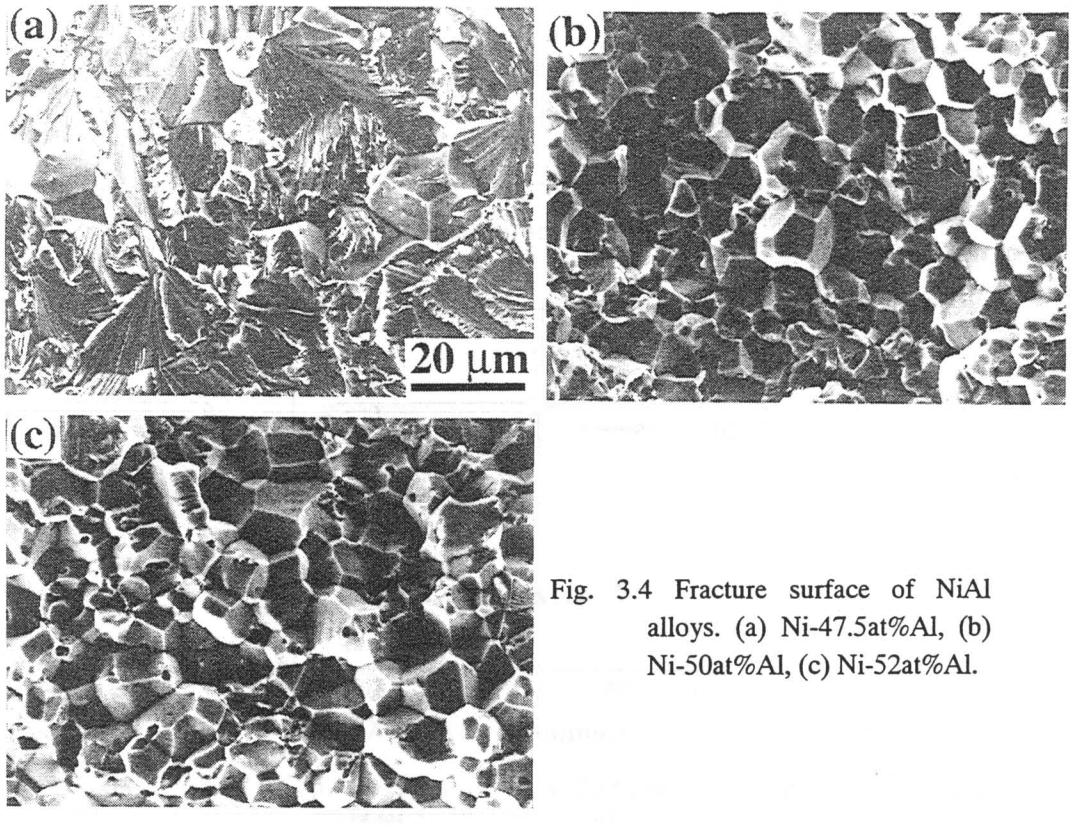

Fig. 3.4 Fracture surface of NiAl alloys. (a) Ni-47.5at%Al, (b) Ni-50at%Al, (c) Ni-52at%Al.

Variation in alloy composition also seem to influence even on their grain boundary cohesion. Figures 3.4 (a)-(c) show SEM micrographs of fracture surfaces of NiAl alloys fabricated by reactive hot-pressing. The alloys with stoichiometric and Al-rich compositions fracture in an intergranular manner. By contrast, the Ni-rich alloys exhibit a transgranular fracture behavior, as shown in Fig. 3.2 (a). The high grain boundary cohesion is possible to be accomplished by high Ni composition on grain boundaries [7]. Unfortunately, the ductility of the alloys cannot be improved by the grain boundary strengthening.

FeAl alloys

As shown in Fig. 3.3 (d), FeAl has the directional bonds similar to NiAl. However, the bond character (net charge and bond overlap population) is quite different from NiAl. FeAl exhibits a higher overlap population of Fe-Al bonds without polarization. The FeAl alloys exhibit the extensive plastic deformability in contrast to NiAl alloy because FeAl has almost no ionicity.

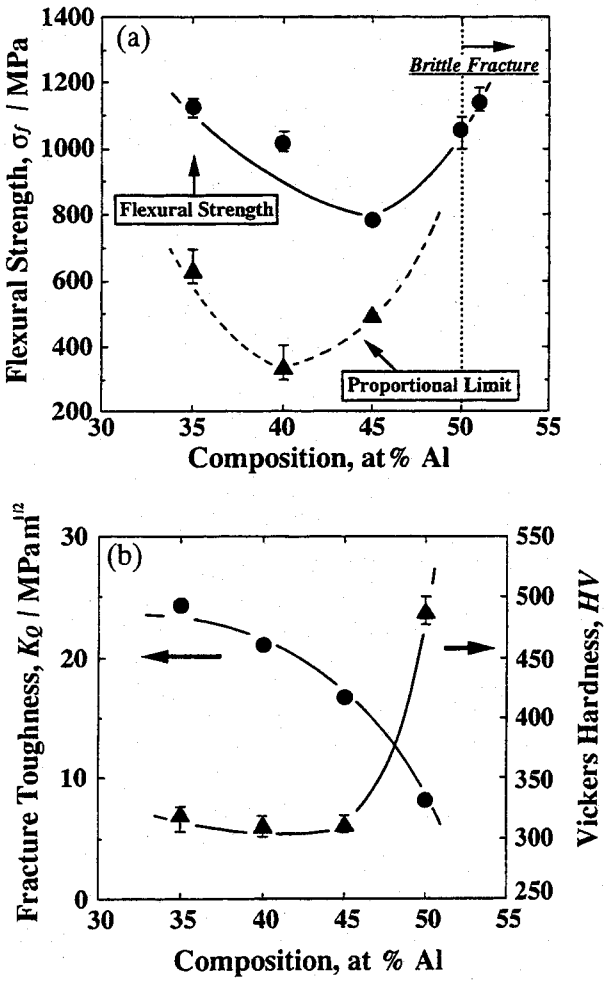

Fig. 3.5 Compositional dependence of (a) flexural strength and (b) Vickers hardness and fracture toughness (10^{-1} MPa $m^{1/2}$ sec^{-1}) of FeAl alloys fabricated by reactive hot-pressing.

Figures 3.5 (a) and (b) show the compositional dependence of the flexural strength, Vickers hardness and fracture toughness (at 10^{-2} MPa $m^{1/2}$ sec^{-1}) of the hot-pressed FeAl alloys. The Fe-50at%Al alloy has high flexural strength of over 1.1 GPa though it fractures in a brittle manner. Its proportional limit and Vickers hardness decreases with decreasing Al content, and the fracture toughness increases with decreasing the proportional limit and hardness. The fracture toughness of the alloys is basically determined by the plastic deformation at a crack tip. Hence, the relationship between fracture toughness and proportional limit or hardness is easily interpreted by their plastic deformability. The retained thermal vacancies reduce the plastic deformability of FeAl alloys because the vacancies seem to sufficiently interfere (with) the dislocation motion. Accordingly, the yield strength and hardness of these alloys corresponds to the concentration of retained vacancies. As Kogachi and Haraguchi [8] have described, the concentration of retained vacancies tends to increases with increasing Al compositions in FeAl alloys. The mechanical properties of FeAl alloys with higher Al compositions indicated in Figs. 3.3 (a) and (b) are likely to originate from this vacancy strengthening. Because the thermal vacancies in FeAl exhibit complicated behavior such as clustering to form di-vacancies [6,8], the behavior of defects should be further investigated in order to understand the mechanical behavior in detail.

(2) Environmental effect

The fracture behavior of certain intermetallics, such as Ni_3Al, FeAl, Ti_3Al, Zr_3Al, Co_3Ti and Ni_3Si, is also dependent on moisture-induced hydrogen embrittlement at ambient temperatures [9]. Damage tolerance design of these alloys is essential to establish their practical applications. However, their fracture mechanism have not been sufficiently clarified due to the complication of environmental effects. The environmental embrittlement is believed to occur in three stages; 1) the generation of atomic hydrogen (H) by surface reaction of moisture, 2) diffusion and agglomeration of H, and 3) deterioration of cohesive bond strength at active sites. In the early stages of studies on environmental embrittlement, the kinetics of the generation of H had been discussed theoretically even though H atoms derived from moisture could not be practically detected [10]. Recently, however, Zhu et. al have proven that the H generation occurs at the surface of alloys by time of flight (TOF) mass spectroscopy [11]. When H atoms generated by surface reactions diffuse sufficiently into the alloys, the inter-atomic bonds are significantly deteriorated because H behaves as an electron acceptor [12-14]. For example, the electron density around Fe sites in FeAl seems to decrease by the charge transfer to H according to a first principle simulation by Fu and Painter [12]. In spite of the progress in the experimental and theoretical studies on environmental effects, the kinetics of the embrittlement processes are still unclear.

The fracture toughness of environmentally-sensitive intermetllics was anticipated to depend on the loading rate. If toughness measurements are completed in a very short space of time, the

environmental factor would have a negligible affect on fracture toughness because there is insufficient time for the diffusion of H. Figure 3.6 shows the loading rate dependence of the fracture toughness of several FeAl alloy compositions. The 40 and 45 at% Al alloys exhibited a significant dependence of fracture toughness on loading rate. However, the toughness of the stoichiometric alloys is independent to loading rate. Klein et. al [15], and Schneibel and Jenkins [16] have also reported a similar loading rate dependence of fracture resistance of Fe-rich FeAl. The loading rate dependence of fracture toughness is confirmed to be originated from the environmental effect because the dependence is not observed in the oil bath. However, the fracture toughness measured at a loading rate of 10 MPa $m^{1/2}$ sec^{-1} in air is equal to that measured in the oil bath. Therefore, the degree of fracture toughness that is unaffected by the environmental (intrinsic toughness) can be estimated above 10 MPa $m^{1/2}$ sec^{-1}.

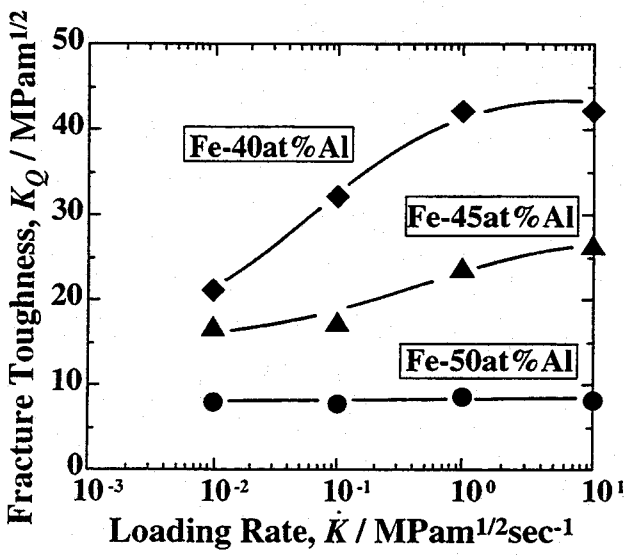

Fig. 3.6 Loading rate dependence of fracture toughness of FeAl alloys at ambient temperatures.

The loading rate dependence of FeAl alloys tends to be suppressed by increasing Al composition in the alloys. The mechanical behavior of the alloys with high Al content is governed by retained vacancies [8]. The stoichiometric alloys are intrinsically brittle due to vacancy hardening. Figure 3.6 also shows the loading rate dependence of the fracture toughness of Fe-40at%Al alloy that was immersed in water for 86.4 ksec prior to the evaluation of fracture toughness. The toughness of the alloys after immersion is consistent with non-immersed toughness. Although the specimens were pre-exposed to a severe environment such as in water, no extra embrittlement was observed. Therefore, the environmental embrittlement is considered to be dynamically enhanced during the

loading process.

Then, variation in the shielding effect at a crack tip during loading should be examined in order to understand the embrittlement mechanism. Latent toughness at certain applied stress intensity factors under the loading with 10^{-2} MPa $m^{1/2}$ sec^{-1} was estimated from bending tests involving a sudden change in loading rate. If the environmental embrittlement occurs before fracture initiation from the notch tip, the latent toughness of the alloys is expect to decrease gradually with increasing of the applied stress intensity factor. Figure 3.7 shows the variation of the latent toughness of the alloys before the fracture initiation by monotonic loading at 10^{-2} MPa $m^{1/2}$ sec^{-1}. Unexpectedly, the latent toughness of the alloys does not decrease until the critical stress intensity factor for fracture initiation under monotonic loading is approached. These results indicate that the environmental embrittlement is rapidly promoted at a critical stress intensity factor. In fact, the toughness values of the alloys measured at 10 MPa $m^{1/2}$ sec^{-1} after maintaining a load of 70-80 % of the critical stress intensity factor for fracture initiation under monotonic loading at 10^{-2} MPa $m^{1/2}$ sec^{-1} for 32.4 ksec, was consistent with the toughness of alloys that did not have pre-loading treatment. The role of stress on the embrittlement process seems to be related to the diffusion and agglomeration of H rather than the surface reaction because Zhu et. al [11] obtained direct evidence for the generation of H without loading. When stress concentration occurs during loading, a plastic deformation zone (process zone) is formed ahead of the notch tip. Because dislocations in metallic materials interact strongly with H, the diffusion and agglomeration of H should be influenced by the dislocation motion in the process zone.

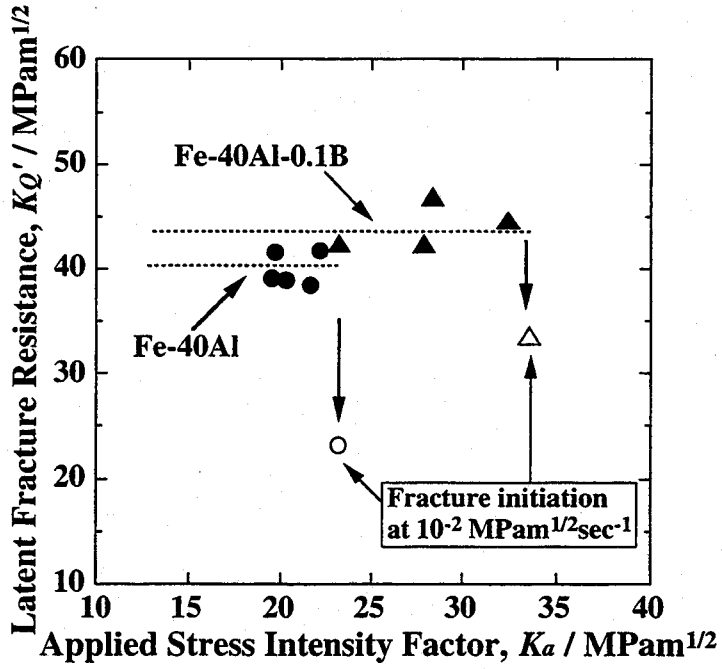

Fig. 3.7 Variation of latent toughness of Fe-40at%Al alloys with and without 0.1at%B doping before fracture initiation by monotonic loading at 10^{-2} MPa $m^{1/2}$ sec^{-1} in air.

Ni_3Al alloys exhibit similar fracture behavior at ambient temperatures, because H in the alloys also degrades chemical bonds between the proximal atoms as shown in Fig. 3.8 (b). Figures 3.8 (a) and (b) show the cluster model and calculation result (total electron density) of the DV-Xα simulation for H in Ni_3Al. The decrease of electron density between Ni and Ni atoms indicates significant bond weakening by H (c.f., Fig. 3.35 : total electron density of Ni_3Al). The present simulation indicated H can predominately degrade the chemical bonds in Ni sublattice in Ni_3Al [17]. Figure 3.9 shows the fracture toughness of Ni-24at%Al alloy both in air and in an oil bath. The toughness of the alloys also exhibits an apparent loading rate dependence in air. This behavior is understood to be caused by the environmental effect which originates from moisture in air because fracture toughness is constant at 19 MPa $m^{1/2}$ regardless of the loading rate in the oil bath. The influence of moisture is suppressed in the oil bath because the specimens are isolated from air.

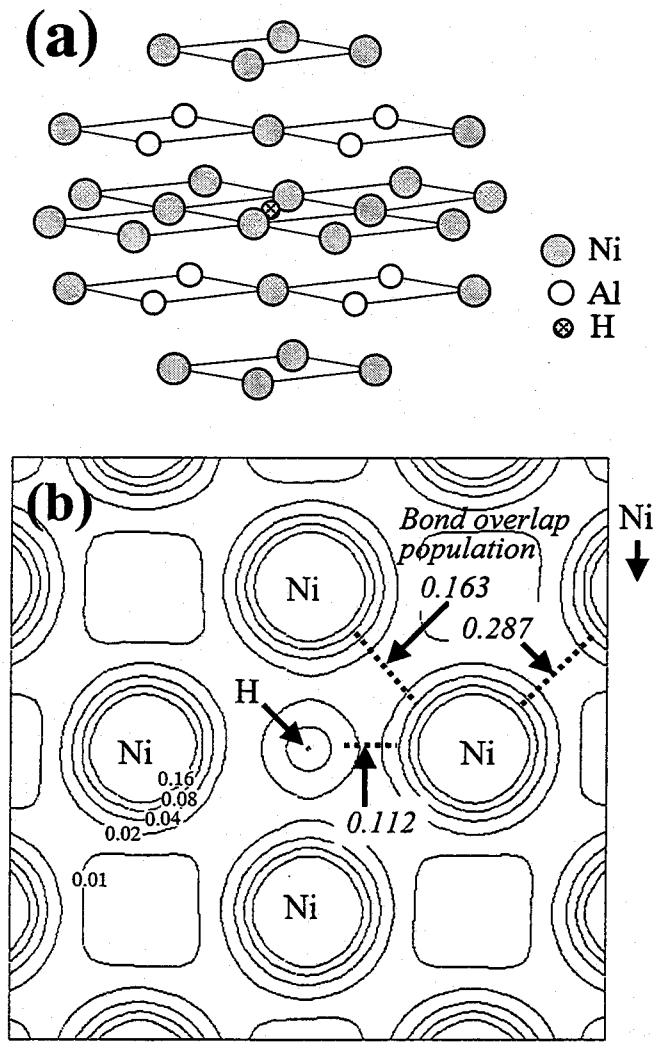

Fig. 3.8 (a) Cluster model and (b) calculation result for total electron density of H in Ni_3Al by the DV-Xα simulation.

Consequently, intermetallics can be briefly divided into two categories relating to their fracture behavior. One category includes alloys that are high sensitive to environmental effects. Although these alloys potentially have significant ductility and toughness, the toughness should be regarded as a variable parameter that is dependent on the kinetics of environmental embrittlement. The other category includes inherently brittle alloys, due to characteristic in chemical bonds and crystal structure. The toughness of these alloys is a constant, independent of loading rate. The guideline for damage tolerance design should be constructed in consideration of these characteristics.

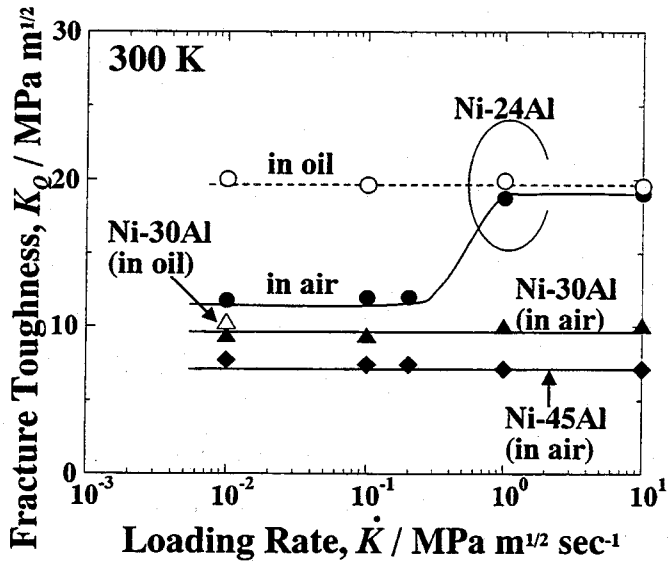

Fig. 3.9 Fracture toughness of Ni-24at%Al and Ni-45at%Al alloys at ambient temperatures in air and in the oil bath.

(3) Effect of alloying elements

(3)-1 *Micro-alloying of B*

Since Aoki and Izumi [18] discovered the effectiveness of B doping for improvement of ductility of Ni_3Al alloys, the ductilizing and toughening mechanism of B doping have been vigorously discussed. The greater proportion of the grain boundaries in polycrystalline Ni_3Al alloys is commonly high-angle random boundaries (RB) [19]. The existence of RB in large quantities is considered to be one of the predominant factors for the intrinsic grain boundary brittleness [19-20] because the transfer of dislocation motion through the grain boundaries, which is essential in realizing extensive ductility, is obstructed. In the early stage of study in B doping, the segregation of

B on the grain boundaries had been clarified to be beneficial to enhancing grain boundary cohesion and to suppressing the intrinsic grain boundary brittleness [21-22]. Recently, suppression of environmental embrittlement by the doping becomes to be believed as the main factor for the toughening of Ni_3Al alloys [23]. Because the diffusivity of H is reduced, the alloys are rendered insensitive to environmental effects [24]. However, there are behaviors that cannot be explained solely by the suppression of environmental effect, such as the dependence of the efficacy of B on alloy composition. Figure 3.10 shows the tensile elongation of Ni-24 and 25 at%Al alloys with and without 0.1at%B doping. The B doping is significantly more effective on Ni-rich alloys than on stoichiometric alloys [21]. To determine the source of the dependency of the efficacy of B doping on matrix composition, the dependence of fracture toughness on loading rate is investigated in air and in an oil bath.

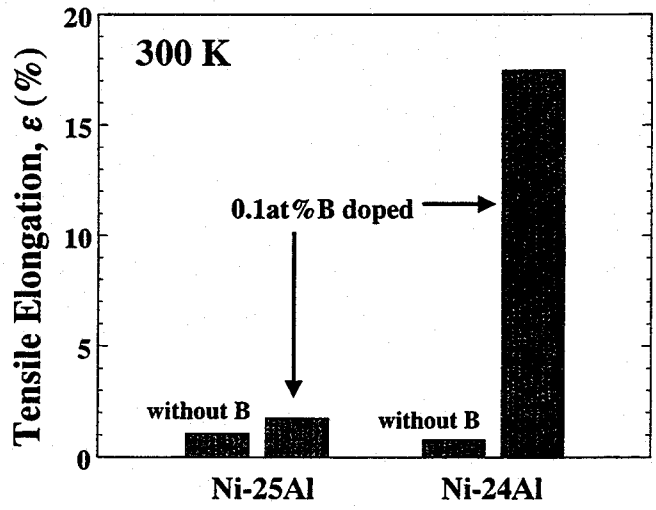

Fig. 3.10 Tensile elongation of Ni_3Al alloys with and without 0.1at%B doping at 300 K.

Figure 3.11 shows the loading rate dependence of fracture toughness for the Ni_3Al alloys. The fracture toughness of the undoped alloys in air decreases with decreasing loading rate, although a similar behavior is not observed in the oil bath. Because moisture induced embrittlement is expected to be inhibited in the oil bath, this loading rate dependence in air is caused by environmental effects. The intrinsic toughness of undoped 24 and 25at%Al alloys are estimated to be 19 and 16 MPa $m^{1/2}$, respectively.

The environmental embrittlement of Ni-25at%Al alloy is successfully inhibited by 0.1at%B doping because the fracture toughness of the doped alloy in air is independent of the loading rate and is equal to that in the oil bath. Concurrently with the suppression of the environmental effect, the

intrinsic fracture toughness of the doped alloy is improved by 30 % over that of the undoped alloy. The chevron-notched testing bars of B doped Ni-24at%Al alloy did not validly fractured under the present conditions because of its remarkable ductility. However, the fracture toughness of the alloy is clearly improved by B doping. If the B doping only suppresses the environmental effect, then the enhancement of fracture toughness should be limited to the intrinsic toughness of the alloy. Hence, a further function of B is necessary to explain the extensive improvement of the the fracture toughness of the alloys.

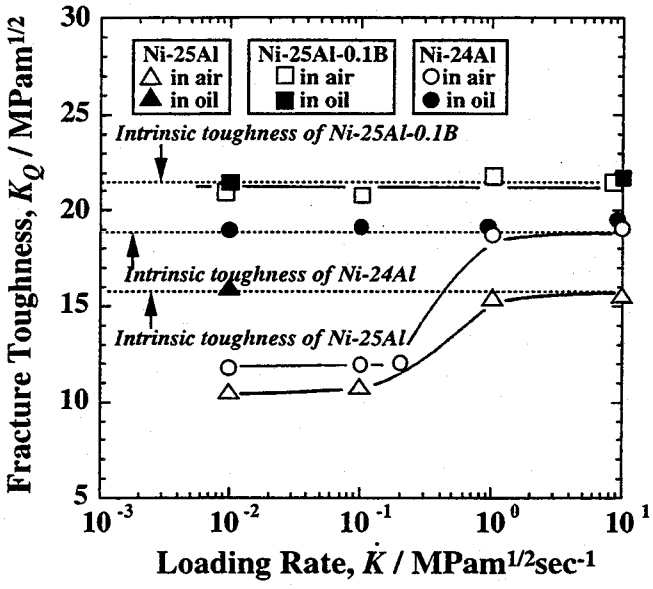

Fig. 3.11 Loading rate dependence of fracture toughness of Ni_3Al alloys with and without B doping at ambient temperatures.

The fracture surfaces of the B-doped alloys are shown in Figs. 3.12 (a)-(c). Although the doped 25at%Al alloy exhibits an intergranular fracture mode similar to that of the non doped alloy, the B-doped 24at%Al one fractured in a transgranular manner. Figure 3.12 (c) illustrates the fracture surface of a chevron-notched test bar of the B-doped Ni-25at%Al alloy fractured in an oil bath. The doped alloy exhibited intergranular fracture even in an inert environment, and therefore the doping does not completely inhibit the intrinsic grain boundary brittleness in this alloy. The enhancement of grain boundary cohesion and consequent suppression of grain boundary brittleness by B doping clearly depends on the alloy composition. Chen et al. [25] performed a computer simulation with embedded-atom style potentials, and demonstrated that the grain boundary cohesion of Ni_3Al alloys is remarkably enhanced when Ni atoms substitute into Al sites at the grain boundaries. The grain boundary cohesion seems to be effectively improved by the segregation of B in the case of Ni-rich Ni_3Al alloys.

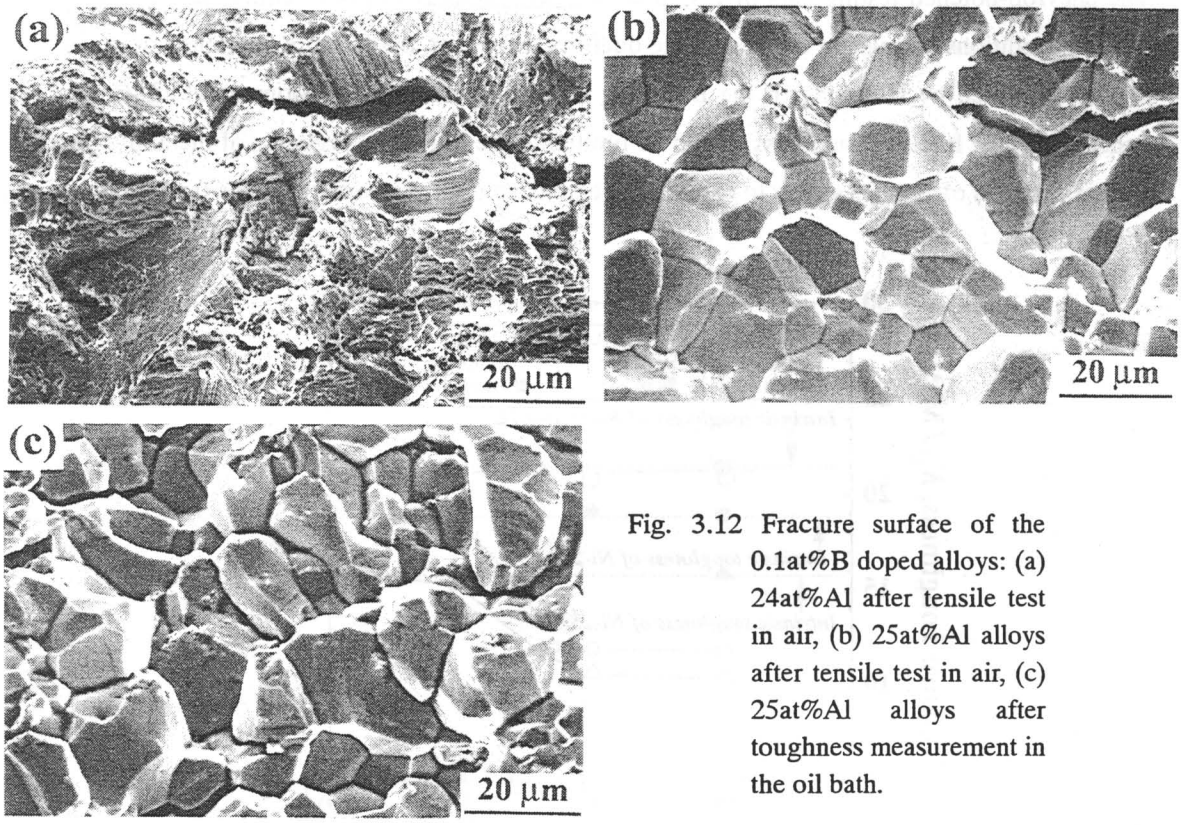

Fig. 3.12 Fracture surface of the 0.1at%B doped alloys: (a) 24at%Al after tensile test in air, (b) 25at%Al alloys after tensile test in air, (c) 25at%Al alloys after toughness measurement in the oil bath.

George et al. [23] have claimed that the suppression of environmental embrittlement is the essential mechanism of toughening Ni_3Al alloys by B doping. However, the present results suggest that the consideration of the enhancement of grain boundary cohesion and the suppression of environmental effects is also needed to fully explain the effect of B on the alloys. The fracture toughness of Ni_3Al alloys is a measure of intrinsic grain boundary brittleness and extrinsic environmental embrittlement. However, the significant improvements in the ductility and fracture toughness of Ni-rich alloys must be predominately caused by grain boundary strengthening rather than suppression of the environmental effect. Unfortunately, the atomic hydrogen derived from severe environments such as a H_2 environment with a pressure above 10 Pa can deteriorate chemical bonds at grain boundaries that have been reinforced by the segregation of B [26-27].

Figure 3.9 also shows the dependence of the fracture toughness of Ni-30 and 45 at%Al alloys on loading rate. The fracture toughness of Ni-45at%Al alloys is ~6 MPa $m^{1/2}$, although fracture is transgranular at ambient temperatures. Furthermore, the toughness is not affected by the environment. The brittleness of these alloys originates from the high APB energy due to high ionicity. Therefore, the ductility and toughness cannot be improved by B doping. The B doping is also ineffective in toughening Ni-30at%Al alloys. Because Ni_3Al, which is included in Ni-30at%Al

alloys, has an Al-rich composition, the grain boundary cohesion among the Ni_3Al grains is marginally improved by doping. Hence, the improvements in the ductility and toughness of Ni-30at%Al alloy are not realized by B doping.

The B doping is well known to be effective in improving the ductility and toughness of Fe-rich FeAl alloys [28]. Figure 3.13 shows the loading rate dependence of the fracture toughness of Fe-40at%Al alloy with 0.1at%B doping in comparison with that of undoped alloys. Environmental embrittlement is effectively suppressed by doping, but not completely inhibited. However, the fracture toughness in the absence of enviornmental effects (intrinsic fracture toughness) of the alloy is not significantly improved. Figures 3.14 (a)-(d) show the fracture surfaces of doped and undoped alloys in air and an oil bath. The undoped alloy fractured in an intergranular manner in these environments. Because the alloy exhibited intergranular fracture even in the inert atmosphere, the cohesive strength at grain boundaries is inherently weaker than the cleavage strength. In contrast to the undoped alloy, the B- doped alloy exhibited transgranular fracture. Therefore, the doping enhanced the inherent grain boundary cohesion of the Fe-40at%Al alloy as well as suppressing the effects of the environment. However, the grain boundary strengthening alone does not account for the improvement in intrinsic toughness. When the undoped alloy is fractured in air, the grain boundary cohesion is considered to be weakened by reaction with H. By contrast, the grain boundary fracture is completely prevented by B doping. Thus, the deterioration of bonding strength in the grains is likely to be a trigger of the environmental embrittlement in the doped alloys.

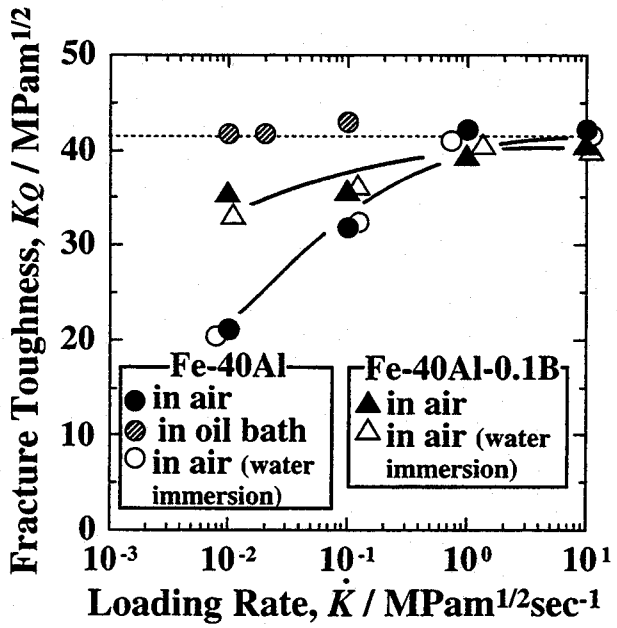

Fig. 3.13 Loading rate dependence of fracture toughness Fe-40at%Al with and without the B doping at ambient temperatures.

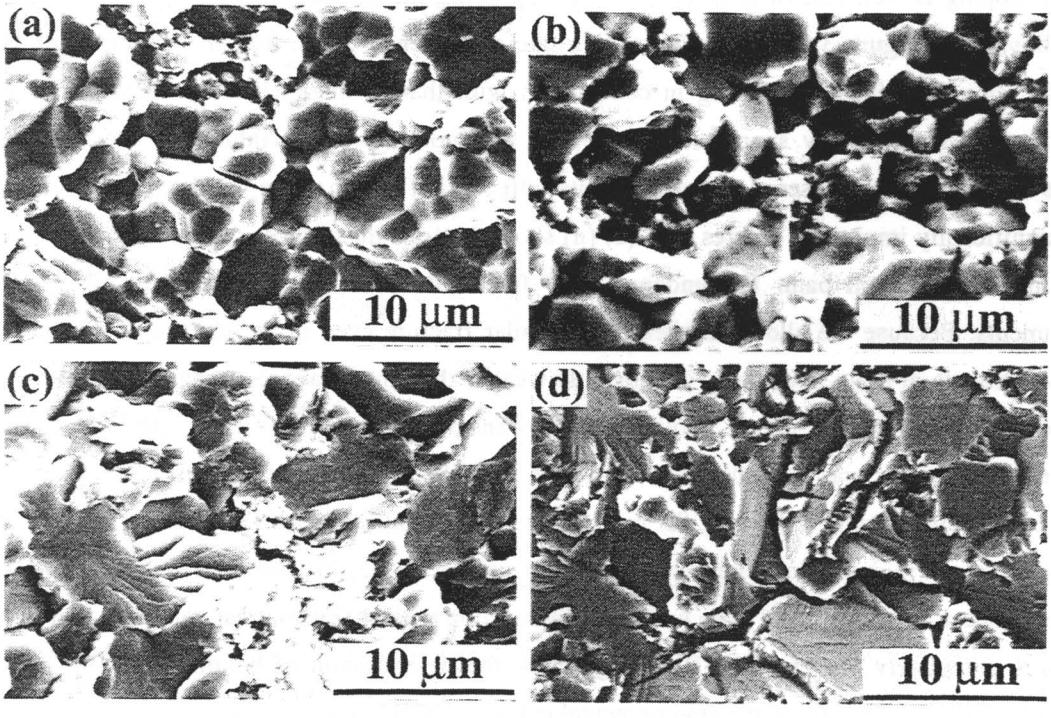

Fig. 3.14 Fracture surface of Fe-40at%Al alloys fractured in air and in the oil bath. (a) non doped alloy in air, (b) non doped alloy in the oil bath, (c) B doped alloy in air and (d) B doped alloy in the oil bath.

(3)-2 *Alloying of Si into FeAl alloys*

The effect of alloying with Si on the mechanical properties of FeAl alloys was investigated. Figure 3.15 shows the flexural strength and fracture toughness of Si doped Fe-40at%Al alloys fabricated by reactive hot-pressing. The formation of other phases, such as iron silicides, is undetectable by microscopic techniques and XRD in the composition range examined in the present work. The proportional limit of the alloys increases remarkably with increasing Si content. In particular, the alloys with 5-7 at%Si exhibit high fracture strengths of over 1.2 GPa, although they fracture in a brittle manner. However, their fracture toughness decreases with strengthening. Because the resistance against dislocation motion becomes great as a result of the defect structures induced by the dissolution of Si, the inherent fracture toughness of such alloys is considered to decrease.

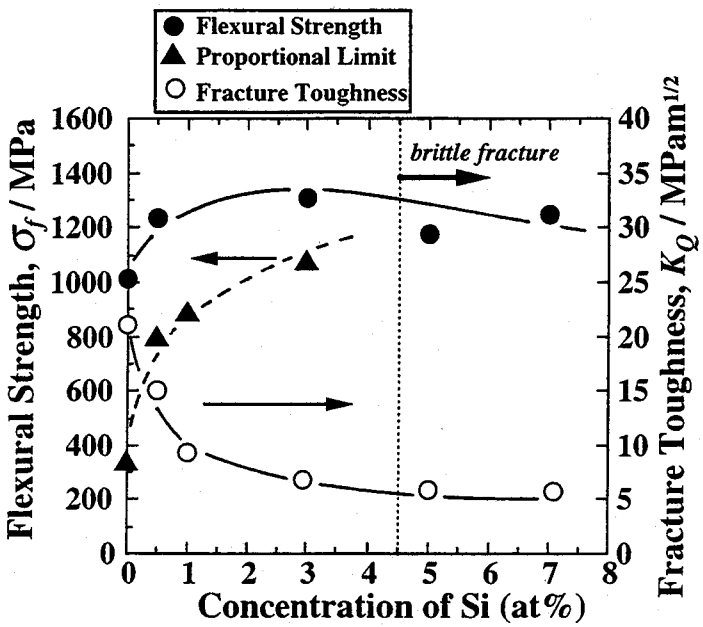

Fig. 3.15 Flexural strength and fracture toughness of the Si doped Fe-40at%Al alloys at ambient temperatures.

(3)-3 *Alloying of Fe into NiAl alloys*

The β-phase (B2 type structure) of Ni-Fe-Al ternary alloys are stable over a wide range of composition [29]. Because the bond nature around Fe atoms in aluminides is quite deferent from that around Ni atoms, the mechanical properties of the ternary alloys are expected to be compositionally depended. Their mechanical properties, such as hardness and tensile strength, have studied by Rudy and Sauthoff [30], Tan et al. [31] and Schneibel [32]. In these previous studies, Schneibel [32] investigated the strengthening of Fe-45at%Al alloys by alloying with Ni. They discovered a deactivation of vacancy hardening and significant solution strengthening by the formation of Ni-vacancy complexes [32]. Tan et al. [31] surveyed the possibility of toughening NiAl alloys by alloying with Fe. Because NiAl alloys have inherent brittleness, the toughening of these alloys is a requirement, regardless of the suppression of environmental effects. However, the effect of Fe atoms on the fracture toughness of NiAl based alloys is still unclear because the previous researchers only measures the Vickers hardness of the alloys. In the present work, the possibility of toughening NiAl alloys by alloying Fe is investigated using the fracture mechanical techniques.

The Al composition of the ternary alloys was fixed at 40, 45 and 50 at%Al in this study. The remaining fraction comprised Ni and Fe. The x value, which indicates the substitutional composition of Fe, is defined as

$$x = [Fe]/\{[Ni]+[Fe]\} \qquad (3\text{-}1)$$

$$\{[Ni]+[Fe]\} = 1 - [Al] \qquad (3\text{-}2)$$

where [Ni], [Fe] and [Al] represent the atomic fraction of these elements.

Figures 3.16 (a) and (b) show the Vickers hardness and fracture toughness of the ternary alloys. In the case of the 50 at%Al alloys, hardness increases with increasing Fe content. On the contrary, the hardness of the 40 and 45 at%Al alloys tends to decrease with increasing Fe content. If the toughness of these alloys predominately depends on the shielding effect of plastic deformation at a crack tip, the fracture toughness can be qualitatively inferred from their hardness. In fact, the fracture toughness of the 50 at%Al alloys, which are hardened by alloying, decreases with increasing Fe content. Although the alloying with Fe is ineffective in toughening of the 50 at%Al alloys, the fracture toughness of the 40 and 45 at%Al alloys is significantly improved. The increment in toughness becomes larger at lower atomic fraction of Al. In the case of binary NiAl with Ni rich composition, some Al sites are substituted by Ni atoms. In the case of Ni-rich ternary alloys, some Ni sites are considered to be substituted by Fe atoms. A detail understanding of the bond nature in this situation is necessary in order to clarify the origin of these mechanical behaviors.

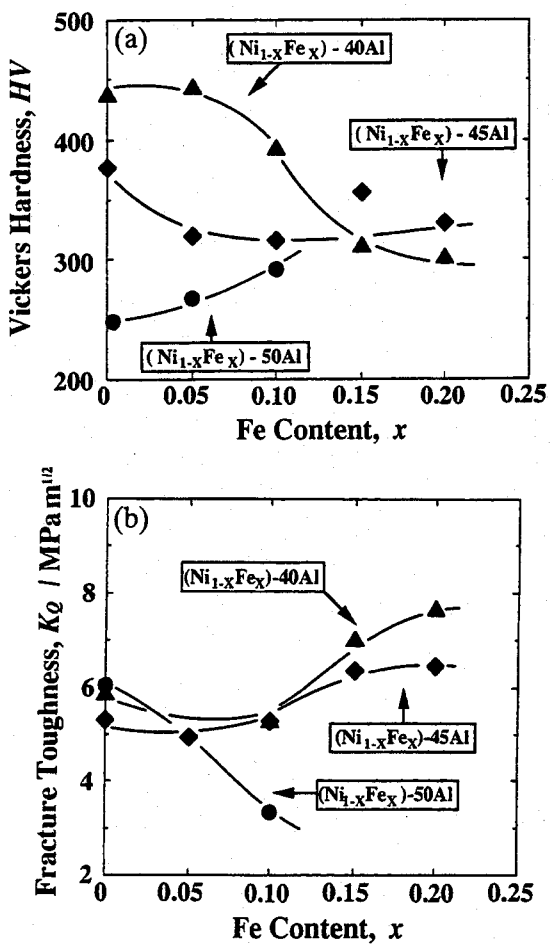

Fig. 3.16 (a) Vickers hardness and (b) fracture toughness of Ni-Fe-Al ternary alloys at ambient temperatures.

Figures 3.17 (a)-(c) show the proportional limit and flexural strength of these alloys. The proportional limit of the 50at%Al alloys increases with alloying, as shown in Fig.3.17 (a), although the fracture strength is not improved significantly. The 40 and 45 at%Al alloys exhibit elastic-plastic deformation behavior after alloying with Fe. These ternary alloys maintain elasticities of up to 400-600 MPa, which corresponds to the flexural strength (in brittle fracture) of the binary alloys. Moreover, the alloys reveal relatively high flexural strength of over 700 MPa. These ternary alloys exhibit expected improvements in mechanical properties over the binary alloys.

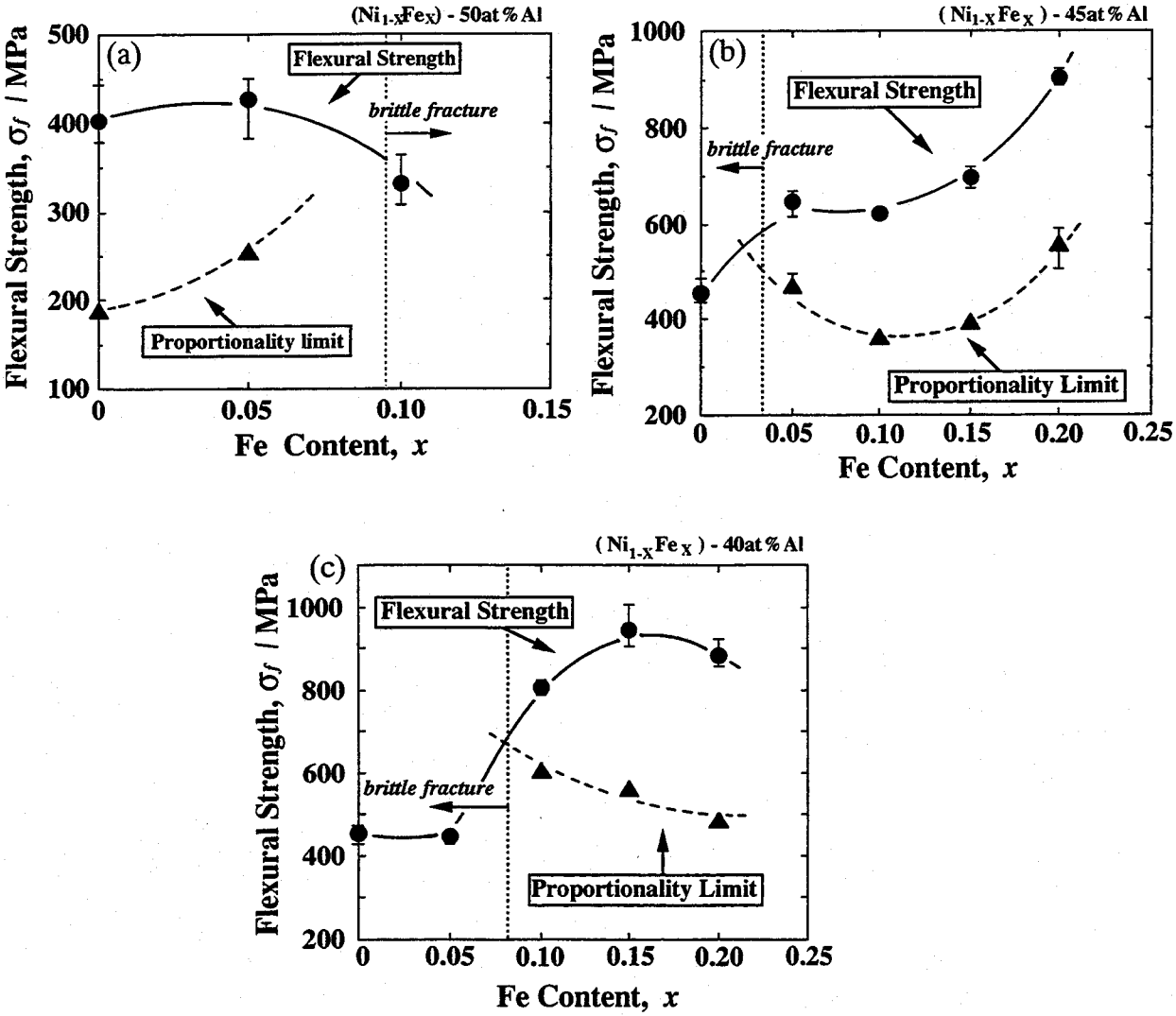

Fig. 3.17 Proportional limit and flexural strength of Ni-Fe-Al ternary alloys at ambient temperatures. (a) 50at%Al, (b) 45at%Al and (c) 40at%Al

3-3-2 Mechanical Properties at Elevated Temperatures

Ni_3Al alloys

Figures 3.18 (a) and (b) show the temperature dependence of the tensile strength and elongation of Ni-24at%Al alloys with and without B doping at temperatures up to 1273 K in air and in Ar. The undoped alloys exhibit brittle fracture below 900 K. The strength and ductility of the undoped alloys are governed by weak grain boundary cohesion in this temperature range. On the other hand, the ductility at ambient temperatures is remarkably improved by the B doping, as described above (c.f., 3-3-1 (3)). However, the doped alloys reveal brittle fracture at 700-1000 K in air as shown in Fig. 3.18 (b), although the yield stress anomaly is observed in Ar. Liu and White [33], and Hippsley and DeVan [34] found that the environmental embrittlement promoted by stress-assisted diffusion of atomic oxygen (O) occurs in Ni_3Al alloys at intermediate temperatures. The dynamic embrittlement resulting from oxygen diffusion is considered to be one of the factors that contribute to deteriorating ductility between 700 K and 1000 K.

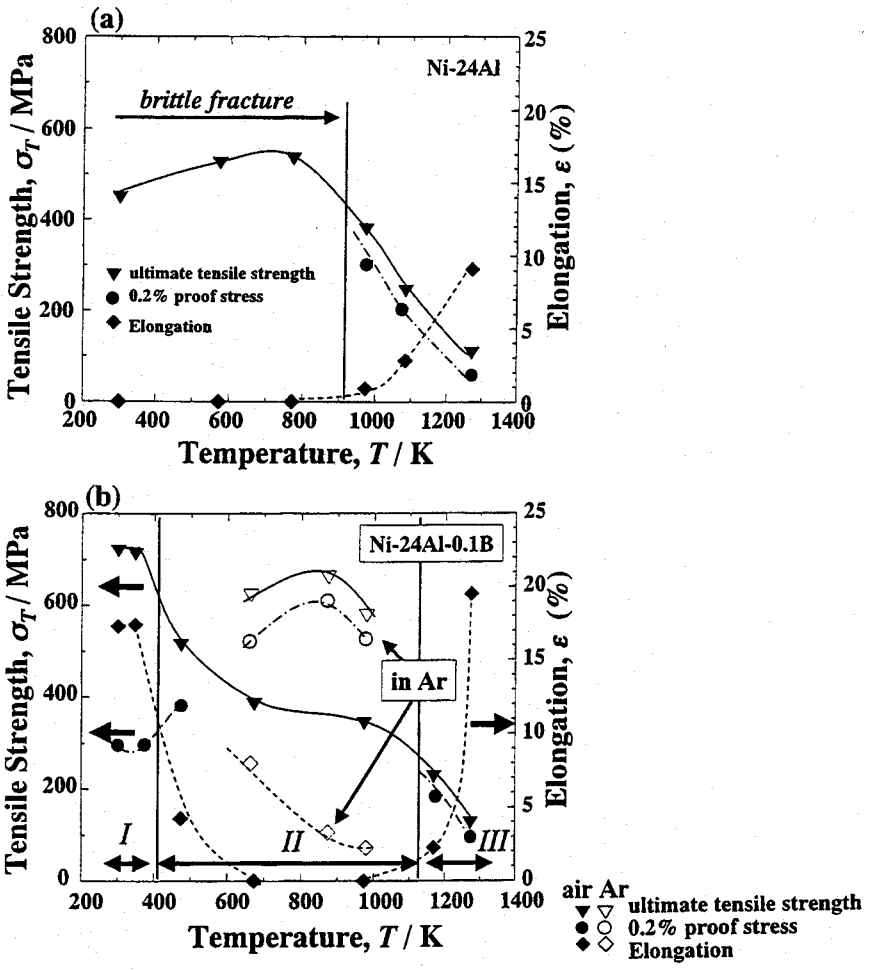

Fig. 3.18 Tensile strength and elongation of Ni-24at%Al alloys (b) with and (a) without B doping in air and in Ar.

In order to infer the oxygen embrittlement mechanism, the DV-Xα simulation was conducted with the clusters shown in Figs. 3.19 (a) and (c), which are models for interstitial O atoms in Ni_3Al crystals. The simulation was also conducted with the models without O atoms in Figs. 3.19 (b) and (d). Table 3.1 shows that the net charge and bond overlap population of these clusters calculated by the Mulliken population analysis. In the case of atomic configuration in Fig. 3.19 (a), the O atom covalently bonds to neighbor Ni atoms with no Coulomb attractive force. The bond formation between O and Ni atoms results in weakening Ni-Ni bonds. The bond weakening is visually confirmed in the total electron density diagrams shown in Fig. 3.20. The bond weakening by the O atoms is considered to cause the oxygen embrittlement of Ni_3Al alloys. On the other hand, the O atom forms strong covalent and ionic attractive interactions with neighbor Al atoms, rather than with Ni atoms, in the atomic configuration of Fig. 3.19 (c). Although the O atom also weakens the bonds among neighbor Ni and Al atoms, the chemical interaction between O and Al atoms is expected to contribute to form a protective aluminum oxide scale. In general, the drastic rearrangement of atomic configuration to form reaction products is governed by the energetic factor as well as the inter-atomic interactions in a short range. Therefore, the chemical interaction between O and Al atoms is needed to be more stabilized by the alloying elements to suppress the oxygen embrittlement.

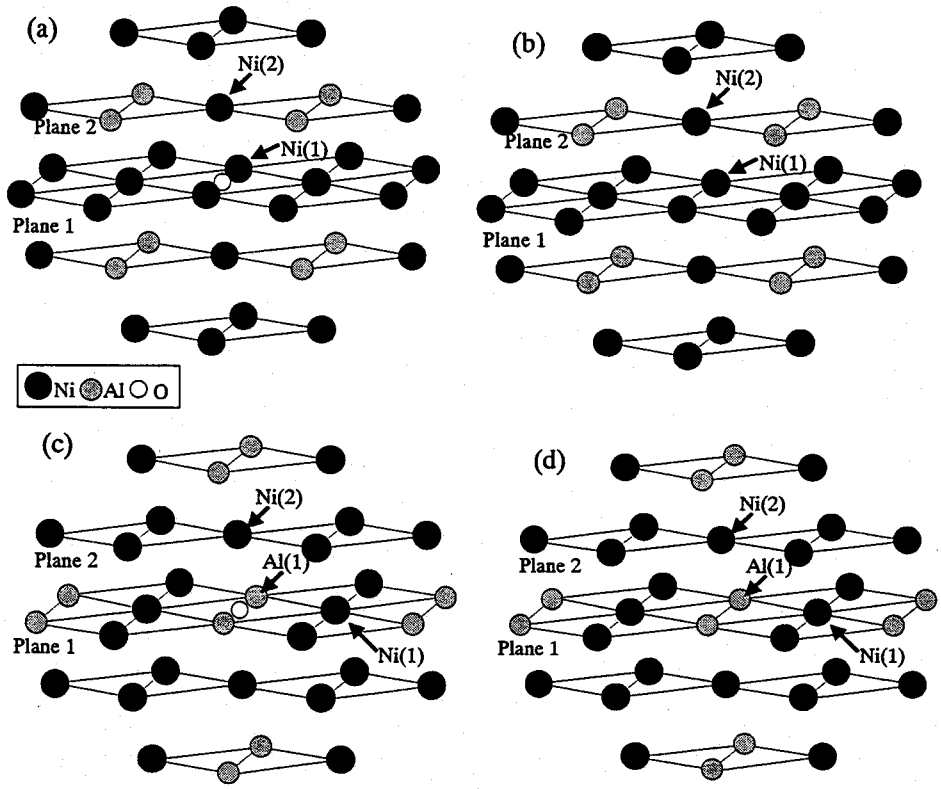

Fig. 3.19 Cluster models of Ni_3Al with and without atomic oxygen for DV-Xα simulation.

Table 3.1 Calculation results of net charge and bond overlap population for the clusters illustrated in Fig. 3.18 (a)-(d) by SCAT code.

model	net charge	bond overlap population
(a)	O : -0.041 Ni(1) : -0.042 Ni(2) : -0.015	O-Ni (plane 1) : 0.241 O-Ni (inter-plane 1-2) : 0.234 Ni-Ni (plane 1) : 0.091 Ni-Ni (inter-plane 1-2) : 0.084
(b)	Ni(1) : -0.108 Ni(2) : -0.053	Ni-Ni (plane 1) : 0.185 Ni-Ni (inter-plane 1-2) : 0.188
(c)	O : -0.210 Ni(1) : 0.086 Al(1) : 0.168 Ni(2) : 0.084	O-Ni (plane 1) : 0.148 O-Al (plane 1) : 0.353 Ni-Al (plane 1) : 0.121 O-Ni (inter-plane 1-2) : 0.165 Ni-Ni (inter-plane 1-2) : 0.090 Al-Ni (inter-plane 1-2) : 0.129
(d)	Ni(1) : 0.007 Al(1) : 0.095 Ni(2) : -0.055	Ni-Al (plane 1) : 0.227 Ni-Ni (inter-plane 1-2) : 0.180 Al-Ni (inter-plane 1-2) : 0.271

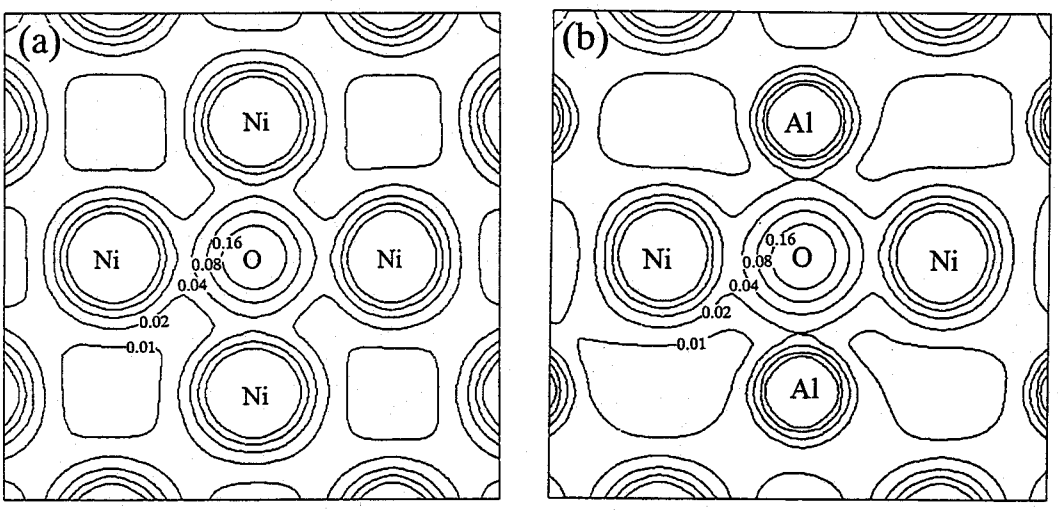

Fig. 3.20 (a), (b) Calculation result of total electron density around O in the cluster model 3.19 (a) and (c), respectively.

In the real alloys, the O atoms agglomerate at the active sites, such as grain boundaries, dislocation cores and point defects, to promote the oxygen embrittlement. However, the bond weakening by interstitial O atoms that is clarified by the present model simulation is believed to provide the fundamental information about the oxygen embrittlement mechanism of Ni_3Al alloys.

The dependence of fracture toughness of these alloys on loading rate was investigated to clarify the embrittlement mechanism at intermediate temperatures. Figure 3.21 illustrates the fracture toughness of the Ni_3Al alloys at 673 and 873 K in air and in Ar. The alloys reveal the characteristic dependence of fracture toughness on loading rate in air. Toughness is linearly reduced by decreasing

the loading rate at 10^{-2}-10 MPa $m^{1/2}$ sec^{-1}. This loading rate dependence originates from oxygen embrittlement, because the dependence is suppressed in Ar.

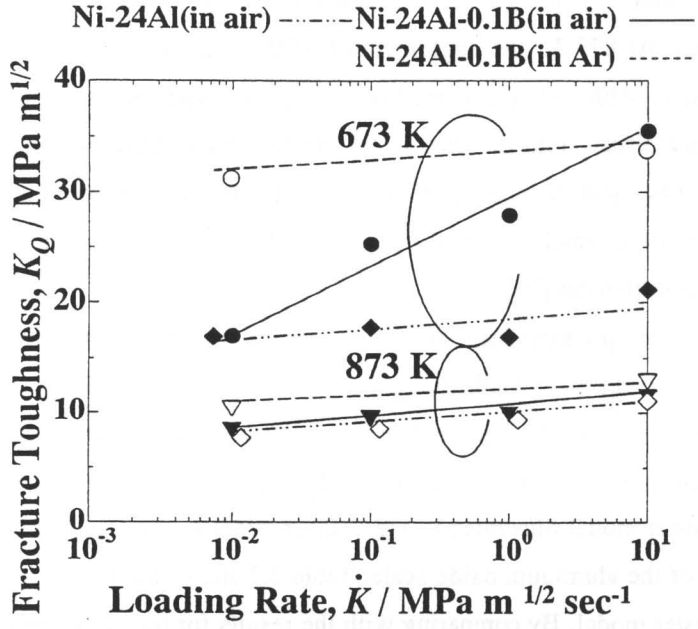

Fig. 3.21 Loading rate dependence of fracture toughness of Ni-24at%Al alloys with and without B doping at 673-873 K.

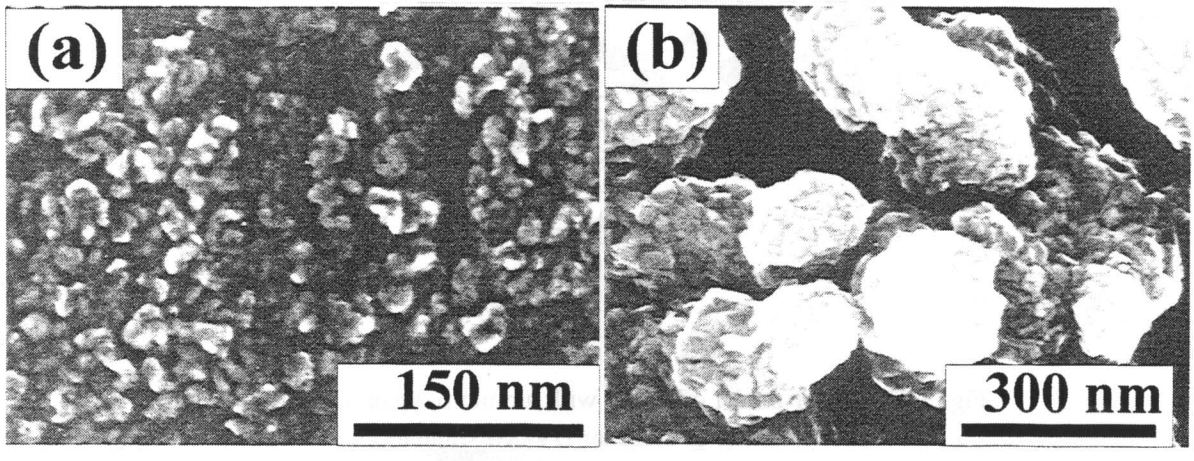

Fig. 3.22 Microstructural features of oxide scale formed on Ni-24at%Al-0.1at%B alloy at (a) 673 and (b) 873 K.

Aluminum oxide scale forms on the surfaces of the alloys in air at elevated temperatures. Figures 3.22 (a) and (b) show the microstructural features of the oxide scale formed on the Ni-24at%Al-0.1at%B alloy at 673 and 873 K. The scale formed at 673 K consists of small particles with diameters of 20-30 nm. At 873 K, the agglomerates of these particles form, accompanied by an increase in particle size. Although the formation of surface scale provides excellent oxidation resistance, O can easily diffuse into the plastic deformation zone when cracks form in the scale. Because Ni_3Al alloys have low Al activity, they are relatively weak in forming stiff oxide scale. Hence, the alloying with Cr, which facilitates oxide scale formation, is expected to be effective in suppressing oxygen embrittlement [35].

The Al sites in Ni_3Al are predominately substituted by Cr atoms [36]. According to the DV-Xα simulation by Morinaga et al.[36], the inherent ductility of Ni_3Al is barely improved by alloying Cr because the bond strength of Ni-Al bonds around Cr atoms is significantly degraded by forming strong covalent bonds between Ni and Cr atoms. In the present work, the DV-Xα simulation was performed with the cluster model illustrated in Fig. 3.23 in order to investigate the effect of alloying with Cr on formation of the aluminum oxide scale. Table 3.2 shows the results of molecular orbital simulation for this cluster model. By comparing with the results for the cluster model shown in Fig. 3.19 (c) (Table 3.1 (c)), the effect of substitutional Cr atom is clearly understood. The bond overlap

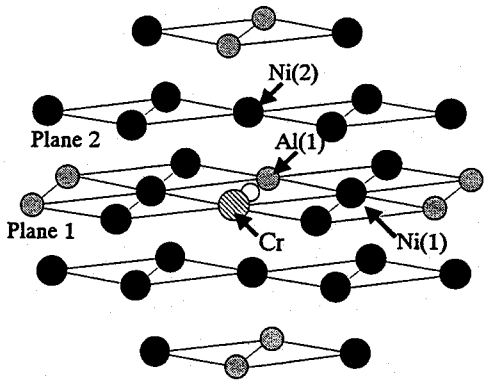

Fig. 3.23 Cluster model of Ni_3Al with atomic oxygen and with substitutional Cr atom for DV-Xα simulation.

Table 3.2 Calculation results of net charge and bond overlap population for the cluster illustrated in Fig. 3.23.

model	net charge	bond overlap population
Fig. 3.23	O : -0.190 Ni(1) : 0.060 Cr : 0.361 Al(1) : 0.231 Ni(2) : 0.012	O-Ni (plane 1) : 0.160 O-Al (plane 1) : 0.346 O-Cr (plane 1) : 0.242 Ni-Al (plane 1) : 0.112 Ni-Cr (plane 1) : 0.118 O-Ni (inter-plane 1-2) : 0.170 Ni-Ni (inter-plane 1-2) : 0.084 Al-Ni (inter-plane 1-2) : 0.128 Cr-Ni (inter-plane 1-2) : 0.112

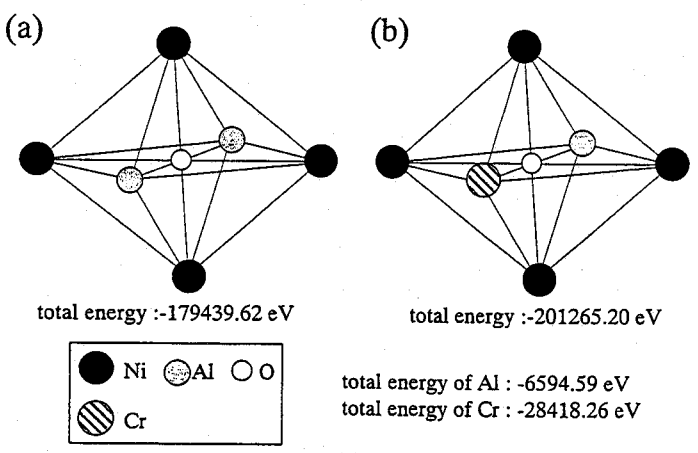

Fig. 3.24 Atomic configuration of (a) $Ni_4Al_2O_1$ and (b) $Ni_4Al_1Cr_1O_1$ clusters. The total energy, that is calculated by the Dmol[3] code, is also shown in this figure.

populations between O and the proximal atoms are unaffected by the substitutional Cr atom. However, the net charge of Al atom proximal to O atom positively increases by substituting another Al site with Cr. The Cr atom also has a positive net charge. Therefore, a strong Coulomb attractive force generates between O and Al atoms, and between O and Cr atoms. In order to briefly estimate relative binding energy in this atomic configuration, the following imaginary reaction is assumed;

$$Ni_4Al_2O_1 + Cr \rightarrow Ni_4Al_1Cr_1O_1 + Al \qquad (3\text{-}3)$$

where, $Ni_4Al_2O_1$ and $Ni_4Al_1Cr_1O_1$ are the clusters (Figs. 3.24 (a) and (b)), which are central units of the cluster models shown in Fig. 3.19 (c) and Fig. 3.23, respectively. The Cr and Al are the isolated

atoms. The total energies of these clusters and atoms, that are calculated by the Dmol[3] code, are shown in Fig. 3.24. The total energy difference of this reaction, which means binding energy change by the rearrangement of atomic configuration, is estimated as;

$$\Delta E_{total} = \{ E(Ni_4Al_1Cr_1O_1) + E(Al) \} - \{ E(Ni_4Al_2O_1) + E(Cr) \} = -1.909 \text{ eV} \qquad (3\text{-}4)$$

Thus, the variation of chemical interaction originating from the substitution with Cr is reasonably enhance the energetic stability of O proximal to Al atoms. Consequently, the alloying with Cr is expected to reduce the diffusivity of O and to facilitate the drastic atomic rearrangement to form the protective oxide scale. Chromium oxide are considered to be included in the oxide scale due to adequate bond overlap population between Cr and O.

As indicated in Fig. 3.21, the B doped alloy exhibits higher toughness at 673 K at a loading rate of 10 MPa $m^{1/2}$ sec^{-1} in air than the undoped alloys. Therefore, the fracture toughness is effectively improved by the doping even at 673 K. Figures 3.25 (a) and (b) show the fracture surface of the alloy with B doping at 673 and 873 K in air. The cracks pass across the grains as well as along the grain boundaries in the doped alloy at 10 MPa $m^{1/2}$ sec^{-1} (Fig. 3.25 (a)). The grain boundary strengthening resulting from segregation of B seems to be sufficiently effective at this temperature,

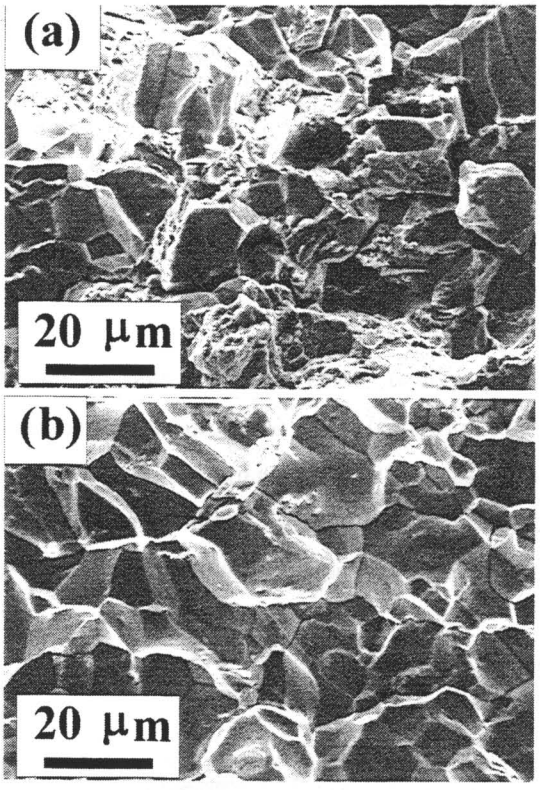

Fig. 3.25 Fracture surface of Ni-24at%Al-0.1at%B alloys at (a) 673 and (b) 873 K in air.

although the cohesive strength at grain boundaries decreases with increasing temperature due to the diffusion of B from the grain boundaries [37-38]. However, the B doping ceases to be effective in toughening the alloy at 10^{-2} MPa $m^{1/2}$ sec^{-1} in air at 673 K. The grain boundary cohesion is considered to completely deteriorate with the dynamic diffusion of oxygen at such a slow loading rate. In fact, the alloy exhibits perfect intergranular fractures at 10^{-2} MPa $m^{1/2}$ sec^{-1} in air, as shown in Fig. 3.25 (b).

In contrast, only a slight loading rate dependence of fracture toughness under oxygen embrittlement is observed in the B doped alloy at 873 K in air. Additionally, the fracture toughness of the doped alloy is equal to that of the undoped alloy at this temperature. Because the doped alloy reveals the intergranular fracture mode even in Ar as shown in Fig. 3.26, the cohesive strength at the grain boundaries is intrinsically degraded. The deterioration of grain boundary cohesion is expected to reduce the fracture toughness of the alloy. However, another mechanism should be considered as a cause of embrittlement, because the toughness of the undoped alloy also decreases. The yield stress anomaly by the Kear-Wilsdorf mechanism [9] is observed in this temperature range. The locking of dislocations intrinsically suppresses the plastic deformability of the alloys. The fracture toughness of these alloys seems to decrease primarily with deterioration of grain boundary cohesion and dislocation locking, rather than with oxygen embrittlement at 873 K.

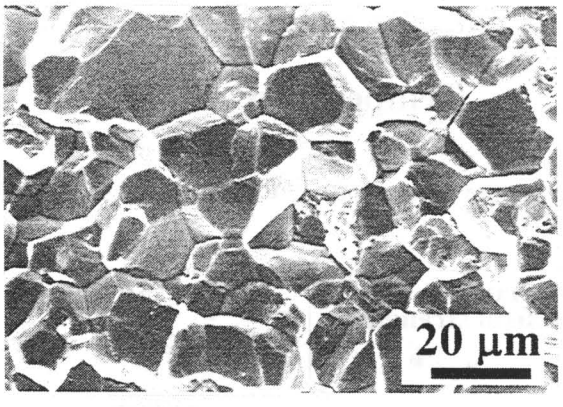

Fig. 3.26 Fracture surface of Ni-24at%Al-0.1at%B alloys fractured at 873 K in Ar.

As temperature increases further, significant softening occurs above 1000 K in both alloys. The Ni_3Al alloys with large grain size were reported to fracture in a brittle manner due to the deterioration of grain boundary cohesion [37-38] although the dislocations can also slip on (100) in this temperature range. However, the Ni_3Al alloys with small grain size can exhibit significant plastic deformation resulting from the relief of stress concentrations at grain boundaries by grain boundary sliding and dynamic recrystallization [37-38]. Because the apparent grain size of the

present alloys is 20-30 μm, they can exhibit significant ductility by these mechanisms above 1000 K.

NiAl and related alloys

NiAl alloys are expected to be used in high temperature structural applications because they have a high melting point above 1773 K. However, these alloys do not exhibit high strength at elevated temperatures in spite of their high melting point. Figure 3.27 shows the temperature dependence of the Vickers hardness of NiAl alloys up to 1100 K. The decrease in Vickers hardness below 650-700 K suggests that remarkable softening occurs in this temperature range. For example,

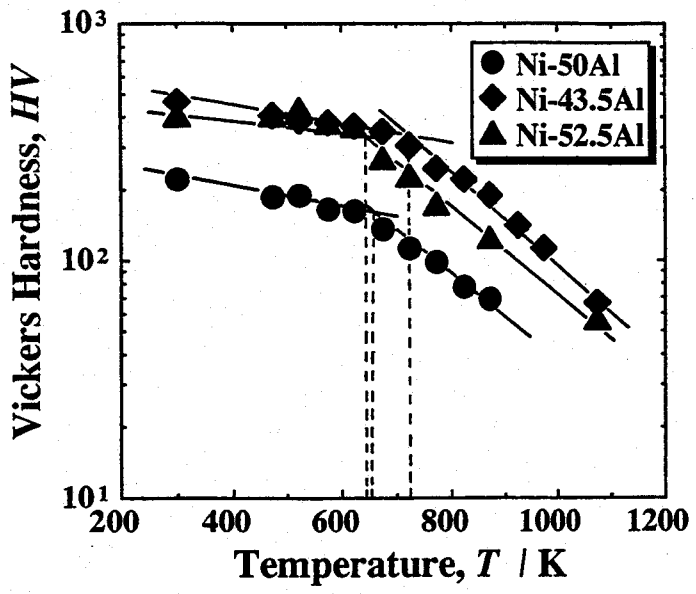

Fig. 3.27 Temperature dependence of Vickers hardness of NiAl alloys.

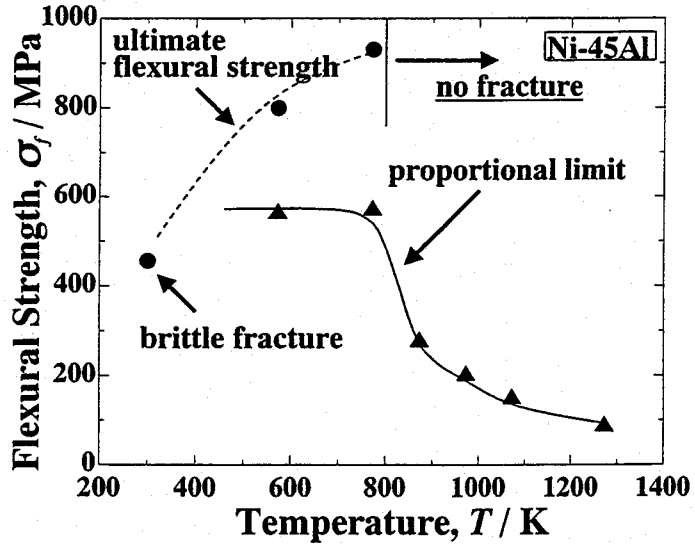

Fig. 3.28 Temperature dependence of flexural strength of Ni-45at%Al alloys in air.

Fig. 3.28 shows the flexural strength of Ni-45at%Al alloy. The alloy fractures in a brittle manner due to the defect strengthening at ambient temperatures, as described previously. The alloy exhibits relatively high strength with elastic-plastic deformation at 400-800 K. Unfortunately, the strength is not maintained over 800 K as shown in Fig. 3.28. The strength above 800 K should be improved in order to establish the practical applications, in addition to toughening at ambient temperatures.

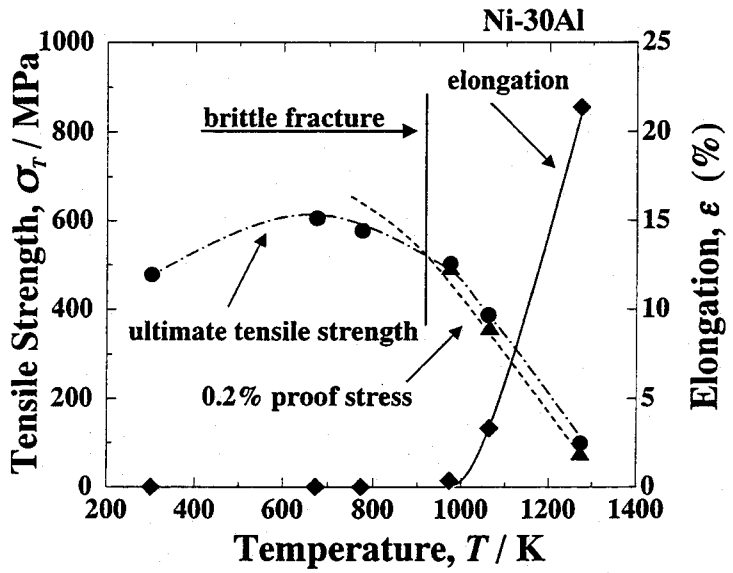

Fig. 3.29 Temperature dependence of tensile strength and elongation of Ni-30at%Al alloys in air.

The Ni-30at%Al alloys that consist of Ni_3Al and NiAl phases exhibit high flexural strength at ambient temperatures, as shown in Fig. 3.2. To investigate the potential of the alloys as an advanced material design of Ni aluminides, the tensile strength of the Ni-30at%Al alloys was measured up to 1273 K (Fig. 3.29). The alloys exhibit brittle fracture below 1000 K although their ultimate strength is ~20% higher than that of Ni_3Al monolith. The alloys have a slight advantage in strength over Ni_3Al alloys, however the ductility and toughness should be improved with an alternate material design.

FeAl alloys

Because FeAl alloys have relatively low melting point (~1473 K), they are restricted in their utility to intermediate temperatures (1000-1100 K). The Fe-40at%Al alloys that are annealed to remove retained thermal vacancies exhibit a yield stress anomaly resulting from the formation of thermal vacancies at 700-800 K [2-3]. Figures 3.30 and 3.31 show the temperature dependence of the Vickers hardness and tensile strength of FeAl alloys. The alloys do not reveal a significant yield stress anomaly. Hence, they seem to include a considerable number of retained vacancies after the

hot-pressing process. Their hardness and strength drastically decrease above 700 K. The FeAl alloys exhibit high deformability by dislocation creep [3] due to the low activation enthalpy for formation and migration of thermal vacancies [39-40] in this temperature range. Therefore, the strength and creep resistance above 700 K is a serious problem to establish their practical applications.

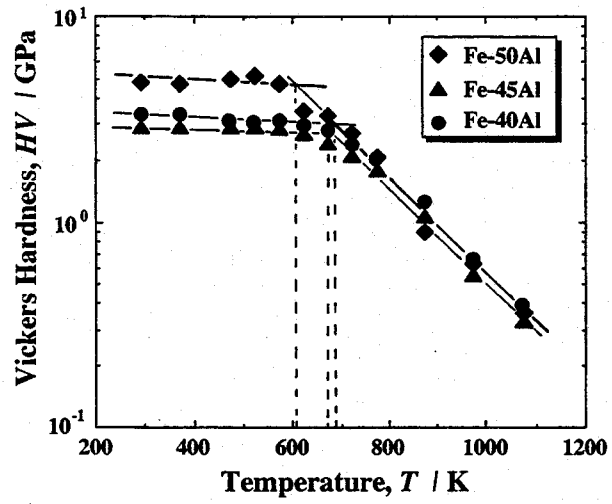

Fig. 3.30 Temperature dependence of Vickers hardness of FeAl alloys.

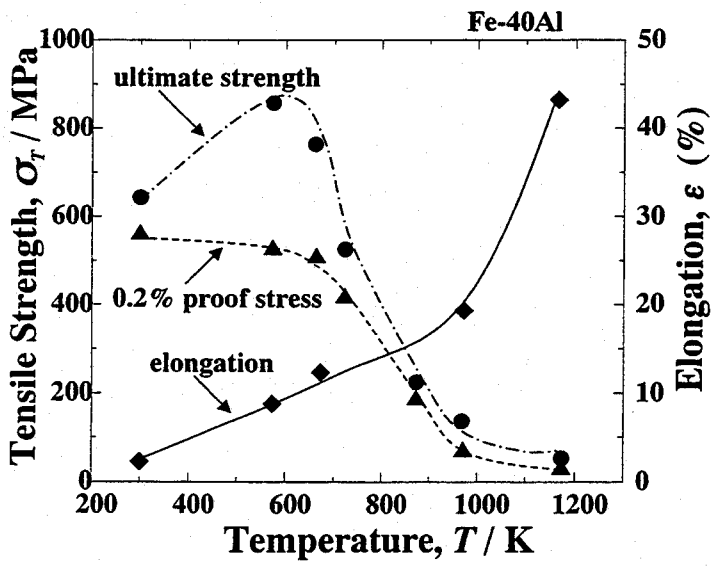

Fig. 3.31 Temperature dependence of tensile strength and elongation of Fe-40at%Al alloys without B doping in air.

Figure 3.32 shows the temperature dependence of tensile strength of the Fe-40at%Al with 0.1at%B doping in air. The B doping is effective in improving ductility and ultimate strength at

ambient temperatures by suppressing environmental embrittlement, as mentioned previously. On the other hand, the 0.2 % proof stress of the alloys is significantly improved by alloying with a few at% Si, rather than by B doping. Figure 3.33 shows the temperature dependence of the tensile strength and elongation of Fe-40at%Al-3at%Si alloy in air. Their yield strength decreases above 800 K. However, the strengthening with Si remains effective at elevated temperatures as well as at ambient temperatures. The Si-doped alloys exhibit a serration at the yield point in the stress-strain curve at temperatures between 500 K and 700 K (Fig. 3.34). The serration of the alloys is considered to be caused by the Portevin-LeChatelier effect with the solute atom atmosphere.

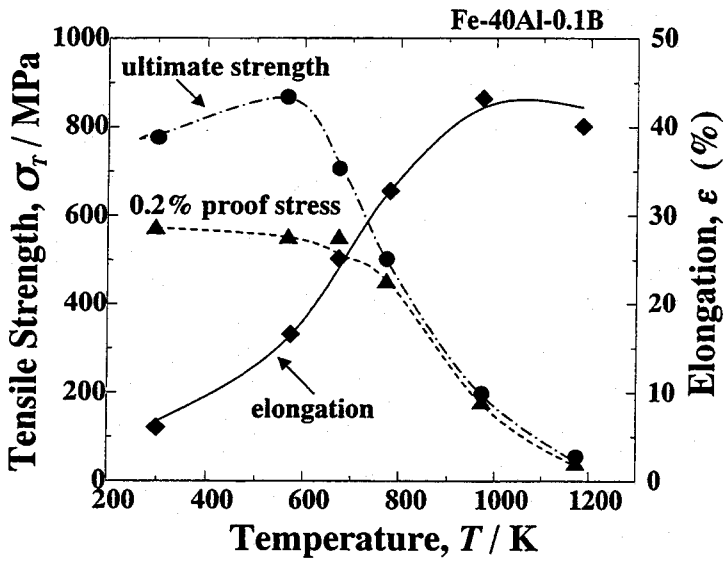

Fig. 3.32 Temperature dependence of tensile strength and elongation of Fe-40at%Al-0.1at%B alloys in air.

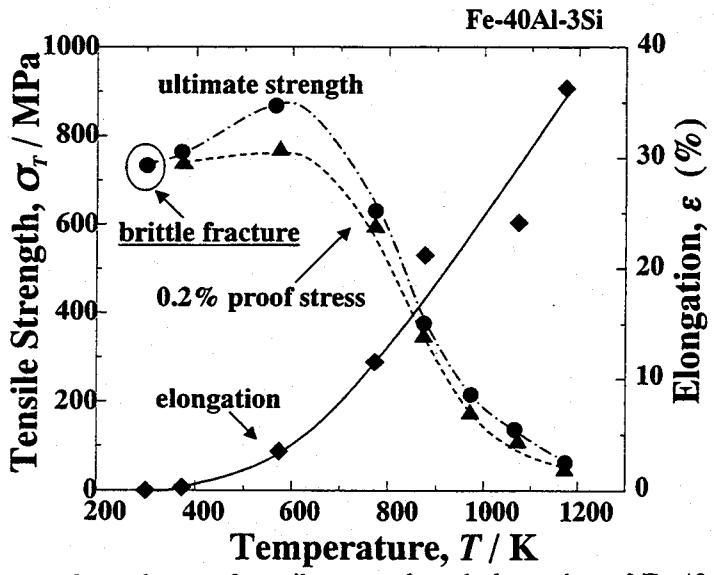

Fig. 3.33 Temperature dependence of tensile strength and elongation of Fe-40at%Al-3at%Si alloys in air.

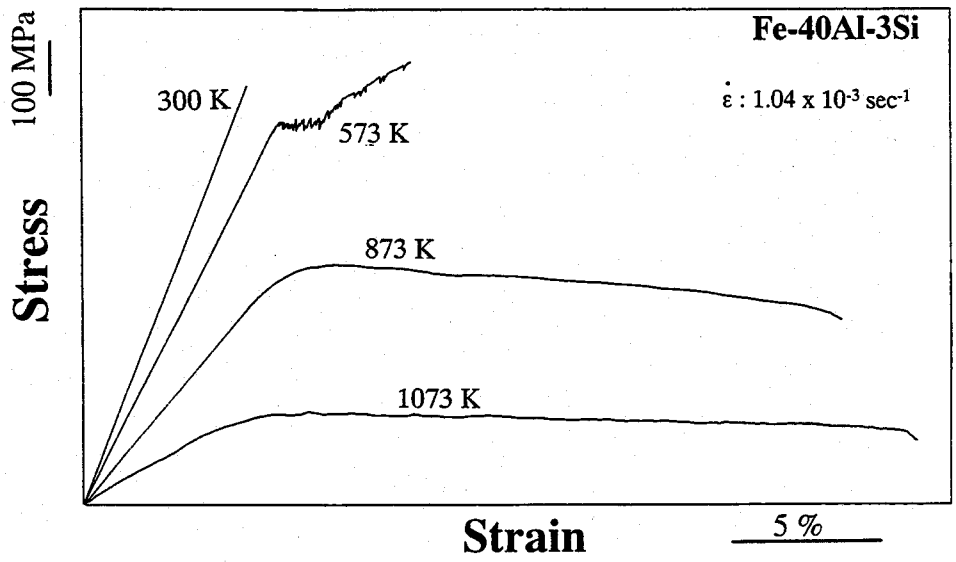

Fig. 3.34 Stress-strain curves detected during tensile test of Fe-40at%Al-3at%Si alloys at 300-1073 K.

3-4 Conclusion

In this chapter, the mechanical properties of Ni and Fe aluminides fabricated by reactive hot-pressing were evaluated in several environments. The main results obtained in this chapter are briefly summarized as below:

FeAl alloys

(1) Strength and hardness increase with increasing Al content due to retained vacancy hardening at ambient temperatures, with a corresponding decrease in fracture toughness.

(2) Fracture toughness is governed by moisture induced environmental embrittlement at ambient temperatures. Toughness is successfully improved by B doping, hence suppressing environmental embrittlement.

(3) The alloys exhibit remarkable plastic deformability by dislocation creep above 700 K as a result of the low activation enthalpy for formation and migration of thermal vacancies in this temperature range.

(4) Si is an effective alloying element for strengthening FeAl alloys.

Ni_3Al alloys

(1) Ductility and toughness are improved remarkably by B doping at ambient temperatures. Although grain boundary segregation of B is effective in enhancing grain boundary cohesion and suppressing environmental embrittlement, the increase in ductility is primarily induced by the segregation of B.

(2) These alloys exhibit significant embrittlement in the intermediate temperature range. Dynamic embrittlement caused by the diffusion of atomic oxygen is the main mechanism at 673 K. However, intrinsic embrittlement by the Kear-Wilsdorf mechanism and the deterioration of grain boundary cohesion is observed at 873-1073 K.

(3) Fatal softening occurs above 1100 K.

NiAl alloys

(1) The strength is strongly dependent on alloy composition due to defect strengthening at ambient temperatures.

(2) Fracture toughness is 5-6 MPa $m^{1/2}$ with no loading rate dependency at ambient temperatures. The toughness of the alloys with 40-45 at%Al is improved by alloying with Fe.

(3) The strength decreases drastically above 800 K although their melting point is over 1773 K.

Appendix ch.3 :
Metallic character (metallic bond) of substances

The chemical bonds in condensed matter are commonly divided into covalent, ionic, metallic bondings, and so on. Many text books commonly explain the concept based on a non-localized free electron model for metallic bonds. The electronic structure of metals is assumed to be "a sea of free electrons with dispersed metal cations" in the elementary text books. The bonding state of typical metals such as Al may be adequately approximated by this free electron model. However, the bonding state of transition metals is not represented by the non-localized free electrons because of the contribution of localized d and f-orbital components. The chemical bonds in intermetallics containing transition metal elements is more complicated due to characteristic orbital hybridization and significant charge transfer.

The metallic character of substances should be represented by the delocality of electron wave function. The molecular orbitals near the Fermi level of the transition metals are generally formed by hybridizing d (or f) basis orbitals with a principal quantum number of n ($n \geqq 3$) and s, p basis orbitals of n+1. Although the basis functions of d orbitals are highly localized, the s, p basis functions are relatively delocalized. The characteristics of these basis orbitals coincide in the characteristics of the

hybridized molecular orbitals. Therefore, the chemical bonds in these substances are the conjugated bonds with high covalency. The hybridization orbitals exist in a shallow energy level due to the extensive conjugation. The conjugated bonds provide electronic states in conduction band to promote the metallic electron conduction. The metallic character of a substance should be represented by the parameters concerning charge distribution [41] and energy level of orbitals. The conjugation of bond orbitals with a high overlap population is the most important factor in determining the metallicity of substances.

We can adequately describe the difference of bond character of Ni_3Al and NiAl using this concept. The chemical bonds in these aluminides is mainly formed by p-d hybridization and charge transfer from Ni to Al atoms. Because the highest occupied state of both alloys exits in a conduction band without a band gap [42], the conjugation of bond orbitals is likely to occur in these alloys (Indeed, they exhibit metallic electron conduction.). However, the differences in bond overlap population between Ni_3Al and NiAl are observed rather than in net charge, as shown in Fig. 3.35. In NiAl, the bond overlap population between same kind atoms is relatively lower although overlap populations of Ni-Al bonding is high. By contrast, Ni_3Al exhibits high overlap population even of bonds between same kind atoms, as well as at Ni-Al bonds. Thus, extensive resonance of bond orbitals is expected to be achieved even in Ni_3Al with charge locality. This is the reason why Ni_3Al has a more metallic character (such as extensive ductility) than NiAl. In conclusion, metallic character can be qualitatively analyzed by net charge (high polarization results in the localization of wave function), bond overlap population and energy eigenvalue of highest occupied orbital.

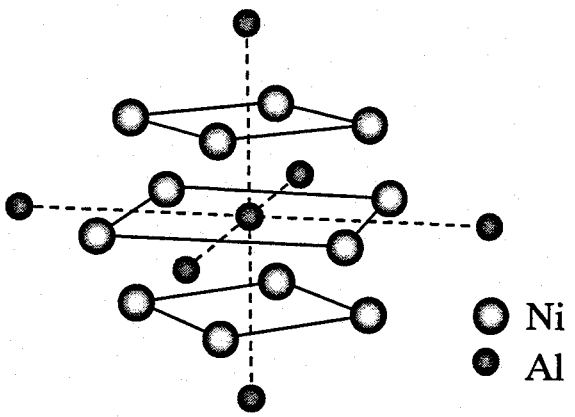

Fig. 3.35 Cluster model and molecular orbital simulation results for Ni_3Al.

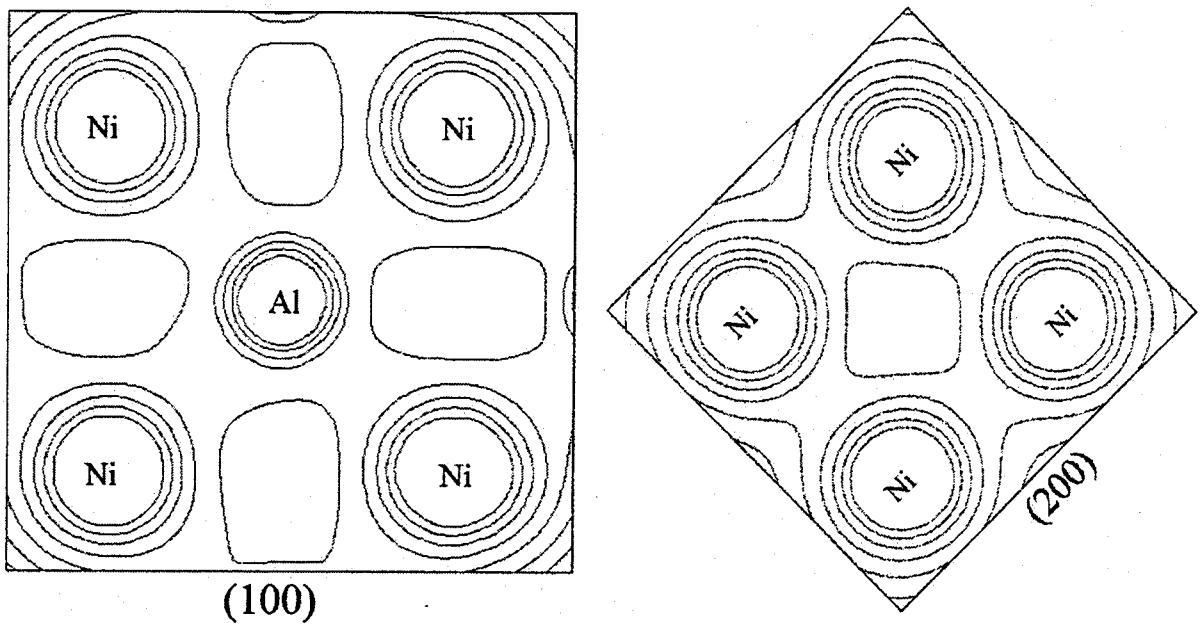

net charge	bond overlap population
Ni : -0.1301	Ni-Al (100) : 0.2337
Al:0.1859	Ni-Ni (100) : 0.2568
	Ni-Al (100)-(200) : 0.2392
	Ni-Ni (100)-(200) : 0.2617

Fig. 3.35 *Continued*

Finally, the author emphasizes the following two points: 1) the chemical bonds in all kinds of substances, including inorganic, organic and metals, can comprehensively understand with the concept of molecular orbital theory, 2) the molecular orbital theory is the most powerful tool for analyzing the inter-material interactions at interfaces and surfaces.

References

[1] T. Haraguchi and M. Kogachi, Mat. Res. Soc. Symp. Proc., vol. 552 (1999) KK.5.33

[2] K. Yoshimi, S. Hanada and M. H. Yoo, Mat. Res. Soc. Symp. Proc., vol. 460 (1997) 313

[3] I. Baker and E. P. George, Mat. Res. Soc. Symp. Proc., vol. 460 (1997) 373

[4] J. H. Westbrook, J. Electrochem. Soc., 103 (1956) 54

[5] Y. Tan, T. Shinoda, Y. Mishima and T. Suzuki, J. Jpn. Inst. Metals, 57 (1993) 220

[6] C. L. Fu, Y.-Y. Ye, M. H. Yoo and K. M. Ho, Phys. Rev., B48 (1993) 6712

[7] M. K. Miller, R. Jayaram and P. P. Camus, Scripta Metall. Mater, 26 (1992) 679

[8] M. Kogachi and T. Haraguchi, Mat. Sci. Eng. A230 (1997) 124
[9] J. H. Westbrook (ed.), Intermetallic compounds, vol.1, John Wiliey & Sons Ltd., (1994)
[10] J. C. M. Li and C. T. Liu, Scripta Mater., 33 (1995) 661
[11] Y. F. Zhu, C. T. Liu and C. H. Chen, Scripta Mater., 35 (1996) 1435
[12] C. L. Fu and G. S. Painter, J. Mater. Res., 6 (1991) 719
[13] H. Adachi and S. Imoto, J. Phys. Soc. Jpn., 46 (1979) 1194
[14] Y. Liu, K. Y. Chen, J. H. Zhang, G. Lu and Z. Q. Hu, J. Mater. Res., 13 (1998) 290
[15] O. Klein, P. Nagpal and I. Barker, Mat. Res. Soc. Symp. Proc., vol.288 (1993) 935
[16] J. H. Schneibel and M. G. Jenkins, Scripta Metall. Mater., 28 (1993) 389
[17] M. Inoue and K. Suganuma, The 3rd Oxford Kobe Materials Seminar (2000)
[18] K. Aoki and O. Izumi, J. Jpn. Inst. Metals, 43 (1979) 1190
[19] T. Watanabe, T. Hirano, T. Ochiai and H. Oikawa, Mater. Sci. Forum., 157-162 (1994) 1103
[20] T. Hirano, Acta Metall. Mater., 38 (1990) 2667
[21] C. T. Liu, C. L. White and J. A. Horton, Acta Metall., 33 (1985) 213
[22] O. Izumi and T. Takasugi, J. Mater. Res., 3 (1988) 426
[23] E. P. George, C. T. Liu and D. P. Pope, Acta Mater., 44 (1996) 1757
[24] X. Y. Cheng, X. J. Wan, J. T. Guo and C. T. Liu, Scripta Mater., 38 (1998) 959
[25] S. P. Chen, A. F. Voter, R. C. Albers, A. M. Boring and P. J. Hay, J. Mater. Res., 5 (1990) 955
[26] K. H. Lee, J. T. Lukowski and C. L. White, Intermetallics, 5 (1997) 483
[27] J. W. Cohron, E. P. George, L. Heatherly, C. T. Liu and R. H. Zee, Acta Mater., 45 (1997) 2801
[28] M. A. Crimp, K. M. Vedula and D. J. Gaydosh, Mat. Res. Soc. Symp., vol.39 (1985) 499
[29] A. J. Bradley, J. Iron Steel Inst., 166 (1949) 19
[30] M. Rudy and G. Sauthoff, Mater. Sci. Eng., 81 (1986) 525
[31] Y. Tan, T. Shinoda, Y. Mishima, T. Suzuki, J. Jpn. Inst. Metals, 57 (1993) 840
[32] J. H. Schneibel, Mater. Sci. Eng., A258 (1998) 181
[33] C. T. Liu and C. L. White, Acta Metall., 35 (1987) 643
[34] C. A. Hippsley and J. H. DeVan, Acta Metall., 37 (1989) 1485
[35] C. T. Liu, E. P. George, V. K. Sikka and S. C. Deevi, Processing and Design Issue in High Temperature Materials, TMS, (1997) 139
[36] M. Morinaga, N. Yukawa and H. Adachi, J. Phys. Soc. Jpn., 53 (1984) 653
[37] M. Takeyama and C. T. Liu, Acta Metall., 36 (1988) 1241
[38] A. Choudhury, C. L. White, C. R. Brooks, Scripta Metall., 20 (1986) 1061
[39] R. Wurschum, C. Grupp and H.-E. Schaefer, Phys. Rev. Lett., 75 (1995) 97
[40] H.-E. Schaefer, K. Frenner and R. Wurscum, Phys. Rev. Lett., 82 (1999) 948
[41] I. Tanaka, Ceramics Japan, 34 (1999) 34
[42] R. Eibler and A. Neckel, J. Phys. F, 10 (1980) 2179

Chapter 4

Thermodynamic Properties and Interfacial Reactivity of Ni and Fe Aluminides

4-1 Introduction

High processing temperatures above 1273 K are necessary to fabricate aluminide matrix composites containing ceramic particles, whiskers and fibers. The interfacial reaction between matrix and reinforcements is the most serious problem in developing aluminide matrix composites because the matrix alloys exhibit remarkable reactivity with the reinforcements at such high temperatures. Chemical interaction at the interface is important in realizing sufficient interfacial cohesion. However, excessive chemical reactions that result in a deterioration of reinforcements is undesirable in the fabrication of high performance composites. Misra [1-5] has reviewed the chemical compatibility of many substances in Ni, Fe, Ti and Nb aluminides based on his original thermodynamic algorithm. Although the reaction mode predicted by Misra is not always observed at real interfaces due some assumption in his calculation, the algorithm is believed to be quite useful for screening for chemical compatibility of reinforcements [6].

In the present chapter, the author applies chemical compatibility assessments using methodologies of thermodynamics and quantum chemistry to Ni and Fe aluminides in the belief that the understanding of interfacial reaction behavior based on quantum chemical concepts can lead to novel interfacial designs in the future.

4-2 Background to Thermodynamic Investigation

4-2-1 Activity of Constitutional Elements in Ni and Fe aluminides

The activity of Al in Ni-Al and Fe-Al alloys had been measured with an electrochemical technique with liquid Al anode [7] and by an isopietic method [8-9] in the 1960's. The activity of Ni or Fe in the binary alloys can be calculated by Gibbs-Duhem integration based on the experimental data of activity of Al [10]. The experimental data and calculation results of Gibbs-Duhem integration were comprehensively reviewed by Libowitz [11] and Neumann et. al [12]. Figure 4.1 shows the activity of elements in Ni-Al and Fe-Al alloys at 1273 K. Although only few composition dependence of activity of the constitutional elements is observed in Fe-Al system, the activity is strongly influenced

by the alloy composition in Ni-Al system. Moreover, their activity in Ni-Al alloys remarkably exhibits negative deviation from the ideal solution behavior.

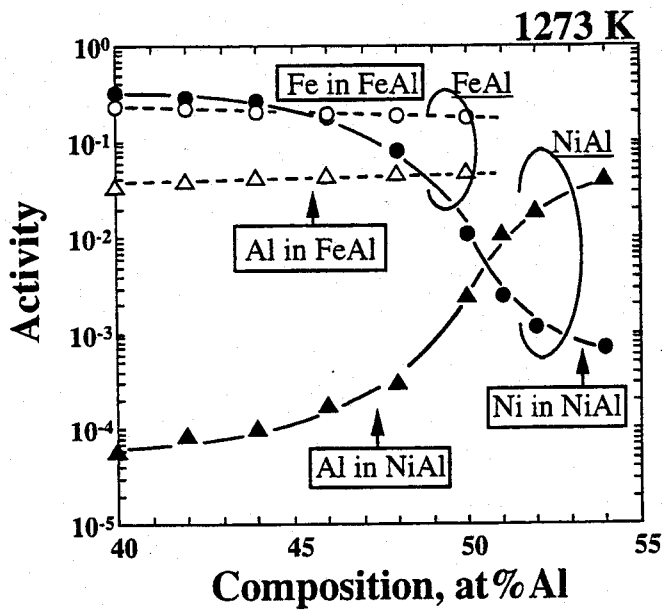

Fig. 4.1 Composition dependence of thermodynamic activity of alloy elements in Ni-Al and Fe-Al binary systems at 1273 K [7-10].

The activity data at 1273 K can be easily extrapolated to a certain temperature (T K) by the following equations ;

$$\ln (a_{Al})_T - \ln (a_{Al})_{1273} = \{ \Delta\bar{H}_{Al} (1/T - 1/1273) \} / R \qquad (4\text{-}1)$$

$$\ln (a_{Ni})_T - \ln (a_{Ni})_{1273} = \{ \Delta\bar{H}_{Ni} (1/T - 1/1273) \} / R \qquad (4\text{-}2)$$

where $\Delta\bar{H}_{Al}$ and $\Delta\bar{H}_{Ni}$ are the partial molar enthalpy of Al and Ni, and R is gas constant. These activity data were used in the following thermodynamic calculation. The interpretation of the activity (chemical potential) by quantum chemistry will be discussed in the below section in this chapter.

4-2-2 Thermodynamic calculation

The thermodynamic calculation algorithm for the chemical compatibility assessment proposed by Misra [1-5] consists with the following three steps; 1) selection of the most stable (binary) compounds in the matrix, 2) analysis of the interfacial reactions, 3) examination of the dissolution of the constitutional elements. By using an imaginary reinforcement CD and a matrix alloy AB, the calculation processes are briefly described below ;

1) Selection of the most stable products in the matrix

The ternary or higher order products are ignored in this analysis due to the lack of thermodynamic data. The most stable products containing the elements of A and B are selected in each binary systems of A-C, A-D, B-C and B-D. The comparison of thermodynamic stability of these compounds is conducted by the calculation of the minimum activity for formation, which is equal to the activity in equilibrium state.

ex. calculation of minimum activity of A necessary to form A_xC_y

A_xC_y are formed by the reaction ;

$$x\,A + y\,C \rightarrow A_xC_y \qquad (4\text{-}3)$$

The equilibrium constant (K_3) at a certain temperature (T) can be easily estimated by the following equation,

$$\Delta G^\circ = -RT \ln K_3 \qquad (4\text{-}4)$$

If the activity of A_xC_y is 1, K_3 is represented by

$$K_3 = 1 / \{ (a_A)^x \cdot (a_C)^y \} \qquad (4\text{-}5)$$

Assuming unit activity for C, the equilibrium activity of A, $(a_A)_{eq}$, is equal to be $(1 / K_3)^{1/x}$.

If the activity of constitutional element in the matrix is lower than the equilibrium activity calculated by the procedure mentioned above, the compound cannot be formed in this system. The compound which has the lowest equilibrium activity is identified as the most stable compounds in the binary system. The similar calculations are applied in the whole binary system. Then, the four possible compounds, which are assumed as A_xC_y, A_pD_q, B_iC_j and B_mD_n here, are selected by the calculation. For the assessment of chemical compatibility, only two products in these compounds are needed to be considered. The relative stability of A_xC_y against B_iC_j in the AB matrix can be predicted by equilibrium calculation for the following reaction ;

$$(j)\,A_xC_y + (i\,y)\,B \rightarrow (y)\,B_iC_j + (x\,j)\,A \qquad (4\text{-}6)$$

Because the activities of A_xC_y and B_iC_j would be 1, the equilibrium constant of this reaction can be represented as;

$$K_6 = (a_A)^{xj} / (a_B)^{iy} \qquad (4\text{-}7)$$

If the activity ratio [$(a_A)^{xj} / (a_B)^{iy}$] of a given a_A and a_B in the matrix alloy is larger than the equilibrium constant, A_xC_y would be the stable compound. On the contrary, if the activity ratio in the alloy is less than K_6, B_iC_j would be the stable compound in the matrix. Similarly, the relative stability of A_pD_q and B_mD_n can be assessed.

The above calculation is simply performed by a commercial thermodynamic database software, MALT2 and CHD (Science and Technology Co., Ltd., Tokyo, 1992). CHD is an attached software to draw chemical potential diagrams based on thermodynamic parameters recorded in MALT2. Stable reaction products can be easily determined as the function of activities of constitutional elements by the chemical potential diagrams.

2) Thermodynamic analysis for interfacial reaction

The possible reactions to form the products are the reduction of the reinforcement material ;

$$x\,\underline{A} + y\,CD \rightarrow A_xC_y + y\,D \qquad (4\text{-}8)$$
$$p\,\underline{A} + q\,CD \rightarrow A_pD_q + q\,C \qquad (4\text{-}9)$$
$$i\,\underline{B} + j\,CD \rightarrow B_iC_j + j\,D \qquad (4\text{-}10)$$
$$m\,\underline{B} + n\,CD \rightarrow B_mD_n + n\,C \qquad (4\text{-}11)$$

where $\underline{A}$ and $\underline{B}$ in the formulas indicate the reduced activity of the elements in the matrix alloy. First criterion of Misra's algorithm is the standard Gibbs free energy change (ΔG°) for these reactions. ΔG° must be negative for inducing the reactions. For the reactions with negative ΔG° , the equilibrium activity of A or B in the reactions (4-8) – (4-11) is compared with the activity in the matrix alloy. If the activity in the matrix is greater than the equilibrium activity, the reaction would occur, and therefore the reinforcement material is incompatible for the matrix.

If the reactions (4-8) – (4-11) is not judged to occur, the simultaneous formation reactions (4-12) – (4-15) must be considered.

$$(qx + py)\,\underline{A} + (qy)\,CD \rightarrow (q)\,A_xC_y + (y)\,A_pD_q \qquad (4\text{-}12)$$
$$(nx)\,\underline{A} + (ym)\,\underline{B} + (ny)\,CD \rightarrow (n)\,A_xC_y + (y)\,B_mD_n \qquad (4\text{-}13)$$
$$(in + jm)\,\underline{B} + (jn)\,CD \rightarrow (n)\,B_iC_j + (j)\,B_mD_n \qquad (4\text{-}14)$$
$$(jp)\,\underline{A} + (iq)\,\underline{B} + (jq)\,CD \rightarrow (j)\,A_pD_q + (q)\,B_iC_j \qquad (4\text{-}15)$$

3) Dissolution of constitutional elements of the reinforcements into the matrix

If any products cannot be formed stably by the reactions (4-8) – (4-15), the dissolution of the

constitutional elements must be examined. In Misra's algorithm, dissolution of the elements of the matrix into the reinforcements is neglected. Hence, the analysis for the equation (4-16) is only carried out.

$$CD \rightarrow \underline{C} + \underline{D} \qquad (4\text{-}16)$$

where $\underline{C}$ and $\underline{D}$ denote the dissolved elements in the matrix alloy. However, the thermodynamic consideration about the equation (4-16) is difficult to be directly performed due to the lack of the thermodynamic data for $\underline{C}$ and $\underline{D}$ in the matrix alloy. Although the equilibrium activities of $\underline{C}$ and $\underline{D}$ cannot be estimated individually, the hypothetical maximum values for a_C and a_D in the matrix can be estimated as described below.

Instead of the equation (4-16), information about the solubility of C can be obtained from consideration of the reactions (4-8) and (4-10). When the activity of C becomes to be $(1 / a_A^x \cdot K_8)^{1/y}$, A_xC_y is formed in the alloy. K_8 means the equilibrium constant of reaction (4-8). If B_iC_j is the most stable C-containing product, it is formed at the activity of $(1 / a_B^i \cdot K_{10})^{1/j}$. Therefore, the maximum possible activity of D is predicted from these values. Similarly, the maximum possible activity of C in the matrix can be estimated.

Misra has assumed that there is strong negative interaction between C or D and the elements A and B in the matrix, and the activity coefficients of C and D in the solid solution is on the order of 10^{-3}. If the hypothetical maximum activities are calculated to be 10^{-5}, the equilibrium mole fractions are estimated to be about 0.01 (1 mol%) because activities are calculated by (activity coefficient x mole fraction). Therefore, the criterion for the activity of dissolved elements was assumed at 10^{-5}. If the equilibrium activities of the constitutional elements are calculated to be less than 10^{-5}, the reinforcement material would be chemically compatible. When the reinforcements have the maximum activities of grater than 10^{-5} and the significant solubility of their constitutional elements is experimentally known, they would be an incompatible with the matrix. The chemical compatibility of the reinforcements which have high maximum possible activities are commented as "Depends on the solubility of the elements" when the experimental data of the solubility is still unclear.

4-3 Background to Molecular Orbital Simulation of Condensed Matters with Cluster Models

The motion of the total particles (atomic nuclei and electrons) in condensed matter is described by Schrödinger equation;

$$H^{total}\,\psi^{total} = E^{total}\,\psi^{total} \qquad (4\text{-}17)$$

where H^{total}, ψ^{total}, E^{total} are Hamiltonian, wave function and energy eigenvalue of whole particles. In this equation, the motion of atomic nuclei can be neglected by Born-Oppenheimer approximation. Furthermore, the motion of electrons in the multi-electron system can be assumed to that in the Self-Consistent-Field (SCF). The wave function of total electrons in SCF, ψ, is represented as;

$$\psi = \phi_1\,\phi_2\,\phi_3\,\cdots\,\phi_n \qquad (4\text{-}18)$$

where $\phi_1\,\phi_2\,\phi_3\,\cdots\,\phi_n$ are one-electron wave functions for each electrons.

In general, the solution of Schrödinger equation is not simple. Hence, several algorithms to solve this equation have been developed with electron density as the key parameter. Hohenberg and Kohn [13] had proposed fundamental concept of the density functional theory (DFT). After that, Kohn and Sham [14] had successfully introduced a very famous equation (Kohn-Sham equation) using the constraints that the total number of electrons are conserved;

$$(-1/2\ \nabla^2 + v_{ext} + v_{ee} + v_{xc})\,\phi_i = \varepsilon_i\,\phi_i \qquad (4\text{-}19)$$

where, v_{ext}, v_{ee}, v_{xc} are external, electron-electron (Coulomb) interaction and exchange-correlation potentials, respectively. Historically and still one of the challenging problems is to find accurate expressions for the exchange-correlation energy among the electrons (electron correlation). In Slater's derivation of an exchange potential (Xα potential) [15], a local potential was constructed from the non-local Hartree-Fock (HF) exchange potential by using the weighted average of HF potential and approximating the electron orbitals by plane wave. The molecular orbital simulations using Xα potential are called as Xα methods.

The discrete variational (DV)-Xα method, one of the Xα methods which is developed by Ellis, Rosén and Adachi [16], is an useful approach to calculate the electronic structure of clusters without periodic boundary conditions. In the DV-Xα method, numerical basis functions, which are obtained as numerical solutions to atomic Hamiltonian for proper electron configuration, are used for representing wave function. These basis functions can provide highly accurate wave functions for molecules and clusters. Therefore, this method is believed to be a powerful and reliable tool for studying local electronic states around point defects and impurities in solids, and their role in material properties. In the present work, DV-Xα cluster calculation is applied to analyze thermodynamic properties and reaction mechanism of Ni and Fe aluminides, in comparing with the thermodynamic investigation.

4-4 Experimental Procedure

The interfacial reaction behavior was experimentally investigated by direct joining of several ceramics and Ni or Fe aluminides. The sintered bodies of several ceramics, such as α-Al_2O_3, Y_2O_3, β-SiC, TiC, TiN, α-Si_3N_4 and TiB_2, with relative density of 85-99 % were prepared by hot-pressing at 1673-2073 K in Ar or N_2. These sintered bodies were cut to be blocks with 10 mm x 10 mm x 3 mm in dimension. The surface of the blocks was polished using a diamond slurry with the particle size of 3 μm. These blocks and a commercial graphite tablet (Kojundo Chem. Co., Ltd. ; 99.99%, 10 mm ϕ x 5 mm t) embeded into the powder mixtures of Ni-Al and Fe-Al in a graphite die. Then, the reactive hot-pressing was performed to fabricate the joining interfaces at 1273-1873 K. After the cutting and polishing, the joining interfaces were observed by OM, SEM and EPMA (electron probe micro analysis).

The interfacial reactivity was thermodynamically analyzed by a commercial software (MALT2 and CHD) and the algorithm proposed by Misra. The DV-Xα cluster simulation was conducted with scat code (The Society for Discrete Variational Xα, Japan) [16] for cluster models of point defects and substitutional atoms in NiAl and FeAl. The structure of cluster models was optimized by eigenvector following method [17] by $Dmol^3$ code (non-local DFT first principle calculation with generalized gradient approximation (GGA)) packaged in Cerius2 (Molecular Simulation Inc.) before the DV-Xα simulation. The energy level of molecular orbitals are shifted to set the highest occupied orbital at zero.

4-5 Results and Discussion

4-5-1 Activity of constitutional elements in Ni and Fe aluminides

Intermetallic alloys reveal more complicated reaction behavior at bi-material interfaces rather than pure metals and disordered alloys because of their characteristic thermodynamic properties. In this section, composition dependence of thermodynamic activity in NiAl and FeAl alloys is discussed from the view point of quantum chemistry. The activity of elements in ideal solutions is represented by Raoult's law. However, the activity in real solutions is not always described by Raoult's law due to significant chemical interaction among these atoms. What is the most reasonable parameter for representing origin of their activity ? The author believes that the frontier orbital theory or frontier reactive orbital theory proposed for explaining reaction mechanism of organic molecules, provides answer of the question even in the field of metallurgy.

The relative thermodynamic properties of solid FeAl and NiAl alloys are derived from the

potentiometric measurements of reversible electromotive force (emf) of the following cell,

$$\text{Al-(liquid) anode} \;\vdots\; Al^{3+}\text{ ions} \;\vdots\; \text{FeAl or NiAl-(solid) cathode} \qquad (4\text{-}20)$$

as the function of temperature and alloy composition [7]. The thermodynamic parameters are derived from the emf data by Nernst's equation. The activity of constituents estimated from emf agrees well with that estimated by an isopiestic method [8-9]. The activity of Al in the alloys can be separately measured from that of transient metal elements by using redox reactions concerning with Al in the cell. Thus, the partial density of state (PDOS) of Al at highest occupied level is expected to be the principal factor for determining activity of Al. Similarly, the activity of Ni (Fe) in these alloys is based on the PDOS of Ni (Fe) at highest occupied level. (cf., Appendix ch.4)

The electronic state in these aluminides strongly depends on the point defects as well as inherent character of the crystal field. In order to analyze the effect of point defects, the DV-Xα molecular orbital simulation was conducted by using cluster models illustrated in Fig. 3.1. These models are too small to precisely analyze the field of the defects. However, we can sufficiently understand the variation of electronic structure due to generation of the defects by comparing the calculation results for the models with and without defects. The NiAl alloys exhibit significant compositional dependence of activity as shown in Fig. 4.1. The high activity of Ni in Ni-rich alloys is considered to

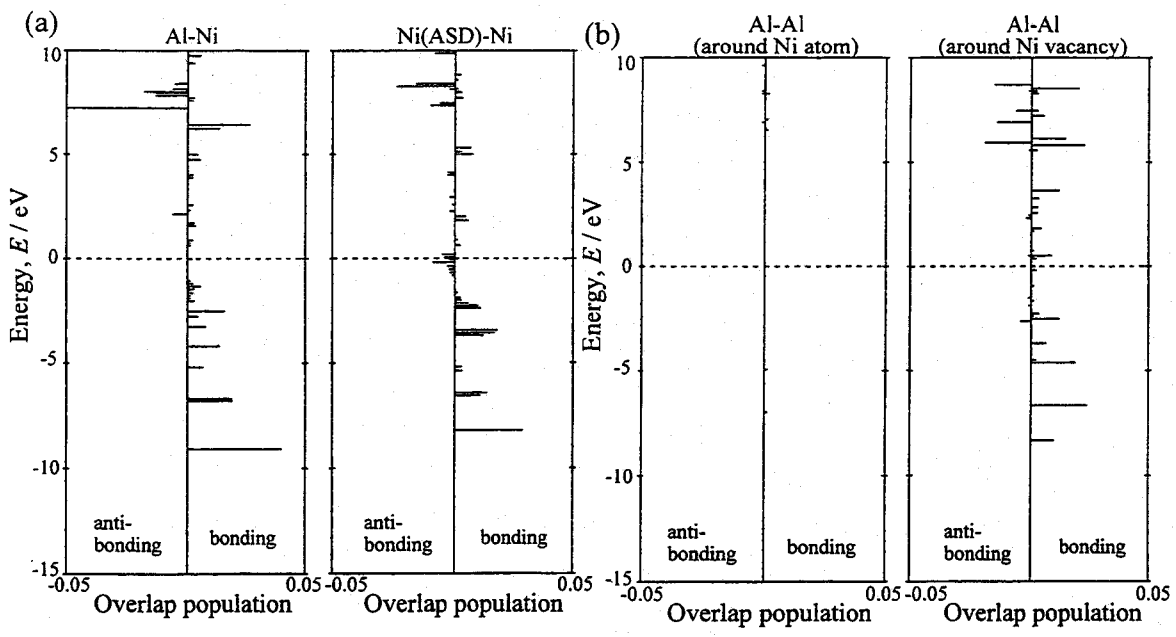

Fig. 4.2 Overlap population diagrams of (a) Al-Ni and Ni(ASD)-Ni bonds, and (b) Al-Al (around Ni atom) and Al-Al (around Ni vacancy) in NiAl.

be originated from ASD Ni atoms. Figure 4.2 (a) shows the overlap population diagram concerning Al-Ni bonds in NiAl alloy, in comparing with that of Ni(ASD)-Ni bonds. The defect states which have anti-bonding character are introduced near the highest occupied level by 3d orbital of ASD Ni atoms. On the other hand, the high activity of Al in Al-rich alloys is expected to be caused by Ni vacancies. Figure 4.2 (b) shows the overlap population diagrams concerning Al-Al bonding proximal to Ni atom and to Ni vacancy. There is relatively low bond overlap population between the Al atoms around Ni atom. However, the bond overlap population and density of state (DOS) remarkably increase with the generation of Ni vacancy. Therefore, the activities of Ni and Al in the alloys are governed by these defect states.

The FeAl alloys exhibit the exceptional compositional dependence of activity. According to the results of neutron diffraction reported by Kogachi et. al [18], the Fe-rich FeAl alloys contain ASD Fe atoms. Figure 4.3 shows the overlap population diagrams simulated by using the cluster models of Fig. 3.1 (d) and (e). The diagram indicates the defect states with anti-bonding character are introduced by the 3d orbital of ASD Fe atoms. The defect structure of FeAl alloys is inadequately represented by the cluster model with ASD Fe atom because the defect states should affect their activity. Kogachi et. al [18] have also clarified that thermal vacancies of Fe and Al generate in the alloys. The thermodynamic properties of FeAl alloys are suggested to strongly depend on the clustering of these defects. The precise analysis about the interaction among these defects (cooperative phenomena) is necessary to understand the true nature of the alloys.

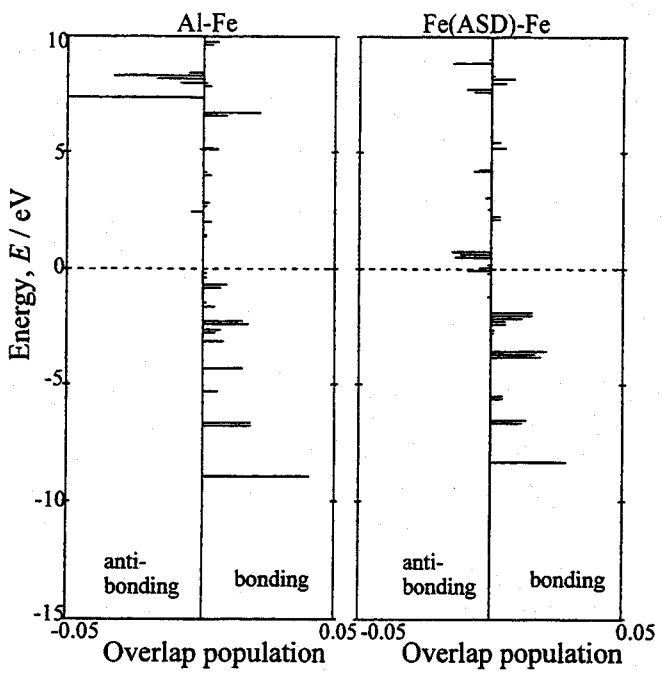

Fig. 4.3 Overlap population diagrams of Al-Fe and Fe(ASD)-Fe bonds FeAl.

4-5-2 General description for interfacial reaction mechanism

When two kinds of substances, that have different work functions, make a contact, the contact potential difference ($\Delta\varphi$) is transiently generated as schematically illustrated in Fig. 4.4. In the case of the Schottky limit, that is an ideal interface without additional surface levels, $\Delta\varphi$ completely depends on the work function of the substances. In contrast, $\Delta\varphi$ is predominantly determined by the energy of surface levels in the Bardeen limit. The ceramics/intermetallics (or metals/intermetallics) interfaces are recognized as an intermediate state between the Schottky and Bardeen limits. Thus, the work function of substances is considered to be an useful parameter to qualitatively discuss the interface phenomena, although the surface levels are not ignored for precise discussions.

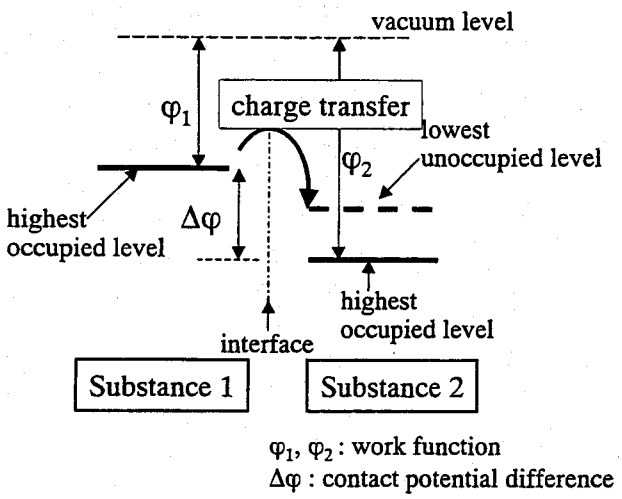

Fig. 4.4 Schematic illustration of contact potential difference and subsequent charge transfer at bi-material interfaces.

The generation of contact potential difference subsequently induces charge transfer through the interface. The charge transfer is considered to be a trigger for the interfacial reaction. In the material with lower work function, the atoms on the interface become to be unstable state with decreasing electron density in highest occupied level by the charge transfer. On the other hand, the atoms on the interface in the material with higher work function also become to be unstable much more with increasing electron density in lowest unoccupied level. This charge transfer process is wholly called as electron delocalization interaction. The active sites for the interfacial reaction relate with electron density and phase of the frontier orbitals. The sites with high electron density in the highest occupied orbitals tend to interact to the sites with high electron density in the lowest unoccupied orbitals by cohering phase of wave function in the frontier orbitals. However, the degree of freedom in determining the reactive sites is strongly restricted by the atomic configuration in crystal structure

when solid/solid interfaces are formed. Eventually, the atomic configurations at the interfaces are determined to achieve energetic minimal. After the electron delocalization, the molecular orbitals are spontaneously rearranged to achieve energetically stable state (hybridization of molecular orbitals) to form cohesive chemical bonds through the interface. In some cases, reaction products are formed by the hybridization of molecular orbitals. The free energy difference (ΔG) of interfacial reactions is a thermodynamic parameter that macroscopically represents these elementary steps.

4-5-3 Interfacial reactivity of Ni aluminides

As an example of interfacial reaction behavior of Ni aluminides, the reaction mechanism of NiAl/graphite interface is examined in detail. Figures 4.5 (a)-(d) show the cross-sectional SEM micrographs of the joining interface between graphite and Ni aluminides with several compositions. Two kinds of reaction products are observed as labeled AC and G in Figs. 4.5 (a)-(d). As the results of XRD and EPMA analyses, AC and G correspond to Al_4C_3 and graphite. Therefore, the interfacial reaction between Ni aluminides and graphite occurs through the following elementary reactions:

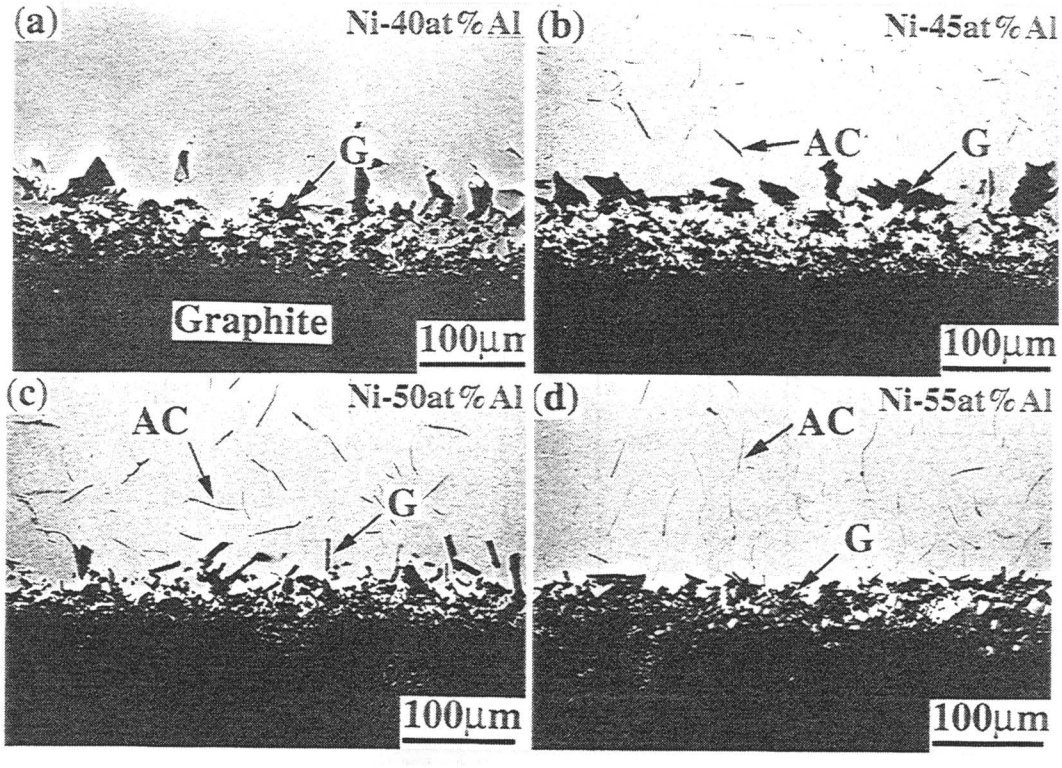

Fig. 4.5 Cross-sectional SEM micrographs of Ni aluminide/graphite interfaces reacted at 1573-1873 K for 24 h. (a) 40 at%Al, (b) 45 at%Al, (c) 50 at%Al and 55 at%Al alloys.

$$C\,(\text{graphite}) \rightarrow \underline{C} \quad (4\text{-}20)$$
$$\underline{C} \rightarrow C\,(\text{graphite}) \quad (4\text{-}21)$$
$$4\,\underline{Al} + 3\,\underline{C} \rightarrow Al_4C_3 \quad (4\text{-}22)$$

C atoms diffused into the alloys can precipitate as graphite or Al_4C_3 depending on the activity of C and Al in the alloys. The graphite particles tend to precipitate near the interface. The Al_4C_3 platelets are formed in the alloys with Al content above 45 at%Al. The activity of Al in the alloys of which composition below 45 at%Al is too low to form the platelets. This compositional dependence of reaction behavior is reasonably explained by thermodynamic consideration. Figures 4.6 (a) and (b) illustrate the chemical potential diagrams of Ni-Al-C ternary system at 1573 and 1873 K, calculated by CHD algorithm based on MALT2 database. The horizontal and vertical axes indicate log a_{Ni}/a_{Al} and log a_C/a_{Al}, respectively. It is recognized that no stable nickel carbides exist in this system. The experimental results qualitatively agree with the chemical potential diagrams, although the boundaries between Al_4C_3 and NiAl in these diagrams are slightly different with the experimental results. This discrepancy is probably caused by inaccuracy of CHD algorithm in estimating interaction parameter in this ternary system.

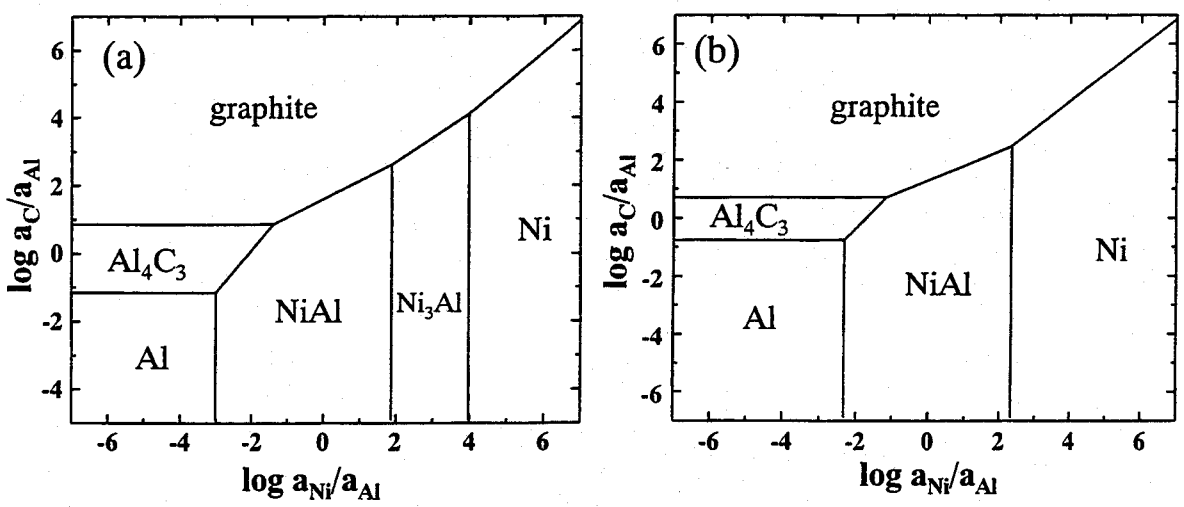

Fig. 4.6 Chemical potential diagram of Ni-Al-C ternary system at (a) 1573 and (b) 1873 K.

This reaction behavior is analyzed by the following quantum chemical scheme. The work function of these materials is briefly estimated by the emprical equations [19-20];

$$\varphi = 2.3\,\chi + 0.34 \tag{4-21}$$

$$\varphi_{A\text{-}B} = \varphi_A + \{1.41\,(2\varphi_A - \varphi_B - 0.34) / d_A\,(\varphi_A + \varphi_B - 0.68)\} \quad (\chi_A < \chi_B) \tag{4-22}$$

where φ, χ and d are work function, electronegativity (Pauling unit) and bond length (single bond), respectively. The work functions of NiAl and graphite are estimated to be ~4.2 and ~6.1 eV by eqs. (4-21) and (4-22). Therefore, the electrons in the highest occupied orbital of NiAl are considered to interact with the lowest unoccupied orbital of graphite in the initial stage of interfacial reaction. Figures 4.7 (a) and (b) illustrate the feature of highest occupied and lowest unoccupied molecular orbitals of the cluster model in Fig. 3.1 (a) simulated by Dmol^3 code. The highest occupied orbital of NiAl forms by p-d hybridization. This molecular orbital should interact with the lowest unoccupied orbital of graphite, that is a π^* type orbital. As the result of the delocalization interaction and subsequent hybridization of these orbitals, the atomic carbon (C) is considered to be extracted to NiAl.

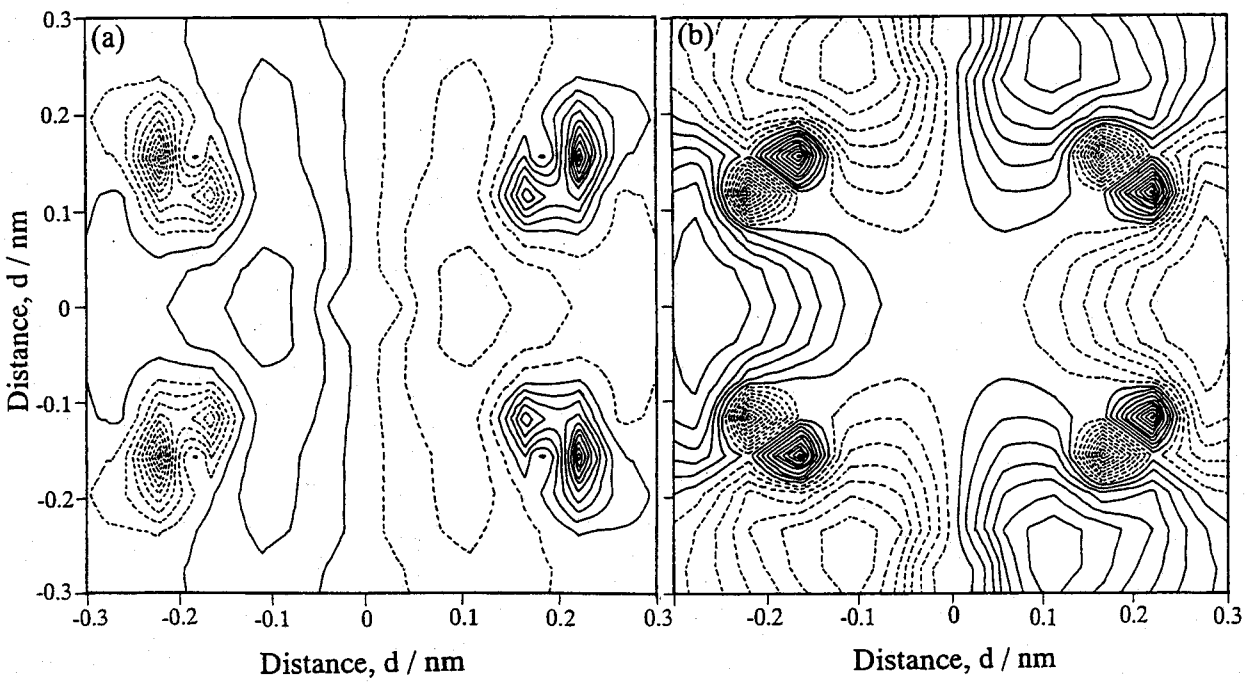

Fig. 4.7 (a) Highest occupied and (b) lowest unoccupied molecular orbitals of the cluster model of Fig. 3.1 (a).

In order to calculate the electronic states around interstitial C, the positions of the atom in NiAl are selected as shown in Figs. 4.8 (a) and (b), based on the DV-Xα simulation in Chapter 3. The lattice distortion by the interstitial C was simulated by Dmol[3] code. The structural optimization shows the C atoms in the alloys form a spherical field of 0.19-0.21 nm in radius. If the diameter of C atom is

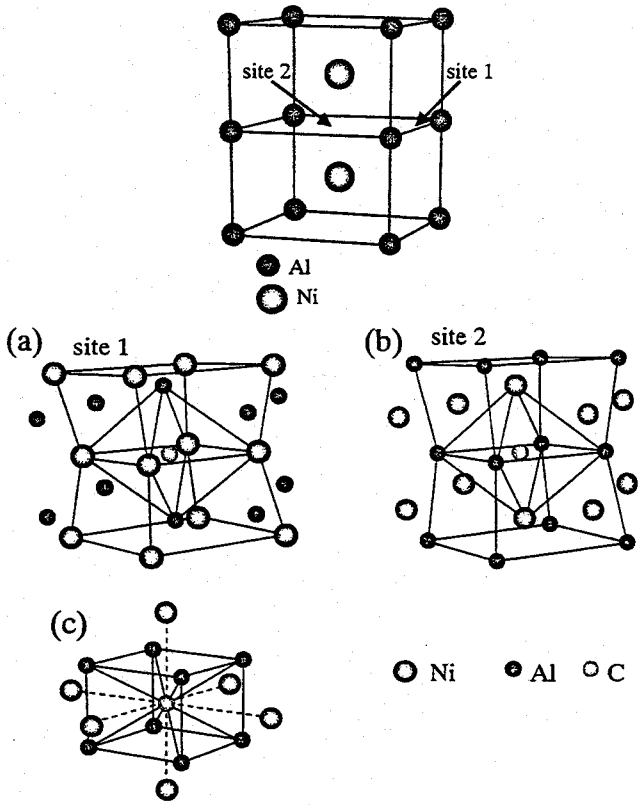

Fig. 4.8 Cluster models of NiAl with interstitial C atoms for molecular orbital simulation.

assumed to be ~0.15 nm, the bond length with neighbor atoms is estimated to be ~0.14 nm. Table 4.1 indicates the results of DV-Xα simulation for these cluster models. Figures 4.9 (a) and (b) illustrate the overlap population diagram of C-Al and C-Ni bonds in these models. Figure 4.10 (a) and (b) show the energy level diagram for these clusters. The chemical environment of C is different depending on the site positions. The C has a positive charge in the site 1. In contrast, the C is negatively charged in the site 2. In the both sites, C exhibits higher bond overlap population with Al, rather than with Ni. The relatively lower bond overlap population with Ni is caused by anti-bonding interaction of Ni 3d orbital for bond formation with C as shown in Fig. 4.9 (a) and (b). No stable Ni carbides are expected to be formed due to the bonding behavior of Ni 3d orbital.

Table 4.1 Results of DV-Xα simulation of cluster models in Fig. 4.8 (a)-(c).

model (Fig.4.8)	net charge	bond overlap population
(a)	C : 0.0356 Al(1) : 0.0619 Ni(1) : -0.1926	C-Al(1) : 0.4750 C-Ni(1) : 0.3305
(b)	C : -0.0830 Ni(1) : -0.2845 Al(1) : 0.1012	C-Ni(1) : 0.3213 C-Al(1) : 0.4217
(c)	C : -0.1657 Al : 0.0698 Ni : -0.0655	C-Al : 0.2704 C-Ni : -0.0057

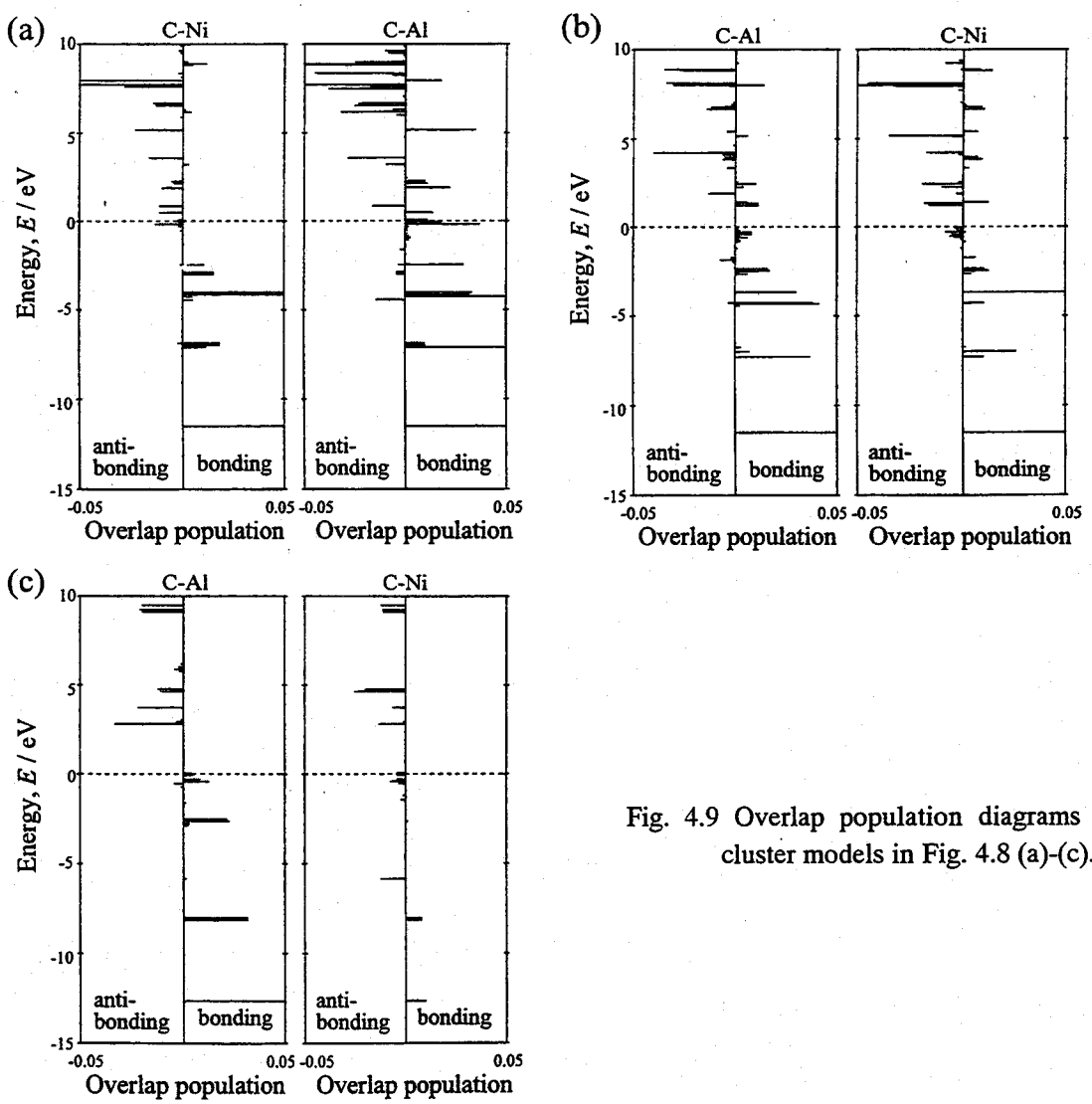

Fig. 4.9 Overlap population diagrams of cluster models in Fig. 4.8 (a)-(c).

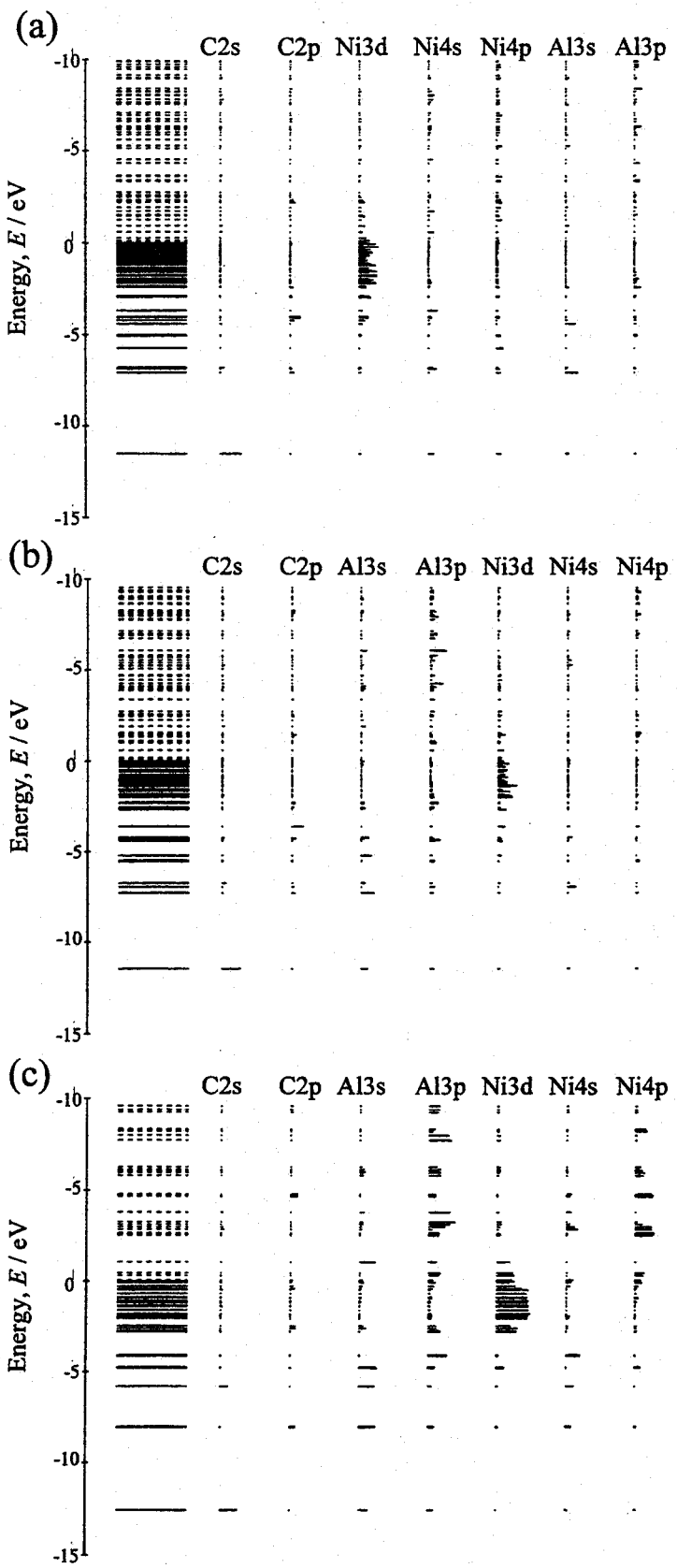

Fig. 4.10 Energy level diagrams of cluster models in Fig. 4.8 (a)-(c).

Additionally, the Ni vacancies in the Al-rich alloys are supposed to be more stable site for forming Al_4C_3. Figure 4.9 (c) shows the results of DV-Xα simulation of the cluster model illustrated in Fig. 4.8 (c). The electrons in bond orbitals among Al atoms proximal to Ni vacancy are depleted by significant charge transfer to create strong Al-C bonds when C diffuses into the vacancy site. Thus, Al_4C_3 is easily synthesized in the Al-rich alloys due to the contribution of Ni vacancies.

The results of compatibility assessments for other reinforcements are summarized in Table 4.2. Figure 4.11 shows joining interface between TiC block and Ni-25at%Al alloy, as a typical example of chemically compatible materials. As shown in this picture, the chemically compatible materials exhibit no significant interfacial reaction even at the joining conditions above 1573 K for 24 h. According to the expectation of chemical compatibility reported by Misra [1], TiB_2 is a chemically compatible reinforcement for NiAl alloys. The compatibility of TiB_2 with the alloys was confirmed in the present work because remarkable interfacial reaction was not observed in the TiB_2/NiAl joints. However, TiB_2 was found to have remarkable reactivity with Ni_3Al alloys. The precipitation of TiB and TiB_2 particles and the dissolution of Ti were observed in the reaction layer. The interfacial reactivity between TiB_2 and Ni_3Al alloys seems to depend on the activity of Ni.

Table 4.2 Results of chemical compatibility assessment for NiAl alloys.

Reinforcements	Work function Φ/ eV (calculation)	Thermodynamic calculation		Experimental result
		Reaction mode	Comment	
SiC	4.8	Formation of Ni_2Si + free carbon	Not compatible	(Ni_3Al) × ($NiAl$) △
TiC	3.9	Dissolution of Ti and C; low solubility	compatible	○
TiN	3.8	Dissolution of Ti; low solubility	compatible	○
AlN	3.4	No reaction	compatible	○
Al_2O_3	3.3	No reaction	compatible	○
Y_2O_3	2.8	Dissolution of Y; low solubility	compatible	○
TiB_2	4.1	Dissolution of Ti and B; low solubility	compatible	(Ni_3Al) × ($NiAl$) ○

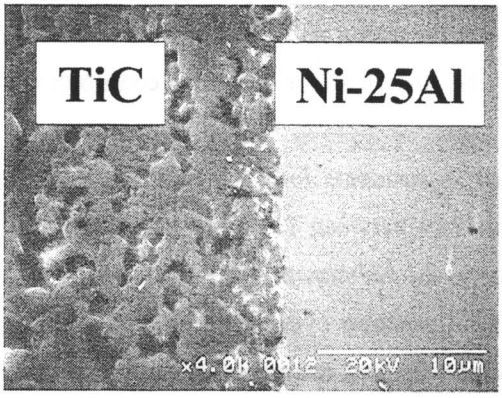

Fig. 4.11 Cross-sectional SEM micrograph of Ni-25at%Al/TiC interface reacted at 1573 K for 24 h.

In general, the work function of the reinforcements seems to correlate with their chemical compatibility. The reinforcements with lower work function than Ni aluminides adequately exhibit the chemical compatibility with the aluminides. The interfacial interaction with these reinforcements is promoted by the charge transfer to aluminides. In this case, the lowest unoccupied orbital of aluminide, which mainly consists from 3d orbitals of Ni with anti-bonding nature (Fig. 4.7 (b)), is used for hybridization with highest occupied orbital of reinforcements. The delocalization interaction in this manner is considered to promote the interfacial reaction for achieving chemical compatibility.

Because the chemical compatibility is considered to depend on difference of reactive orbitals, the molecular orbital theory is the most effective concept in analyzing interfacial reaction behaviors.

4-5-4 Interfacial reactivity of FeAl alloys

In the case of FeAl/graphite interfaces, Al_4C_3 is predicted to be the most stable product by Misra's algorithm [2]. However, a ternary perovskite compound $Fe_3AlC_{0.5}$ is stably formed by the reaction of graphite with the alloys below 35 at% Al [21-22]. Thus, a_{Fe}, a_{Al} and a_C seem to be influential parameters in determining reaction behavior in this system. Because the work function of FeAl is estimated to be ~4.2 eV by eqs. (21) and (22), the electron delocalization interaction occurs at FeAl/graphite interfaces in a similar manner to NiAl/graphite reaction couples. The highest occupied orbital illustrated in Fig. 4.12 (a) plays an important role in the interfacial reaction with graphite.

Figure 4.13 (a) shows the cross-sectional view of the Fe-40at%Al/graphite joint fabricated at 1373 K for 24 h. The granules and platelets of reaction products were dispersed in the FeAl side. Figure 4.13 (b) shows the XRD pattern of cross-section of the joint. The reaction product is identified to be

Al_4C_3 by these analyses. The formation of Al_4C_3 was confirmed in the composition range of 35-50 at%Al.

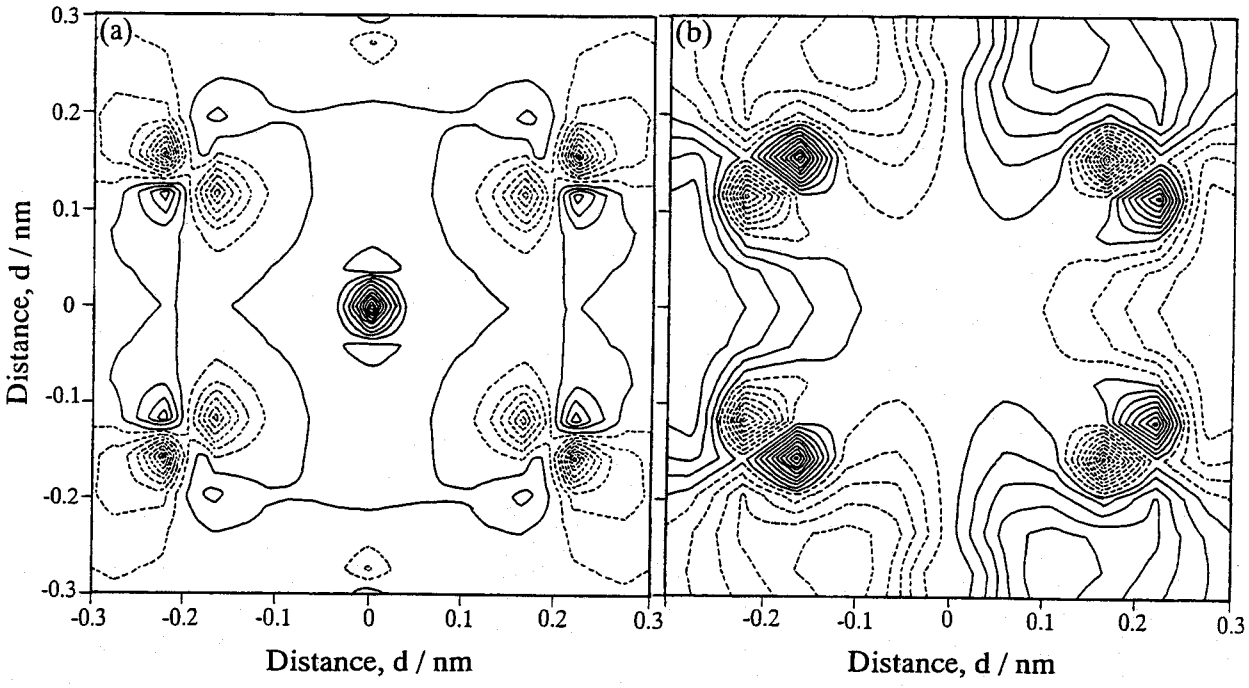

Fig. 4.12 (a) Highest occupied and (b) lowest unoccupied molecular orbitals of the cluster model of Fig. 3.1 (d).

Because the thermodynamic properties of FeAl alloys significantly depend on interaction among the point defects, the molecular orbital simulation including clustering the defects is needed to precisely understand the reaction mechanism. Although the difficulty in molecular orbital simulation for such a situation, DV-Xα simulation was conducted by using the cluster models in Fig. 4.14 (a) and (b) to obtain qualitative information about the reaction mechanism (Table 4.3, Figs. 4.15-16). In the site 1, the positively-charged C exhibits equivalent bond overlap population with Al and Fe. In contrast, the negatively-charged C forms strong covalent bonds with Fe, rather than with Al in the site 2. As shown in Fig. 4.15 (b), the anti-bonding interaction of Fe 3d orbital dose not contribute for bond formation with C. Hence, the higher bond overlap population is achieved between C-Fe in the site 2. The simulation results suggest that the stable reaction products (Al_4C_3 or $Fe_3AlC_{0.5}$) in this system are determined depending on the defect structures of the alloys.

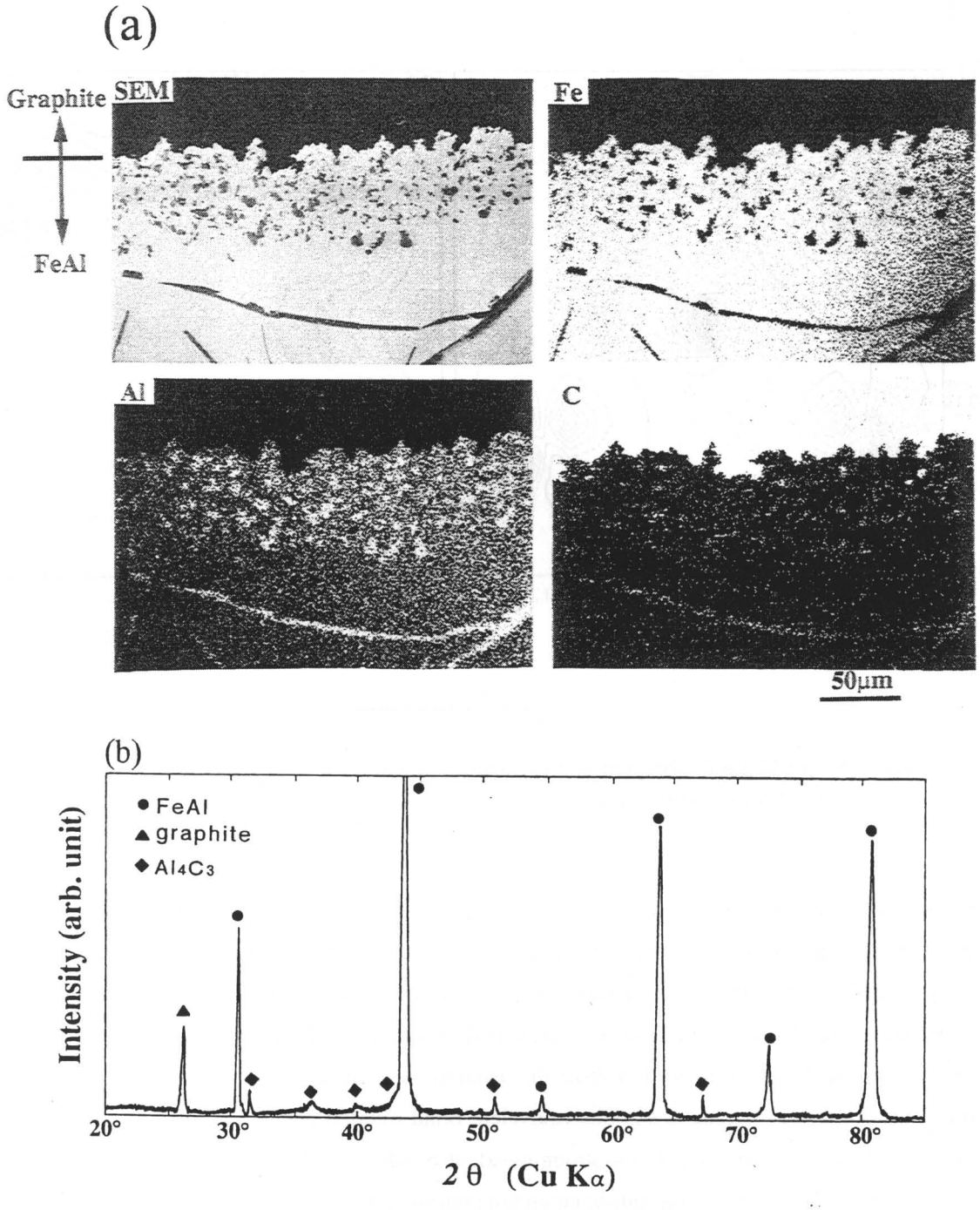

Fig. 4.13 (a) Result of EMPA and (b) XRD pattern of Fe-40at%Al/graphite joint reacted at 1373 K for 24 h.

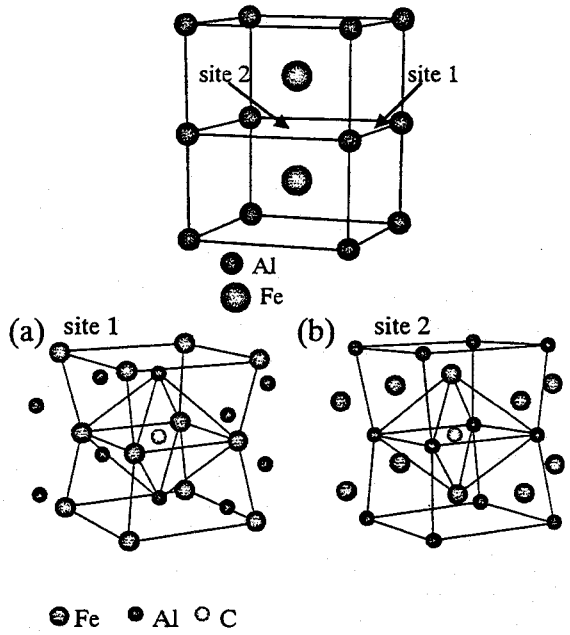

Fig. 4.14 Cluster models of FeAl with C atom for molecular orbital simulation.

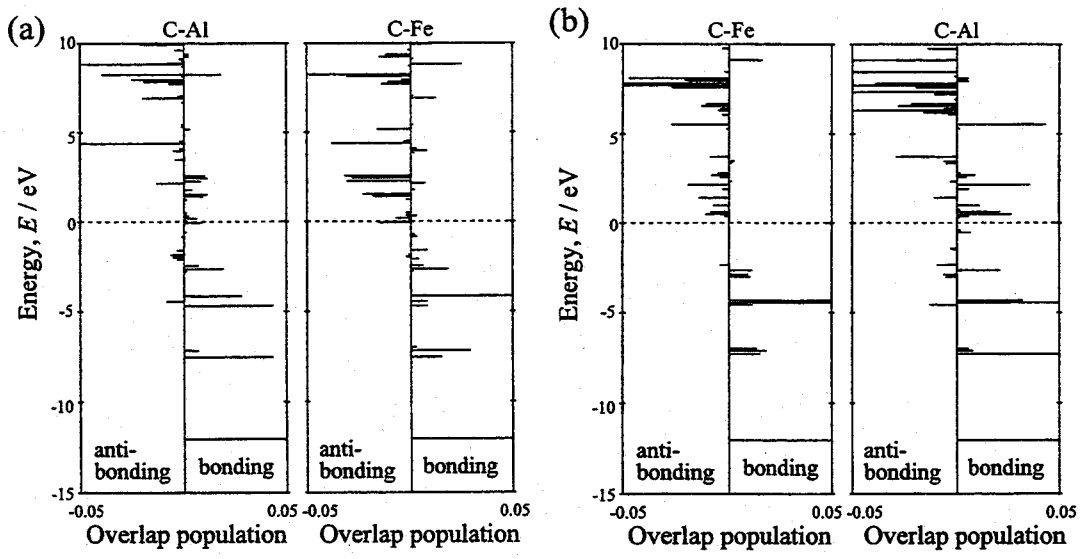

Fig. 4.15 Overlap population diagrams of cluster models in Fig. 4.14 (a) and (b).

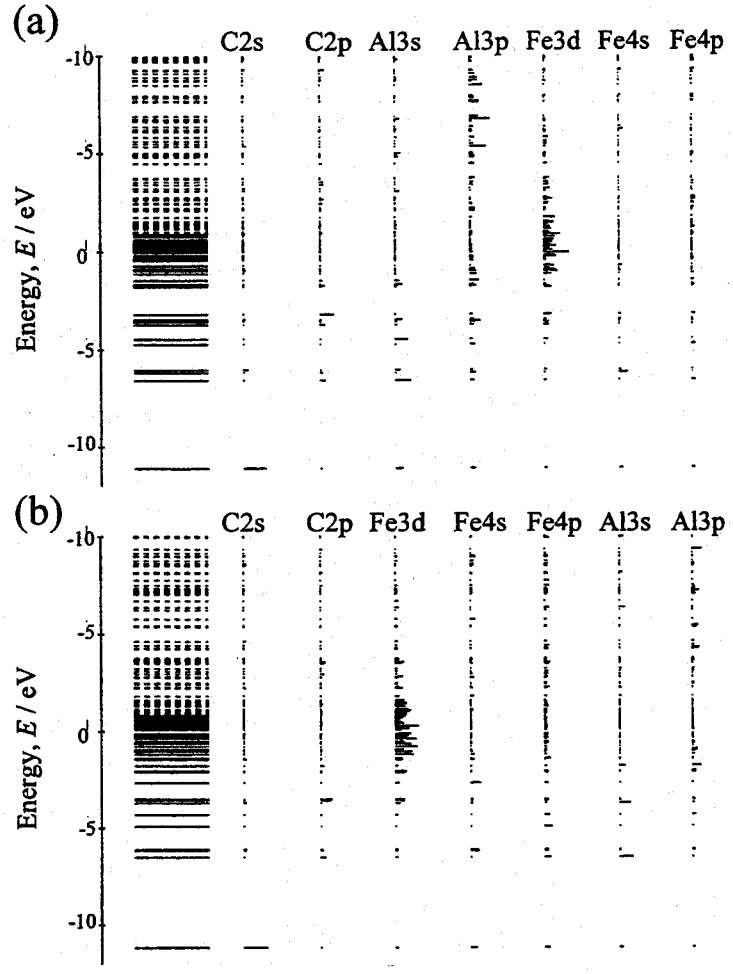

Fig. 4.16 Energy level diagrams of cluster models in Fig. 4.14 (a) and (b).

Table 4.3 Results of DV-Xα simulation of cluster models in Fig. 14 (a) and (b).

model (Fig.4.14)	net charge	bond overlap population
(a)	C : 0.0365 Al(1) : -0.1254 Fe(1) : -0.0762	C-Al(1) : 0.3905 C-Fe(1) : 0.3889
(b)	C : -0.0192 Fe(1) : -0.1132 Al(1) : 0.0485	C-Fe(1) : 0.4369 C-Al(1) : 0.3475

SiC and Si_3N_4 are also predicted to exhibit remarkable reactivity with FeAl alloys at elevated temperatures by thermodynamic calculation. Figure 4.17 (a) shows the interface between Fe-40at%Al and β-SiC block joined at 1373 K for 24 h. The continuous reaction layer of about 70 μm in thickness is formed at the interface. Figure 4.17 (b) shows the microstructural feature of the reaction layer observed by SEM. The reaction layer was found to be a Fe-Al-Si ternary compound with the precipitation of graphite and Al_4C_3 by EPMA and XRD. Drapper et al. also reported the formation of similar reaction layer by annealing of SiC continuous fiber reinforced composites [6]. The constitutional elements of SiC predominantly diffuse into FeAl alloys at elevated temperatures.

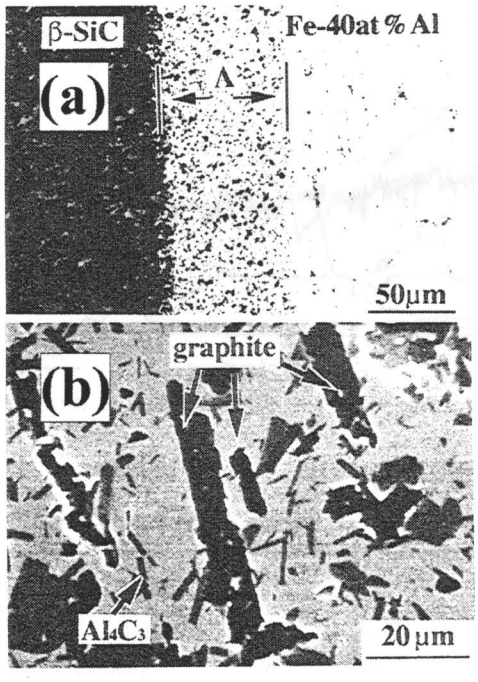

Fig. 4.17 (a) OM and (b) SEM micrographs of Fe-40at%Al/β-SiC joining interface reacted at 1373 K for 24 h.

As the result of present investigation, Si_3N_4 is found to be more reactive with Fe-40at%Al alloys than graphite and β-SiC. Figures 4.18 (a) and (b) indicates OM micrograph and EPMA line profile of the joining interface between Fe-40at%Al and α-Si_3N_4 block reacted at 1373 K for 1h. The reaction layer consists with two regions as indicated A and B in Fig. 4.18 (a). In the region A adjacent to Fe-40at%Al side, the characteristic X-ray signals of Al, Fe, Si and N are detected by EPMA. In contrast, no signal of Fe can be detected in the region B. The existence of Al in the region B indicates that Al atoms can easily diffuse into Si_3N_4. Because these two materials have higher work function than FeAl alloys, the electron delocalization interaction occurs in a similar manner to FeAl/graphite interfaces in the initial stage of interfacial reaction. Thus, the electron delocalization to their lowest unoccupied orbitals, those are σ^* type ones, results in the extraction of elements to

FeAl.

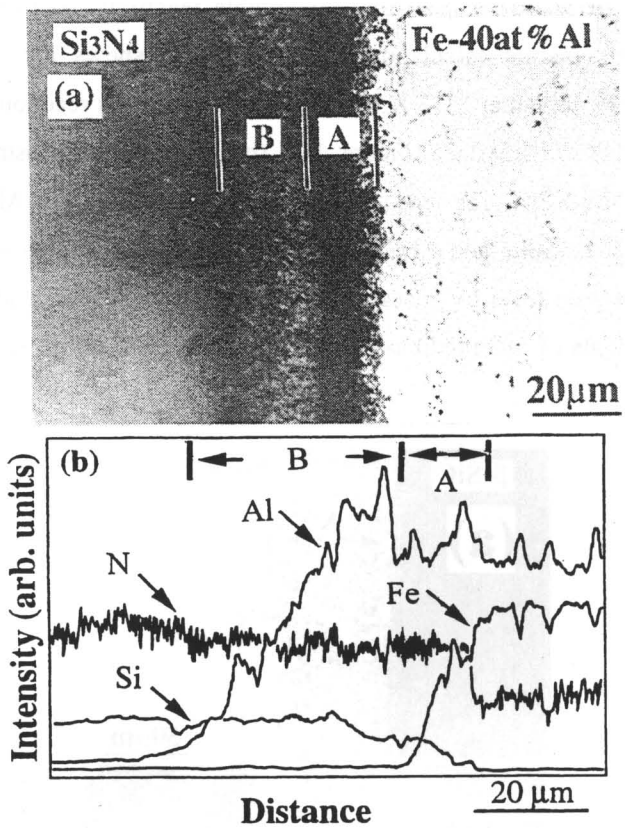

Fig. 4.18 (a) Cross-sectional view and (b) EPMA line profile of Fe-40at%Al/α-Si_3N_4

Table 4.4 Results of chemical compatibility assessment for FeAl alloys.

Reinforcements	Work function Φ/ eV (calculation)	Thermodynamic calculation		Experimental result
		Reaction mode	Comment	
SiC	4.8	Formation of FeSi + Al_4C_3	Not compatible	△
TiC	3.9	Dissolution of Ti and C; low solubility	compatible	○
Si_3N_4	4.6	Formation of AlN + free Si	Not compatible	×
AlN	3.4	No reaction	compatible	○
Al_2O_3	3.3	No reaction	compatible	○
Y_2O_3	2.8	Dissolution of Y; low solubility	compatible	○
TiB_2	4.1	Dissolution of Ti and B; low solubility	compatible	○
ZrB_2	3.8	Dissolution of Ti and B; low solubility	compatible	○

Table 4.4 shows the results of compatibility assessments for several materials with FeAl alloys. TiC, TiB_2, ZrB_2, Al_2O_3, Y_2O_3 and AlN are experimentally confirmed to be chemically compatible with FeAl alloys. These chemically compatible materials have a lower work function than that of FeAl alloys. The lowest unoccupied orbital of the alloys shown in Fig. 4.12 (b) is used as the reactive orbital for interfacial reaction with these materials. Therefore, the chemical compatibility of these materials is also expected to be explained by the frontier reactive orbital concept.

4-6 Conclusion

In this chapter, chemical compatibility of several ceramics with Ni and Fe aluminides is experimentally and thermodynamically analyzed. The results of compatibility assessments are summarized in Tables 4.2 and 4.4. The interfacial reaction mechanism of these aluminides is also discussed by quantum chemical concept. The frontier reactive orbital is suggested to be one of the important factor in determining their chemical compatibility. The lowest unoccupied state of these aluminides is used as reactive orbital in the interfacial reaction of chemically compatible materials.

The advanced molecular orbital theory will be a fundamental concept of materials science in the 21st century.

Appendix ch.4 :
Relationship between thermodynamic parameters estimated by inter-atomic potential and by molecular orbital

When the thermodynamic properties of condensed matters are nonemprically estimated, the inter-atomic potential is essential to be determined. The inter-atomic potential can be directly introduced from the total energy, which is estimated by a first principle (band structure or molecular orbital) simulation, by Hellmann-Feynman theorem. As another estimation method, the formation energy curves, which are the relationship between total energy and cell constant, can be fitted to appropriate functions such as Lennard-Jones and Morse type potentials. The cluster variation method (CVM) [23], which is a statistic mechanical calculation technique including cooperation factors, is a powerful algorithm to estimate thermodynamic parameters from the inter-atomic potentials.

The deviation of chemical potential of the constitutional elements in real alloys is originated from the inter-atomic interaction. Hence, it is reasonably considered to be related with characteristics of the bonding orbitals. In the case of intermetallic compounds containing point defects, the localized

quantum structure introduced by the defects is expected to influence the deviation of chemical potential, although the chemical potential cannot be directly estimated only by the quantum chemical parameters. Therefore, characteristics of the localized quantum structure by point defects is considered in this chapter. This idea is useful to discuss the interfacial reactivity by the molecular orbital theory.

References

[1] A. K. Misra, NASA contractor report 4171 (1988)

[2] A. K. Misra, NASA contractor report 4172 (1988)

[3] A. K. Misra, NASA contractor report 4173 (1988)

[4] A. K. Misra, Metal Trans. 22A (1991) 715

[5] A. K. Misra, in "Interface in Metal-Ceramic composites", ed. by R. Y. Lin and R. J. Arsenault, TMS (1989) 85

[6] S. L. Draper, D. J. Gaydosh, M. V. Nathal and A. K. Misra, J. Mater. Res., 5 (1990) 1976

[7] S. V. Radcliffe, B. L. Averbach and M. Cohen, Acta Metall., 9 (1961) 169

[8] J. Eldridge and K. L. Komarek, Trans. Metall. Soc. AIME, 230 (1964) 226

[9] A. Steiner and K. L. Komarek, Trans. Metall. Soc. AIME, 230 (1964) 786

[10] R. E. Hanneman and A. U. Seybolt, Trans. Metall. Soc. AIME, 245 (1969) 434

[11] G. G. Libowitz, Metall. Trans., 2 (1971) 85

[12] J. P. Neumann, Y. A. Chang and C. M. Lee, Acta Metall., 24 (1976) 593

[13] P. Hohenberg and W. Kohn, Phys. Rev., 136 (1964) 864

[14] W. Kohn and L. J. Sham, Phys. Rev., 140 (1965) A1133

[15] J. C. Slater, Phys. Rev., 81 (1951) 385

[16] H. Adachi, M. Tsukada and C. Satoko, J. Phys. Soc. Jpn., 45 (1978) 875

[17] manual book of $Dmol^3$ for Cerius2 (Molecular Simulation Inc.)

[18] M. Kogachi, T. Haraguchi and S. M. Kim, Intermetallics, 6 (1998) 499

[19] W. Gordy and W. J. Thomas, J. Chem. Phys., 24, 439 (1956)

[20] S. Yamamoto, K. Susa and U. Kawabe, J. Chem. Phys., 60, 4076 (1974)

[21] B. H. Rabin and R. N. Wright, Metall. Trans. 22A (1991) 277

[22] L. Pang and K. S. Kumar, Mater. Sci. Eng. A258 (1998) 161

[23] R. Kikuchi and T. Mohri, Cluster variation method, Morikita publication Ltd., Tokyo (1997)

Chapter 5

Composite Material Designs for FeAl alloys

5-1 Introduction

Fe aluminides have been promised as one of the candidates in substituting conventional structural materials which are utilized up to intermediate temperatures (~1000 K), because they potentially offer high specific strength, excellent oxidation and sulfidation resistance, and relatively low material cost [1]. However, the alloys have serious problems such as low toughness at ambient temperatures and insufficient strength at elevated temperatures, as described in Chapter 3. The toughness of these alloys at ambient temperatures can be improved by the B doping as a result of the suppression of environmental embrittlement. Unfortunately, their strength at elevated temperatures is hardly improved only by alloy designs. Therefore, the composite material design is an expectable approach in improving strength and reliability. In this chapter, the mechanical behaviors of FeAl matrix composites with ceramic particles, whiskers and continuous fibers are investigated to establish the design concept for high performance Fe aluminide matrix composites with high performance.

5-2 Experimental Procedure

5-2-1 Processing

The reactive hot-pressing was applied in fabricating FeAl matrix composites. The metallic raw powders for starting materials of the matrix have been already described in Chapters 2 and 3. The reinforcement materials for the composite design are listed in Table 5.1. The metallic raw powders were mixed to obtain powder mixtures for the matrix. The reinforcements of 5-20 vol% were further mixed by ball milling in ethanol for 24 h to fabricate the composites reinforced with particles, whiskers and short fibers. Subsequently, the dried mixtures were hot-pressed at 1273-1373 K for 0.5-1 h with an applied pressure of 30 MPa in vacuum (~10^{-4} Torr). The cooling rate from isothermal holding temperatures was $9 \times 10^{-2} - 2 \times 10^{-2}$ K sec^{-1}.

For the continuous fiber reinforced composites, preforms of the composites were prepared before hot-pressing. The mixture of raw powders was dispersed in ethanol to be a slurry. The fibers, which

were immersed in the slurry, were unidirectionally put in a mold. Then, the layers of fibers were stacked by pouring the slurry between the layers to prepare the preforms. After drying them, the hot-pressing was conducted at similar conditions to those for the other composites. The direction of fibers was perpendicular to the hot-pressing axis.

Table 5.1 Reinforcement materials of FeAl matrix composites.

reinforcements	size	manufacturer
particles		
β-SiC	0.2 μm	Ibiden
TiC	0.7 μm	Japan new metals
TiN	0.7 μm	Japan new metals
α-Si_3N_4	0.2 μm	Ube industry
α-Al_2O_3	0.4 μm	Sumitomo chemical
TiB_2	1.8 μm	Japan new metals
ZrB_2	1.8 μm	Japan new metals
whiskers and short fibers		
β-SiC w	ϕ 0.4 μm	Tateho chemical
TiC w	ϕ 0.86 μm	Central glass
δ-Al_2O_3 sf	ϕ 1.8 μm	ICI Japan
continuous fibers		
Al_2O_3	ϕ 10 μm	Sumitomo chemical

5-2-2 Characterization and evaluation

The microstructure of the composites was analyzed by SEM, TEM and EDX. The mechanical tests were performed in accordance with the procedures described in Chapter 3. Additionally, the tensile test with a strain rate of $1.04 \times 10^{-2} - 1.04 \times 10^{-5}$ sec^{-1} was performed to discuss their deformation mechanism at 973 K.

5-3 Results and Discussion

5-3-1 FeAl matrix composites with particles, whiskers and short fibers

(1) Fabrication

FeAl (35-50 at%Al) matrix composites containing various ceramic particles were fabricated by the reactive hot-pressing at 1273-1373 K for 1 h. These conditions were sufficient to densify the composites with 5-15 vol% α-Al_2O_3, TiC and TiB_2 particles. The composites with β-SiC particles, which have significant reactivity with the matrix alloys [2], are also successfully densified up to 98-99 % of relative density at the same conditions. Figure 5.1 (a) shows TEM micrograph of the Fe-40at%Al matrix composites with 10 vol% β-SiC particles. The β-SiC particles remained along the grain boundaries and within the matrix grain. However, the EDX spectrum of the matrix (Fig. 5.1 (b)) indicates a few at% of Si dissolve into the matrix. Although the dissolution of small amount of C may also occur, the evidence for it could not be detected in the present work. The large thermal stress resulting from thermal expansion coefficient (CTE) mismatch between the matrix and the particles is generated around the particles. The dislocation network, which was caused by the thermal stress, is observed around the particles as shown in Fig. 5.1 (a). In spite of the difference in interfacial reactivity, the apparent matrix grain size of these composites reveals similar growth behavior with increasing volume fraction, regardless of the kinds of reinforcement materials. The matrix grain size of these composites predominantly depends on volume fraction of the reinforcements as shown in Fig. 5.2.

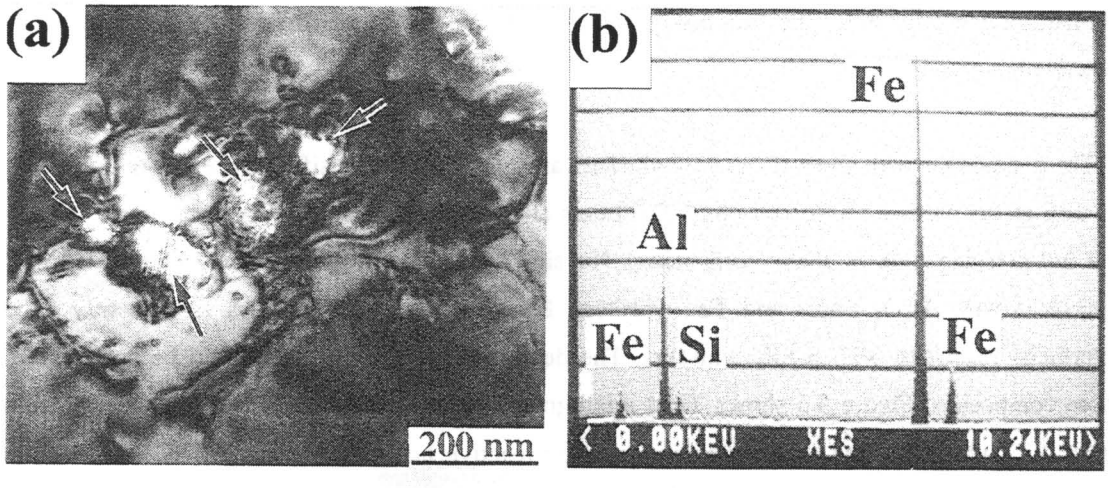

Fig. 5.1 (a) TEM micrograph of intragranular β-SiC particles, (b) EDX spectrum of the matrix of Fe-40at%Al/10vol% β-SiC particles.

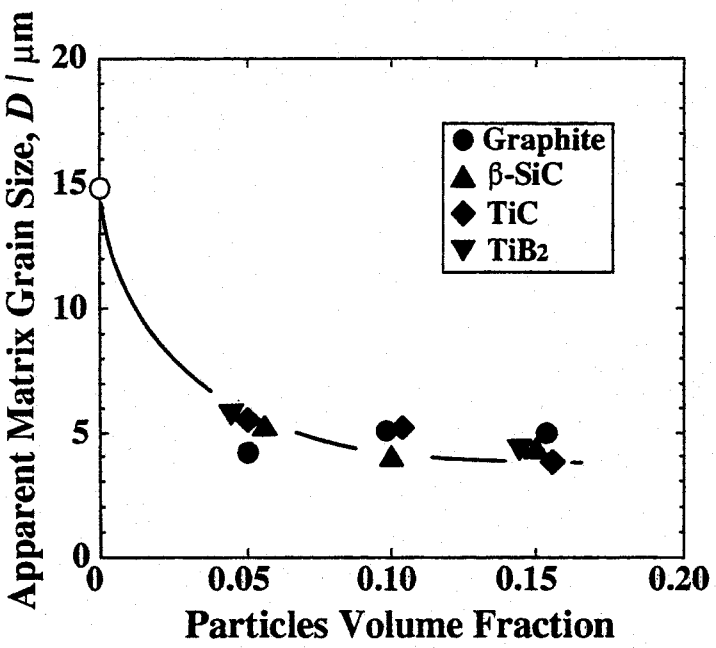

Fig. 5.2 Volume fraction dependence of apparent matrix grain size of Fe-40at%Al matrix composites with various particles.

In contrast, the composites with α-Si_3N_4 particles were not fully densified by hot-pressing at 1273-1373 K. There were many precipitates in the composites as shown in Figs. 5.3 (a) and (b). One of the reaction products was identified to be β-sialon by XRD. The precipitates in the pore free region is suggested to correspond to β-sialon, because the characteristic X-ray signals of Si, Al, N and O are detected by EDX (Fig. 5.4 (a)). In contrast, the precipitates on pores contain the elements of Si, Al and O without N as shown in Fig. 5.4 (b). The decomposition of Si_3N_4 seems to lead to gaseous pore formation. Unfortunately, the composites with Si_3N_4 particles are difficult to be fabricated by reactive hot-pressing.

The composites with short fibers and whiskers are successfully densified by reactive hot-pressing, as well as the particle reinforced ones. The fibers and whiskers tend to be oriented perpendicular to the hot-pressing axis in these composites. No significant interfacial reaction is observed at the interfaces with Al_2O_3 fibers and TiC whiskers. However, the matrix alloys significantly exhibit interfacial reactivity with β-SiC whiskers. The deterioration of whiskers should be suppressed in these composites. Figure 5.5 shows TEM micrograph of the interface between Fe-40at%Al matrix and β-SiC whisker in the composite fabricated by reactive hot-pressing at 1373 K for 0.5 h. Any significant reaction layer and damage of whiskers are not observed. Thus, the FeAl matrix composites with β-SiC whiskers are successfully fabricated by reactive hot-pressing.

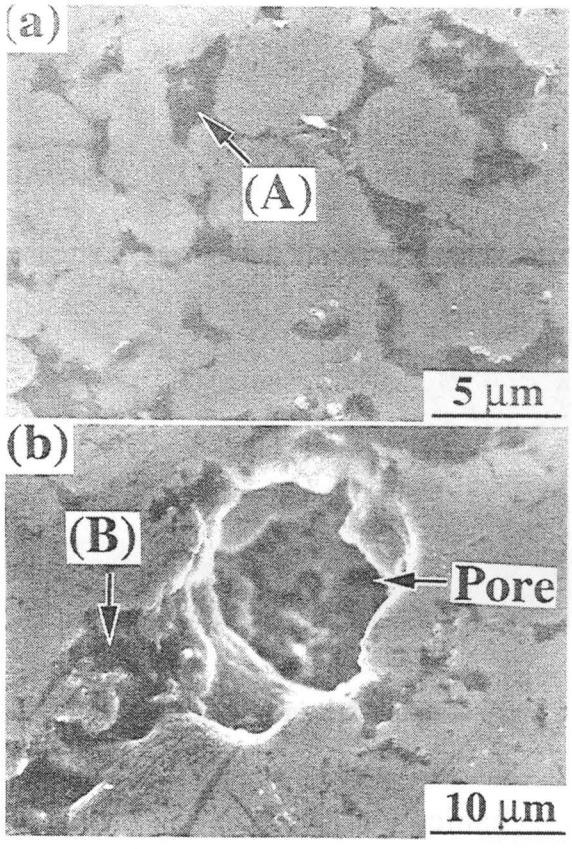

Fig. 5.3 SEM micrographs of Fe-40at%Al/α-Si_3N_4 composites; reaction products (a) in pore free region and (b) on a pore.

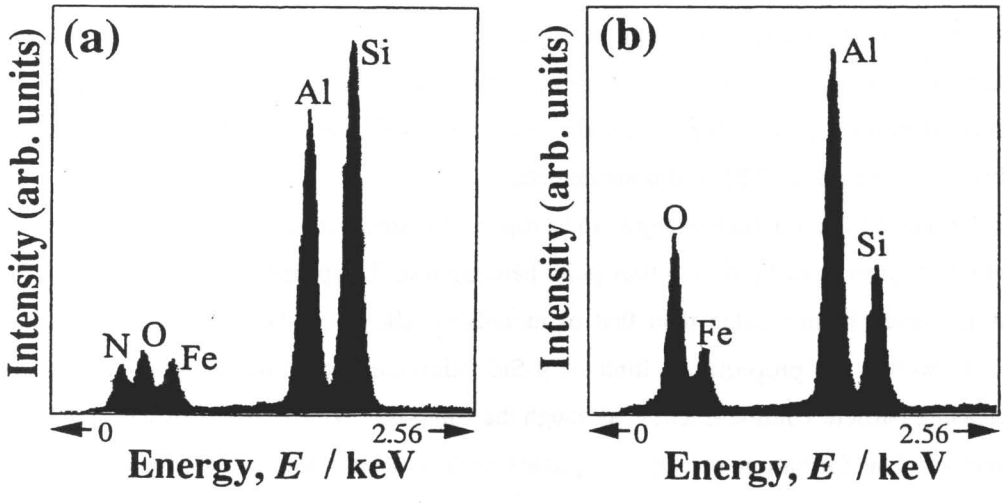

Fig. 5.4 EDX spectra of reaction products (A) and (B) shown in Fig. 5.3.

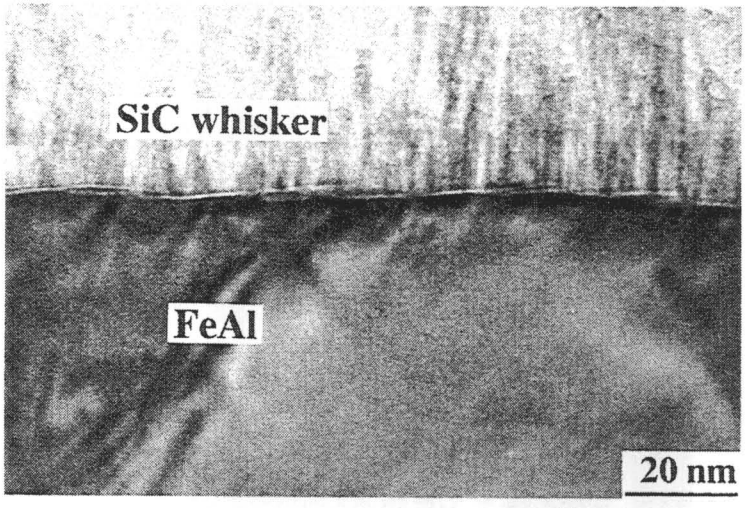

Fig. 5.5 TEM micrograph of an interface in Fe-40at%Al/β-SiC whisker composites.

(2) Screening test of mechanical properties

Particle reinforced composites

The strength of particle reinforced intermetallic matrix composites is determined by the following mechanisms [3-4]. One is the resistance against moving dislocations by obstacles which locate at intervals of a few μm or less such as reinforcement particles and grain boundaries. The resistance for the dislocation motion across grain boundaries is one of the important mechanisms as well as the dislocation pinning effect by the particles because the grain size of the matrix often decreases with the addition of particles. The other mechanism is the frictional resistance of dislocations originating from lattice defects such as APB and point defects.

Figure 5.6 shows the fracture strength and proportional limit of Fe-40at%Al matrix composites with several particles measured by a four point bending test. The proportional limit is improved up to about 1.5 times higher value than that of monolithic alloys by the addition of reinforcement particles. However, the proportional limit of β-SiC reinforced composites significantly increases with increasing particle volume fraction, although the composite with 15vol% particles fractures in a brittle manner. The formation of impurity phases such as iron silicides was not observed in the composites, as described above. Therefore, marked strengthening of the β-SiC reinforced composites is considered to be caused by the dissolution of Si into the matrix. This result indicates that the yield strength of Fe-40at%Al matrix composites at ambient temperatures sensitively depends on the frictional interference of dislocation motion based on the defect structure. Rather than strengthening

at ambient temperatures, the dispersion of particles in Fe-40at%Al matrix is expected to be more meaningful to enhance the creep resistance at elevated temperatures because the dislocation motion is remarkably activated.

Contrary, the shielding effect by plastic deformation of the matrix alloy at a crack tip should be reduced by the reinforcement particles. The fracture toughness of the composites consequently decreases with increasing the particle volume fraction as shown in Fig. 5.7. The toughness of the composites with β-SiC particles is much lower than that of the others due to the significant solution strengthening.

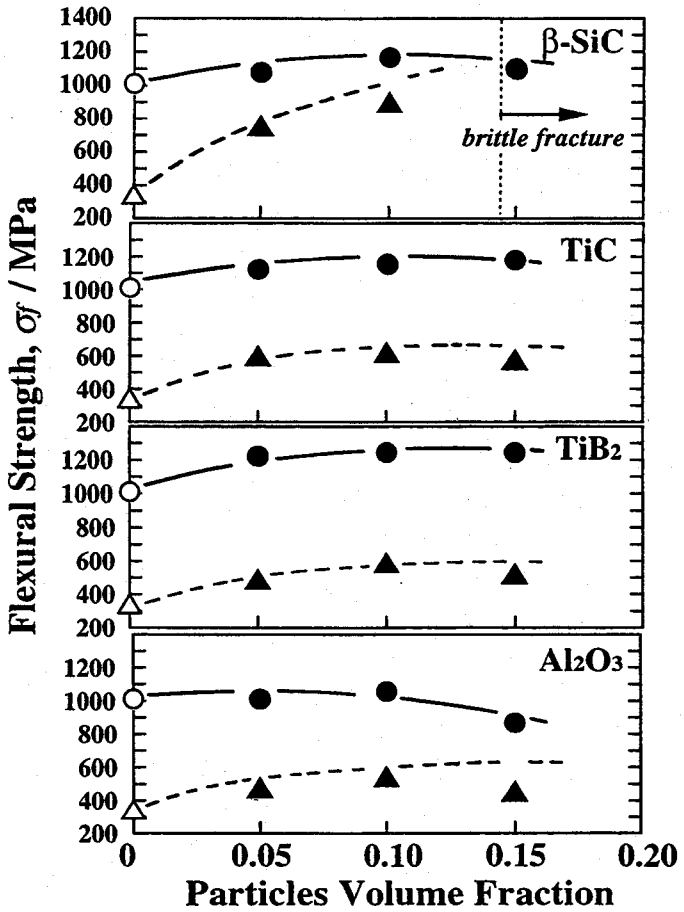

Fig. 5.6 Flexural strength of Fe-40at%Al matrix composites with several particles at ambient temperatures. The dotted curves indicate proportional limit of these composites.

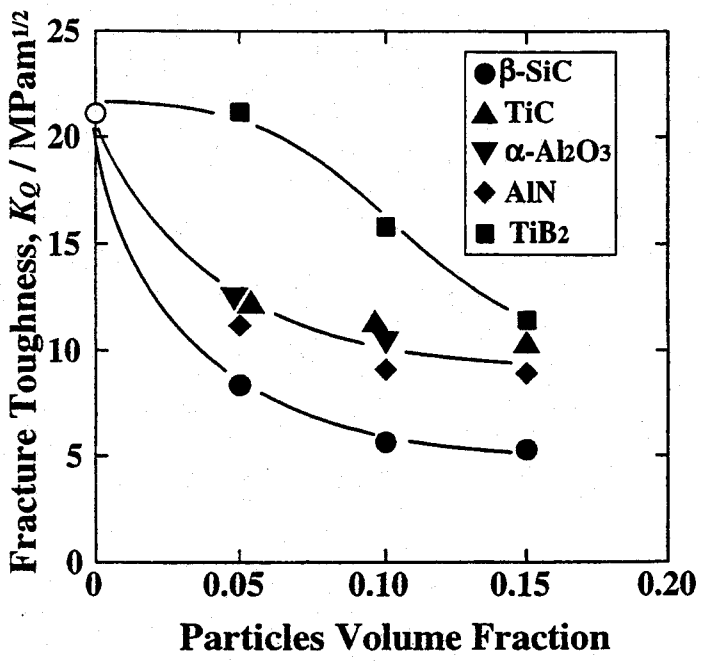

Fig. 5.7 Volume fraction dependence of fracture toughness of Fe-40at%Al matrix composites at 10^{-2} MPa $m^{1/2}$ sec^{-1}.

Whisker and short fiber reinforced composites

Figure 5.8 indicates the flexural strength of the composites with Al_2O_3 short fibers at ambient temperatures. The proportional limit is improved up to 1.5 times higher than that of the monolithic alloy. However, the proportional limit of the composites saturates at 500-600 MPa, regardless of volume fraction of the fibers. Furthermore, the ultimate flexural strength decreases with increasing volume fraction of the fibers. Figure 5.9 shows the fracture surface of the composite after the bending test. The fiber/matrix interfaces which are parallel to the fracture surface exfoliates from the matrix. Such cracks formed at the fiber/matrix interfaces are likely to be the fracture origin of the composites is likely to be a crack formed.

Figure 5.10 shows the flexural strength of the composites with β-SiC whiskers at ambient temperatures. The composites with 5-10 vol% β-SiC whiskers exhibit elastic-plastic deformation behavior. The proportional limit is improved up to 2.5 times above the monolithic alloy when the volume fraction is 10 vol%. However, the composites with 15-20 vol% whiskers fracture in a brittle manner at an ultimate strength of 700-500 MPa. As the result of SEM observation, many agglomerates of whiskers are observed as shown in Fig. 5.11. The decrease of strength of the composites with high volume fraction of whiskers is caused by brittle fracture which occurs from these agglomerates.

The fracture toughness is expected to be improved with the addition of whiskers and short fibers, if the stress shielding effect at a crack tip is effectively enhanced due to the crack bridging [5]. Unfortunately, the fracture toughness of the composites decreases with increasing fiber volume fraction of fibers as illustrated in Fig. 5.12. The plastic deformability of the matrix, which causes large shielding effect by stress relaxation, is predominately diminished with increasing the fiber volume fraction. The details of fracture behavior will be discussed in the following sections.

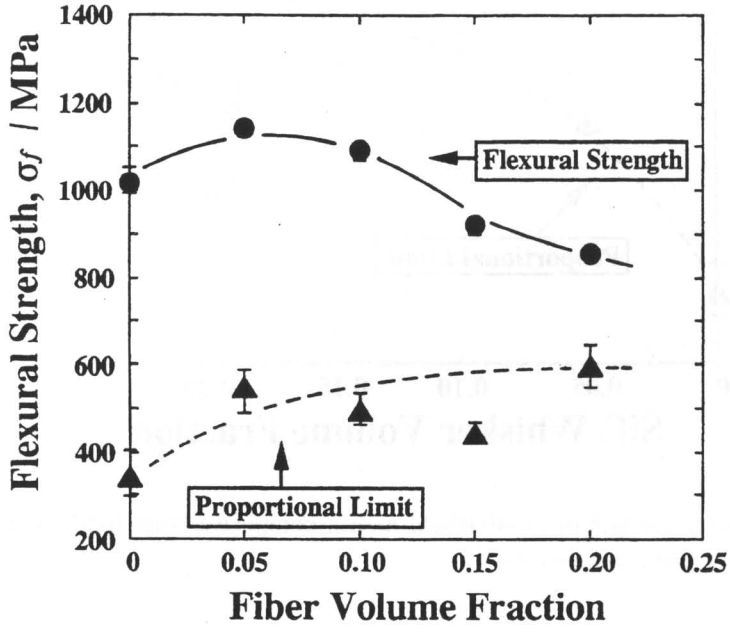

Fig. 5.8 Flexural strength of Fe-40at%Al matrix composites with Al_2O_3 short fibers at ambient temperatures.

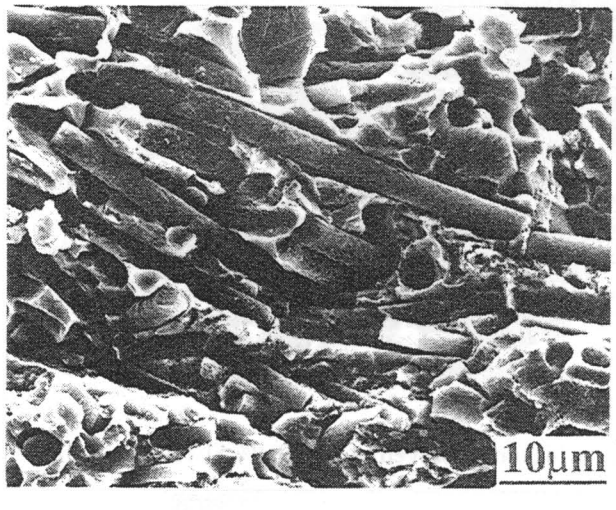

Fig. 5.9 Fracture surface of Fe-40at%Al matrix composites with Al_2O_3 short fibers.

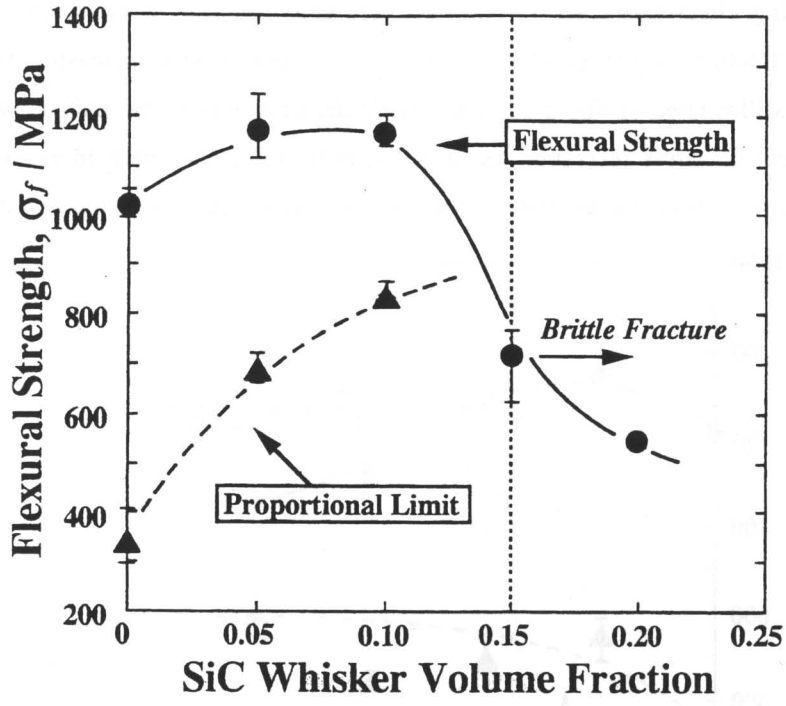

Fig. 5.10 Flexural strength of Fe-40at%Al matrix composites with β-SiC whiskers at ambient temperatures.

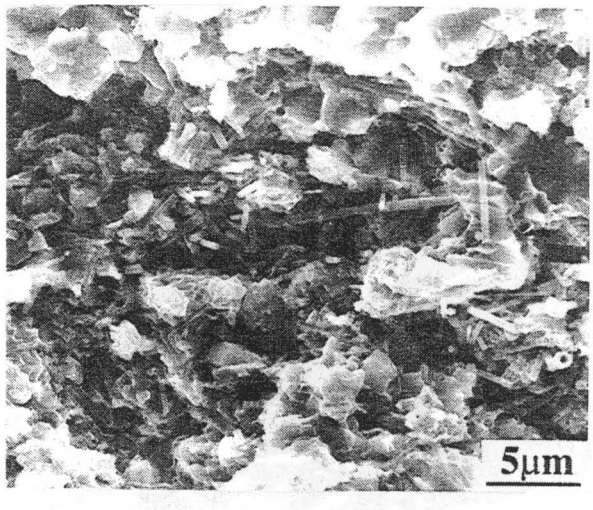

Fig. 5.11 Agglomerates of whiskers obsreved in Fe-40at%Al/15vol% β-SiC whisker composites.

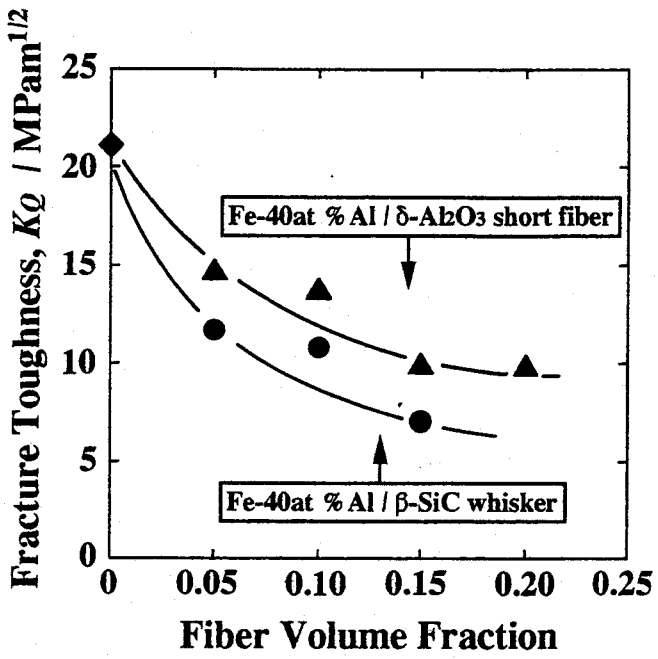

Fig. 5.12 Volume fraction dependence of fracture toughness of Fe-40at%Al matrix composites with short fibers and whiskers at 10^{-2} MPa $m^{1/2}$ sec^{-1}.

(3) Fracture mechanism of particle reinforced composites at ambient temperatures

Figure 5.13 shows loading rate dependence of fracture toughness of Fe-40at%Al matrix composites with several particles in air and the oil bath. The fracture toughness of Fe-40at%Al alloys is basically governed by the plastic deformability at a crack tip. The fracture toughness reasonably decreases with the addition of reinforcement particles due to the suppression of deformability. Furthermore, the fracture toughness of the composites decreases with decreasing loading rate, although the toughness at a loading rate of 10 MPa $m^{1/2}$ sec^{-1} in air agrees with that in the oil bath. The loading rate dependence of fracture toughness is likely to be caused by the moisture induced embrittlement [6]. The decrement of toughness resulting from the environmental effect apparently depends on the kinds of particles. The fracture toughness of these composites is about 25 MPa $m^{1/2}$ at 10 MPa $m^{1/2}$ sec^{-1}. However, the TiB_2 and ZrB_2 particles reinforced ones have relatively higher toughness than the others at 10^{-2} MPa $m^{1/2}$ sec^{-1} as a result of the suppression of the environmental effect.

Figure 5.14 shows loading rate dependence of fracture toughness of the composites with 5-15 vol% TiC and TiB_2 particles. The fracture toughness of these composites intrinsically decreases with increasing particle volume fraction due to the suppression of ductility. The fracture toughness of the

composites at slow loading rates can be improved when TiB_2 particles are used instead of TiC particles by the suppression of the environmental effect in the volume fraction range of 5-10 vol%. The fracture toughness of inherently brittle composites, such as these composites with 15 vol% particles, is hardly improved by the suppression of the environmental embrittlement.

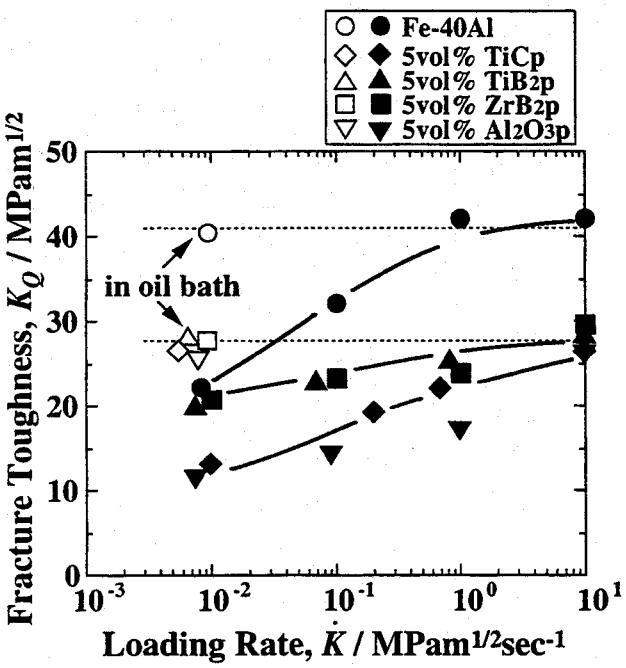

Fig. 5.13 Loading rate dependence of fracture toughness of Fe-40at%Al matrix composites with 5 vol% particles in air and in the oil bath.

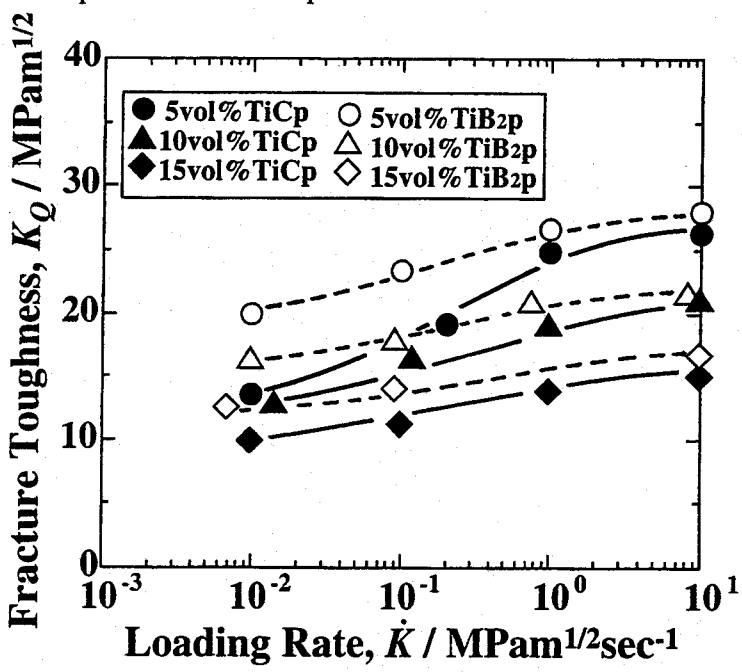

Fig. 5.14 Loading rate dependence of fracture toughness of Fe-40at%Al matrix composites with 5-15 vol% TiC and TiB_2 particles.

The latent fracture resistance at certain stress intensity factors is expected to be estimated by the bending test of notched testing bars involving quick change of loading rate to 10 MPa $m^{1/2}$ sec^{-1} (see Chapter 3). Figure 5.15 shows the variation of latent fracture resistance of the composites with 5 vol% of TiC and TiB_2 particles during loading at 10^{-2} MPa $m^{1/2}$ sec^{-1} estimated by three point bending test. The latent fracture resistance of these composites sharply decreases at certain applied stress intensity factors to initiate the crack propagation. The environmental embrittlement is promoted near the critical stress intensity factors in a very short time. Therefore, the stress applied to the specimens is an important parameter to accelerate the environmental embrittlement. The diffusivity of atomic hydrogen (H) is expected to sensitively depend on the plastic deformation of the matrix, because H in metallic materials has a strong affinity with dislocations [7]. The diffusion process of H in the stress field should be further considered for establishing damage tolerance designs of the composites.

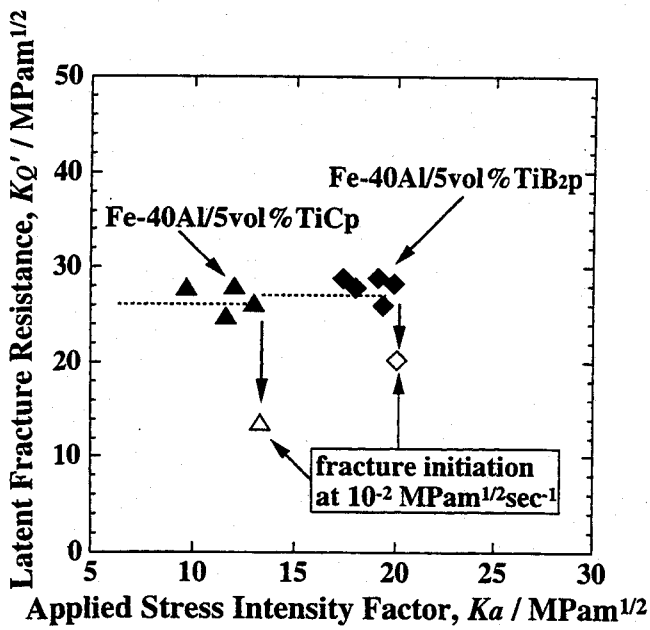

Fig. 5.15 Variation of latent fracture resistance of the composites with 5 vol% TiC and TiB_2 particles during loading at 10^{-2} MPa $m^{1/2}$ sec^{-1}.

Figures 5.16 and 5.17 comparatively show fracture surfaces of these composites after the toughness measurement in air. These composites reveal similar fracture mode both in air and in the oil bath. The TiC composites without B doping fractured in an intergranular manner in air due to relatively low grain boundary cohesion of the matrix and extrinsic deterioration by the environmental effect. However, the TiB_2 and ZrB_2 particle reinforced composites exhibit a transgranular fracture. Therefore, the grain boundary nature of the matrix is considered to be

changed by the addition of the boride particles. These particles have excellent chemical compatibility with FeAl alloys as described in Chapter 4. Hence, B in these particles is not considered to dissolve into the matrix. In fact, Moser et al. [8] have also reported that the dissolution of B is not detected at FeAl/TiB_2 interfaces by any analytical techniques. The strong interfacial cohesion between TiB_2 and FeAl alloys is considered to be the clue to clarify the effect of these boride particles on grain boundary stregthening.

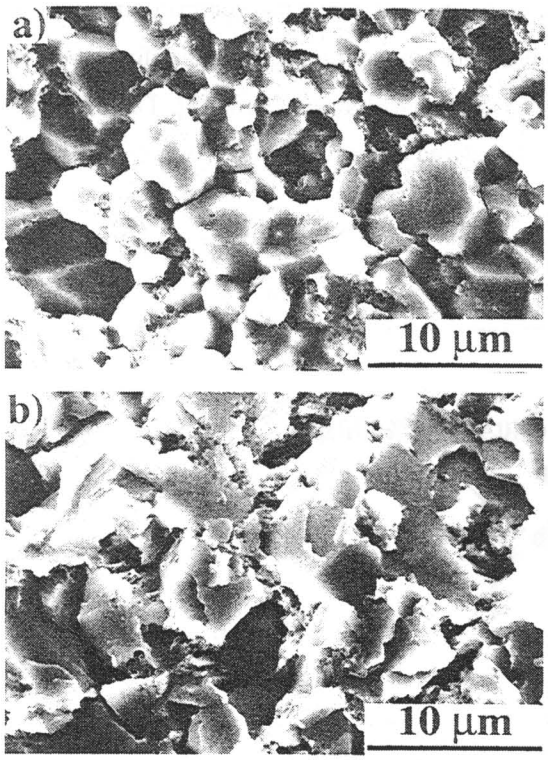

Fig. 5.16 Fracture surface of Fe-40at%Al/5 vol% TiC particle composites (a) without the B doping and (b) with the doping in air.

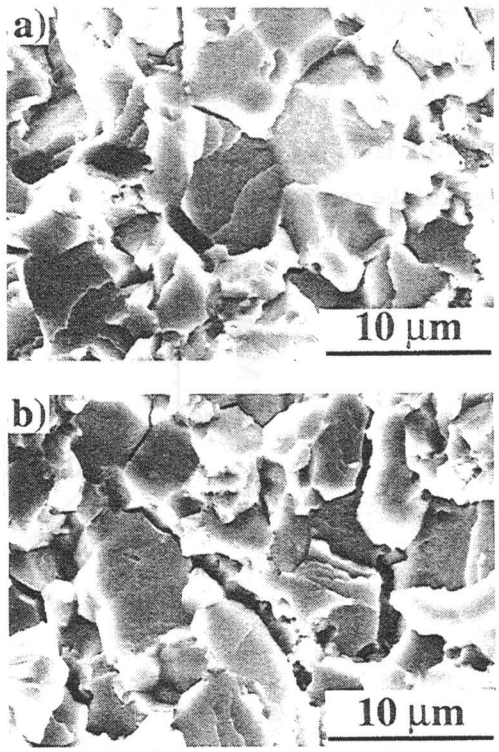

Fig. 5.17 Fracture surface of Fe-40at%Al matrix composites with 5 vol% (a) TiB_2 and (b) ZrB_2 particles.

As discussed in Chapter 3, the environmental embrittlement of Fe-40at%Al alloys is successfully suppressed by the B doping. The critical stress intensity factor of the environmental embrittlement is remarkably raised by the doping. The effect of B on the fracture property is also caused by the change of grain boundary nature similar to the case of boride particles reinforced composites. The environmental embrittlement of the composites is also expected to be suppressed by the B doping into the matrix. Figure 5.18 shows the fracture toughness of the 0.1at%B doped composites in air and in oil bath. The loading rate dependence of fracture toughness for the composites with TiC and Al_2O_3 particles is effectively suppressed by the doping, without significant improvement of their intrinsic toughness.

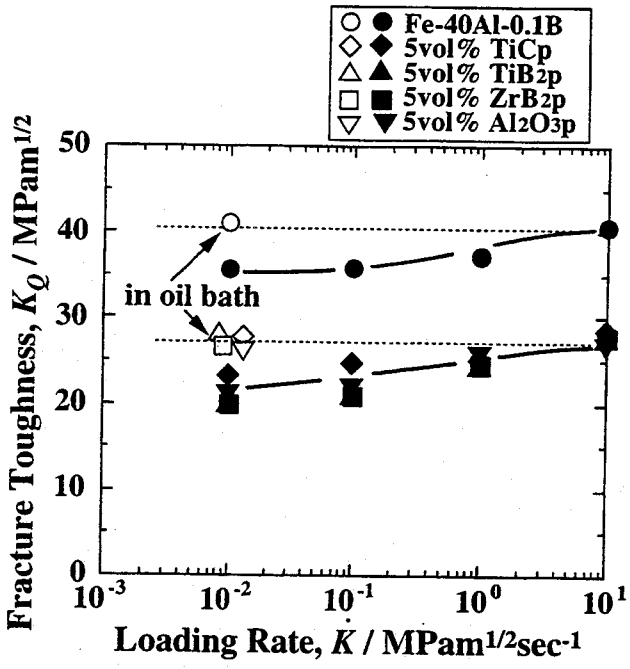

Fig. 5.18 Loading rate dependence of fracture toughness of Fe-40at%Al matrix composites with 0.1 at%B doping.

The fracture surfaces of the TiC particle reinforced ones with and without the B doping ruptured in air are shown in Figs. 5.16 (a) and (b). The doped composites fractured in a transgranular manner, in contrast to the case of non doped ones which exhibit an intergranular fracture mode. Because the fracture surfaces of these composites ruptured in the oil bath exhibit similar feature, the grain boundary cohesion is intrinsically enhanced by the doping. However, the main effect of B on toughening of Fe-40at%Al matrix composites is caused by the reduction of chemical reactivity with H rather than the grain boundary strengthening. The feature of the fracture surface of these composites suggests that the deterioration of chemical bonds on grain boundaries by the reaction with H is inhibited by the B doping. The critical stress intensity factor of the environmental embrittlement is considered to increase in the B doped composites, because H should be sufficiently transported in the matrix grains with a large plastic deformation to promote the embrittlement.

(4) Fracture mechanism of whisker and short fiber reinforced composites at ambient temperatures

Figure 5.19 shows the fracture toughness of the TiC whisker and Al_2O_3 short fiber reinforced composites with and without the B doping. These discontinuous fiber reinforced composites also exhibit the loading rate dependence of fracture toughness caused by the environmental effect. The fracture toughness of the composites at 10^{-2} MPa m$^{1/2}$ sec^{-1} is about 50 % lower than the intrinsic

toughness. The environmental effect for these composites is successfully suppressed by the B doping similar to the case of particles reinforced ones.

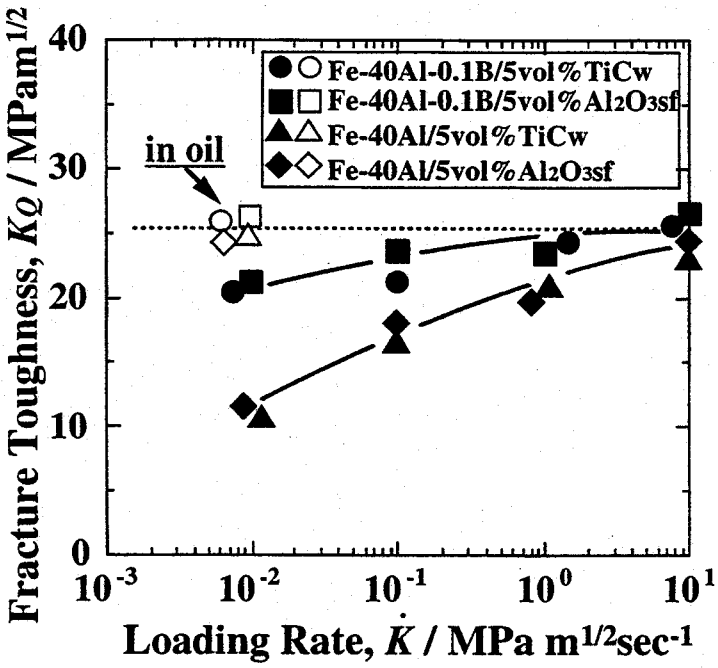

Fig. 5.19 Fracture toughness of Fe-40at%Al matrix composites containing TiC whiskers and Al_2O_3 short fibers with and without the B doping.

In the case of fiber reinforced composites with a brittle matrix, significant toughening will be achieved if extrinsic shielding mechanisms such as crack bridging by the fibers are effectively induced during fracture process [5]. Figures 5.20 (a) and (b) show the fracture behavior of the composites during toughness measurement. In these composites, the ultimate strain of the matrix (ε_m) is much larger than that of the reinforcements (ε_f). In this situation, the multiple fracture of fibers and the interface debonding predominantly occur in the plastic deformation zone before propagation of main crack as shown in Fig. 5.20. When the load direction is almost parallel to the fiber axis, the load carried by the fibers reaches to their fracture strength before the matrix cracking. The fibers consequently break into the short fragments. On the other hand, the interfaces between the matrix and fiber are predominately split when the load direction is perpendicular to the fiber axis. The flaw formed by the interfacial splitting will be a fatal fracture origin of the composites. Because the fibers and whiskers perpendicular to the direction of crack propagation are broken into short species less than 10 μm as shown in Fig. 5.20, the crack bridging and the subsequent fiber pull-out cannot effectively occur. In fact, the signs of fiber pull-out is not observed on the fracture surface of these composites as shown in Figs. 5.21 (a) and (b). Therefore, the interaction between a growing crack and fibers cannot effectively contribute in toughening these Fe-40at%Al matrix composites.

Figure 5.22 shows the R-curve behavior of the fiber reinforced composites compared with that of the monolithic alloys and the particle reinforced ones. Unfortunately, the fracture resistance of Fe-40at%Al distinctly decreases by the addition of the reinforcements due to the suppression of ductility. The fracture resistance of the composites with the discontinuous fibers is similar to that of the particle reinforced composites because of the ineffective fiber bridging and pull-out.

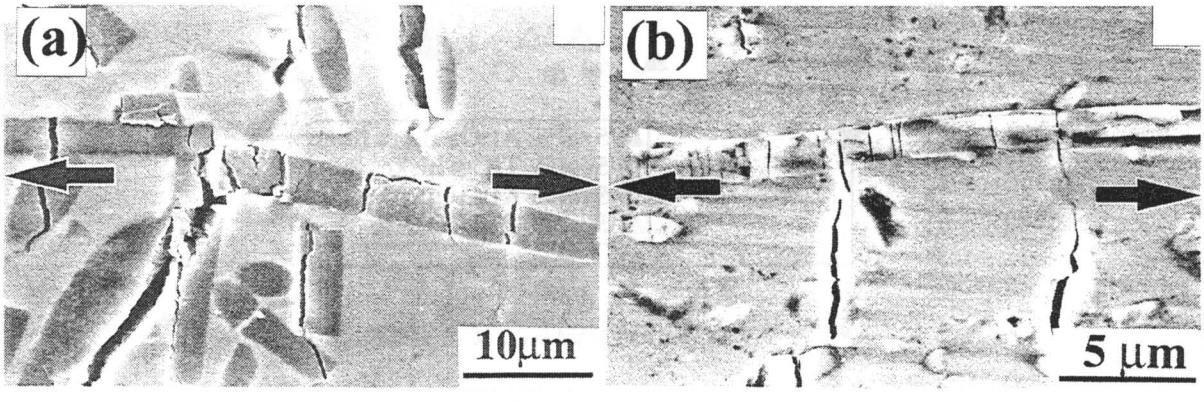

Fig. 5.20 Fracture behavior of (a) Al_2O_3 short fiber and (b) TiC whisker reinforced Fe-40at%Al matrix composites. Arrows indicate the load direction.

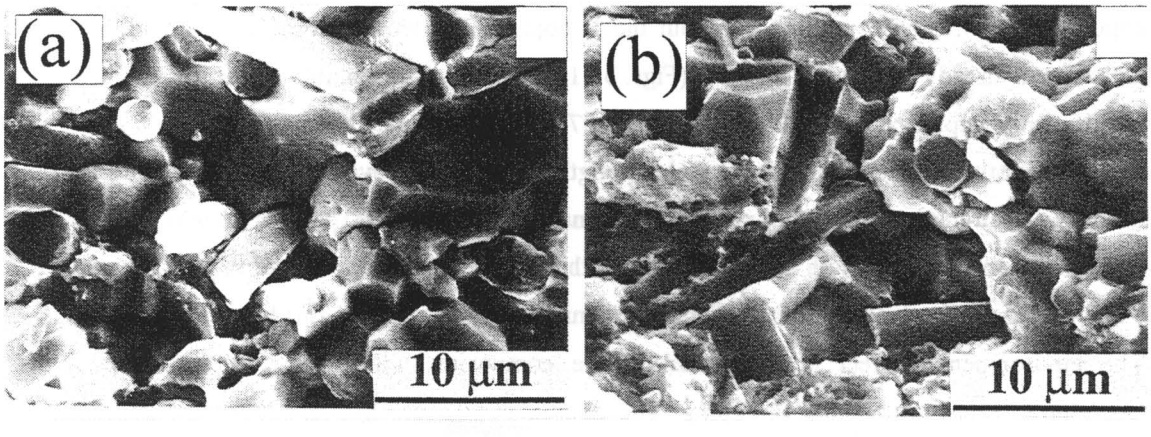

Fig. 5.21 Fracture surface of (a) Al_2O_3 short fiber and (b) TiC whisker reinforced Fe-40at%Al matrix composites.

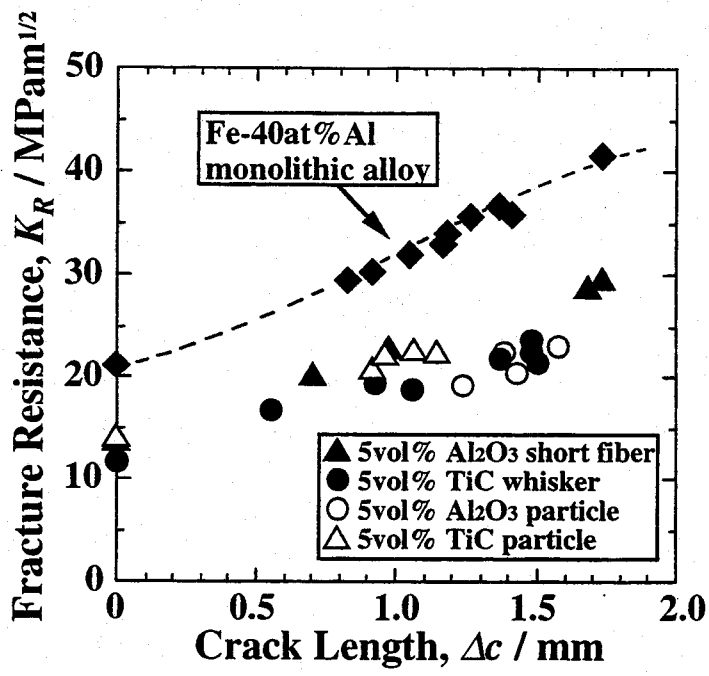

Fig. 5.22 R-curve behavior of Fe-40at%Al monolithic alloy and its composites with particles and discontinuous fibers.

(5) Tensile properties at ambient and elevated temperatures

The composites with β-SiC, TiC, TiB_2 particles and β-SiC whiskers are selected for tensile test at ambient and elevated temperatures. Figures 5.23 (a)-(b) show tensile strength of the TiC particle composites (V_f : 5 vol%) with and without the B doping. The tensile strength of monolithic Fe-40at%Al was already shown in Chapter 3 (Figs. 3.31 and 3.32). The ductility of the TiC composites is significantly improved by the B doping at 300-573 K. The ultimate tensile strength concurrently increases with the doping, although the yield strength is hardly improved in this temperature range. Moreover, the strength of the doped composites is maintained above 400 MPa up to 900 K. Because their ultimate and yield strength at 900 K is higher than that of the monolithic alloy with the doping, the TiC particles effectively contribute for strengthening the composites in this temperature range.

The environmental effect is suppressed in the composites with TiB_2 particles at ambient temperatures, even without the B doping. The doping is not effective in improving mechanical properties of the TiB_2 composites. Figure 5.24 illustrates the tensile strength of Fe-40at%Al matrix composites with 5 vol% TiB_2 particles up to 1173 K in air. They exhibit high ultimate strength below 700 K in a similar manner to the TiC composites with the B doping. However, their strength

drastically decreases above 800 K. The difference in strengthening ability between the TiB_2 and TiC particles is mainly caused by the difference in inter-particles spacing. The inter-particle spacing in the TiB_2 composites is much larger than that in the TiC composites due to the large particle size of TiB_2 (TiB_2 : 1.8 μm, TiC : 0.7 μm).

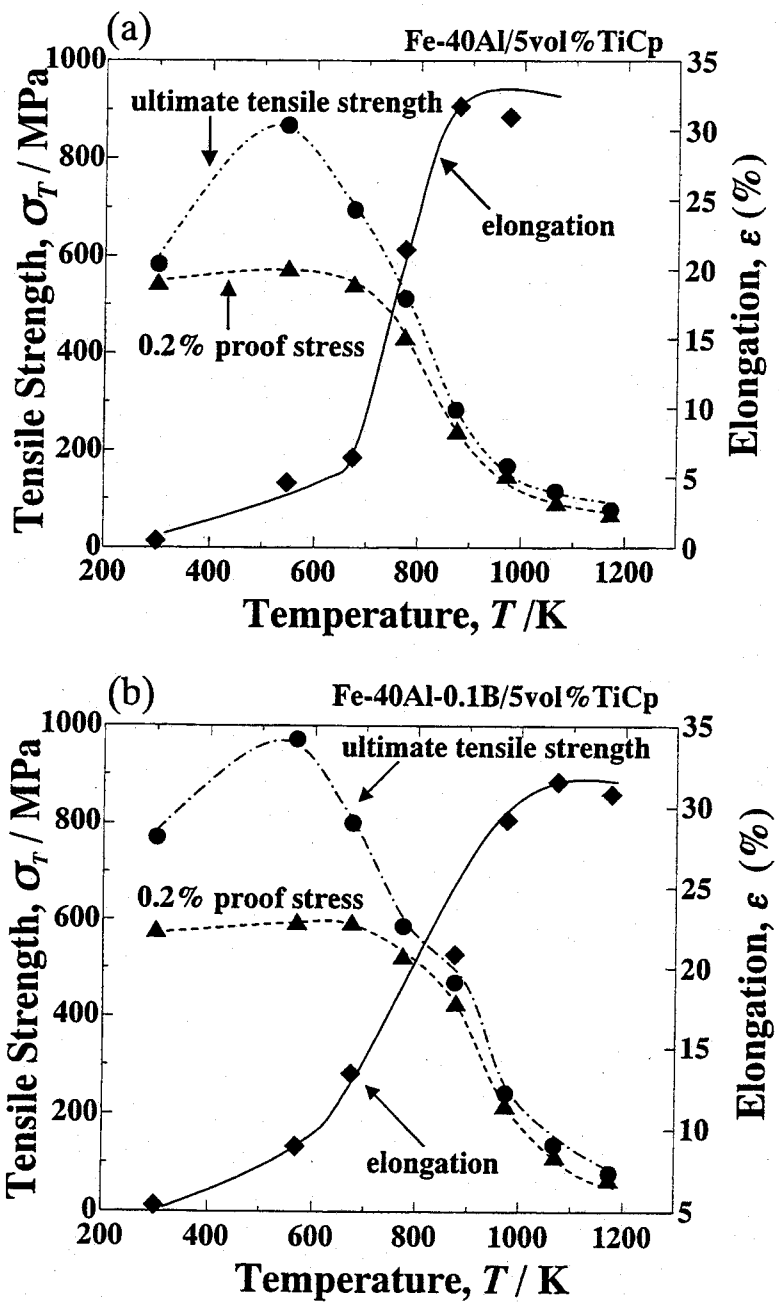

Fig. 5.23 Tensile strength and elongation of Fe-40at%Al composites with 5 vol% TiC particles (b) with and (a) without the B doping.

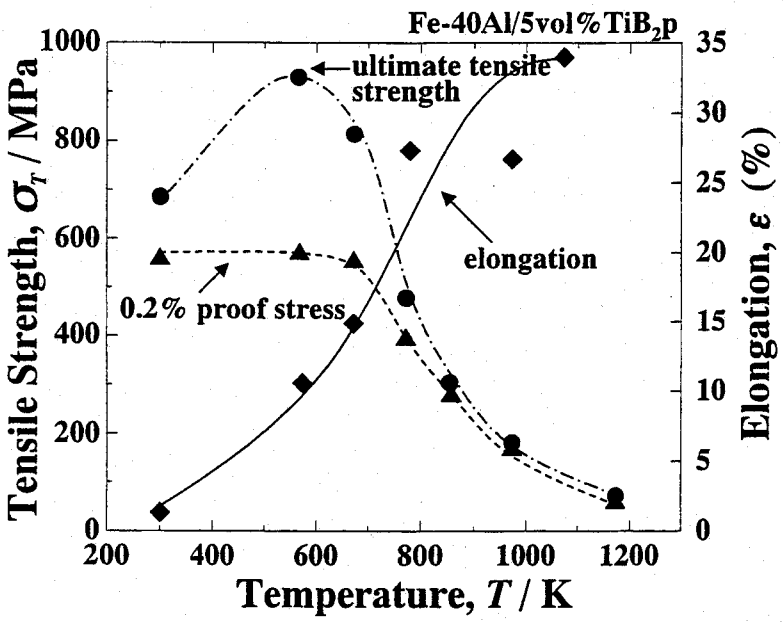

Fig. 5.24 Tensile strength and elongation of Fe-40at%Al matrix composites with 5 vol% TiB_2 particles.

The Fe-40at%Al composites with β-SiC particles and whiskers exhibit higher strength than the other composites at ambient temperatures. Figures 5.25 (a)-(b) show the temperature dependence of tensile strength of the composites with 10 vol% β-SiC particles and whiskers. The composites also show higher strength at elevated temperatures. The strengthening by the particles and whiskers is clearly recognized at 900-1000 K, by comparison with the tensile strength of the Si doped alloy (Fig. 3.27). However, their tensile strength exhibit a strain rate dependency because the matrix alloy deforms by dislocation creep in this temperature range. Figure 5.26 shows the strain rate dependence of 0.2% proof stress of the alloys and composites at 973 K. The proof stress clearly decreases with decreasing strain rate. The decrease of proof stress originates from the recovery process of dislocations in the matrix [9]. The recovery rate seems to be unrelated with the dispersion of reinforcements and the dissolution of Si. Thus, the predominant factor in determining their strength at elevated temperatures is the resistance against dislocation motion. The dislocation pinning by the dispersoids effectively occurs as well as by the solute atom atmosphere at elevated temperatures. The composites with the β-SiC particles reveal higher proof stress than the whisker reinforced ones. The fine particle reinforced composites is advantageous in interfering dislocation motion due to the small inter-particle spacing. If the whiskers showed significant load bearing effect, the whisker composites is expected to provide high strength and creep resistance. The composites with disconnected whiskers, such as the present case, is ineffective design to improve the strength and creep resistance at elevated temperatures because of remarkable interfacial sliding at elevated temperatures. When whiskers are used as the reinforcements, the composites with skeletal reinforcement structure by connecting whiskers are adequate design in improving the strength and creep resistance.

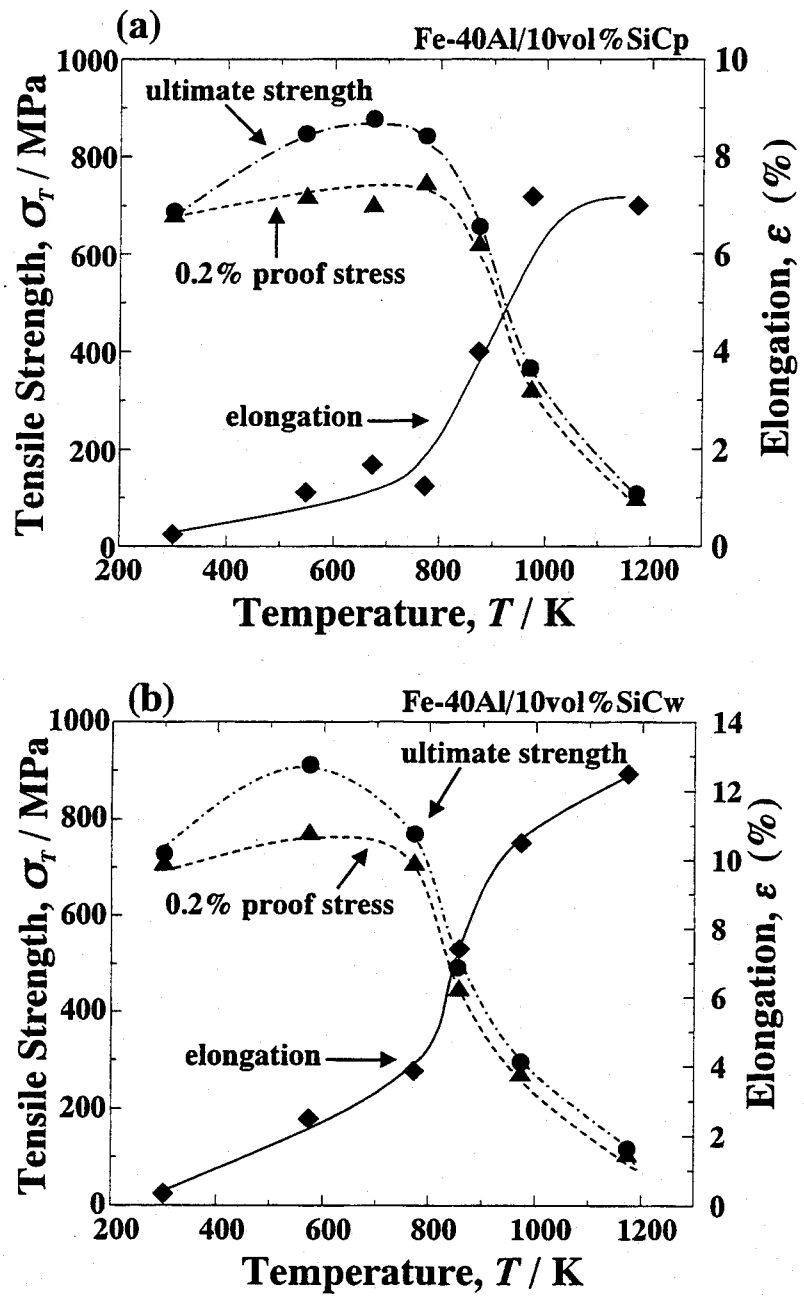

Fig. 5.25 Temperature dependence of tensile strength and elongation of FeAl matrix composites with (a) 10 vol% β-SiC particles and (b) 10 vol% β-SiC whiskers.

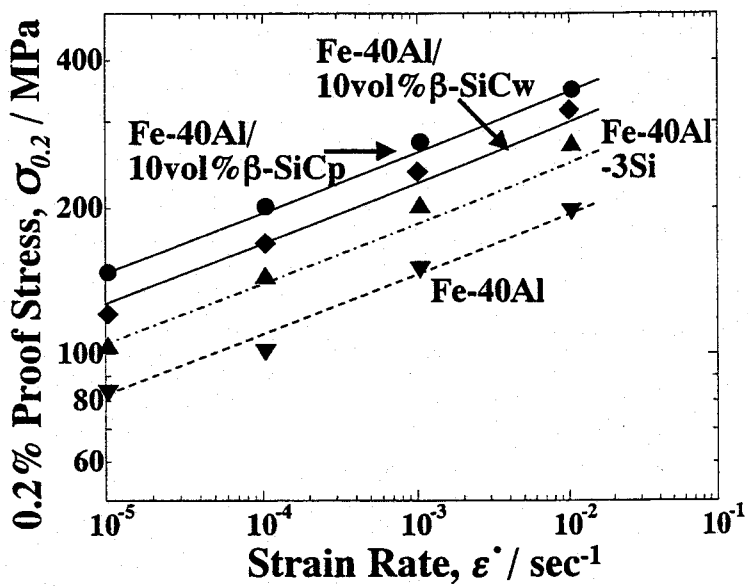

Fig. 5.26 Strain rate dependence of 0.2 % proof stress of Fe-40at%Al alloys and composites with β-SiC particles and whiskers at 973 K.

5-3-2 Continuous fiber reinforced composites

Because FeAl alloys have excellent chemical compatibility with Al_2O_3, no reaction product is observed at the interfaces between the Al_2O_3 fibers and the matrix as shown in Fig. 5.27. The fibers are not degraded by interfacial reaction. However, large CTE (coefficient of thermal expansion) mismatch exists between the fibers (9.4×10^{-6} K^{-1}) and the matrix alloy (21.8×10^{-6} K^{-1}). Hence, thermal stress originating from the CTE mismatch generates on cooling process of hot-pressing. The thermal stress seems to be sufficiently relaxed by the plastic deformation of the matrix because neither cracking nor debonding of fibers is observed in the composites.

In general, the most important strengthening mechanism of continuous fiber reinforced composites is the load bearing effect by the fibers. The composites reinforced with unidirectionally oriented continuous fibers are expected to exhibit the largest strengthening effect when the load direction is parallel to the fiber axis. The contribution of load bearing effect is expressed as a mean property [10] which is determined by the properties of the constituent phases and their volume fraction (V_f);

$$\sigma_{comp} = \sigma_f V_f + \sigma_m (1-V_f) \qquad (5\text{-}1)$$

where σ_{comp}, σ_f, σ_m are the total stress in the composite, the partial stresses in the fiber and the

matrix, respectively. The term of $\sigma_f V_f$ indicates sum of the stress carried by the fibers. The interfacial cohesion between the fibers and the matrix is the primary factor to achieve effective strengthening because high stress transfer efficiency across the interfaces is needed for significant load bearing. On the other hand, the ultimate fracture strength of the composites is not always represented by a simple rule of mixtures such as eq. (5-1), because it strongly depends on their fracture behavior [11-12]. In the case of Fe-40at%Al/Al_2O_3 fiber composites, the ultimate strain of the matrix is much larger than that of the fibers. According to a classical model for fracture behavior of composites proposed by Cooper [11], the fracture strength of fibers is often accomplished before the crack initiation in the matrix in such a situation. The fibers break into relatively long pieces in the initial stage of the fiber breaking. On loading the fiber fragments, which remain longer than the critical length (l_c), can provide significant strengthening by load bearing. The l_c is defined as the following equation;

$$l_c = r_f / \tau_i \sigma_{fu} \qquad (5\text{-}2)$$

where is r_f, τ_i, σ_{fu} are radius of fiber, shear stress at interface and ultimate fracture stress of fiber, respectively. The σ_{fu} is not achieved in the fibers, which are shorter than l_c. The l_c is a criterion of fiber length for obtaining effective strengthening.

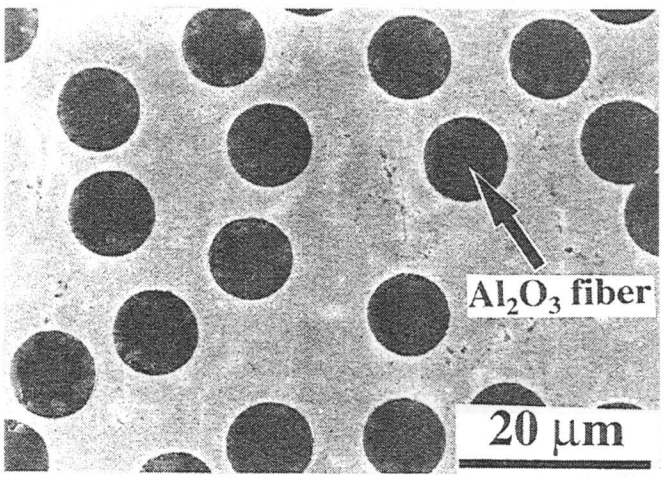

Fig. 5.27 Cross-sectional view of Fe-40at%Al matrix composites with Al_2O_3 continuous fibers.

The fracture behavior of composites after the fiber breakage is governed by the toughness of the matrix. When the matrix has an extensive toughness, the cracks in fibers cannot propagate due to the shielding effect by plastic deformation of matrix. Then, the ultimate fracture strength of the composites is significantly improved with the load bearing by the fiber fragments though the fibers

continue to break into shorter species (multiple fracture). On the contrary, the matrix simultaneously fractures with the fibers if the matrix does not have enough toughness. Hence, the composites with a brittle matrix exhibit lower fracture strength. Because the fracture strength of fiber reinforced composites largely depends on their fracture behavior, the strength is not always represented by a simple rule of mixture. The rule of mixture, eq. (5-1), is restrictively valid for estimation of total stress in the composites until the fiber breakage occurs.

In the Fe-40at%Al matrix composites with 10 vol% Al_2O_3 continuous fibers, the multiple fracture of fibers was induced as shown in Fig. 5.28 (b). Figure 5.29 (a) indicates that the fracture strength of the fiber reinforced composites is much higher than that of the fine particle reinforced ones due to the bearing of load by the fibers. The stress concentration at the tip of flaws in the fibers can be relaxed with the plastic deformation of the matrix. Because the ductility and toughness of the Fe-40at%Al matrix are sensitive to the environmental effect, the crack propagation from the tip of flaws in multiple-fractured fibers should occur at a critical stress intensity factor for the environmental embrittlement. In fact, the fracture strength of the composites in air is about 15 % lower than that in an oil bath. Their fracture strength in air can be improved by the doping of 0.1at%B into the matrix due to the suppression of the environmental embrittlement as shown in Fig. 5.29 (a).

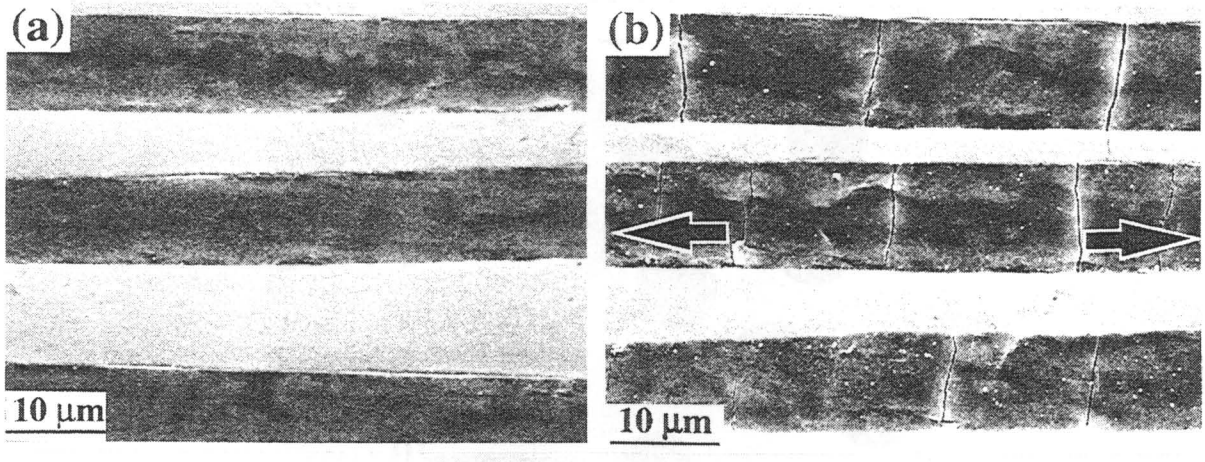

Fig. 5.28 (a) SEM micrograph of a Fe-40at%Al /10vol% Al_2O_3 continuous fiber composite. (b) Multiple fracture of fibers observed in this composite during four point bending test. Arrows indicate direction of applied load.

Because the inter-fiber spacing (~10-50 μm) is too wide to effectively interfere slip deformation of the matrix alloys, further strengthening is expected by increasing the resistance against dislocation

motion in the space among the fibers. For example, significant strengthening of Fe-40at%Al matrix is achieved by the alloying with Si as described in Chapter 3. Figure 5.29 (b) shows the relationship between flexural stress and cross-head displacement during the four point bending test of the Si doped matrix composites. The proportional limit of the composites increases as the concentration of Si increases. However, the fracture strength of the composites decreases because of the lack of matrix toughness. Therefore, the control of the toughness of matrix is essential to obtain high performance FeAl matrix composites.

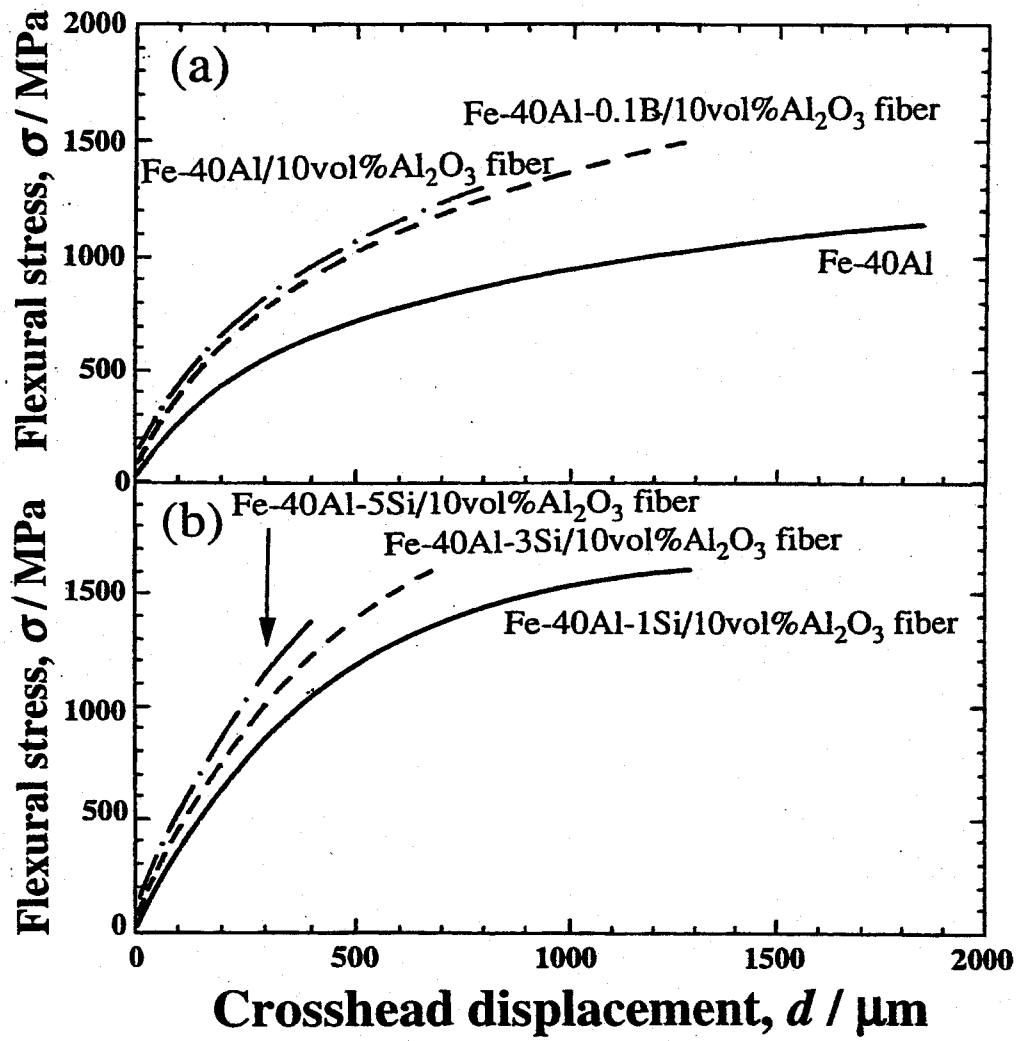

Fig. 5.29 Flexural strength of Fe-40at%Al matrix composites with 10 vol% Al_2O_3 continuous fibers; (a) with 0.1at%B doping, (b) with alloying 3-5at% Si.

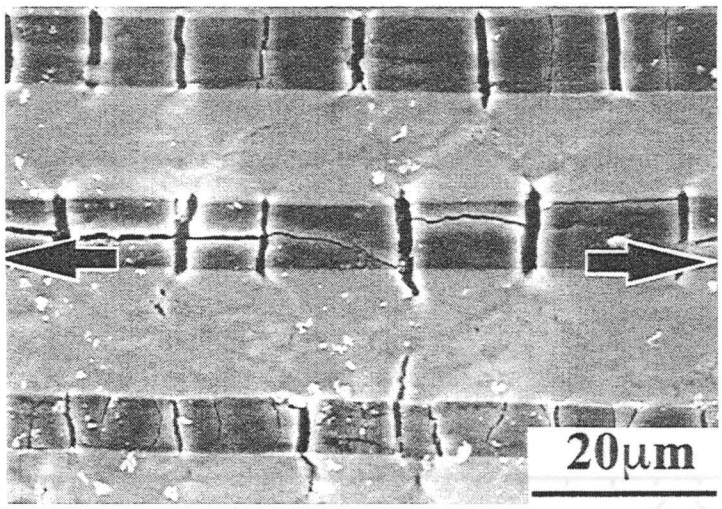

Fig. 5.30 Fracture behavior of Fe-40at%Al matrix composites with Al_2O_3 continuous fibers at 573 K.

The strengthening of the composites at elevated temperatures is predominantly attained by the load bearing effect of the fibers because the residual stress in the matrix is expected to be sufficiently relaxed with increasing temperature. The multiple fracture of fibers is also observed at elevated temperatures as indicated in Fig. 5.30, which shows the fracture behavior at 573 K. Figures 5.31 (a)-(c) show the results of three point bending test of the composites with 0.1 at%B and 3 at%Si doping at 573-973 K. The strength of these composites decreases with increasing temperature. Because the interface sliding occurs with significant softening of the matrix, the stress transfer efficiency decreases at elevated temperatures. The Si doped composites have higher strength than the other composites up to 973 K.

The load bearing effect by continuous fibers is effective to improve ultimate strength. However, the yield stress of the fiber reinforced composites is comparable to that of the particle reinforced one. For improving the yield stress of the fiber reinforced composites, the resistance against dislocation motion in the space among the fibers is necessary to be increased. The load bearing effect by the fibers decreases at elevated temperatures. In order to achieve high strength at elevated temperatures, the improvement of creep resistance by the matrix modification is important to maintain high stress transfer efficiency to the fibers.

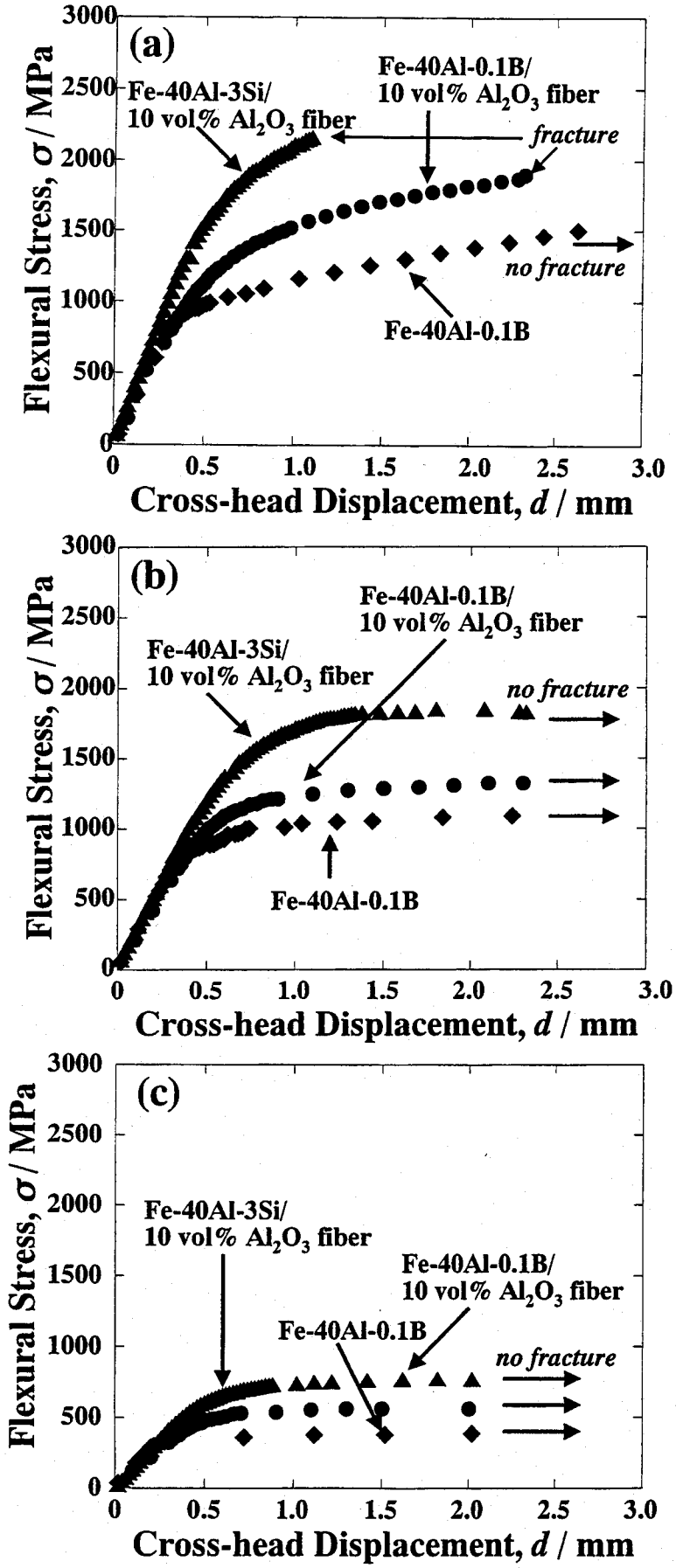

Fig. 5.31 Flexural strength of Fe-40at%Al matrix composites with Al_2O_3 continuous fibers at (a) 573, (b) 773 and (c) 973 K.

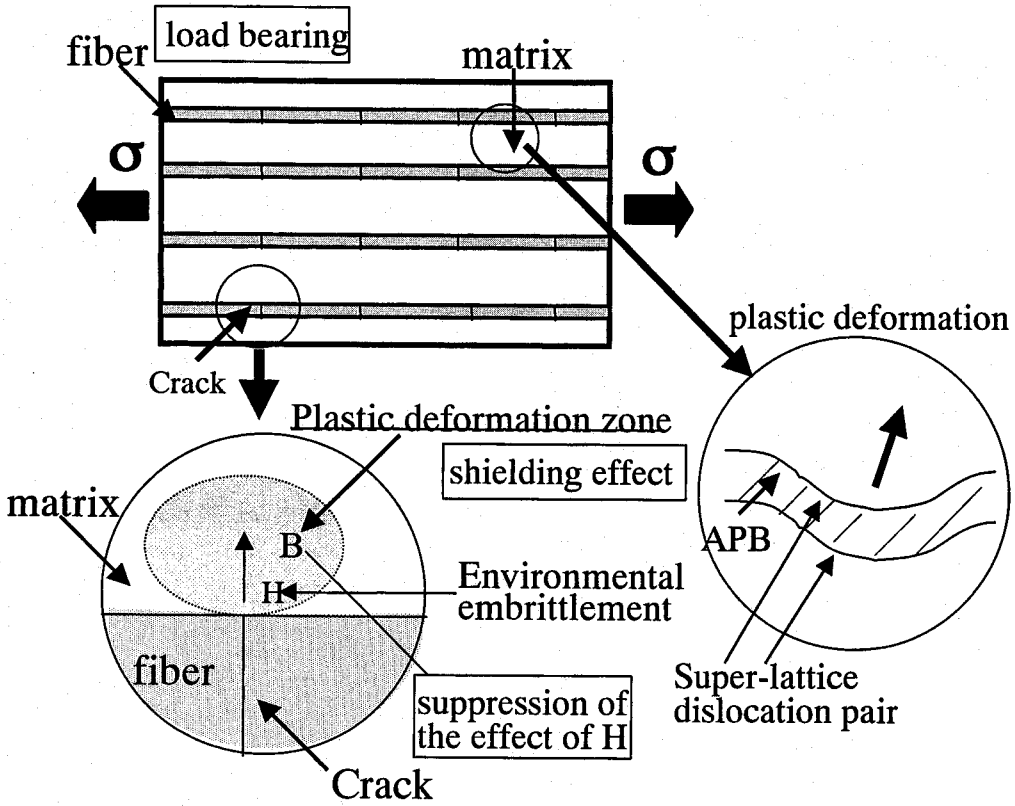

Fig. 5.32 Schematic illustration of design concept of FeAl matrix composites with ceramic continuous fibers.

Figure 5.32 shows the schematic illustration of the design concept for continuous ceramic fiber reinforced FeAl matrix composites. The control of interfacial bonding between the fibers and the matrix is important because the fibers can provide strengthening by the load bearing effect. Moreover, the modification of the matrix is also necessary for developing the high performance composites. However, the excess solution strengthening results in decreasing fracture resistance of the matrix. The strength of the composites conversely decreases by the strengthening of the matrix alloy when no significant multiple fracture of fibers is induced. The strengthening of the matrix alloys is effective strategy in improving the strength of the composites on a premise of significant multiple fracture of fibers.

5-4 Conclusion

In this chapter, the mechanical properties of Fe-40at%Al matrix composites fabricated by reactive hot-pressing were evaluated in order to discuss suitable design concepts for the composites. The main results obtained in this chapter are briefly summarized below:

(1) The composites with β-SiC particles and whiskers exhibit strength higher than the other composites at ambient temperatures. Marked strengthening of the β-SiC composites is predominately caused by the dissolution of small amount of Si into the matrix.
(2) The strength is improved by the interference of dislocation motion with the reinforcements at elevated temperatures although the recovery rate is not changed.
(3) When whiskers are used as reinforcements, the composites with a skeletal reinforcement structure formed by connection of whiskers are considered to be suitable design in improving their strength and creep resistance.
(4) The fracture strength of the composites with continuous Al_2O_3 fibers is significantly improved as a result of the load carrying by the fiber fragments even though the multiple fracture of fibers occurs prior to the matrix cracking. The solution strengthening by Si of the matrix alloy is effective in improving strength. However, the strength of the composites conversely decreases when the excess solution strengthening occurs, because the toughness of the matrix is one of the important parameters in determining their ultimate fracture strength.

References

[1] C. G. McKamey, J. H. DeVan, P. F. Tortorelli and V. K. Sikka, J. Mater. Res., 6 (1991) 1779

[2] A. K. Misra, NASA Contractor Report 4172 (1989)

[3] S. Takagi, Materia Jpn., 36 (1997) 675

[4] E. Arzt, Acta Mater., 46 (1998) 5611

[5] A. G. Evans, J. Am. Ceram. Soc., 73 (1990) 187

[6] C. T. Liu, E. H. Lee and C. G. McKamey, Scripta Metall., 23 (1989) 875

[7] D. Delafosse, J.-P. Chateau, A. Chambreuil and T. Magnin, Mater. Sci. Eng., 234-236A (1997) 889

[8] J. A. Moser, M. Aindow, W. A. T. Clark, S. Draper and H. L. Fraser, Mat. Res. Soc. Symp. Proc., 194 (1990) 379

[9] K. Yoshimi, S. Hanada and M. H. Yoo, Mat. Res. Soc. Symp. Proc., vol. 460 (1997) 313

[10] D. K. Hale, J. Mater. Sci., 11 (1976) 2105

[11] G. A. Cooper, Ch. 10, in: Composite Materials, vol. 5, Fracture and Fatigue, Academic Press, New York, (1974), pp. 415

[12]S. Ochiai and M. Hojo, Materia Japan, 33 (1994) 1397

Chapter 6

Composite Material Designs for Ni Aluminides

6-1 Introduction

Ni_3Al and NiAl alloys, that are one of the most promising intermetallics for novel high temperature structural applications, have been intensively investigated in the last 20 years [1-2]. However, we face hard sledding in establishing practical applications only by the conventional alloy design. The Ni_3Al alloy exhibits low strength and creep resistance above 1000 K. The NiAl alloy is inferior in toughness at ambient temperatures and in strength at elevated temperatures. Therefore, the composite material design is expected to be one of the effective strategies in improving such mechanical properties. As described in Chapter 3, the mechanical properties of these alloys are quite different due to the differences in their crystal structures and bond characters. The guideline for composite designing should be based on peculiar mechanical behaviors of the matrix alloys. Although great progress in processing techniques for intermetallic matrix composites in the last 10 years, the guideline of composite design has never been discussed in detail. In this chapter, the influence of characteristics of the matrix alloys on mechanical behaviors of Ni aluminide matrix composites with ceramic fine particles and continuous fibers is investigated to obtain suitable composite designs for achieving high strength and reliability.

6-2 Experimental Procedure

The raw powders of Ni, Al and B, which are described in Chapters 2 and 3, were used as the starting materials of the matrix alloys. The ceramic fine particles in Table 5.1, and SiC fibers (Si-Ti-C-O Tyranno fiber, UBE Industries, Ltd.; ϕ 8.5 μm, 50.4Si : 29.7C : 17.9O : 2.0Ti (mass%)) were selected as reinforcements for Ni_3Al and NiAl alloys. The nickel aluminides and their composites are expected to be utilized up to ~1273 K. The SiC fibers are one of the attractive reinforcements for these matrix alloys because of their excellent mechanical properties at elevated temperatures. In the present work, the potential of the SiC fibers for reinforcing Ni alumindes were investigated. The processing details and material characterization method have been already described in Chapters 3 and 5.

6-3 Results and Discussion

6-3-1 Composites with ceramic fine particles

(1) Ni_3Al matrix composites

Screening test

The reactive hot-pressing temperature, 1573 K, was sufficiently high in fabricating Ni-25at%Al matrix composites with the reinforcement particles. β-SiC and TiB_2 exhibit remarkable reaction with Ni_3Al alloys at 1573 K as described in Chapter 4. The details of discussion for the chemical compatibility were described in Chapter 4.

Figure 6.1 (a) shows the microstructure of the composite when the β-SiC particles were used as the reinforcements. The β-SiC particles disappeared by reaction with the matrix. Figure 6.1 (b) shows the XRD pattern of this composite. The reaction products were identified to be graphite and Ni_2Si. Furthermore, the dissolution of a few at% Si was also detected by EDX. The XRD pattern also indicates that the matrix include NiAl, as well as Ni_3Al.

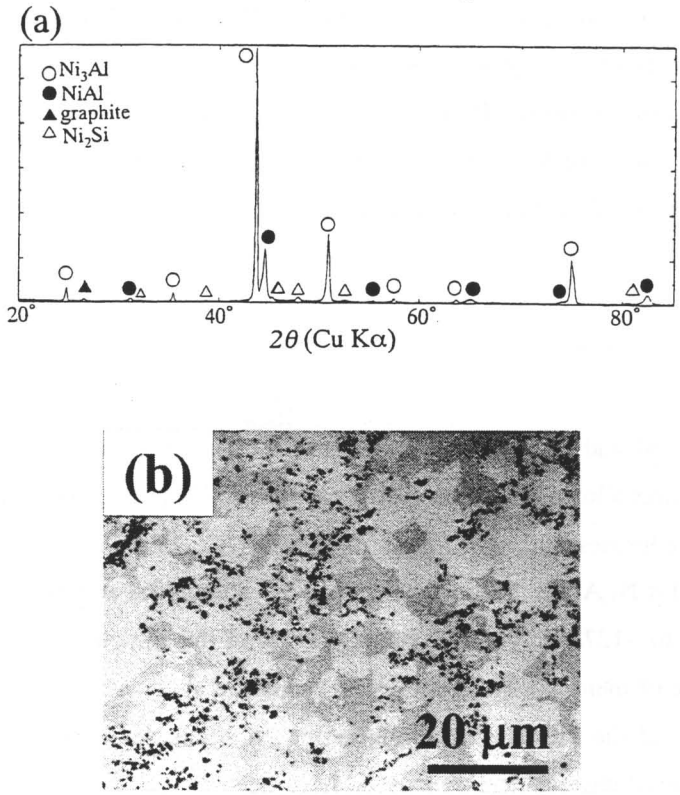

Fig. 6.1 (a) XRD pattern and (b) microstructural feature of Ni-25at%Al matrix composite with β-SiC particles fabricated by reactive hot-pressing.

In the case of TiB_2 composites, the stable existence of TiB_2 in the matrix was detected by XRD as shown in Fig 6.2 (a). Figure 6.2 (b) shows the typical microstructure of the Ni-25at%Al/TiB_2 composites. The finer particles indicated with A in Fig.6.2 (b) are Al_2O_3, which come from impurity oxygen in the starting materials. The faceted TiB_2 particles, with the size of 1-2 μm, were adjacent to aluminum oxide particles. The aluminum oxide particles were also observed within the TiB_2 particle. The SEM-EDX analysis also suggested the dissolution of a few at% Ti into the matrix. Although the detail mechanism for such a microstructural evolution is still unclear, the starting TiB_2 particles were considered to react with the Ni-25at%Al matrix during hot-pressing. Figure 6.2 (a) also shows the formation of NiAl in the matrix.

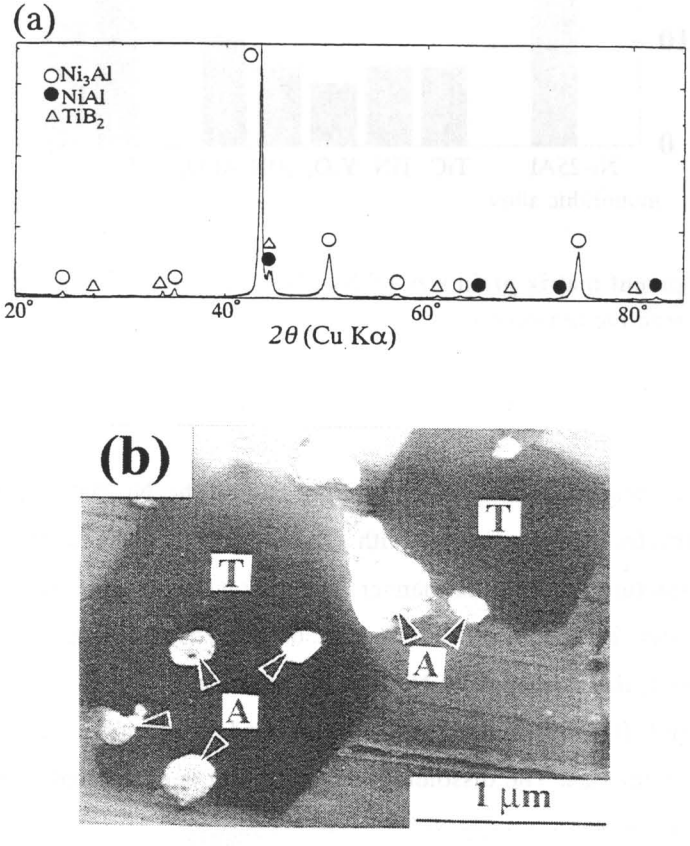

Fig. 6.2 (a) XRD pattern and (b) typical microstructure of Ni-25at%Al/TiB_2 composites fabricated by reactive hot-pressing.

The reinforcements except of SiC and TiB_2 particles do not exhibit significant reaction with the matrix. Figure 6.3 shows the apparent matrix grain size of these composites with 10 vol% reinforcement particles, in comparing with that of Ni-25at%Al monolithic alloys. The matrix grain size of composites with chemically compatible reinforcements (5-10 μm) is much lower than that of the monolithic alloy (~50 μm). The Ni-25at%Al/TiB_2 composites have a large matrix grain size of about 30 μm.

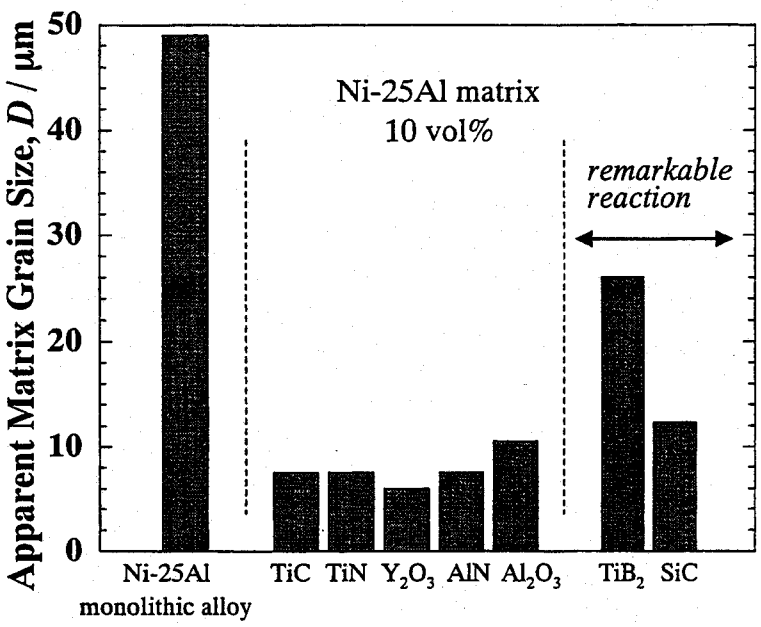

Fig. 6.3 Apparent matrix grain size of Ni-25at%Al matrix composites fabricated by reactive hot-pressing.

Figure 6.4 shows the results of four point bending test of the Ni-25at%Al matrix composites containing 10vol% particles. The composites with TiB_2 and SiC particles exhibit an elasticity above 1 GPa although they fractured in a brittle manner. The dissolution of constitutional elements of the particles into the matrix is considered to be one of the strengthening mechanisms of these composites. Furthermore, the formation of NiAl in the matrix also contributes to the strengthening as described in Chapter 3. It is unique that the TiB_2 reinforced composites have such high strength in spite of larger matrix grain size. The dissolution strengthening is considered to predominate to the effect of grain size refinement.

The strength of the composites with α-Al_2O_3, AlN and Y_2O_3 particles, which have excellent chemical compatibility with the matrix, is almost explained by the decrease of matrix grain size because Hall-Petch parameter of Ni_3Al alloys is $\sim$0.75 MPa $m^{-1/2}$ [3] In the case of the composites with Y_2O_3 particles, which include rare earth oxides (such as CeO_2, Pr_3O_2, Nd_2O_3, Sm_2O_3, Tb_4O_7, Dy_2O_3) and alkaline earth oxides (such as CaO) (a few hundreds ppm) [4], the dissolution of impurity elements may be considered. Because some of these elements exhibit reactivity with the matrix and are effective to improve yield strength [2]. In contrast to these composites, the TiC and TiN reinforced composites exhibit significant strengthening as shown in Fig. 6.4. Although these particles do not exhibit significant reaction with the matrix, the dissolution of impurity, such as free carbon in TiC particles, may contribute to strengthening. However, the origin of such a large

strengthening effect of these particles is not disclosed definitely within the limit of the present work.

Based on the results of this screening experiments, the mechanical properties of Ni_3Al matrix composites with TiC, TiN and α-Al_2O_3 particles, which have both of excellent chemical compatibility and strengthening ability, are investigated in the following section.

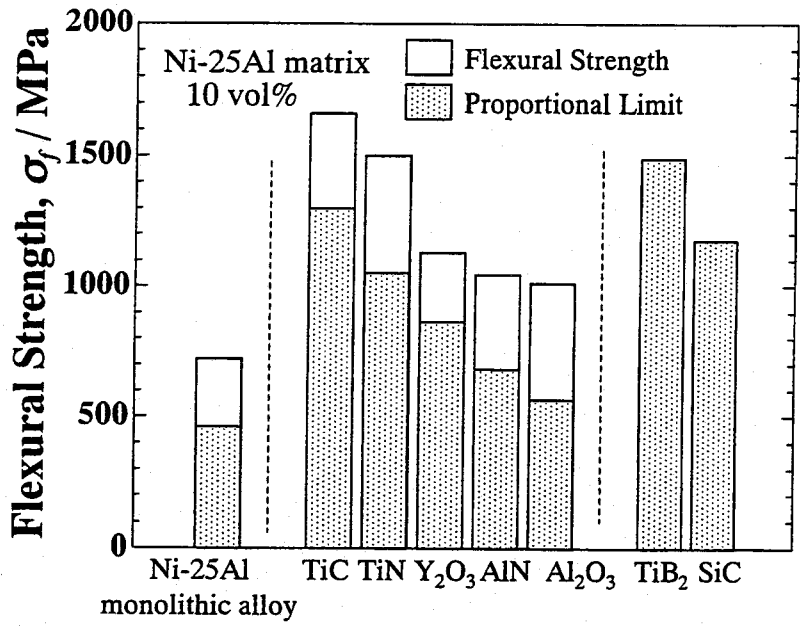

Fig. 6.4 Flexural strength of Ni-25at%Al matrix composites with 10 vol% several particles at ambient temperatures.

Mechanical properties of TiC, TiN and α-Al_2O_3 composites

Figure 6.5 shows the flexural strength and fracture toughness of Ni-24at%Al matrix composites with 10 vol% of TiC, TiN and α-Al_2O_3 particles. The TiC and TiN composites are more effective in strengthening the Ni-24at%Al matrix rather than the α-Al_2O_3 reinforced ones. In particular, the TiC particle reinforced composite has high strength although it exhibits brittle fracture. On the contrary, the fracture toughness decreases by the particle dispersion. Because the Ni_3Al matrix inherently has a sufficient number of slip system for extensive ductility, the fracture toughness strongly depends on the shielding effect by blunting of a crack tip (stress relaxation by plastic deformation) as described in Chapter 3. The strengthening effect, which is obtained by obstructing dislocation motion, results in decreasing their fracture toughness.

The fracture behaviors of Ni_3Al matrix composites at ambient temperatures are also affected by the grain boundary weakness [5-6]. Therefore, the ductility and toughness of these composites are expected to be improved by modifying their grain boundary natures with B doping. Figure 6.6 shows the flexural strength and fracture toughness of the Ni-24at%Al matrix composites with 0.1at% B

doping. The fracture toughness of the B doped monolithic alloy was not estimated by the bending test because the crack does not initiate in the chevron-notched specimens. The fracture toughness of the B doped composites with TiN and α-Al_2O_3 particles is 2-3 times higher than that of the non-doped composites although little increment of toughness is found in the TiC particles reinforced one. Because the TiC composite is intrinsically brittle, its fracture toughness is hardly contributed by the grain boundary brittleness. The B doped TiC reinforced composite exhibits elastic-plastic deformation with proportional limit of 1.5 GPa. The ductility of TiC composites is only slightly improved by the doping.

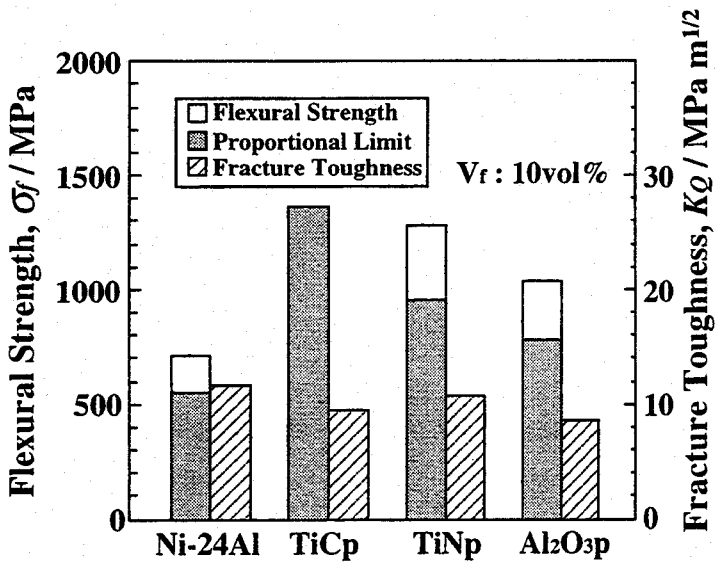

Fig. 6.5 Flexural strength and fracture toughness of Ni-24at%Al matrix composites with 10 vol% TiC, TiN and α-Al_2O_3 particles at ambient temperatures.

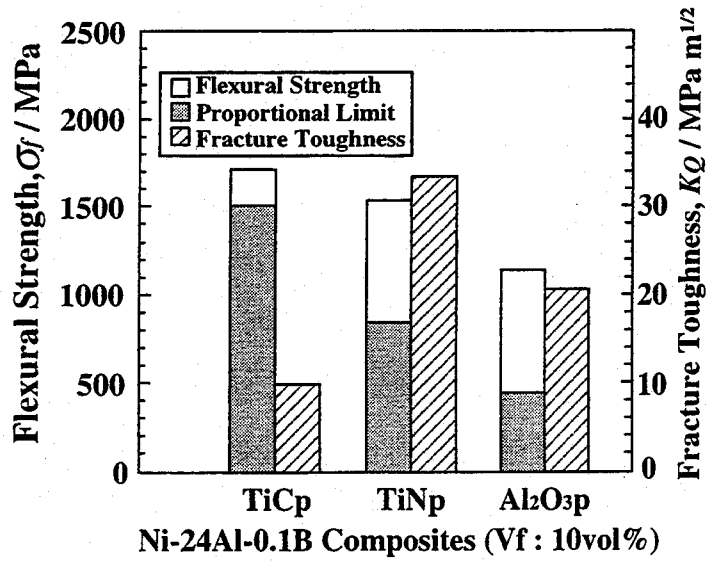

Fig. 6.6 Effect of 0.1at%B doping into the Ni-24at%Al matrix on flexural strength and fracture toughness of the composites at ambient temperatures.

Fracture mechanism of TiC, TiN and α-Al_2O_3 composites

According to Sakai [7-8], fracture toughness of materials, K_c, can be generally represented by SSC (stress shielding coefficient) and K*;

$$K_c = SSC \cdot K^* \qquad (6.1)$$

K* is expressed in terms of the interatomic binding potential of constituent atoms;

$$K^* = \beta\,(\kappa_0 u_0)^{1/2} / r_0^{3/2} \qquad (6.2)$$

where β is a constant depending on the pair potentials, u(r). κ_0 and u_0 are the curvature of potential curve and the depth of potential curve at equilibrium atomic position (r_0). K* of metals is generally estimated to be < 1 MPa $m^{1/2}$ [8]. Because K* is proportional to κ_0, K* of ceramics is slightly higher rather than that of metals. Hence, the fracture toughness (K_c) of metals strongly depends on SSC, that is originated from high plastic deformability. SSC of ceramics is related with the physical obstruction for a growing crack. The magnitudes of SSC in metals and ceramics are briefly estimated to be 10-100 and 2-5, respectively.

Figure 6.7 shows the schematic illustration of R-curve behavior in ductile materials and ceramic matrix composites with discontinuous reinforcements. In the case of ceramic matrix composites, the reinforcements can provide toughening effect by crack bridging, deflection and bowing [9]. These toughening mechanisms are basically represented as the rising R-curve in Fig. 6.7 (b). Although the stable crack propagation length is very short, the fracture resistance slightly increases by the interaction between a growing crack and the dispersoids. In this case, the contribution of the toughening effect by dispersoids to SSC is considered to be < 2, because the increase of fracture toughness in ceramic matrix composites with discontinuous reinforcements is generally less than 2 times of that of monolith. In contrast, the critical stress intensity factor for crack initiation of ductile materials, which strongly depends on the plastic deformation at a crack tip, is much higher than that of ceramics. Furthermore, the stable crack growth is continued in ductile materials after the crack initiation. In this case, the fracture resistance increases due to the plastic deformation at a crack tip during the stable crack growth (Fig. 6.7 (a)) [10]. In the case of the composites with ductile matrix, the fracture toughness and resistance are determined by the ductility at a crack tip, because the stress shielding effect by the plastic deformation is extremely higher than that by the interaction between a growing crack and the dispersoids. For example, the fracture toughness of Ni_3Al alloys without environmental embrittlement is >20 MPa $m^{1/2}$ as shown in Chapter 3, the magnitude of SSC by plastic deformation in Ni_3Al must be 10 times or more higher than that by the effect of dispersoids.

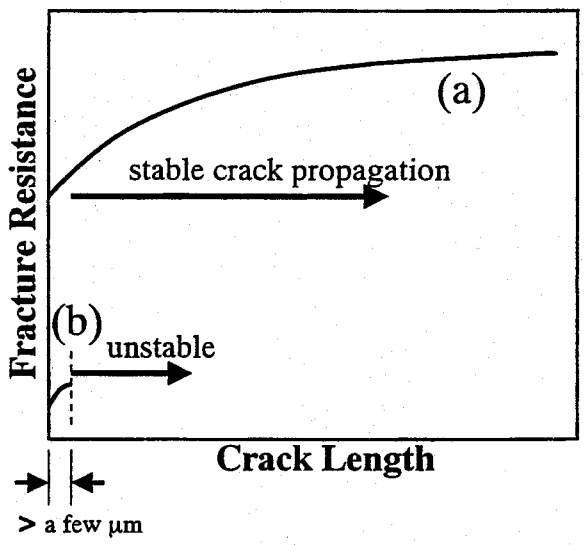

Fig 6.7 Schematic illustration of R-curve behavior of (a) ductile materials and (b) ceramic matrix composites.

The fracture toughness of the composites with 5-20 vol% of reinforcements is also influenced by the environmental effect as well as the intrinsic grain boundary brittleness. For example, the loading rate dependence of fracture toughness in air for the Ni-24at%Al matrix composites with 10 vol% of several particles is shown in Figs. 6.8 (a)-(c). The toughness of these composites exhibits a significant dependence on loading rate similar to the monolithic alloys. The toughness values at 10 MPa $m^{1/2}$ sec^{-1} show good agreement with those in the oil bath. Hence, the toughness values at 10 MPa $m^{1/2}$ sec^{-1} can be regarded as the intrinsic toughness independent of environmental effects. The intrinsic toughness of the composites with TiN particles is almost as same as that of α-Al_2O_3 particle reinforced ones. However, the environmental effect is slightly suppressed in the TiN reinforced ones. In contrast, the TiC composites are intrinsically brittle. From the fact that the yield strength remarkably increased by the addition of TiC particles, the mobility of dislocations in the matrix is supposed to be extremely reduced.

Figures 6.8 (a)-(c) also show the loading rate dependence of fracture toughness of the 0.1at%B doped matrix composites. Although their fracture toughness is improved by the doping, the effectiveness of B is quite different among these composite systems. In the case of the composites with α-Al_2O_3 particles, the fracture toughness is 28 MPa $m^{1/2}$ regardless of the loading rate both in air and in the oil bath. If the doping is only effective in suppressing environmental effects, increment of their fracture toughness is limited until the intrinsic toughness of the non-doped composites. In this case, however, the suppression of the environmental embrittlement contributes only 23 % in the whole effect of the doping. The additional increase in fracture toughness may be caused by the enhancement of grain boundary cohesion.

Although the extrinsic toughening effect of B in the TiN particle reinforced composites is estimated to be about 14 %, its fracture toughness is much larger than that of composites with α-Al_2O_3 particles. Furthermore, the TiN reinforcement can slightly reduce sensitivity to the environmental effect even without the B doping as shown in Fig. 6.8 (b). The effect of TiN has never been clarified in the present work. At this moment, the peculiarity of the composites with TiN particles is considered to be caused by the another phenomenon such as the dissolution of N into the

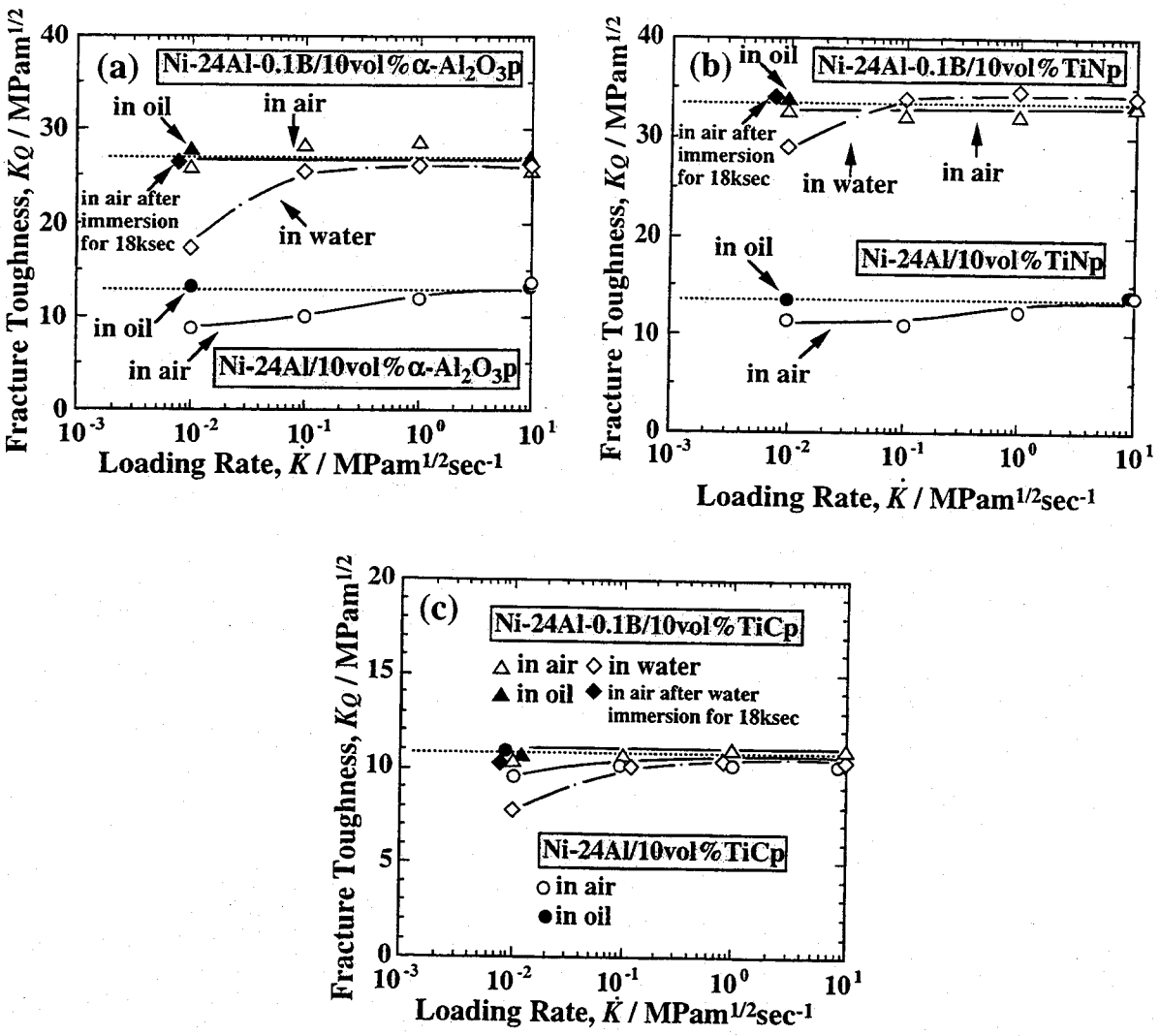

Fig. 6.8 Loading rate dependence of fracture toughness measured in air, oil bath and water bath for 10 vol% (a) α-Al_2O_3, (b) TiN and (c) TiC particles reinforced Ni-24at%Al matrix composites with and without 0.1at%B doping. Toughness values of these composites in air at 10^{-2} MPa $m^{1/2}$ sec^{-1} after the water immersion for 18 ksec are also shown in this figure.

matrix because the segregation of N can enhance the grain boundary cohesion [11]. On the other hand, the doping is not so effective in improving the fracture toughness of the composites with TiC particles. The environmental embrittlement of the composites can be also suppressed by the doping, although the intrinsic improvement of fracture toughness is not achieved.

The environmental effect is not always suppressed completely by the B doping in every atmospheres. The loading rate dependence of fracture toughness of the B doped matrix composites in a water bath is indicated in Figs. 6.8 (a)-(c). The fracture toughness of the B doped ones at a loading rate of 10^{-2} MPa $m^{1/2}$ sec^{-1} in water is about 20 % lower than that in air and an oil bath. This result indicates that the environmental effect influences the fracture toughness of the B doped ones in such a severe environment. In the case of loading at 10^{-2} MPa $m^{1/2}$ sec^{-1}, it takes 1.2 - 3.0 ksec until the crack propagation from the notch tip. From these experimental results, it is recognized to be a sufficient time for the diffusion of H derived from liquid H_2O. Then, the toughness measurement was also conducted in air after the immersion of the specimens in water for 18 ksec without loading. However, the extra embrittlement is never induced by the immersion in water without loading as shown in Figs. 6.8 (a)-(c). Therefore, the environmental embrittlement is manifested to be a dynamic phenomenon which occurs during loading.

Mechanical behaviors at elevated temperatures

Figures 6.9 (a)-(c) show the results of tensile test in air of the Ni-24at%Al-0.1at%B matrix composites with 10vol% α-Al_2O_3, TiN and TiC particles, respectively. The composites with α-Al_2O_3 particles are expected to exhibit typical mechanical behavior of the composites reinforced only by the physical mechanism because the particles have excellent chemical compatibility with the matrix alloys [12]. The 0.2% proof stress is improved to 1.5 times higher than that of the monolithic alloy at ambient temperatures by the effect of the particles. However, the ductility decreases with the addition of reinforcement particles, although the grain boundary brittleness and the moisture induced embrittlement can be suppressed by the B doping. Their ductility further decreases with increasing temperature up to ~800 K, corresponding to the dislocation locking by the Kear-Wilsdorf mechanism. The composites fracture in a brittle manner at 773 K. Subsequently, the ductility gradually increases with decrease in the 0.2% proof stress and the ultimate strength above 900 K.

For the composites with TiN particles, the tensile strength and ductility are higher than those with α-Al_2O_3 as illustrated in Fig. 6.9 (b). Although the composites do not fracture in a brittle manner, the ductility decreases at intermediate temperatures. On the other hand, the tensile strength of the composite with TiC particles is remarkably higher than that of the other composites. However, the composites reveal brittle fracture below 900 K, as shown in Fig. 6.9 (c). The magnitude of the strengthening effect is quite different, depending on the kind of reinforcement particles. The chemical effect of a small amount of constitutional elements dissolved in the matrix is suggested to

contribute to the mechanical behavior of the composites as well as to the physical reinforcing mechanism such as the pinning effect against dislocation motion.

Figures 6.10 (a) and (b) show the fracture toughness of the Ni-24at%Al-0.1at%B matrix composites with 10 vol% reinforcement particles at 673 and 873 K, respectively. The toughness of the composites at a loading rate of 10 MPa $m^{1/2}$ sec^{-1} at 673 K are almost the same as those at 300 K. Thus, their toughness does not decrease at 673 K. However, the toughness of the TiN and α-Al_2O_3 composites shows significant loading rate dependence in air. Therefore, the dynamic embrittlement caused by diffusion of oxygen [13-14] is the predominant mechanism governing their fracture toughness at 673 K. However, the toughness of the composites decreases at 873 K, in a similar manner to the monolithic alloy.

The toughness of the TiC composites is exceptionally constant regardless of loading rate, as shown in Figs. 6.10 (a) and (b). Furthermore, the toughness at these temperatures approximately coincides with that at 300 K. Thus, the toughness of the TiC composites is unrelated to the environmental effect and to the characteristic dislocation motion at intermediate temperatures. As a result of the remarkable strengthening with the addition of TiC particles, the dislocation motion is restricted. Hence, the fracture toughness of the TiC composites becomes constant in the temperature range of 300-900 K.

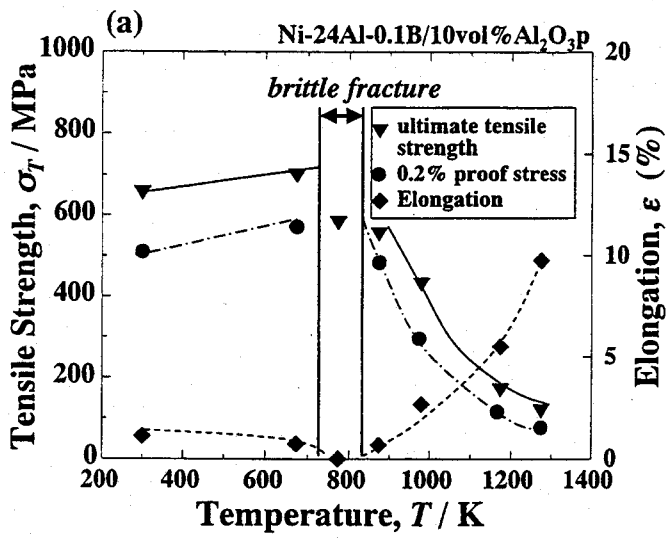

Fig. 6.9 Temperature dependence of tensile strength and elongation of Ni-24at%Al-0.1at%B matrix composites with 10 vol% (a) α-Al_2O_3, (b) TiN and (c) TiC particles.

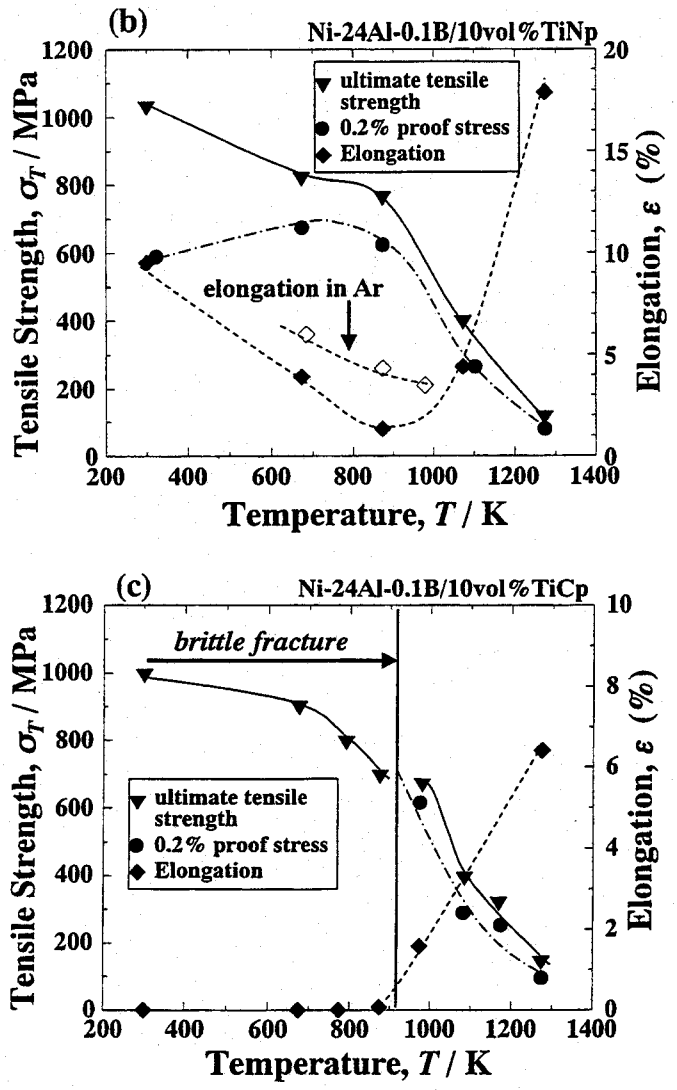

Fig. 6.9 *Continued*

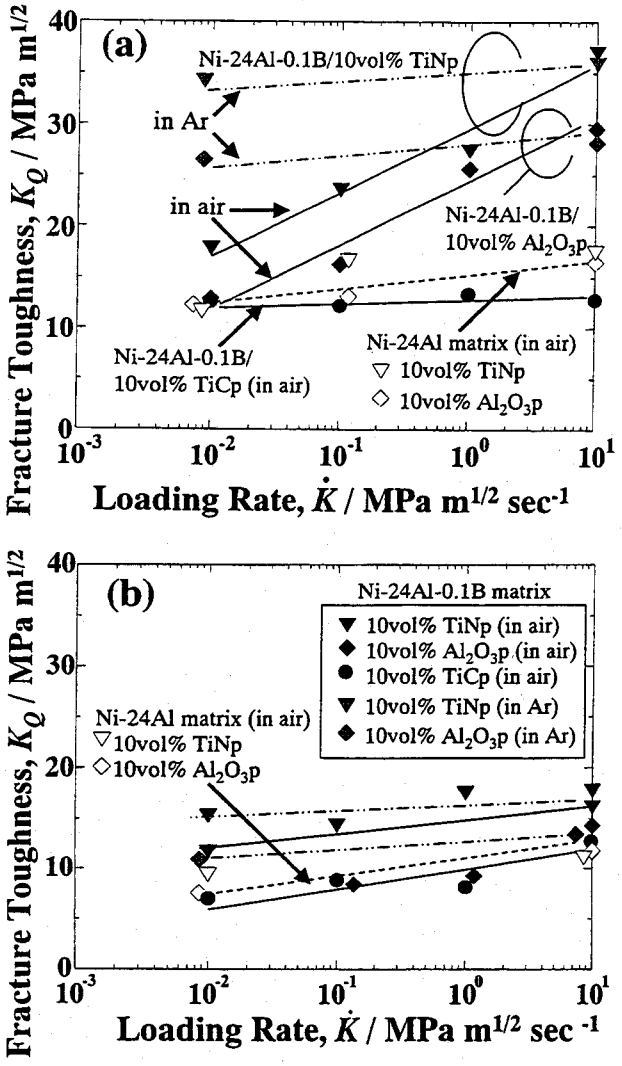

Fig. 6.10 Loading rate dependence of fracture toughness of Ni-24at%Al-0.1at%B matrix composites with 10 vol% α-Al_2O_3, TiN and TiC particles at (a) 673 and (b) 873 K.

(2) NiAl matrix composites

In the present work, Ni-45at%Al was selected as the matrix of NiAl composites because of high strength and good sinterability (c.f., Chapters 2 and 3). Figure 6.11 shows flexural strength of the matrix composites. The composites except the TiB_2 and ZrB_2 reinforced ones fractured in a brittle manner at 400-500 MPa, which corresponds to the fracture strength of the monolithic alloy. Because NiAl matrices intrinsically have the high APB energy [2], the dispersion strengthening with ceramic fine particles is hardly expected at ambient temperatures. Figure 6.11 indicates the Ni-45at%Al

composites with TiB_2 and ZrB_2 particles exceptionally have high flexural strength with elastic-plastic deformation behavior. The strengthening mechanism of these boride particles is not disclosed definitely. For example, the possibility of dissolution of B is considered as a hypothesis for the strengthening mechanism because George and Liu [15] have pointed out the potential of B as the solid-solution strengthener for NiAl alloys. The dissolution of constitutional elements into the matrix was not practically detected in these composites. Furthermore, the flexural strength of Ni-45at%Al alloy with 0.5 at% B doping was measured to be 500-550 MPa, which is equivalent to that of the non doped alloy. Therefore, the solution strengthening seems to be rejected as the main strengthening mechanism. Moreover, the fracture toughness is slightly improved by the dispersion of these particles as shown in Fig. 6.11.

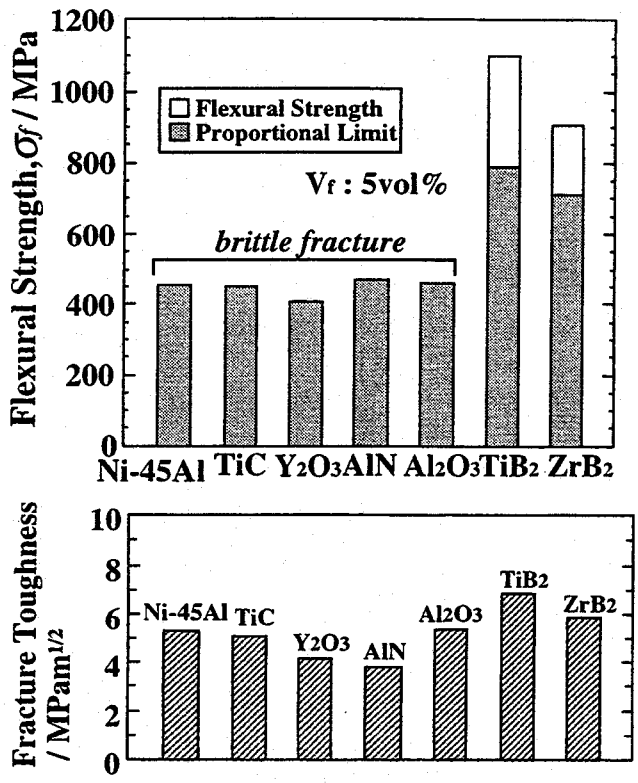

Fig. 6.11 Flexural strength and toughness of Ni-45at%Al matrix composites with 5 vol% several particles at ambient temperatures.

Based on this screening examination, Ni-45at%Al matrix composites with TiB_2 particles are selected for bending test at elevated temperatures. Because the matrix alloy reveals significant plastic deformability above 1000 K by "pure-metal type creep" [16], which is a deformation behavior controlled by dislocation substructure rather than lattice friction, the strengthening in this temperature range is only expected by the composite material design. Figure 6.12 shows temperature dependence of flexural strength of the composites with 5-10 vol% TiB_2 composites. The strength is successfully improved by the addition of TiB_2 particles. The composites with 10 vol% TiB_2 particles exhibit significant strengthening even above 1000 K. Thus, the composite design with boride fine particles is one of the useful approaches to improve the mechanical properties of NiAl alloys with Ni-rich compositions.

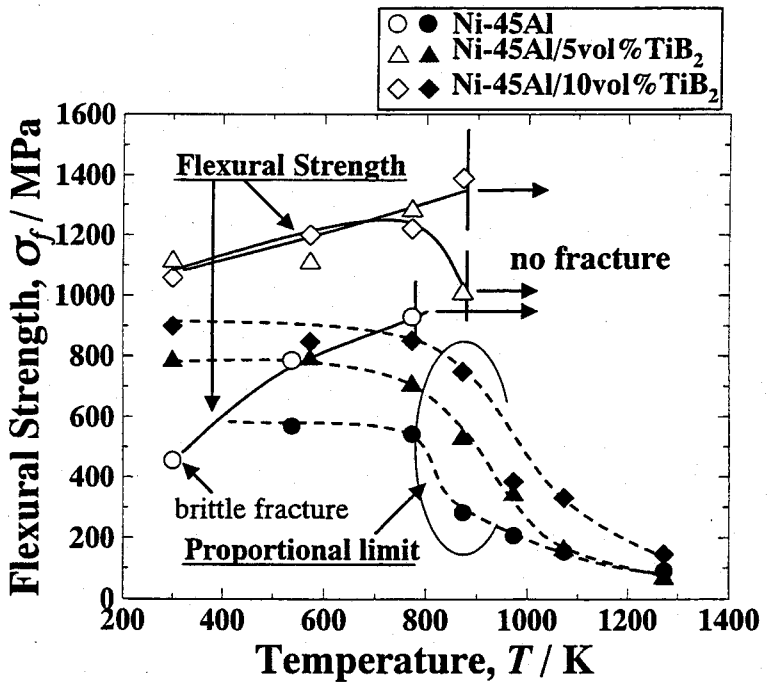

Fig. 6.12 Temperature dependence of flexural strength of Ni-45at%Al matrix composites with 5-10 vol%TiB_2 particles.

(3) Theoretical consideration of optimum dispersoid radius for dispersion strengthening of NiAl at elevated temperatures

The dispersion strengthening mechanism at elevated temperatures is discussed in this section. The theoretical background have been proposed by Arzt et al [17-19]. In intermetallic (ordered) alloys, the dislocations dissociate into superpartial dislocation pairs. The superpartial dislocations can individually interact with the dispersoids to achieve dispersion strengthening [20]. The model for the

pinning of superpartial dislocations by a particle is shown in Fig. 6.13 (b). The spacing between the partials and particle radius are represented as w and R, respectively.

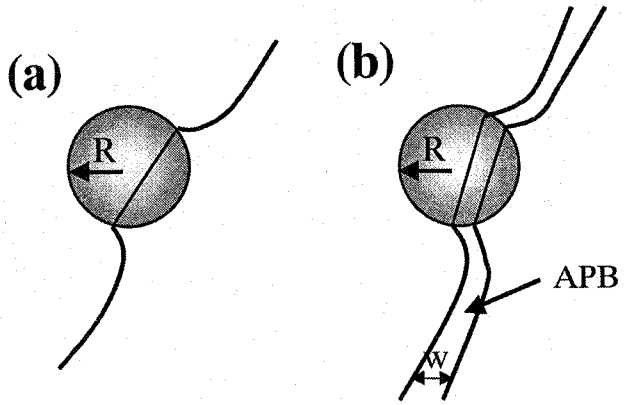

Fig. 6.13 Models of dislocation pinning by a spherical dispersoid. (a) single dislocation, (b) superpartial dislocation pair.

When the leading partial detaches from a dispersoid, the detachment stress largely depends on the position of the trailing partial. At the condition of $w \ll 2R$, the trailing partial, which have a large detachment barrier, cannot enhance the escape of the leading partial. Therefore, high creep resistance is obtained by the dispersion strengthening at this condition. Furthermore, if the trailing partial can still climb uphill at the arrival side of the dispersoid, high back stresses generate on both partials.

In contrast, the trailing partial transmits an additional shear stress to the leading partial when the trailing partial easily climb down the dispersoid. In this case, the dispersion strengthening effect is extremely lowered. Arzt and his colleagues claimed that w/2R is an useful parameter to estimate the magnitude of dispersion strengthening [18-19]. They have concluded that the optimum strengthening is obtained when $w/2R \fallingdotseq 0.6$.

Although the above-mentioned theoretical scheme is essential to discuss the dispersion strengthening in intermetallic alloys with relatively low APB energy (such as Ni_3Al and FeAl), the strengthening effect in the alloys with high APB energy (such as NiAl) can be satisfactorily discussed by the single dislocation model (Fig. 6.13 (a)) because w is extremely low value. The dispersoids impede the climb and glide motion of dislocations at elevated temperatures by exerting an attractive force. At the same time, thermally–activated detachment of dislocations sufficiently occurs at elevated temperatures. By considering thermally–activated detachment of dislocations, Rösler and Arzt [18] have introduced the following equation for the creep strength by dispersion strengthening ;

$$\tau/\tau_d = 1 - [(1/1-\kappa)\ \{(kT \ln \dot{\varepsilon}_0/\dot{\varepsilon})/\ Gb^2R\}^{2/3}] \qquad (6\text{-}3)$$

where, τ, τ_d, κ, k, T, $\dot{\varepsilon}_0$, $\dot{\varepsilon}$, G, b, R are share stress, detachment share stress, relaxation factor, Boltzmann constant, temperature, a factor containing diffusivity and mobile dislocation density, strain rate, share modulus, Burgers vector, dispersoid radius, respectively. The $\dot{\varepsilon}_0$ is estimated by the following equation ;

$$\dot{\varepsilon}_0 = 6\ D_v\ \lambda\ \rho/b \qquad (6\text{-}4)$$

where, D_v, λ, ρ are volume diffusivity, dispersoid spacing and density of mobile dislocations. Figure 6.14 shows the schematic diagram of normalized creep strength, $\{(\tau/G)/(1-\kappa^2)^{1/2}\}$, as a function of normalized dispersoid radius, R/b. The optimum dispersoid radius, R_{opt}, is estimated by ;

$$R_{opt} \fallingdotseq (kT/Gb^2)\ \{(2 \ln \dot{\varepsilon}_0/\dot{\varepsilon})\ /\ (1-\kappa)^{3/2}\} \qquad (6\text{-}3)$$

The R_{opt} for NiAl can be discussed by using the equation (6-3). The share modulus (G) of NiAl [2] is represented by ;

$$G\ (GPa) = 76.6 - 0.017\ T \qquad (6\text{-}4)$$

The experimental data for D_v is reported to be $\sim 10^{-13}$-10^{-15} $m^2\ sec^{-1}$ (1000-1400 K) [21]. The λ and ρ are assumed to be $\sim$200 nm and $\sim 10^{13}$ m^{-2} [17]. The relaxation factor (κ), which depends on the dispersoid-dislocation interaction, seems to be 0.8-0.95 in many intermetallic alloys [18-19]. Because the Burgers vector (*b*) is a<001> [2], R_{opt} can be estimated as the function of strain rate and temperature. For example, R_{opt} is briefly estimated to be 10-20 nm for the deformation at a strain rate of 10^{-5}-10^{-8} sec^{-1} at 1000-1400 K.

In the present work, the commercial powders with relatively large mean particle size and wide size distribution were used as the reinforcements. Thus, the composite design with ceramic particles in the present work are not optimized for obtaining maximum creep resistance at elevated temperatures. In order to achieve the optimization of creep strength, novel processes for synthesizing nano-particles [20] are necessary to be applied for fabricating the composites.

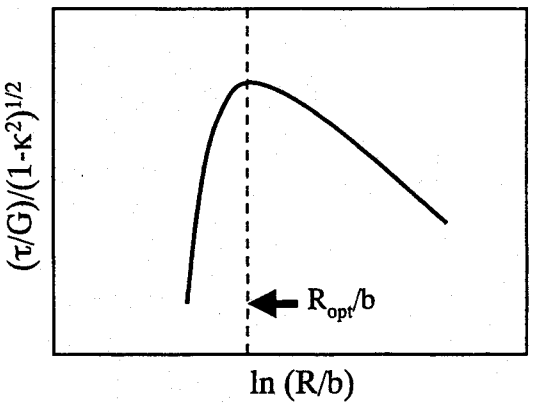

Fig. 6.14 Schematic illustration of normalized creep strength as a function of normalized dispersoid radius.

6-3-2 Fiber reinforced composites

Continuous fiber reinforced Ni_3Al matrix composites

The purposes of composite material design with continuous fibers are divided into two aspects, i.e., strengthening and toughening. In the case of the composites with continuous ceramic fibers, these aspects are different design concepts which are incompatibly achieved as shown in Fig. 6.15. For B doped Ni_3Al alloys, which exhibit extensive ductility, the strategy for toughening by ceramic fibers is meaningless. Hence, the objective of composite design with continuous ceramic fibers focuses on strengthening for Ni_3Al alloys.

SiC severely reacts with the alloys according to Misra's thermodynamic calculation [12]. Hence, the interfacial reaction seems to be a serious problem in the SiC fiber reinforced composites. Figure 6.16 (a) shows the cross-sectional SEM micrograph of the Ni-24at%Al-0.1at%B matrix composites. The thickness of reaction layer is about 0.5 μm. The reaction product is identified as graphite by XRD. The EDX analysis also indicates the dissolution of 1-2 at% Si into the matrix. Figure 6.17 shows the surface morphology of the fibers which are etched out from the Ni_3Al matrix composites. Although many grooves which are formed due to the interfacial reaction are observed on the surface of the fibers, the interfacial reaction is suppressed by the present processing technique.

Figures 6.18 (a)-(d) show the flexural strength of the Ni-24at%Al-0.1at%B matrix composite with 10 vol% SiC fibers at 300-1273 K. In spite of the degradation of fibers due to the interfacial reaction, significant strengthening is successfully achieved in this composite at 300 K. In this case, The fibers

predominantly break into short fragments before the matrix cracking (multiple fracture of fibers [22]) as indicated in Fig. 6.19. The fiber cracking is induced by stress concentration at the grooves. When the composites exhibit the multiple fracture of fibers, the ultimate strength of the composites strongly depends on the matrix toughness [22]. Because the B doped Ni_3Al matrix alloy has excellent ductility, high ultimate strength is achieved in this composite at ambient temperatures.

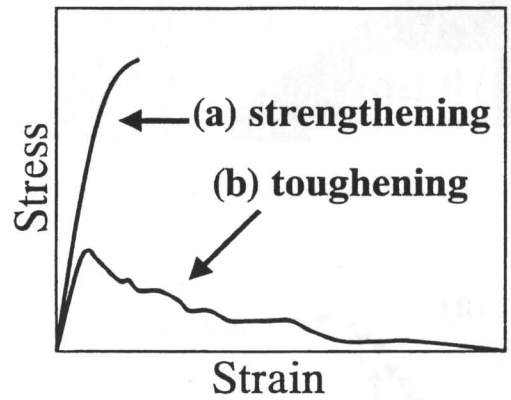

Fig. 6.15 Composite material design concept with continuous fibers.

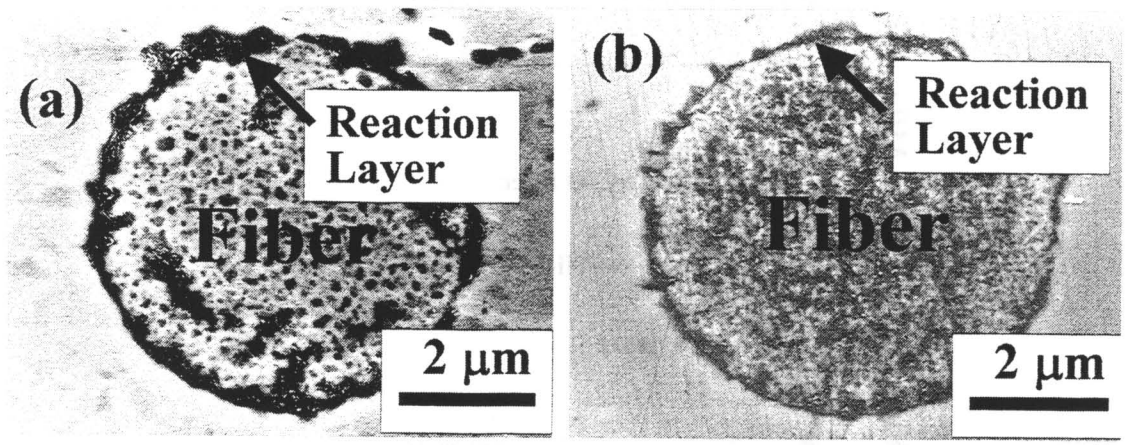

Fig. 6.16 Cross-sectional SEM micrographs of SiC continuous fiber reinforced (a) Ni-24at%Al-0.1at%B and (b) Ni-45at%Al matrix composites.

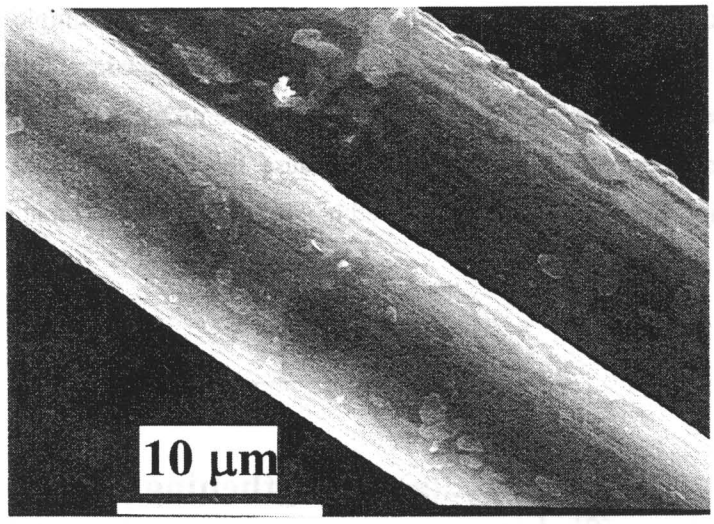

Fig. 6.17 Surface morphology of SiC fibers etched out from the Ni_3Al matrix composites.

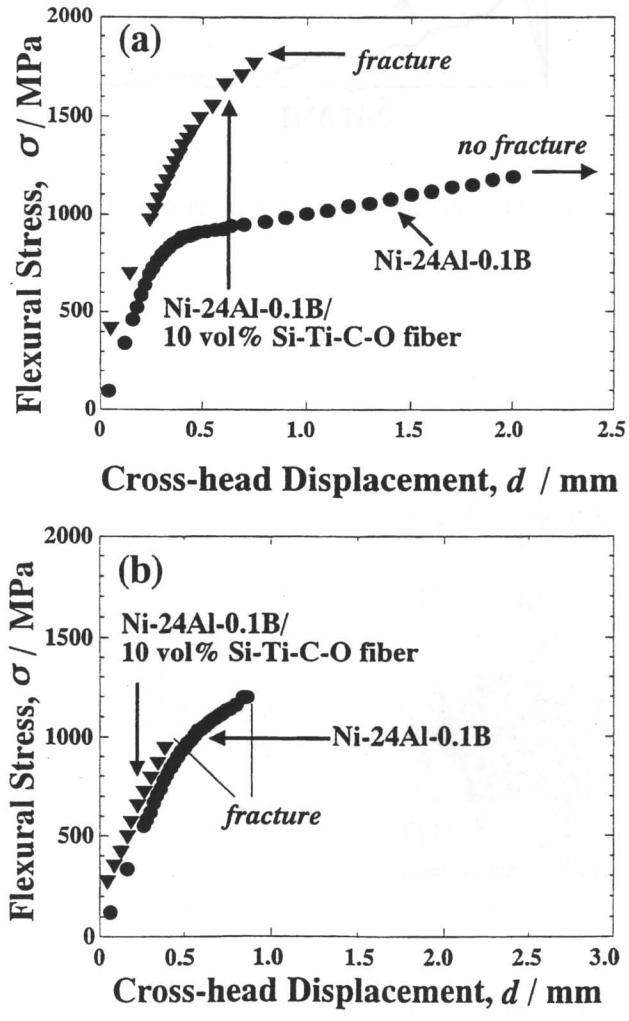

Fig. 6.18 Flexural strength of Ni-24at%Al-0.1at%B matrix composites with 10 vol% SiC fibers at (a) 300, (b) 873, (c) 973 and (d) 1273 K.

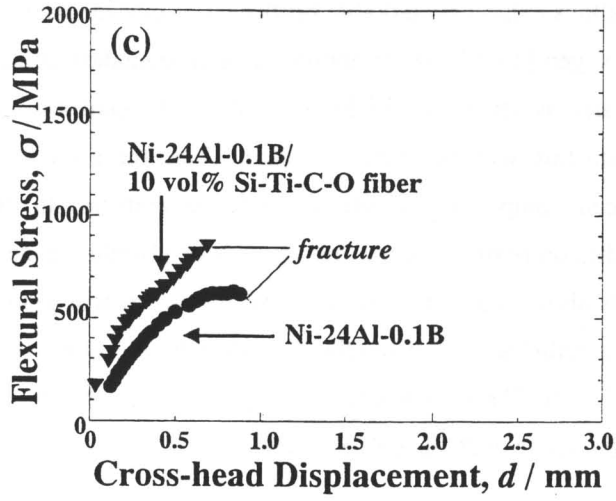

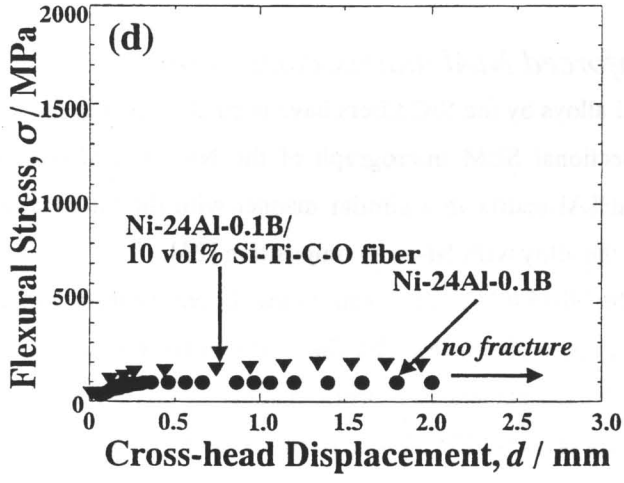

Fig. 6.18 *continued*

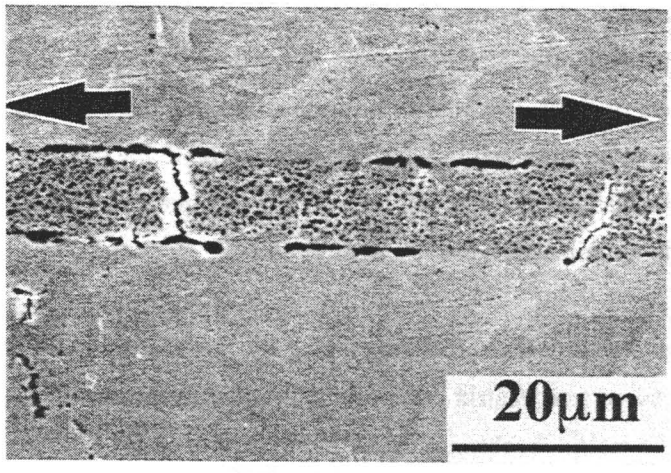

Fig. 6.19 Multiple fracture of SiC fiber observed at ambient temperatures.

On the other hand, Ni_3Al alloys exhibit remarkable brittleness at intermediate temperatures due to stress assisted diffusion of oxygen [13-14], deterioration of grain boundary cohesion and cross-slip of super-lattice dislocation pairs, as described in Chapter 3. When the matrix has low toughness, the composites simultaneously fracture with the fiber cracking. Thus, the alloy is unfavorable to the matrix of the fiber reinforced composites at intermediate temperatures. In fact, the fibers are ineffective in strengthening the composite because they fracture in a brittle manner at 873 K.

As increasing temperature above 1073 K, the ductility of the matrix gradually increases by unlocking of dislocations. Nevertheless, the strengthening effect by the fibers is hardly observed at 1073 K as shown in Fig. 6.12 (d). The load transfer efficiency is supposed to decrease due to the remarkable softening of matrix above 1000 K (c.f., Fig 3.18).

Continuous fiber reinforced NiAl matrix composites

The strengthening of NiAl alloys by the SiC fibers have been also tried in the present work. Figure 6.16 (b) shows the cross-sectional SEM micrograph of the Ni-45at%Al matrix composites. The fibers react with the Ni-45at%Al matrix in a similar manner with the Ni-24at%Al-0.1at%B matrix due to high activity of Ni in the alloy with Ni-rich composition [23].

The flexural strength of the Ni-45at%Al alloy and its matrix composites with 10 vol% SiC fibers at 300-1273 K is shown in Figs. 6.20 (a)-(e). The fibers are ineffective to improve the strength of NiAl below 773 K because NiAl fractures in a brittle manner in this temperature range. When the softening of the matrix occurs at 873-1073 K, the strengthening effect by the fibers is actualized. However, the fiber reinforcement does not provide significant strengthening even above high temperature range. The stress transfer efficiency across the fiber/matrix interfaces is reduced by remarkable softening of the matrix (c.f., Fig. 3.28).

In the early stage of the studies of intermetallic matrix composites, their strength was numerically simulated by the conventional theories [24]. However, these theories cannot always represent the actual mechanical properties of these composites because it ignores the characteristic mechanical behaviors of the matrix alloys. In composite material designs suitable for intermetallics, the matrix alloy designs must be considered as well as the control of interfacial reaction to suppress deterioration of fibers and to optimize cohesive strength.

In the case of NiAl matrix composites, the toughening by the fibers is also attractive theme, similar to the fiber reinforced ceramic matrix composites. In order to improve fracture resistance of NiAl alloys by the fibers, the matrix cracking must be induced prior to the fiber breakage [23]. The toughening of the alloys is expected to be achieved when the multiple fracture of the matrix occurs. For promoting the multiple fracture of the NiAl matrix alloys in the composites with ceramic fibers,

the maximum bearing load of fibers should be higher than the stress for matrix cracking. Therefore, the higher volume fraction of fibers with large diameter is desirable to promote the multiple fracture. Furthermore, the interfacial cohesion between the matrix and fibers should be weakened to easily induce the interfacial splitting. Unfortunately, the multiple fracture of NiAl matrix is not induced in the fiber reinforced composites in the present work.

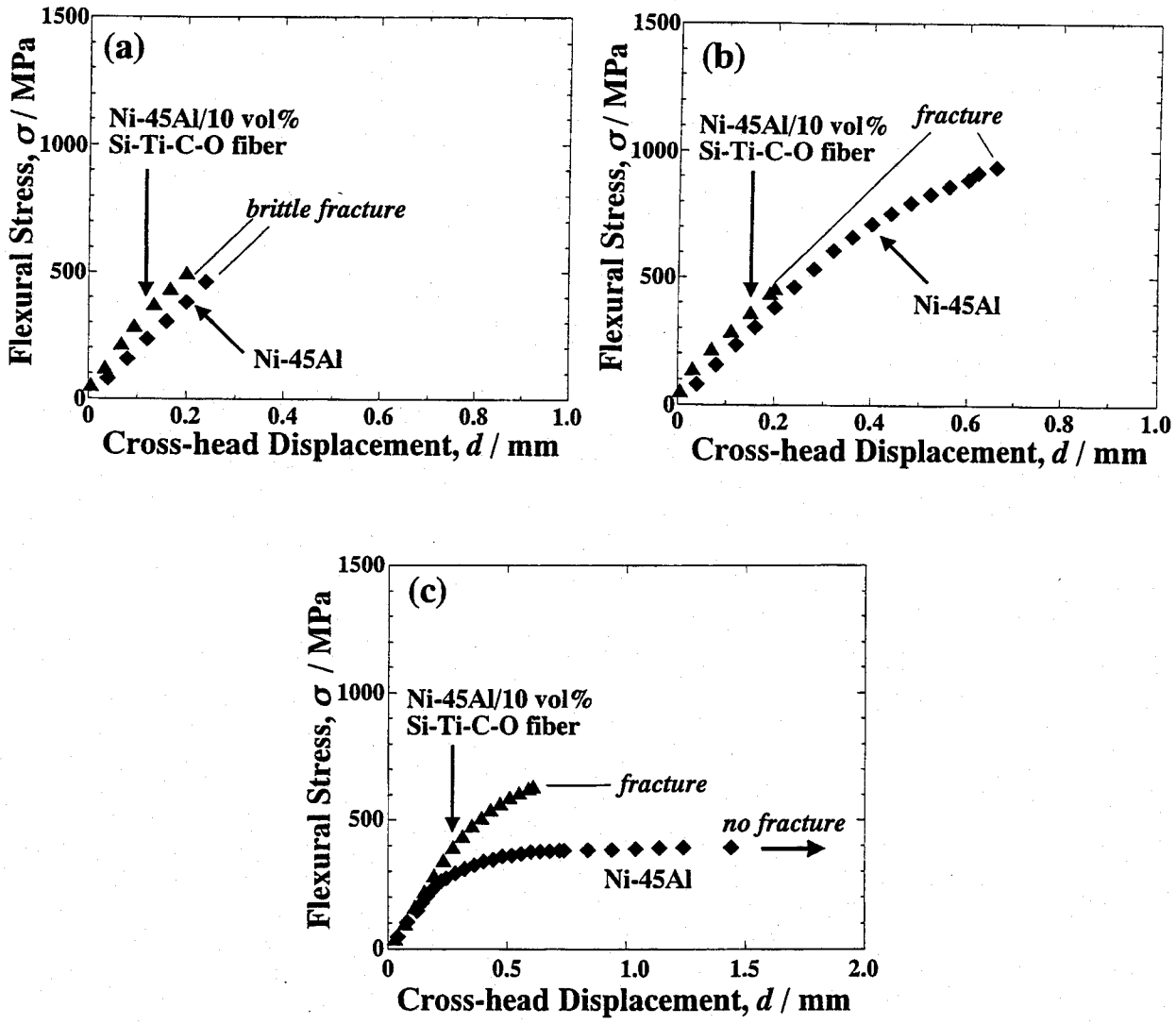

Fig. 6.20 Flexural strength of Ni-45at%Al matrix composites with 10 vol% SiC fibers at (a) 300, (b) 873, (c) 973, (d) 1073 and (e) 1273 K.

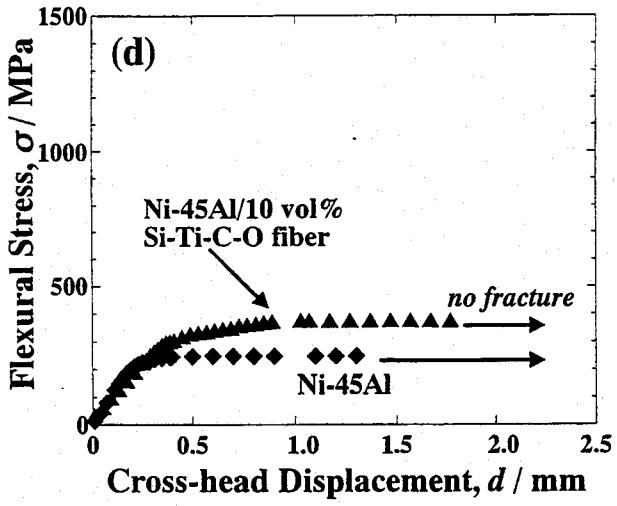

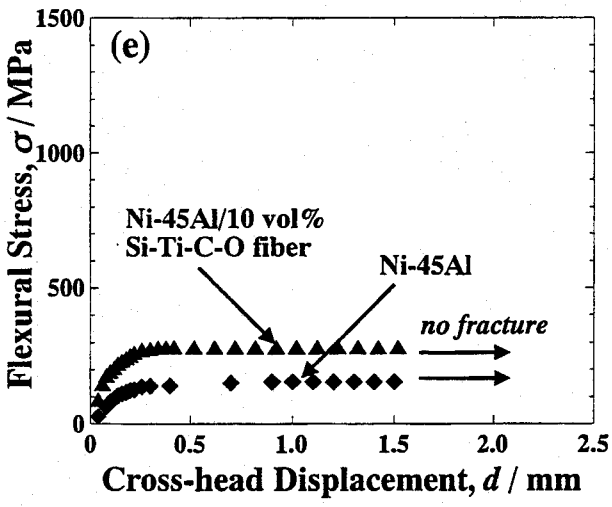

Fig. 6.20 *continued*

6-4 Conclusion

In this chapter, the mechanical properties of Ni_3Al and NiAl matrix composites fabricated by reactive hot-pressing were evaluated. The main results obtained in this chapter are briefly summarized as below:

Ni_3Al matrix composites

(1) The composites with TiC and TiN particles exhibit high strength at ambient temperatures rather than α-Al_2O_3 reinforced composites.

(2) The fracture toughness of the composites, except of TiC reinforced ones, is successfully improved by the B doping due to the enhancement of grain boundary cohesion and the suppression of the environmental embrittlement, as a similar manner to monolithic Ni_3Al alloys.

(3) The TiN composites exhibit higher ductility than the monolithic alloys at intermediate temperatures. However, their toughness in this temperature range is also governed by oxygen embrittlement, intrinsic degradation of grain boundary cohesion and unique dislocation motion. The toughness of the TiC composites is constant in the temperature range of 300-900 K.

(4) The composites with SiC continuous fibers exhibit high strength at ambient temperatures. However, there are some problems in their mechanical properties at intermediate and elevated temperatures.

NiAl matrix composites

(1) Ni-45at%Al composites with TiB_2 and ZrB_2 particles have high flexural strength with elastic-plastic deformation behavior at ambient temperatures.

(2) The yield strength above 800 K is successfully improved by the addition of 10 vol% TiB_2 particles.

(3) The strengthening effect by SiC continuous fibers is actualized only at 873-1073 K. The inherent brittleness of the matrix below 800 K is a serious problem in developing the continuous fiber reinforced composites with high performance.

References

[1] F. H. Froes, JOM, (9) (1989) 6

[2] D. B. Miracle, Acta Metall. Mater., 41 (1993) 649

[3] Y. Ohya, Y. Mishima, K. Yamada and T. Suzuki, *Tetsu-to-Hagane*, 70 (1984) 1879

[4] Analytical data from manufacturer (Nippon yttrium Co., Ltd.)

[5] C. T. Liu, C. L. White and J. A. Horton, Acta Metall., 33 (1985) 213

[6] E. P. George, C. T. Liu and D. P. Pope, Acta Mater., 44 (1996) 1757

[7] M. Sakai, J. Mater. Res., 8 (1993) 668

[8] M. Sakai, Ceramics Japan, 27 (1992) 281

[9] A. G. Evans, J. Am. Ceram.Soc., 73 (1990) 187

[10] J. Weertman, "Dislocation based fracture mechanics", World Scientific, Sigapore, (1996) pp.159

[11] G. S. Painter and F. W. Averill, Phys. Rev. B39, (1989) 7522

[12] A. K. Misra, NASA Contractor Report 4171 (1989)

[13] C. T. Liu and C. L. White, Acta Metall., 35 (1987) 643

[14] C. A. Hippsley and J. H. DeVan, Acta Metall., 37 (1989) 1485

[15] E. P. George and C. T. Liu, J. Mater. Res., 5 (1990) 754

[16] D. L. Yaney and W. D. Nix, J. Mater. Sci., 23 (1988) 3088

[17] J. Rösler and E, Arzt, Acta Metall., 38 (1990) 671

[18] E. Arzt, Acta Mater., 46 (1998) 5611

[19] E. Arzt and E. Göhring, Acta Mater., 46 (1998) 6575

[20] R. Behr, J. Mayer and E. Arzt, Scripta Mater., 36 (1997) 341

[21] T. Suzuki and H. Hosoda, JIM seminar "Intermetallic compounds", Jpn. Inst. Metals, Sendai, (1990), pp.17

[22] G. A. Cooper, Ch. 10, in: Composite Materials, vol. 5, Fracture and Fatigue, Academic Press, New York, (1974), pp. 415

[23] R. E. Hanneman and A. U. Seybolt, Trans. Metall. Soc. AIME, 245 (1969) 434

[24] G. Bao, F. Genna, J. Hutchinson and R. M. McMeeking, Mat. Res. Soc. Symp. Proc., vol. 194, (1990) 3

Chapter 7

Direct Surface Modification of TiAl Alloys by Reactive Plasma Processing

7-1 Introduction

The importance of extending material lifetime has been recognized as a means of efficiently using finite resources, as well improving mechanical properties. The surface treatment of metals and intermetallics is believed to be an important technique for extending material lifetimes. In the case of TiAl alloys, appropriate surface treatment is expected to suppress extrinsic damage, such as environmental embrittlement and high temperature oxidation, as well as improve heat and wear resistance [1]. Because the environmental effect is one of the most serious problems that prevents the utilization of TiAl alloys, the surface treatment can provide a breakthrough for structural applications of the alloys [2-3].

In this chapter, reactive plasma process is investigated as a novel processing for the direct surface modification of TiAl alloys. Nunogaki and his colleagues have already succeeded in carbonization and nitridation of Ti, Zr, Al, Fe and Ta surfaces by this plasma process which is performed using reactive plasma generated at low gas pressure [4-7]. In the present work, the surface modification of TiAl alloys by nitrogen plasma is investigated, because the ternary compounds in Ti-Al-N system have high melting points, hardnesses and wear resistancees, and oxidation resistancees (up to 1073 K) [8-11].

7-2 Reactive Plasma Processing

The apparatus is composed of a processing chamber and a source plasma chamber, as shown in Fig. 7.1. The source plasma is generated with penning ion gauge (PIG) discharge at gas pressure of 1-5 x 10^{-4} Torr. A direct current (DC) bias of a few kilovolts is applied between the diffused plasma and the sample (which acts as the cathode) in order to accelerate ions in the diffused plasma toward the sample. The sample holder can be heated to over 1000 K. This process has the following advantages in comparison with conventional ion nitriding processes; 1) specimens can be heated to above 1273 K independently of plasma production, 2) powerful micro wave plasma can be scaled up, and 3) homogeneous modified layer is formed, even on surfaces of complex shaped specimens. Moreover, in-situ composites, such as Ti/TiC whisker ones (Fig. 7.2), are successfully fabricated by

this plasma process as well as receiving surface modification, depending on the process conditions. A localized area of large mechanical components can be transformed to composite by this process to satisfy performance demands.

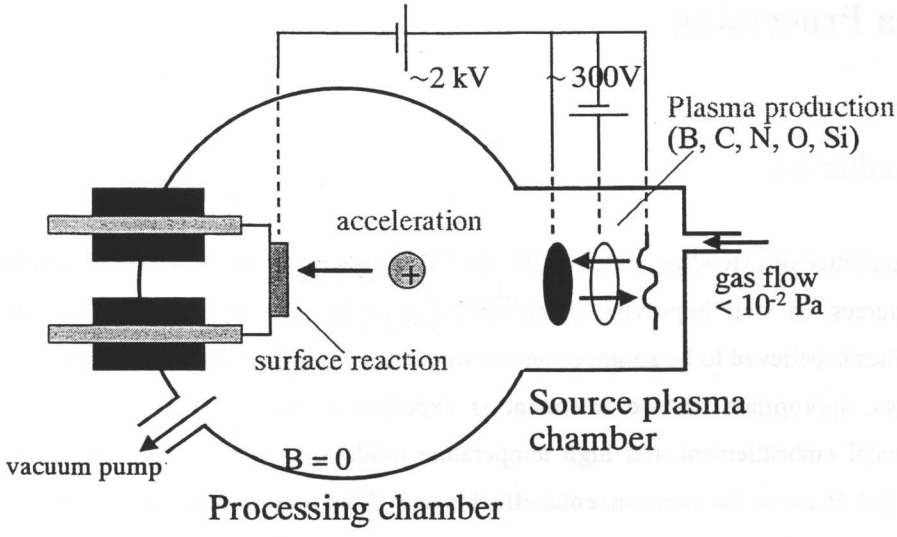

Fig. 7.1 Apparatus of reactive plasma process for direct surface modification of metals and intermetallics.

In this process, pre-treatment with ion and electron beams are effective in facilitating the formation of a modified layer by the subsequent surface reaction. For example, pre-implantation of Mo or Ti ions into an Al surface, which is naturally oxidized by air, effectively lowers the activation energy of nitrogen diffusion and promotes surface nitridation [6]. For nitriding Fe surface, the thickness of modified layers can be successfully controlled by pre-implantation of Ni ions [7]. Furthermore, the effect of pre-irradiation of electron beam is currently being investigated by Nunogaki and the present author [12].

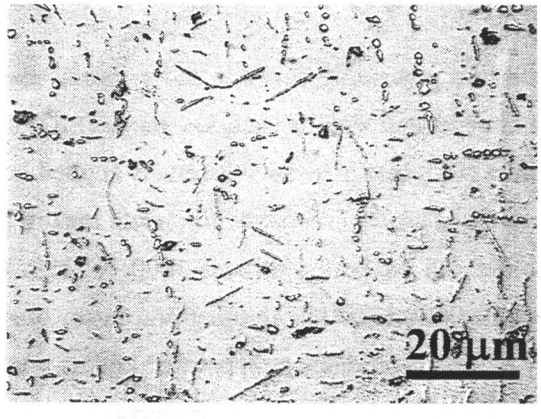

Fig. 7.2 Typical microstructure of Ti/TiC in-situ composite fabricated by reactive plasma process.

7-3 Experimental Procedure

TiAl plates of 5 mm x 8 mm x 1 mm in dimension fabricated by vacuum hot-pressing an alloy powder prepared by self-propagating high temperature synthesis (SHS) and subsequent mechanical crushing (Kyouritu ceramic materials Co., Ltd.), were nitrided at 1373 K for 2 h. The source plasma was generated by PIG discharge under gas pressure of 4.5×10^{-4} Torr ($N_2 : H_2 = 5 : 2$). The cross-sectional microstructure of the modified layer was observed by SEM. The polished surface was chemically etched with Kroll's reagent for SEM observation. The constituent phases of the layers were identified by XRD. An indentation test of the modified layers was conducted using a triangular indenter (tip angle : 68°) [13]. The relationship between the load and penetration depth of the indenter during loading-unloading process [13-14] was measured using an indentation system (MICRO ZONE TEST SYSTEM : MZT-4, Akashi). A load of up to 98 mN was applied at a loading rate of 49 mN sec^{-1}. After maintaining the maximum load for 5 sec, the load was removed at 49 mN sec^{-1}. The hardness was calculated by the following equation:

$$H = F / A = K \cdot F / h^2 \qquad (7\text{-}1)$$

where H, F, A, K, h are hardness (HUT[68]), maximum indentation load (mN), projected area of hardness impression, geometrical constant (2.972 for the present indenter) and maximum penetration depth (μm), respectively. Oxidation behavior was characterized by microstructural observations of the specimens after exposure in air at 1073-1273 K for 260 ksec.

In order to qualitatively consider the formation mechanism of the modified layers, the molecular orbitals around the interstitial N atoms in the ground state were simulated using several first principle algorithms. To estimate the lattice distortion by an interstitial N atom, the geometrical optimization of the eigenvector following method for the cluster models ($Ti_4Al_2N_1$ and $Ti_2Al_4N_1$) illustrated in Figs.7.3 (a) and (b), that represent interstitial atomic nitrogen (N) in the Ti and Al planes of the TiAl alloy, was conducted using a commercial program, namely $Dmol^3$ code, with a non-local density function of the generalized gradient approximation (GGA) (packaged in Cerius2, Molecular Simulation Inc.). In addition to the geometrical optimization, the total and binding energies of these cluster models were calculated with $Dmol^3$ code. By using the result of the geometrical optimization, the cluster models of the $Ti_{20}Al_{18}N_1$ and $Ti_{18}Al_{20}N_1$ (Figs. 7.4 (a) and (b)), which include the distortions by interstitial N atoms, were constructed for the DV-Xα simulation by a program, namely SCAT code [5-7]. Because the convergence to a self-consistent field was barely achieved for these large metallic cluster models by the $Dmol^3$ code, the DV-Xα method was adopted for the simulation of these models. The Mulliken population analysis was also performed by the SCAT code to obtain useful parameters to qualitatively discuss the bond nature, such as bond overlap

population and net charge. Furthermore, the DV-Xα simulation of the cluster model of the $Ti_{16}Al_8N_{27}$ shown in Fig. 7.5, that is extracted from the Ti_2AlN crystal, was conducted to understand the characteristics of chemical bonds in this ternary nitride. Madelung potentials were not arranged around the cluster models for the first principle simulations. The energy levels of the molecular orbitals are shifted to set the highest occupied orbital at zero.

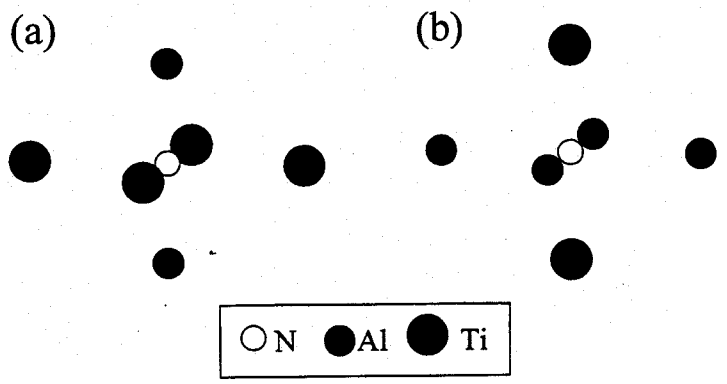

Fig. 7.3 Cluster models of (a) $Ti_4Al_2N_1$ and (b) $Ti_2Al_4N_1$ before geometry optimization by eigenvector following method.

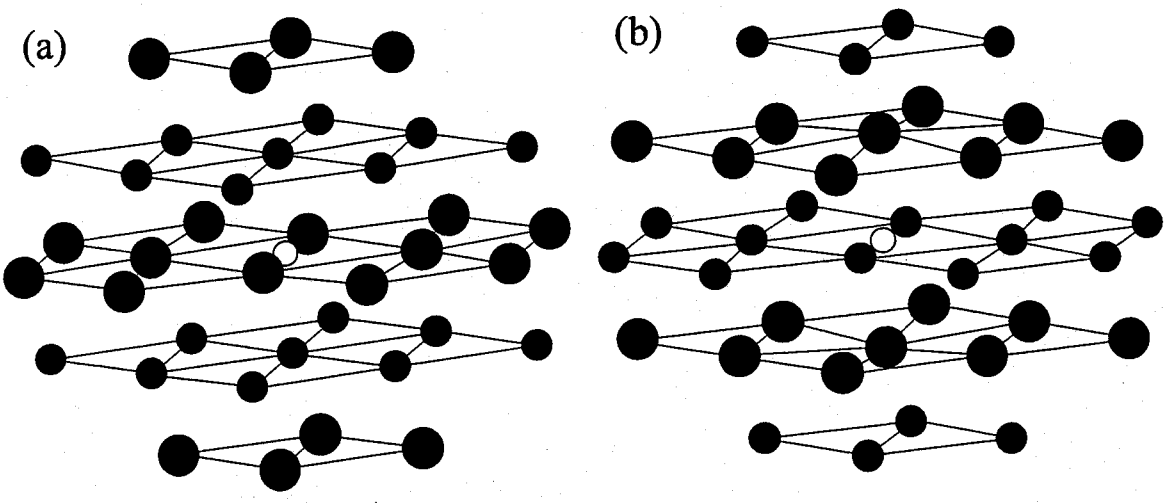

Fig. 7.4Cluster models of (a) $Ti_{20}Al_{18}N_1$ and (b) $Ti_{18}Al_{20}N_1$ including with lattice distortion of nearest neighbor Ti and Al atoms induced by N atom. Models (c) $Ti_{20}Al_{18}$ and (d) $Ti_{18}Al_{20}$ are referential clusters for the models (a) and (b), respectively.

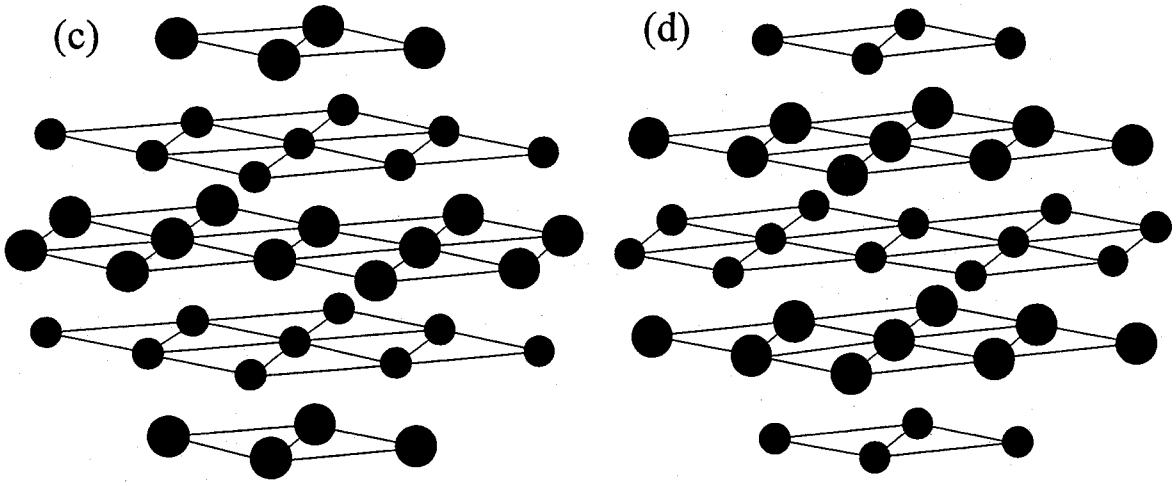

Fig. 7.4 *continued*

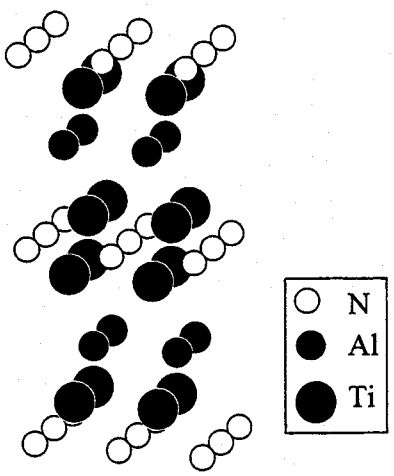

Fig. 7.5 Cluster model of $Ti_{16}Al_8N_{27}$ that is extracted from crystal structure of Ti_2AlN.

7-4 Results and Discussion

7-4-1 Structure and mechanical properties of nitrided layers

In Ti-Al binary system, the activity of constituent elements exhibits strong negative deviations from ideal solution behavior [15-16]. This negative deviation is indicative of substantial chemical interactions between these atoms in the alloys. Thus, the chemical reactivity of the alloy in respect to nitrogen plasma must be quite different from that of pure Ti due to the ordering of Ti and Al atoms by extensive inter-atomic interactions. Although TiAl alloys have relatively lower reactivities than Ti, surface modification of the alloys were successfully achieved by the reactive plasma process. Figure 7.6 shows a cross-sectional SEM micrograph of the modified layer on Ti-48at%Al alloy formed at 1373 K for 2 h. The modified layer consists of layers 1 and 2 that are formed on the TiAl alloy with lamella structure. The total thickness of the modified layer is ~10 μm.

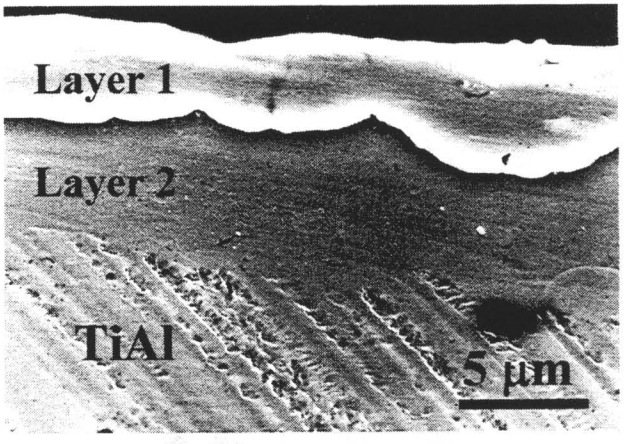

Fig. 7.6 Cross-sectional SEM micrograph of surface modified layers on TiAl alloy synthesized with nitrogen plasma at 1373 K for 2 h.

Figure 7.7 shows XRD patterns of a Ti-48at%Al specimen after surface treatment by reactive plasma process at 1373 K for 2 h. The specimen was composed of TiAl and Ti_3Al phases before surface treatment. As a result of exposure to nitrogen plasma, Ti_2AlN, AlN and TiN are formed on the surface of the alloy.

Figure 7.8 shows the loading-unloading profiles for the indentation test in layers 1 and 2, compared with the TiAl alloy. Table 7.1 summarizes their hardness and deformability as determined from the indentation test. Layer 1 is much harder than either layer 2 or the TiAl alloy. Layer 1 is

considered to be fully nitrided by the reactive plasma process. Although a minor degree of solution hardening is observed in the layer 2, it retains extensive ductility compared to layer 1. In general, Ti-Al-N coatings are fabricated by physical vapor deposition (PVD) because they have high melting point and excellent mechanical properties [9-11]. The PVD coating has a serious problem in that it exhibit exfoliation by thermal fatigue. The reliability of the cohesion between the TiAl alloy and the modified layers formed by the present plasma process is expected to be much higher than that of PVD coatings.

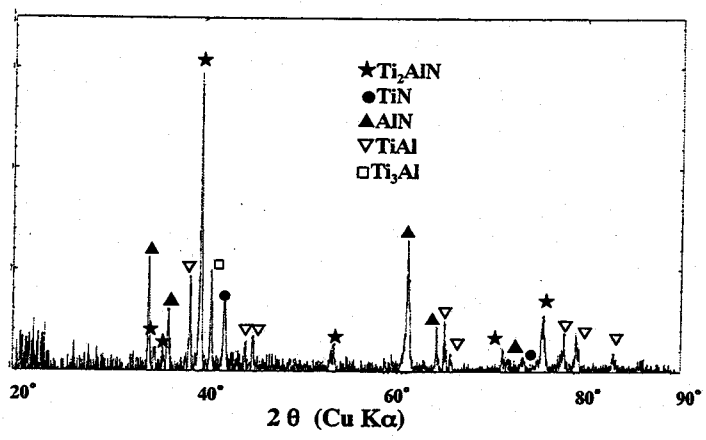

Fig. 7.7 XRD patterns of Ti-48at%Al alloy after reactive plasma process at 1373 K for 2 h.

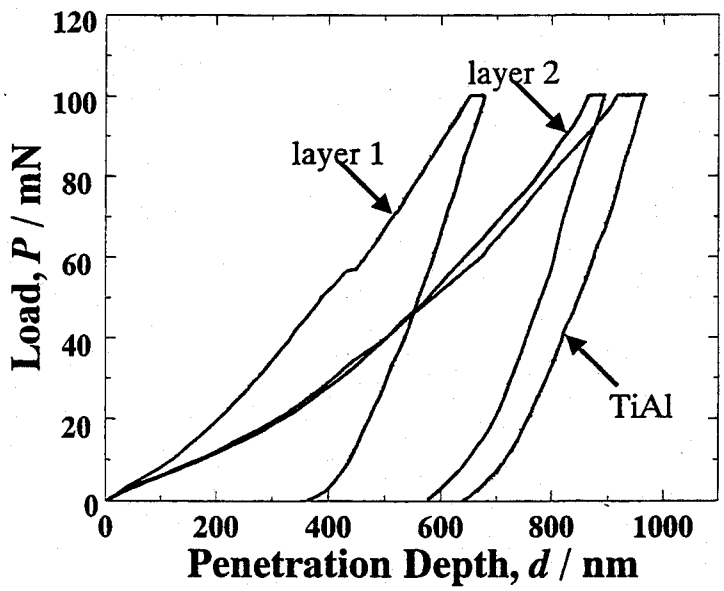

Fig. 7.8 Loading-unloading profiles during indentation test of TiAl alloy and layer 1 and 2 in Fig. 7.6.

Table 7.1 Results of dynamic indentation test with a triangular indenter (tip angle 68°)

	Hardness *	total deformation (nm)	plastic deformation (nm)	elastic recovery (%)	deformation during holding at 98 mN (nm)
layer 1	641	674	360	46.6	26
layer 2	359	901	573	36.4	30
TiAl alloy	313	964	638	33.8	50

* calculated by eq. (7-1)

7-4-2 Formation mechanism of Ti_2AlN layer

The formation process of the modified layers is briefly divided into three steps, i.e., 1) surface reaction, 2) diffusion of atomic nitrogen (N), and 3) rearrangement of the atomic configuration (formation of reaction product). In this plasma processing apparatus, the gas mixture of N_2 and H_2 was transformed to a reactive plasma using a PIG-type discharge, which is a type of radio frequency (RF) discharge utilizing a tandem motion of electrons with acceleration and deceleration between a hot tungsten filament and an anticathode at low gas pressure. This reactive plasma contained abundant ions and molcules (N^+, NH_3, etc) in excited states. The effective excitation of chemical species in the plasma results in decreasing the activation energy for diffusing N into the alloy. When the chemical potential of the N reaches a critical value in the alloy, the rearrangement of atomic configuration should occur to form Ti_2AlN.

In order to consider the formation mechanism of the Ti_2AlN, the chemical environments around the interstitial N in the TiAl were simulated by the quantum chemical algorithms. TiAl has an $L1_0$ type crystal structure that contains alternately-stacked Ti and Al planes in the direction of the c axis [1]. In the present simulation, the interstitial N atoms are arranged in these planes. As a result of geometrical optimization for the cluster models of the $Ti_4Al_2N_1$ and $Ti_2Al_4N_1$ (Figs. 7.3 (a) and (b)) by an eigenvector following method, an anisotropic distortion of the lattice is predicted to be induced by the interstitial N atoms. Due to the interstitial N atoms in the Ti plane, the nearest neighbor Ti and Al atoms are forced to be 11.60 and 0.61% further from the standard positions in TiAl, respectively

(Table 7.2 (a)). However, the interstitial N atoms in the Al plane forces nearest neighbor Al and Ti atoms to be 5.38 and 8.17 % further from the standard positions in TiAl, respectively (Table 7.2 (b)).

Table 7.2 Results of geometry optimization and total energy calculation of (a) $Ti_4Al_2N_1$ and (b) $Ti_2Al_4N_1$ clusters. (c) total energy of the clusters and isolated atoms calculated by Dmol[3] code.

(a) cluster model : $Ti_4Al_2N_1$

	bond	interatomic distance (nm)	binding energy (eV)	total energy (eV)
initial	N-Ti	0.19995		
	N-Al	0.20400		
optimized	N-Ti	0.22214	-53.94	-1.072×10^5
	N-Al	0.20525		

(b) cluster model : $Ti_2Al_4N_1$

	bond	interatomic distance (nm)	binding energy (eV)	total energy (eV)
initial	N-Al	0.19995		
	N-Ti	0.20400		
optimized	N-Al	0.21070	-42.56	-7.413×10^4
	N-Ti	0.22067		

(c)

models	Ti_4Al_2N	Ti_2Al_4N	Al	Ti
total energy ($\times 10^3$ eV)	-107.71783	-74.13131	-6.59841	-23.12130

To briefly estimate the relative energetic difference between these atomic configurations, the following reactions are assumed;

$$4\,Ti + 4\,Al + N \rightarrow Ti_4Al_2N_1 + 2\,Al \qquad (7\text{-}2)$$
$$4\,Ti + 4\,Al + N \rightarrow Ti_2Al_4N_1 + 2\,Ti \qquad (7\text{-}3)$$

where Al, Ti and N are the isolated atoms. Thus, the energetic stability of these clusters can be compared by the following formula;

$$Ti_4Al_2N_1 + 2\,Al \rightarrow Ti_2Al_4N_1 + 2\,Ti \qquad (7\text{-}4)$$

The total energies of $Ti_4Al_2N_1$, $Ti_2Al_4N_1$, Al, Ti are shown in Table 2. Thus, the energetic difference in the reaction (7-4) is estimated

$$\Delta E_{total} = \{E(Ti_2Al_4N_1) + 2\,E(Ti)\} - \{E(Ti_4Al_2N_1) + 2\,E(Al)\} = 1.24\ eV \qquad (7\text{-}5)$$

Therefore, the atomic configuration in the $Ti_4Al_2N_1$ cluster is more stable than that in the $Ti_2Al_4N_1$ cluster. Although the precise estimation of defect energies, which is based on the total energy of crystal using a model with periodical boundary condition, is necessary to discuss the stability of defect structures, the stable atomic configuration for the interstitial N atoms is briefly inferred by the above consideration. The interstitial N atoms in the Ti planes are expected to be more stable than those in the Al planes.

Based on these calculation results, the cluster models of $Ti_{20}Al_{18}N_1$ and $Ti_{18}Al_{20}N_1$, which include the geometrically optimized clusters of $Ti_4Al_2N_1$ and $Ti_2Al_4N_1$ as a central unit, are constructed as shown in Figs. 7.4 (a) and (b). To obtain qualitative information about the chemical bonds, the DV-Xα simulation of these models was conducted with and without interstitial N atoms in the $Ti_{20}Al_{18}$ and $Ti_{18}Al_{20}$ (Figs. 7.4 (a)-(d)).

Figures 7.9 (a) and (b) show the bond overlap population and net charge in the cluster models of $Ti_{20}Al_{18}$ and $Ti_{20}Al_{18}N_1$ respectively, which represents the interstitial N atoms in the Ti plane. The net charge values indicate significant charge transfer to N atom from neighbor Ti and Al atoms. In addition to the charge transfer, the covalent bond strength of the Al-Ti and Ti-Ti bonds, which is in proportion to the bond overlap population, decreases with interspersing N atom. Figure 7.10 (b) shows the overlap population diagram for the chemical bonds of N atom with first nearest neighbor Ti and Al atoms for the $Ti_{20}Al_{18}N_1$ cluster model. By comparison with the results of the population analysis illustrated in Fig. 7.10 (a), the atomic orbital components that contribute to forming these chemical bonds can be deduced. The Ti-N bonds have a relatively low bond overlap population due

to the lack of bonding components from Ti3d orbitals, although the N2p components significantly contribute to bonding characteristics. However, the net charge of the N and Ti atoms indicates that the stability of the Ti-N bonds in the Ti planes is compensated by the strong ionic attractive interaction between these atoms. In contrast, the chemical bonds of the N atom with neighbor Al atoms exhibit significant covalency that is originated from hybridization of the sp components.

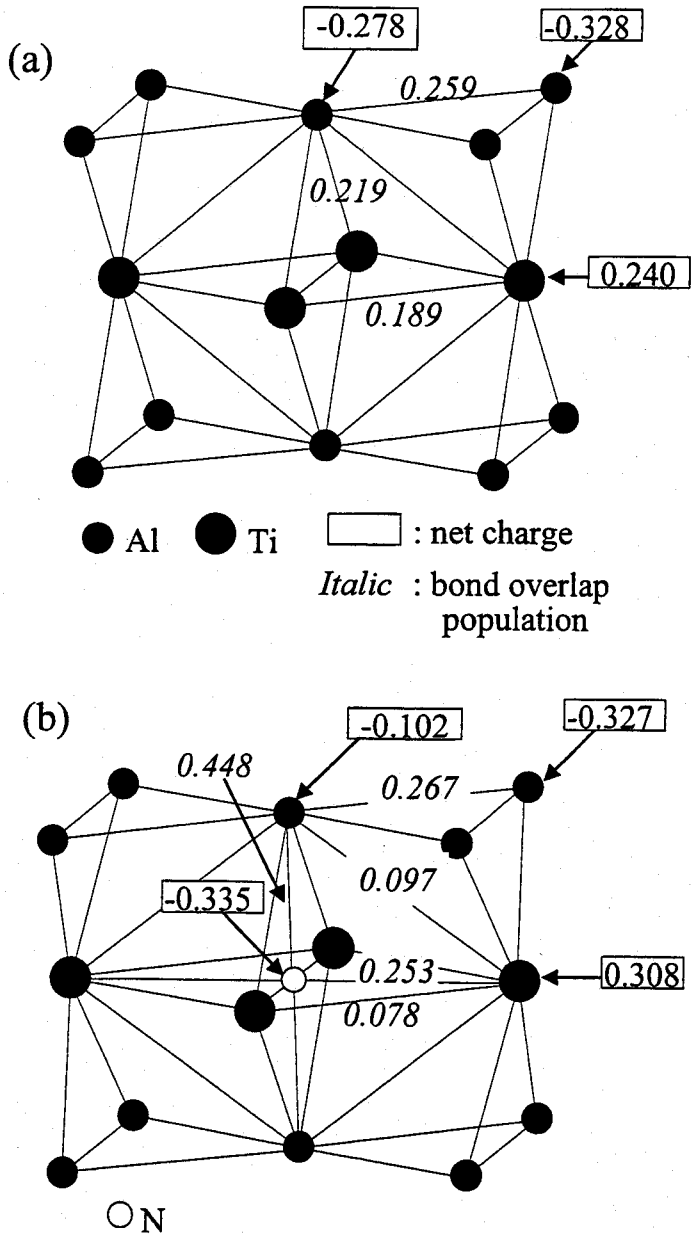

Fig. 7.9 Bond overlap population and net charge in central units of (a) $Ti_{20}Al_{18}$ and (b) $Ti_{20}Al_{18}N_1$ cluster models.

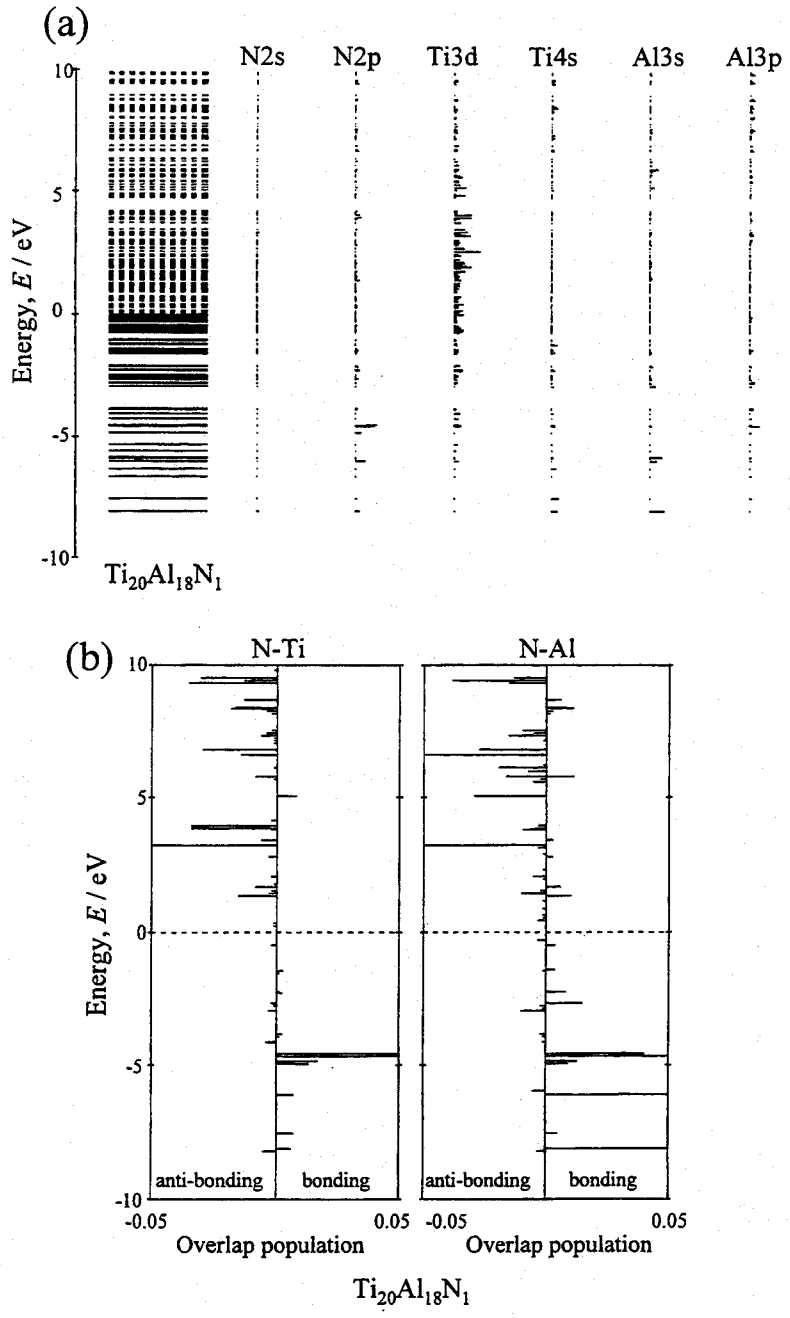

Fig. 7.10 (a) Energy level diagram and population analysis of $Ti_{20}Al_{18}N_1$ cluster model, (b) overlap population diagram for N-Ti and N-Al bonds.

Figures 7.11 (a) and (b) show the bond overlap population and net charge in the clusters of $Ti_{18}Al_{20}$ and $Ti_{18}Al_{20}N_1$, which represents the interstitial N atoms in the Al plane. In this situation, the charge transfer to N atom mostly occurs from neighboring Al atoms. Moreover, the covalent bond strength of the Al-Al and Al-Ti bonds is reduced by the N atom. Figure 7.12 (b) shows the overlap population diagram for the chemical bonds of the N atom with first nearest neighbor Al and Ti atoms

of the $Ti_{18}Al_{20}N_1$ cluster model. Although the characteristics of chemical bonds in this model are analogous to that in the $Ti_{20}Al_{18}N_1$ cluster model, two different features are clarified by the results of this calculation. One is insufficient ionic attraction for compensating for the low bond overlap population between the N and Ti atoms. The other is the anti-bonding interactions that create energy levels with anti-bonding characteristics on the highest occupied level. In this atomic configuration, the contribution of anti-bonding components is much larger than that in the $Ti_{20}Al_{18}N_1$ model. The anti-bonding components are also considered to be one of the factors for energetic destabilization.

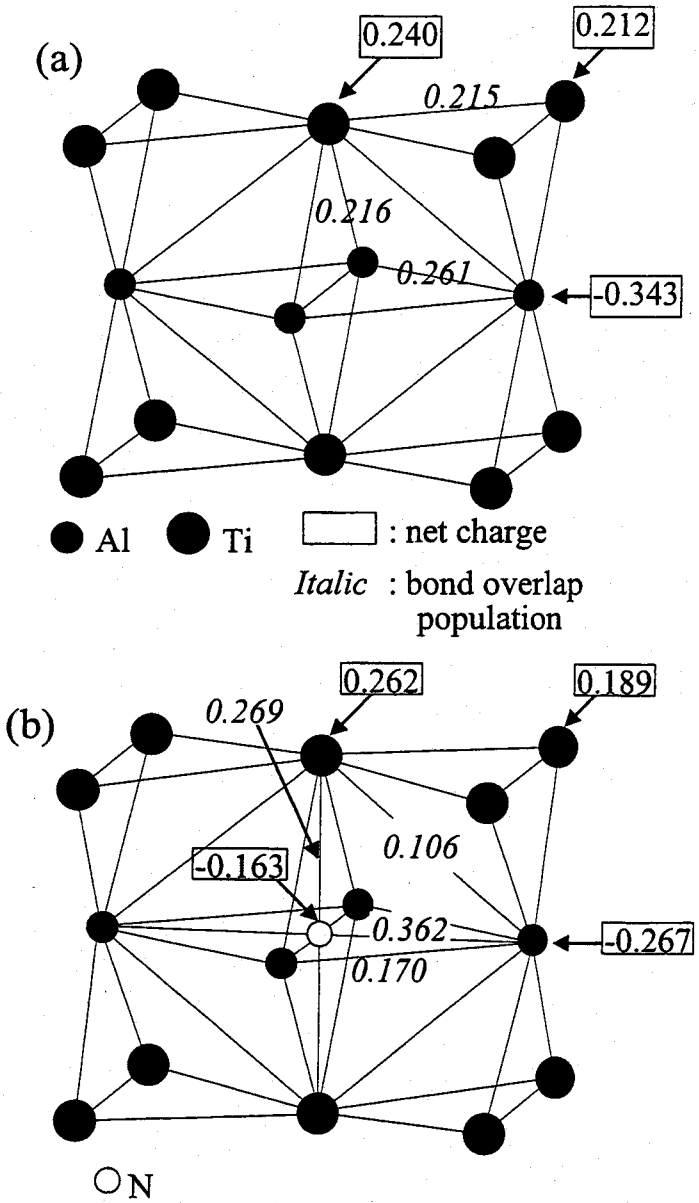

Fig. 7.11 Bond overlap population and net charge in central units of (a) $Ti_{18}Al_{20}$ and (b) $Ti_{18}Al_{20}N_1$ cluster models.

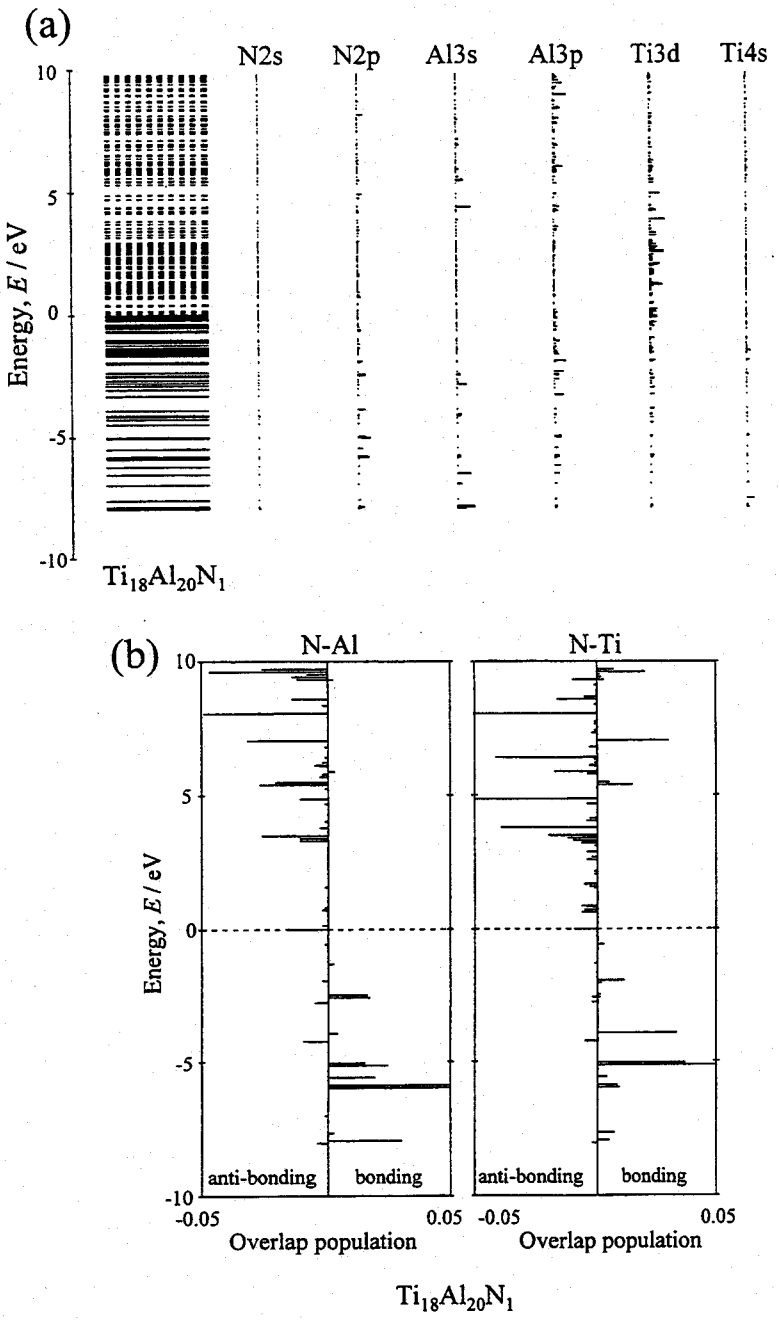

Fig. 7.12 (a) Energy level diagram and population analysis of $Ti_{18}Al_{20}N_1$ cluster model, (b) overlap population diagram for N-Ti and N-Al bonds.

Although the rearrangement process of atomic configuration to form Ti_2AlN cannot be wholly explained only by local atomic interactions, it is likely to be based on these characteristic chemical interactions between the interstitial N and neighbor atoms. Figure 7.13 shows the results of the DV-Xα simulation for the $Ti_{16}Al_8N_{27}$ cluster model that is constructed from the crystal structure of Ti_2AlN. To simply understand the characteristics of the chemical bonds, Fig. 7.13 only shows the

results of a central unit in the cluster model. The result of population analysis for the $Ti_{16}Al_8N_{27}$ cluster model shows that the covalent bonds are not formed between neighboring N atoms. The Coulomb repulsive interaction is also induced between these N atoms. Hence, the atomic configuration of the N atoms is determined by competition between the ionicity of the Ti-N bonds and the covalency of the Al-N bonds in the TiAl alloy, but not clustering of N atoms.

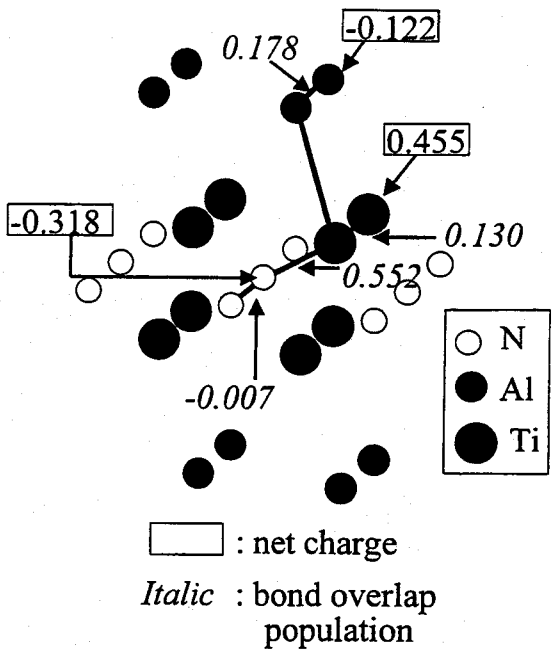

Fig. 7.13 Results of molecular orbital simulation for $Ti_{16}Al_8N_{27}$ cluster. A central unit of the cluster model is only indicated in this figure.

The net charge of neighboring Ti and N atoms in the $Ti_{16}Al_8N_{27}$ cluster indicates significant charge transfer from Ti atoms to N atoms. The strong covalent bonds can be formed between the Ti and N atoms because of the high bond overlap population, as well as the Coulomb attractive force. Therefore, the strong Coulomb attractive interaction between the Ti and N atoms is inferred to play an important role in rearranging the atomic configuration from TiAl to Ti_2AlN, rather than the strong covalency between Al and N atoms. The stability of the $Ti_4Al_2N_1$ cluster suggests that the interstitial N atoms in the Ti planes of TiAl contribute to rearrange the atomic configuration rather than those in the Al plane. Therefore, the interstitial N atoms in the Ti planes are expected to make a predominant contribution for forming Ti_2AlN lattice. After the rearrangement of atomic configuration, the strong covalency is created between Ti and N atoms, as well as the ionic attractive interaction.

7-4-3 Oxidation behavior at elevated temperatures

The ternary compounds in Ti-Al-N system sufficiently have excellent oxidation resistance up to ~1073 K [10]. The oxidation behavior of the nitrided specimens was examined at 1073-1273 K. Figure 7.14 (a) shows cross-section of a specimen after oxidation at 1073 K for 260 ksec. The modified layer exhibits significant oxidation resistance at this temperature. However, the specimens with surface nitridation irreparably damaged by high temperature oxidation at 1273 K for 260 ksec, as shown in Fig. 7.14 (b). The oxidation behavior seems to already enter into the final stage [17-18]. The oxidation resistance of the nitrided layers is limited to 1100 K.

Yoshihara et. al. [2] clarified the effectiveness of heat treatment at low oxygen pressure for the formation of Al-rich oxide scale on TiAl surface. They performed low pressure oxidation after the synthesis of a $TiAl_3$ surface layer by Al penetration. The oxidation resistance is successfully improved by this complicated process. However, the extensive cracking was often observed in the surface modified layer due to the brittleness of $TiAl_3$. The author considers that the surface oxidation by the reactive plasma process is expected to be useful for forming the Al-rich oxide scale at low temperatures without the need for such a complicated process [19]. The reactive plasma oxidation is expected to provide even better oxidation resistance in combination with electron and ion beam pre-irradiation.

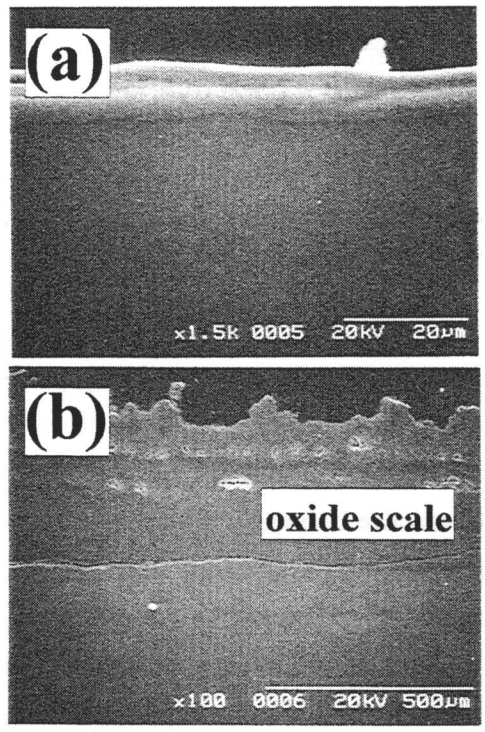

Fig. 7.14 Cross-sectional SEM micrographs of the alloys with surface nitridation after the oxidation at (a) 1073 and (b) 1273 K for 260 ksec.

7-5 Conclusion

The surface nitrided layers of Ti-48at%Al alloys as fabricated by the reactive plasma process were characterized by SEM and XRD. Their mechanical and oxidation behaviors were also investigated. The results obtained in this work are summarized below:

(1) A modified layer consisting of Ti_2AlN, AlN and TiN can be successfully synthesized on the surface of Ti-48at%Al alloys.

(2) The rearrangement of atomic configuration to form Ti_2AlN is predominantly governed by the strong attractive ionicity between Ti and interstitial N atoms in TiAl alloys.

(3) The hardness of the surface layer is much higher than the sub-surface modified layer and the TiAl matrix.

(4) Because the sub-surface layer retains extensive ductility, the modified layers seems to retain sufficiently reliable adhesion with the alloys.

(5) The oxidation resistance of the nitrided layers is limited to 1100 K. To further improve the oxidation resistance, which is desirable, Al-rich oxide scale can be fabricated by exposure to oxygen plasma, instead of nitrogen plasma.

References

[1] G. H. Meier, Oxidation of Intermetallics, ed. by H. J. Grabke and M. Schutze, Wiley-VCH, (1997) 15

[2] M. Yoshihara, T. Suzuki and R. Tanaka, *Tetsu-to-Hagane*, 77 (1991) 274

[3] H. Kawaura, K. Nishino and T. Saito, J. Japan Inst. Metals, 63 (1999) 1584

[4] M. Nunogaki, Y. Susuki, K. Kitahama, Y. Nakata, F. Hori, R. Oshima and S. Emura, Proc. Mat. Res. Soc. Symp., vol.551, 303 (1999)

[5] M. Nunogaki, Y. Susuki, and A. Ohmura, Materials and Design, *in press*

[6] M. Nunogaki, H. Suezawa and K. Miyazaki, Vacuum, 39 (1989) 281

[7] M. Nunogaki, H. Suezawa, S. Nishijima and T. Okada, Proc. Int. Conf. On Evolution in Beam Applications, (1991) 108

[8] K. Zeng, R. S. Fetzer, Thermodynamics of Alloy Foramation, TMS, (1997) 275

[9] J. C. Schuster and J. Bauer, J. Solid State Chem., 53 (1984) 260

[10] T. Ikeda and H. Saito, Thin Solid Films, 195 (1991) 99

[11] S. Inamura, K. Nobugai and F. Kanamaru, J. Solid State Chem., 68 (1987) 124

[12] M. Nunogaki, M. Inoue and K. Kitahama, Proc. 2nd COE Symp. on Atomic Scale Processing and Novel properties in Nanoscopic Materials, ISIR, Osaka University (1999) 75

[13] W. C. Oliver and G. M. Pharr, J. Mater. Res., 7 (1992) 1564

[14] G. M. Pharr and R. F. Cook, J. Mater. Res., 5 (1990) 847

[15] J. H. Norman, G. H. Reynolds and L. Brewer, Mat. Res. Soc. Sym. Proc., vol.194 (1990) 369

[16] M. Eckert and K. Hilpert, in ref.1, 239

[17] F. Dettenwanger, E. Schumann, J. Rakowski, G. H. Meier and M. Ruhle, in ref. 1, 265

[18] W. J. Quadakkers, P. Schaaf, N. Zheng, A. Gil and E. Wallura, in ref. 1, 276

[19] M. Inoue, M. Nunogaki and K. Suganuma, Proc. 7th Japan International SAMPE Symp., *in press*

Chapter 8

Remarks and Conclusion

This thesis deals with processing and mechanical characterization of transition metal aluminides and their matrix composites. The aluminide matrix composites reinforced with several ceramic particles and fibers were successfully developed based on the scientific knowledge about the reactive synthesis mechanism and the interfacial reactivity at bi-material interfaces. Furthermore, a novel surface modification technique for extending lifetime of intermetallic based materials was proposed. The contents of the present work are summarized below:

In Chapter 1, the background and objectives of the present thesis were described as the general introduction.

In Chapter 2, the author had clarified the reactive synthesis and consolidation mechanisms of Ni and Fe aluminides by reactive hot-pressing and infiltration processes. The reactive synthetic processes discussed in this thesis will be useful to realize various types of material designs which cover from nano- to mezzo-scale for intermetallics.

In Chapter 3, the mechanical properties of Ni_3Al, NiAl and FeAl alloys fabricated by reactive hot-pressing were investigated at 300-1273 K in several environments. Their mechanical behaviors were found to be governed by intrinsic and extrinsic (environmental) factors. For example, the ductilization of Ni_3Al alloys at ambient temperatures by B doping is originated from enhancement of grain boundary cohesion and suppression of moisture induced embrittlement. However, the ductilization predominately relates to the grain boundary strengthening. The Ni_3Al alloys exhibit another embrittlement phenomenon, which is caused by extrinsic (oxygen embrittlement) and intrinsic effects, at intermediate temperatures. Moreover, the alloys reveal significant softening above 1100 K by grain boundary sliding and dynamic recrystallization.

The strength of NiAl alloys strongly depends on the alloy composition (defect strengthening). Although the alloys are intrinsically brittle at ambient temperatures, their strength drastically decreases above 800 K due to remarkable softening. On the other hand, FeAl alloys inherently have extensive ductility by <111> slip deformation though they have same crystal structure as NiAl alloys. While the B doping is effective to suppress the environmental embrittlement of FeAl alloys, their

intrinsic toughness cannot be improved by the doping. The alloys exhibit remarkable plastic deformability by dislocation creep above 700 K.

In Chapter 4, the interfacial reactivity between these aluminides and several ceramics was analyzed by both theoretical and experimental investigations. As the results of these investigation, the candidate materials for the reinforcements were selected.

Chapters 5 and 6 described the mechanical behaviors of Ni and Fe aluminide matrix composites with ceramic fine particles and fibers. Their mechanical behaviors are briefly summarized below:

1) fine particle composites

The yield strength of the composites with ceramic particles was improved up to 1.5 times above that of the monolithic alloys by the dislocation pinning effect. Remarkable strengthening was exceptionally attained in some systems such as FeAl/SiC, Ni_3Al/TiC and Ni_3Al/TiN. In these cases, the effect of dissolution of constitutional elements into the matrix seems to predominate to the dispersion strengthening by the particles at ambient temperatures. The mechanical behavior of the composites with 5-10 vol% particles is considerably governed by characteristic fracture mechanism of the matrix.

2) fiber composites

The composites reinforced with unidirectionally oriented continuous fibers exhibit the largest strengthening effect when the load direction is parallel to the fiber axis. The load bearing effect of the fibers is most important mechanism in strengthening due to wide inter-fiber spacing in these composites. In this case, the ultimate strength of the composites strongly depends on ductility of the matrix. If the matrix alloy has extensive ductility, the fibers provide significant strengthening through the multiple fracture behavior. On the contrary, the composites simultaneously fracture with the fiber cracking when the matrix is too brittle. Therefore, the ductile matrix is suitable to develop the composites with high strength and reliability. Moreover, their mechanical behavior is synergically influenced by the alloying elements in the matrix alloys. The alloying of B is effective to improve the fracture resistance of the matrix. Although solution strengthening of the matrix is effective for strengthening the composites, their strength contrary decreases by excess matrix strengthening.

The composites with random oriented discontinuous fibers (whiskers and short fibers), except of FeAl/SiC whisker composites, are relatively inadequate for strengthening intermetallics. Their strength decreases with increasing temperature due to significant interface sliding, even in the continuous fiber reinforced ones. These problems are expected to be overcome by novel composite

design with a skeleton structure of reinforcements.

In Chapter 7, the reactive plasma process was proposed as a surface modification technique for lifetime extension. As a typical example of this process, the direct surface modification of TiAl alloys was successfully achieved by this plasma process.

Intermetallics are believed to be one of the leading materials for aerospace and automobile industries on the 21st century. The author hopes that the design concept proposed in this thesis will be useful in the future for material scientists and engineers who study intermetallics and their related materials.

List of Publications

1) M. Inoue and K. Suganuma : Reactive sintering behavior of intermetallic compounds in Ni-Al system, J. Japan Inst. Light Metals, **44** (1994) 658-662 (*in Japanese*)

2) M. Inoue and K. Suganuma : Microstructure of in-situ reaction formed Ni aluminides by squeeze casting, J. Japan Inst. Light Metals, **45** (1995) 209-213 (*in Japanese*)

3) M. Inoue and K. Suganuma : Mechanical properties of Ni-Fe-Al ternary alloys and their matrix composites, J. Japan. Soc. Powder and Powder Metallurgy, **42** (1995) 1258-1263 (*in Japanese*)

4) M. Inoue, K. Komatsu, K. Kudoh and K. Suganuma : Fabrication of discontinuous ceramic fibers/ FeAl composites by reactive sintering, J. Japan Inst. Metals, **59** (1995) 1185-1191 (*in Japanese*)

5) M. Inoue, Y. Itoh and K. Suganuma : Fabrication condition of FeAl by reactive sintering and squeeze casting processes, J. Japan Inst. Light Metals, **46** (1996) 327-333 (*in Japanese*)

6) M. Inoue, H. Watanabe, K. Niihara and K. Suganuma : Synthetic processes of uniform nickel aluminides by reactive infiltration and post hot-pressing of infiltrated precursors, Materials Letters, **34** (1998) 55-59

7) M. Inoue, K. Takahashi, K. Suganuma and K. Niihara : Effects of boron doping on fracture properties of Ni_3Al matrix composites with ceramic particles, Scripta Mater., **39** (1998) 887-892

8) M. Inoue, K. Suganuma and K. Niihara : Fracture properties of Fe-40at%Al alloys fabricated by reactive hot-pressing, Scripta Mater., **39** (1998) 1477-1482

9) M. Inoue, H. Nagao, K. Suganuma and K. Niihara : Fracture properties of Fe-40at%Al matrix composites reinforced with ceramic particles and fibers, Mater. Sci. and Eng. **A258**, (1998) 298-305 (*invited paper*)

10) M. Inoue, K. Suganuma and K. Niihara : Toughening mechanism of Ni_3Al alloys by B doping, J. Mater. Sci. Lett., **17** (1998) 1967-1969

11) M. Inoue, K. Suganuma and K. Niihara : Fracture mechanism of FeAl matrix composites with discontinuous reinforcements, Mater. Sci. and Eng. **A265** (1999) 240-245

12) M. Inoue, K. Suganuma and K. Niihara : Fracture mechanism of Ni_3Al alloys and their composites with ceramic particles at elevated temperatures, Intermetallics, **8** (2000) 365-370

13) M. Inoue, K. Suganuma and K. Niihara : Mechanical properties of aluminide matrix composites fabricated by reactive hot-pressing in several environments, Intermetallics, **8** (2000) 1035-1042

14) M. Inoue, K. Suganuma and K. Niihara : Environmental effect on mechanical properties of

aluminide matrix composites, J. Mater. Eng. Perform., **9** (2000) 678-682

15) M. Inoue, M. Nunogaki and K. Suganuma: Chemical reaction of TiAl intermetallics with a nitrogen plasma, J. Solid State Chemistry, **157** (2001) 339-346

(proceedings)

1) M. Inoue, K. Suganuma and K. Niihara : Mechanical behavior of reactively hot-pressed aluminide matrix composites, Mat. Res. Soc. Symp. Proc., vol.460 (1997) 755-759

2) M. Inoue, K. Suganuma and K. Niihara : Microstructure and mechanical properties of reactive-hot-pressed nickel aluminide matrix composites, Proc. 5th Japan International SAMPE Symp. (1997) 469-474

3) M. Inoue, K. Suganuma and K. Niihara : Strength and fracture behavior of aluminide matrix composites with ceramic fibers, Mat. Res. Soc. Symp. Proc., vol. 552 (1999) KK8.24.1-5

4) M. Inoue, K. Suganuma and K. Niihara : Mechanical behaviors of nickel aluminides and their composites at elevated temperatures, Proc. 6th Japan International SAMPE Symp. (1999) 477-480

5) M. Inoue and M. Nunogaki : Microstructural observation of cermets transformed from metals by reactive plasma processing, Proc. 6th Japan International SAMPE Symp. (1999) 428-431

(supplementary publications)

1) M. Inoue, J-Y. Kim, Z. Kato, N. Uchida, K. Uematsu, K. Saito : Development of direct observation method for internal structure in silicon nitride granule and green body, Trans. Mat. Res. Soc. Jpn., **1** (1991) 192-199

2) J.-Y. Kim, M. Inoue, Z. Kato, N. Uchida, K. Saito, K. Uematsu : Direct observation of internal structure in spray-dried yttria-doped zirconia granule, J. Mater. Sci., **26** (1991) 2215-2218

3) M. Inoue, A. Nakahira and K. Niihara : Sintering mechanism of Al_2O_3/SiC nanocomposites, J. Japan Soc. Powder and Powder Metallurgy, **39** (1992) 484-487 (*in Japanese*)

4) J.-Y. Kim, M. Miyashita, M. Inoue, N. Uchida, K. Saito, K. Uematsu : Characterization of internal

structure in Y-TZP powder compacts, J. Mater. Sci., **27** (1992) 587-591

5) T. Kotani, M. Inoue and K. Niihara : An analytic procedure for evaluating grain-size and grain-aspect-ratio distribution in polycrystalline sintered bodies based on Monte Carlo simulation, J. Ceram. Soc. Japan, **100** (1992) 1235-1238 (*in Japanese*)

6) M. Inoue, M. Yoshimoto, H. Ohkubo and H. Koinuma : Nonstoichiometry control and carrier doping of infinite-layer cuprate films, Trans. Mat. Res. Soc. Jpn., **19A** (1994) 505-508

7) H. Kitayama, M. Inoue and K. Niihara : Effects of adsorbed species on microstructure and mechanical properties of Al_2O_3, Ceramic Transactions, **44** (1994) 435-443

8) K. Suganuma, M. Inoue, K. Nagatomo and N. Tanaka, Fabrication of SiC whisker preform with γ-Al_2O_3 fine powder binder and its 6061 aluminum alloy matrix composites, J. Japan Inst. Light Metals, **45** (1995) 150-155 (*in Japanese*)

9) K. Sakamoto, A. Nakahira, M. Okazaki, J. Ichihara, M. Inoue and S. Yamaguchi : Shape-controlled synthesis of hydroxyapatite in organic media, Mat. Res. Soc. Symp. Proc., vol. 519 (1998) 407-411

10) M. Ueshima, T. Oku, M. Inoue, K. Tanihata, M. Takahashi and K. Suganuma : Microstructure and Fracture Strength of TiN/Al and Al Alloys Interface, Key Engineering Materials, **164-163** (1999) 667-670

11) T. Matsumoto, M. Okazaki, M. Inoue and J. Takahashi : Role of amino acids in the regulation of crystallinity of hydroxyapatite, Bioceramics, **12** (1999) 365-368

12) K. Sakamoto, M. Okazaki, J. Takahashi, T. Matsumoto, A. Nakahira, S. Yamaguchi and M. Inoue : Bioactive bone cements of calcium phosphate-mono (methacryloyloxyethyl) acid phosphate composite, Bioceramics, **12** (1999) 541-544

13) H. Abe and M. Inoue : Pattern formation associated with kinetics of martensitic transformation in an Au-47.5at%Cd alloy, Memories of National Defense Academy, Japan, vol. **40**, No. 2 (2001) pp.1-8

14) T. Matsumoto, M. Okazaki, M. Inoue, Y. Hamada, M. Taira and J. Takahashi : Organ-Derived Dependence of Biomineralization in Type I Collagen Gel,, Key Engineering Materials, **192-195** (2001) 709-712

15) M. Nunogaki, M. Inoue and K. Kitahama: Preparation of thick functionally graded layers of ceramics by surface modification of tantalum and titanium using high temperature plasma processing, Mater. Trans., **42** (2001) 457-459

16) M.Inoue, M. Yamashita, K. Suganuma and M. Nunogaki : Surface transformation of zirconium to

ceramics with a graded composition by reactive plasma processing at elevated temperatures, J. Nucl. Sci. Technol., *in press*

17) T. Matsumoto, M. Okazaki, M. Inoue, S. Ode, C. Chang-chien, H. Nakao, Y. Hamada and J. Takahashi : Biodegradation of carbonate apatite/collagen composite membrane and its controlled release of carbonate apatite, IADR 2001, *in press*

18) M. Inoue, M. Nunogaki and K. Suganuma : Surface modification technology for TiAl alloys using reactive plasma process, Proc. 7th Japan International SAMPE Symp., *in press*

(review)

1) M. Inoue, J-Y. Kim, Z. Kato, N. Uchida, K. Uematsu, K. Saito : Development of direct observation method for internal structure in silicon nitride granule and green body, "*Shin-sozai*", pp.59-67, *Uchida Rokakuho* (1990) (*in Japanese*)

2) M. Inoue and K. Suganuma : Reinforcing mechanism of aluminide matrix composites, Boundary, **14** [3] (1998)39-45 (*in Japanese*)

3) M. Inoue and K. Suganuma : Mechanical properties of ceramic fiber reinforced aluminide matrix composites, Materia Japan, **37** (1998) 230-233 (*in Japanese*)

4) M. Inoue and K. Suganuma : Material designs of intermetallics for structural applications, Ceramics Japan, **34** (1999) 450-454 (*in Japanese*)

Acknowledgment

This study was carried out at National Defense Academy (April, 1993 – September, 1996) and at The Institute of Scientific and Industrial Research, Osaka University (October, 1996 –). The author is deeply grateful to Professor K. Suganuma and Professor K. Niihara for their kind guidance and helpful suggestions. Special thanks are given to Professors H. Koinuma, K. Uematsu, T. Yoshio, K. Oda and Y. Watanabe for their continuous advise and hearty encouragement.

The author would like to express his gratitude to Professors T. Oku, T. Sekino, T. Matsumoto, K. Ota, Drs. M. Nunogaki, S. Yamaguchi, H. Tanaka, Y-H Choa, T. Kusunose, T. Nakayama, Messrs. K. Tanihata, M. Kakuichi, M. Ohnishi and Misses. Y. Yuasa and N. Minami for their helpful support. The author's gratitude is extended to his best friends, Drs. H. Abe, N. Kitazawa and Mr. J. Tani, for their stimulating discussions.

Finally, the author is indebted to his parents for their understanding and support.

M. Inoue

Masahiro Inoue